ANALYSIS OF EXTREME PRECIPITATION EVENTS OVER THE EASTERN RED SEA COAST FOR RECENT AND FUTURE CLIMATE CONDITIONS

By

MOHAMMAD MOSAED EID ALAHMADI ALHARBI

A thesis submitted to University of Birmingham for the degree of

DOCTOR OF PHILOSOPHY

School of Geography, Earth and Environmental Sciences

College of Life and Environmental Sciences

University of Birmingham, UK

21 May 2018

UNIVERSITYOF
BIRMINGHAM

University of Birmingham Research Archive

e-theses repository

ABSTRACT

The investigation of extreme precipitation events over the western coast of Saudi Arabia is necessary to estimate their potential impact on both socioeconomic activities and the regional environment. The current study aims at understanding the atmospheric dynamics leading to extreme precipitation, to improve weather forecasting in the target region and the development of long-term adaptation policies.

Preliminary results reveal that extreme precipitation events in this region occur during the wet season (Nov–Jan). The synoptic mechanisms of these events are a function of the complex interaction between tropical, subtropical and middle-latitude dynamics. The synoptic dynamic processes were identified by a subjective study of the highest 30 extreme events. In addition, the weather circulation patterns (WCPs) of all extreme events were classified objectively by means of an empirical orthogonal function (EOF) analysis based on the mean sea level pressure. WCPs were linked with synoptic dynamic processes and teleconnected with large-scale climate variability modes. Furthermore, WCPs, precipitation and data regarding other atmospheric variables from different regional climate models were used to investigate future changes in extreme precipitation events under climate change.

The most important weather circulation patterns, which are associated with extreme precipitation events, were identified. The possibility of extreme precipitation events increases with great uncertainty.

هذا الإنجاز إهداء إلى أمي الغالية
وزوجتي الحبيبة وبناتي الحلوات وابنائي الرائعين
الاثنين ٥ رمضان ١٤٣٩ هـ

This achievement is dedicated to my precious mother, lovely wife, sweet daughters and wonderful sons.

21 May 2018

TABLE OF CONTENTS

TABLE OF FIGURES

ix

TABLE OF TABLES

LIST OF ABBREVIATIONS

ARST	Active Red Sea Trough
A1B	Low Emissions Scenario
A2	Intermediate Emissions Scenarios
AA	Arabian Anticyclone
AGT	Arabian Or Persian Gulf Trough
AL	Arabian Low
AOGCMs	Atmosphere-Ocean General Circulation Model
AP	Arabian Peninsula
AR4	IPCC's Fourth Assessment Report
AR5	Fifth Assessment Report
ASCII	American Standard Code For Information Interchange
B1	High Emissions Scenarios
BADC	British Atmospheric Data Centre
CDO	Climate Data Operators
CEDA	Centre For Environmental Data Analysis
CL	Cut-Off Low
CMIP	Coupled Model Intercomparison Project

CMIP3	Couple Model Intercomparison Project 3
CMIP5	Couple Model Intercomparison Project 5
COADS	Comprehensive Ocean-Atmosphere Data Set
CORDEX	Coordinated Regional Climate Downscaling Experiment
CORDEX-Africa	CORDEX Africa Domain
CORDEX-MENA	CORDEX Middle-East And North Africa Domain
CORR	Correlation Coefficient
CPC	Climate Prediction Center
DKRZ	German Climate Computing Centre
DMI	Dipole Mode Index
ECMWF	European Centre For Medium-Range Weather Forecasts
EM	Eastern Mediterranean
ENSO	El Niño/Southern Oscillation
EOF	Empirical Orthogonal Function
ESGF	Earth System Grid Federation
ESPI	ENSO Precipitation Index
ESRL	Earth System Research Laboratory
FMAM	February, March, April, May

GCMs	Global Circulation Models Or Global Climate Models
GPCC	Global Precipitation Climatology Centre
GPH	Geopotential Height
GTS	Global Telecommunication System
IOD	Indian Ocean Dipole
IPCC	Intergovernmental Panel On Climate Change
IPCC	Intergovernmental Panel On Climate Change
ISM	Indian Summer Monsoon
ISS	Integrated Sounding System
ITCZ	Intertropical Convergence Zone
JJA	June, July, August
JMASTEC	Japan Agency For Marine-Earth Science Technology
LL	Levant Low
MDs	Mediterranean Depressions
MEI	Multivariate Enso Index
METEX	Meteorological Data Explorer
MLs	Mediterranean Lows
MSLP	Mean Sea Level Pressure

NAH	North Africa High
NAO	North Atlantic Oscillation
NCAR	National Center For Atmospheric Research (USA)
NCDC	National Climate Data Center (Usa)
netCDF	Network Common Data Format
NOAA	National Oceanic And Atmospheric Administration (USA)
NSD	Normalised Standard Deviation
PCA	Principal Components Analysis
PME	Meteorology & Environmental Protection For Saudi Arabia
PSD	Physical Sciences Division
RCMs	Regional Climate Models
RCP8.5	Representative Concentration Pathway High Emission Scenarios
RGCM	Regional And Global Climate Modelling
RSCZ	Red Sea Convergence Zone
RSL	Red Sea Low
RST	Red Sea Trough
SH	Siberian High
SL	Sudan Monsoon Low Or Sudan Low

SOI	Southern Oscillation Index
SREX	Special Report Of Extreme Events
SST	Sea Surface Temperature
STJ	Subtropical Jet Streams
UT	Upper Atmospheric Level Trough
UTC	Coordinated Universal Time
UTC	Universal Time Coordinated
VIWVF	Vertical Integrated Water Vapour Flux
Wajh	Al-Wajh
WCPs	Weather Circulation Patterns
WCRP	World Climate Research Programme
WCSA	West Coast Of The Saudi Arabia
WGCM	Working Group On Coupled Modelling
WGI	Working Groups I
WGII	Working Groups Ii
WMO	World Meteorological Organisation

Chapter 1. INTRODUCTION

1.1.   Overview:

The rainfall amounts in the Arabian Peninsula are extremely scarce in some regions and low to medium in others, revealing a strong dependency of the precipitation distribution on topography and location. The Arabian Peninsula topography is highly complex and characterised by two long flat coastal plains, a basaltic plateau, vast deserts and high mountains. The climate in general is classified as subtropical (Al-Ahmadi and Al-Ahmadi, 2014), but is nevertheless influenced by multiple climate regimes, including influences of Mediterranean and tropical origin. Consequently, studies have shown significant relations to the Intertropical Convergence Zone (Kucera et al., 2013), the Indian Summer Monsoon (ISM) system (Fleitmann et al., 2004), synoptic systems like the Siberian High (Abdullah and Ibrahim, 1989), the Sudan monsoon Low or Sudan Low (SL) (El-Fandy, 1948), the Red Sea Trough (Black et al., 2010), and the Azores High (Vorhees, 2006), as well as from more dynamical features in the upper troposphere as the Subtropical Jet (Tippett et al., 2015).

There are two rainfall seasons, the wet and dry seasons, in the Arabian Peninsula. The *wet season* affects the whole region of the Arabian Peninsula from late autumn to late spring (June to September) (Almazroui et al., 2013), whereas the *dry season* affects only the southwest in summer (JJA) (Mashat and Basset, 2011). In addition, the rainfall amount decreases from west to east and from south to north over the Arabian Peninsula (Alyamani and Sen, 1993). However, the station-based annual rainfall amount is decreasing from south to north for the Red Sea Coastal zone, for example, the Gizan station in the south is mainly affected by the Indian Summer Monsoon in the dry season (Subyani et al., 2010). Further, it has to be

considered that precipitation at Gizan is relatively low (128 mm/year), compared to nearby stations in the mountains, such as Abha, where the mean annual precipitation is 229 mm (Almazroui et al., 2012b). In contrast, during the wet season, the rainfall amount is more homogenous between all stations across the Red Sea Coastal zone.

In a regional study of the Saudi Arabian climate, Almazroui et al. (2014) applied principal components and correlation analysis for mean temperature, diurnal temperature range and the monthly total precipitation, and suggested five climatic divisions for Saudi Arabia; Northern, Southern, Interior, Highland and Red Sea Coastal could be developed.

The Red Sea Coastal region is of utmost importance to Saudi Arabia. Aside from its high population, it is home to four of the most important cities: Makkah, regarded as the holiest city in the religion of Islam, Madinah, the second revered holiest city in Islam, Jeddah, the second largest city in the Kingdom of Saudi Arabia and the main port of the Kingdom on the Red Sea, and Yanbu, an important petroleum shipping terminal and home to three oil refineries, a plastics facility and several other petrochemical plants. This region has rapid population growth (Rahman et al., 2017) and a fast growing urbanisation due to the megaproject, King Abdullah Economic City, between Thuwal and Rabigh northward of Jeddah. In recent years, the Saudi government interest has increased in other areas on this coast. In the far south, Gizan City for Primary and Downstream Industries has been established, and in the far north, between Yanbu and Al-Wajh (Wajh), a plan has been established to develop this area to become the first leading tourism area on the Red Sea coast.

All these cities are regularly affected by extreme precipitation events which can cause destruction and loss of life and property (Subyani, 2011). Thus, extreme rainfall over the Arabian Peninsula plays an important role in any precipitation statistic and may be a

2

significant factor for semiarid regions (Vincent, 2008). In addition, the classification of extreme precipitation is difficult because of the irregularity of climate extreme events (Øystein et al., 2013), particularly in the arid and semi-arid areas, such as the Arabian Peninsula, because of the infrequent rainfall events, consequently leading to a lack of extreme rainfall cases (Ferro, 2007). Another difficulty arises due to the limited amount of available observational data for this region, which has short-term climate records and low-quality data (Easterling et al., 2000).

In recent years, researchers have shown an increased interest in anthropogenic climate change and the effects of climate change on the weather conditions and its impact on the environment, society and economy in many parts of the world. The world concern of the increasing in the temperature, because it influence on the climate regimes. Several Atmosphere–Ocean General Circulation Models have been established and are used to provide future climate change projections (IPCC, 2013). To date, most of these models are still low spatial (grid cells; vertical and horizontal direction) and temporal (time steps) resolution, which does not help to consider the local and regional scale factors that affect the climate, especially with extreme events (Giorgi et al., 2009). However, under the increasing demand on Global Climate Models and climate change effects, there is a need to increase the accuracy and resolution of these outputs by using dynamical downscaling or statistical downscaling for climate projection.

1.2.   Research Gap:

Most of the previous studies looking at the synoptic and mesoscale dynamic processes of extreme precipitation events over the western coast of Saudi Arabia have only been focused on the control of the Red Sea and carried out in Jeddah events, particularly the Jeddah 2009

3

event (e.g. Alkhalaf and Basset, 2013, Almazroui, 2011b, Almazroui, 2012, de Vries et al., 2016, de Vries et al., 2013, Haggag and El-Badry, 2013, Yesubabu et al., 2015). Up until now, no previous study has investigated the dynamic processes of extreme precipitation events over the southern and northwest coast of Saudi Arabia. In addition, there is no standard classification in Saudi Arabia specifically designed for extreme precipitation at daily accumulation.

However, the classification of large-scale weather circulation patterns is a statistical process to reduce the enormous dimensions of atmospheric variable data, such as mean sea-level pressure. It can be collected as common representative clusters so that it can be linked easily to other regional climate variables, such as precipitation (Jones et al., 2014). Furthermore, this classification makes data more spatially and temporally homogeneous by putting the spatial distribution of rainfall days, which are associated with the same weather circulation pattern, together in one group. As a result, the analysis variability bias is reduced.

To date, no previous study has classified extreme precipitation events along the West Coast of Saudi Arabia, but there are two studies which have investigated the classification of synoptic circulation patterns and linked it with rainfall over whole Saudi Arabia by objective classification method. One study by Almazroui et al. (2015a) used the principal component analysis in the wet season from October to May, and in another study, Kenawy et al. (2014) employed the automated Lamb weather type method in all seasons. The objective Lamb weather type scheme could be applied between ~30° −70° latitude (Jones et al., 2013). However, The objective Lamb weather type scheme is not suitable to apply below the 30° latitude because it depends on the vorticity (Jones et al., 1993) and also applies just for the daily mean sea level pressure (Milionis and Davies, 2008).

4

In addition, a number of further questions remain about the influence of anthropogenic forcing on the precipitation and extreme precipitation. Few researchers that have used the Atmosphere–Ocean General Circulation Models have been carried out on the Arabian Peninsula (e.g.Almazroui et al., 2017, Almazroui et al., 2016b). Moreover, no previous study has assessed the influence of global warming on the extreme precipitation over the Red Sea coast rather by used Atmosphere–Ocean General Circulation Models or the high resolution future climate projections by Regional Climate models or statistical downscale.

1.3.   Aim and Objective:

The overarching aims of this study are to:

- Diagnostic the extreme rainfall extreme precipitation events over Saudi Arabia's coastline along the Red Sea in practical time (wet season).

- Increase and improve the knowledge about the dynamics of atmospheric circulations which accompany these events, thereby providing a more comprehensive picture to identify its synoptic circulation patterns by subjective and objective classification.

- Use these classifications as tools to assess potential future climate changes in amount and frequency of extreme precipitation events under influence of anthropogenic forcing over this region.

This study employed survey methodology to investigate the extreme precipitation events in the wet season over the West Coast of Saudi Arabia and the impact of the warming world on its frequency and amount in the future. The main objectives are as follows:

- First, diagnostics of observed and historic extreme precipitation events along the west coast of Saudi Arabia will be performed and the wet season period will be identified.

- Second, synoptic dynamic processes that are associated with extreme precipitation events during the wet season will be subjectively identified.

- Third, the weather circulation patterns objectively associated with extreme precipitation events during the wet season will be classified and linked with synoptic dynamic processes, as well as the teleconnection with large scale climate variability modes.

- Finally, these classifications will be used as the tool to investigate the change in extreme precipitation events under climate change by different regional climate models, which are nested into different global climate models.

Furthermore, the research data are drawn from three main sources: rain gauge observations from weather station data held at the archive of the General Authority of Meteorology & Environmental Protection for Saudi Arabia (PME, 2015), reanalysis data produced by the European Centre for Medium-Range Weather Forecasts (Dee et al., 2011) and the Regional Climate models data from the Coordinated Regional climate Downscaling Experiment data (Giorgi et al., 2009).

1.4. Thesis Outline:

The thesis is divided into 8 chapters and have been organised in the following way;

- **Chapter 1** includes an introduction and explains the research gap, aim, objectives and the outlining of the thesis.

- **Chapter 2** contextualises the research by providing background information on climate extremes definition (Section 1.1), the west coast of the Saudi Arabia Area Study, (Section 1.2), extreme precipitation events over the west coast of the Saudi Arabia (Section 1.3), the synoptic-scale dynamic processes of extreme precipitation

events over the west coast of the Saudi Arabia (Section 1.4), past and future changes in precipitation over the study area (Section 1.5), high-resolution future climate projections (Section 1.6) and teleconnection patterns with precipitation over WCSA (Section 1.7).

- **Chapter 3** describes the specific data and methods by which the research and analyses were conducted. It introduces and describes the historical observation precipitation, ERA-Interim reanalysis and regional climate downscaling data, the teleconnection Indices (Section 3.2), and the methodologies used in this research (Section 3.3).

- **Chapter 4** illustrates the diagnostics of observed and historic primary precipitation characteristics over WCSA and identifies extreme precipitation events occurrence and determines the wet season time (Section 4.2). It also shows diagnostics synoptic dynamics of extreme events (Section 4.3) and analyses of subjective selected extreme event case studies (Section 4.4). The final section summaries and the significant findings.

- **Chapter 5** evaluates the performance of ERA-Interim reanalysis by historical observed precipitation dataset and Global Precipitation Climatology Centre data (Section 5.2) and evaluates atmospheric data from several regional climate model hindcast simulations in two domains (CORDEX-MENA and CORDEX-AFRICA domain) using ERA-Interim as reference over area study (Section 5.3) and the summary (Section 5.4).

- **Chapter 6** provides an objective classification of weather circulation patterns by generating weather circulation patterns (Section 6.3) to assess a spatial and temporal weather circulation patterns distribution (Section 6.3) and diagnostics characteristics of these weather circulation patterns (Section 6.4). Links these weather circulation patterns with individual extreme precipitation cases (Section 6.5). Generates weather

circulation patterns as section 6.3 but based on ERA-Interim precipitation days (Section 6.6). Furthermore, (Section 6.7) linking extreme rainfall with large scale modes and the final section summaries and the significant findings.

- **Chapter 7** identifies the Anthropogenic Climate Change signal of extreme precipitation in the west coast of the Saudi Arabia by future climate change predictions models from CORDEX-AFRICA (Section 7.2) and CORDEX-MENA (Section 7.3) domains.

- **Chapter 8** discusses and concludes the research findings and suggests future research and recommendations.

Chapter 2. LITERATURE REVIEW

2.1.   Climate Extremes Definition:

The research on extreme climatic events is a very important topic, not just because of its impact on social, economic, and ecological systems and the natural physical environment, but also because the complexity of the processes involved. These require consideration of different scales, such as small- and large-scale weather patterns, modes of variability and thermodynamic processes (Stocker et al., 2013). Related research has shown an improvement in the scientific knowledge of some fundamental atmospheric processes and help e.g., to develop numerical weather and climate models (Stephenson, 2008).

According to the Special Report of Extreme Events (SREX), which was prepared by Working Groups I (WGI) and II (WGII) of the Intergovernmental Panel on Climate Change (IPCC), weather and climate extremes are rare events at a specific time and location when a weather observation variable exceeds its climatic threshold value during a specified reference period. This threshold varies from place to place in an absolute sense (Field, 2012). It refers to two terms; extreme weather events which happen during a small time scale, such as hours to weeks, whereas an extreme climate event is a set of extreme weather events which extend for a long period of time, such as a season (Stocker et al., 2013). There are considerable disasters that sometimes coincide with these extreme events, which may be produced by signal variables, such as for heatwaves, but more often result from several variables and an accumulation of distinctive dynamical weather systems, e.g. extra-tropical cyclones or Hurricanes.

Extreme weather events are a result of the interaction of many processes: rapid growth of storms due to instabilities, displacement of a weather system (location or time), simultaneous coincidence of several non-extreme conditions, localisation of activity into intermittent regions, persistence or frequent recurrence of weather leading to chronic extremes and/or natural stochastic variations (Solomon, 2007). Understanding these processes leads to improve diagnostics and knowledge of extreme event behaviours (Stephenson, 2008).

Despite the fact that several different elements (rate of occurrence, magnitude (intensity)), temporal duration and timing, spatial structure, and multivariate dependencies) may form extremes, these events are very often described by use of a single climate variable, such as maximum temperature, maximum wind speed at landfall or precipitation (Stephenson, 2008). Some of these climate variables, such as extreme precipitation events, are difficult to provide in a single extreme definition because it involves various areas of the world, which have several aspects to be considered in the definition and analysis (Field, 2012). Another problem is to account for the regional background climatology in defining a threshold for the definition of extremity.

However, when studying extreme precipitation, the values that characterise the presence of the indicator threshold at the far distribution tail are used in the frequency or amount (Zhang et al., 2011). Often relative thresholds, such as the probability of occurrence e.g. 90th percentiles and a specific threshold (definition of thresholds vary), are used to defined extreme precipitation events quantitatively (Kumar et al., 2015).

2.2.   The West Coast of the Saudi Arabia (WCSA) Area Study:

The West Coast of the Saudi Arabia area, hereafter referred to as WCSA, comprises of the western part of the Arabian Peninsula (AP), and mainly consists of sandy beaches of the

eastern Red Sea coastal plain. It is bounded by a region with a very complex topography from the east comprising mountain ranges to the south (e.g. Jabal Al-Sodah, 3,015 m high), to the north (e.g. Jabil Allawz, 2,594 m high), the Hijaz mountains (ranging between 2,100 m and 2,500 m high), and lava fields, islands, beaches and steep valleys (SGS, 2012).The long coastal area (15°N and 35°N) is subject to significant variations in the weather along the coast, as shown in Figure 2.1.
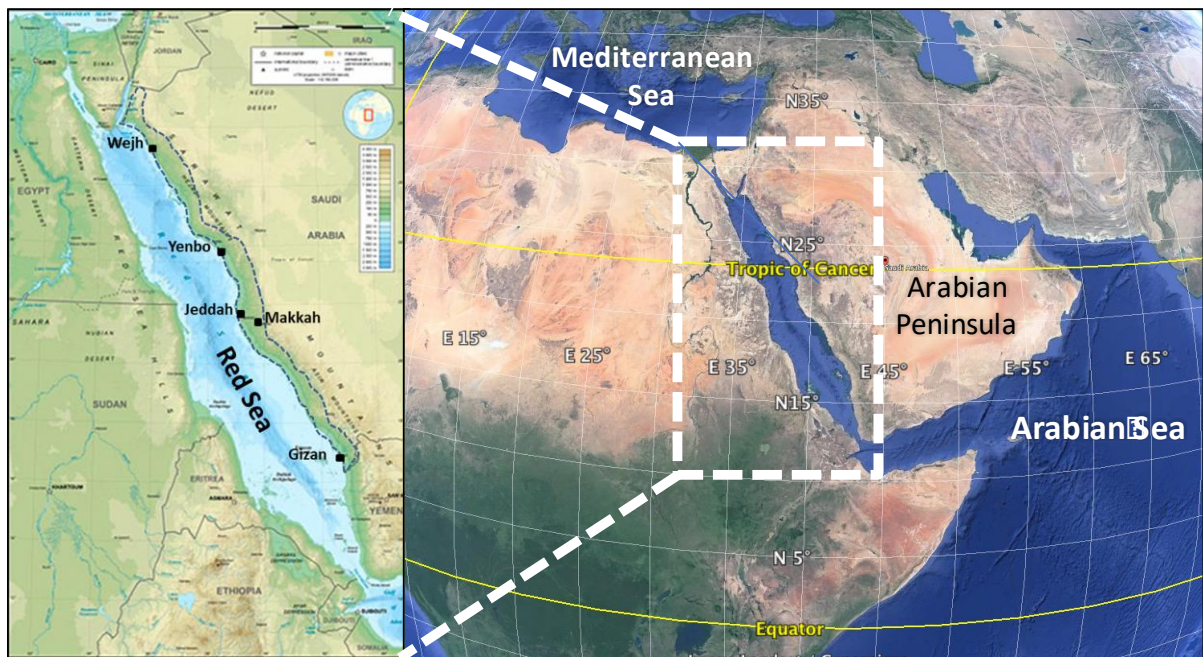
Figure 2.1. Saudi Arabia map showing the location of the 5 weather stations.

AlSarmi and Washington (2011) divided the AP into two climate zones: the monsoonal area south of 20°N and the non-monsoonal area north of 20°N. Ghulam (2007) offered an alternative division of the AP, dividing it into three zones based on the number of days of heavy thunderstorms. This created a zone north of 26°N, south of 21°N, and a central zone (26°N - 21°N). Athar and Ammar (2015) used two domains over AP, southern (12–22°N) and northern (22–32°N), to analyse the moisture flux transport.

The central part of the eastern Red Sea is where there is an exchange between northward warm advection from the tropical and southward region and cold advection from the mid-

11

latitudinal region (Kenawy and McCabe, 2015, Alkhalaf and Basset, 2013). In this region, the Red Sea Convergence Zone (RSCZ) is generated in winter by the interaction between the south-easterly airstream flow from the Arabian Sea and the northerly to north-westerly airstream flow from Mediterranean Sea (Sarhan, 2006, Pedgley, 1966).

Furthermore, this area is the gate for the SL to affect central Saudi Arabia in spring (Ghulam, 2007). In addition, the Red Sea Trough (RST), which is formed over the southern Red Sea and extends to the Eastern Mediterranean and the Levant (Tsvieli and Zangvil, 2007), influences the central part of the eastern Red Sea which is the main factor for thunderstorm formation in this area (Ghulam, 2007).

2.3.   Extreme precipitation events over WCSA Area:

On November 26 2009, 122 people were killed and 350 reported missing in Jeddah on the central west coast of Saudi Arabia following a rare heavy rainfall event (Haggag and El-Badry, 2013), where more than 90 millimetres of rain fell in just four hours (Alkhalaf and Basset, 2013). This extreme event received considerable attention by many researchers which focussed on the role of Red Sea trough (de Vries et al., 2013), the diagnostic analysis of the interaction between midlatitude and subtropical systems (Alkhalaf and Basset, 2013), mesoscale numerical studies (Haggag and El-Badry, 2013, Yesubabu et al., 2015), and the recent study of the synoptic-scale dynamics of this extreme precipitation event (de Vries et al., 2016). This incident was attributed to water vapour movements, which are formed by evaporation from the Arabian Sea and the Red Sea (Haggag and El-Badry, 2013). These movements mainly occur in the lower atmosphere and the low-level jet and Hejaz plateau to the east of the Jeddah coastal area, which played an active role in the enhancement of deep convection (Ban et al., 2009).

12

In addition, similar extreme events also affected Jeddah on 30 December 2010 and 26 January 2011 (Yesubabu et al., 2015), with 4 and 11 people killed, respectively (Haggag and El-Badry, 2013). Yanbu, which is located on the north of Jeddah, recorded the heaviest rainfall in its history which was 92.5 mm on 22 December 2009, according to daily historical data for Saudi Arabia Meteorological stations from General Authority of Meteorology & Environmental Protection (PME).

Further, Wajh, which is the most northern city on the coast, recorded 116.4 mm of rainfall on November 17, 1996, which was the highest amount recorded during the history of observation over the western costal of Saudi Arabia (Almazroui, 2012).In the latest study of the Jeddah Disaster in 2009, Haggag and El-Badry (2013) expected that, in the future, the Jeddah area will be prone to severe rainfall events similar or worse to the 25 November 2009 event. This is because of the expected moving of the ITCZ towards the north and the warming of the Arabian and Red Sea

On the other hand, Gizan, located in the south, has recorded many floods which resulted in a number of deaths and widespread damage. For example, the floods in August 2003, April 2004 and July 2010 (Tekeli and Fouli, 2016) resulted in 13000 affected pope, 5 and 14 deaths, respectively (de Vries et al., 2016). It also has many high rainfall events that occur during winter, as it only has two seasons (Hasanean and Almazroui, 2015). Gizan has the highest annual precipitation along the coast by 127mm/year mainly due to the Indian Ocean monsoons between October and March (Amin et al., 2016). Further, this area is also affected by the interaction between cold air with Siberian High (SH) and warm humid air from SL during winter time (Furl et al., 2014).

2.4. The synoptic-scale dynamics of WCSA extreme precipitation events:

The location of WCSA and its topography characteristics are subject to complex meteorological interactions resulting from large-scale processes, such as the Indian monsoon, and small scale processes, such as the circulation of land and sea breeze. For example, the climate along the northern portion of the WCSA shelf is arid and may be considered a drier area after Empty Quarter Desert in the Arabian Peninsula (Hasanean and Almazroui, 2015), and may be impacted by the weak Mediterranean or North African weather systems from November to April (Gosling et al., 2011). The Red Sea experiences strong evaporation and very little precipitation and is subject to northwest winds throughout the year, which are affected by the strong diurnal land–sea breeze cycle from the coastal regions (Sofianos and Johns, 2003). In the winter, because of the gap in the mountain ranges, the speeds of easterly zonal surface wind jets in the north area of the Red Sea reach over $15 m.s^{-1}$ (Jiang et al., 2009). In addition, the Red Sea is an active region for enhanced cyclonic activity during the winter (Maheras et al., 2001).

In contrast, the monsoon weather system heavily influences the climate of the southern portion of the eastern Red Sea shelf, especially in summer. This produces large amounts of rainfall on elevated land regions, due to the favourable latitudinal positions of the Inter Tropical Convergence Zone (ITCZ), which is located further north, at a greater distance from the equator (Dayan et al., 2001, Scott, 2013).

Meanwhile, the central part of the WCSA is subject to meteorological phenomena created by the exchange between tropical and subtropical systems. In this region, the Red Sea Convergence Zone, climatic features predominate in winter that arise from the interaction

between the south-easterly airflow from the Arabian Sea and the north-westerly airflow from the Mediterranean Sea region (Pedgley, 1966). November is the wettest month for the majority of the stations on the WCSA, except for Gizan (Almazroui et al., 2014), where rainfall occurs during both the winter and the summer seasons (Almazroui, 2011a). This area is also the gateway to the SL influences, which is the east African/subtropical thermal low-pressure system (Tsvieli and Zangvil, 2005). This low pressure system enters central Saudi Arabia in springtime (Ghulam, 2007).

An additional feature of significance is the RST, which is a surface trough in the lower layers of the atmosphere and extends from the southern Red Sea along the mountains of the Arabian Peninsula into the Eastern Mediterranean and the Levant (Tsvieli and Zangvil, 2007). Once the low level trough is interacting with a mid- to upper-troposphere trough from the mid-latitudes over the southern Mediterranean basin (Kahana et al., 2002), this feature is transformed and called Active Red Sea Trough (ARST). These active systems can lead to heavy precipitation and flooding throughout the countries of the eastern Mediterranean (Krichak et al., 1997) and WCSA (Krichak et al., 2012), typifying tropical-extratropical interactions in this region (Ulbrich et al., 2012). de Vries et al. (2013) identified RST as a trough which extends from SL over equatorial Africa to the southern Red Sea and extends northward the eastern Mediterranean.

However, the RST is also attributable to local topography, thermal force factors, and the moist airflow from the Red Sea (Yesubabu et al., 2015, de Vries et al., 2013). The highest frequency of events occur during late autumn to early spring (Alpert et al., 2006), with the highest concentration occurring in November (Tsvieli and Zangvil, 2005), and, in some cases, its influence extends to the north of the AP and into western Iran (Ghaedi and Movahedi, 2013).

The RST axis oscillates between the east and west coast of the Red Sea where it may be placed over the eastern coast in spring and to the western coast in winter and early autumn (Awad and Almazroui, 2016).

According to de Vries et al. (2013), the ARST occurs when the semi-permanent quasi-stationary RST extends northward between two intensified high pressure systems. One is the North Africa High (NAH), which is a subtropical anticyclone over North Africa at lower- and middle-tropospheric levels and is the extension from the North Atlantic Subtropical High (Azores High) and the intensification Arabian Anticyclone (AA) which is a quasi-stationary subtropical anticyclone over the AP at lower- and middle-tropospheric levels (de Vries et al., 2016) encountering a transient Mid-latitude Upper Atmospheric Level Trough (UT) and an intensified the Subtropical Jet Streams (STJ). These process enhanced moisture transport from the adjacent seas and favours upward motions due to convergence in the low and the divergence in the upper atmospheric level. The ARST can be represented schematically as shown in Figure 2.2.

Many studies decreed and identified these dynamic processes of ARST. The movement of the lower tropospheric, AA is associated with the movement of Siberian High (SH), which is located in central Asia and dominant on Arabian Peninsula during the winter (Hasanean et al., 2013). This movement enhances the AA using the cold air flowing through the Hindu Kush Mountains (Jiang et al., 2009).In the mid-level of tropospheric, the UT extends southward in the winter (Funatsu et al., 2008) to bring the cold polar air over lower latitudes (Kahana et al., 2002), which causes unstable conditions over the Eastern (Tsvieli and Zangvil, 2005) and southern Mediterranean (Xoplaki et al., 2012).In the upper level of tropospheric, the STJ is

displaced southwards from a latitude of 36°N during the transitional season to 28°N (Dayan et al., 2001).
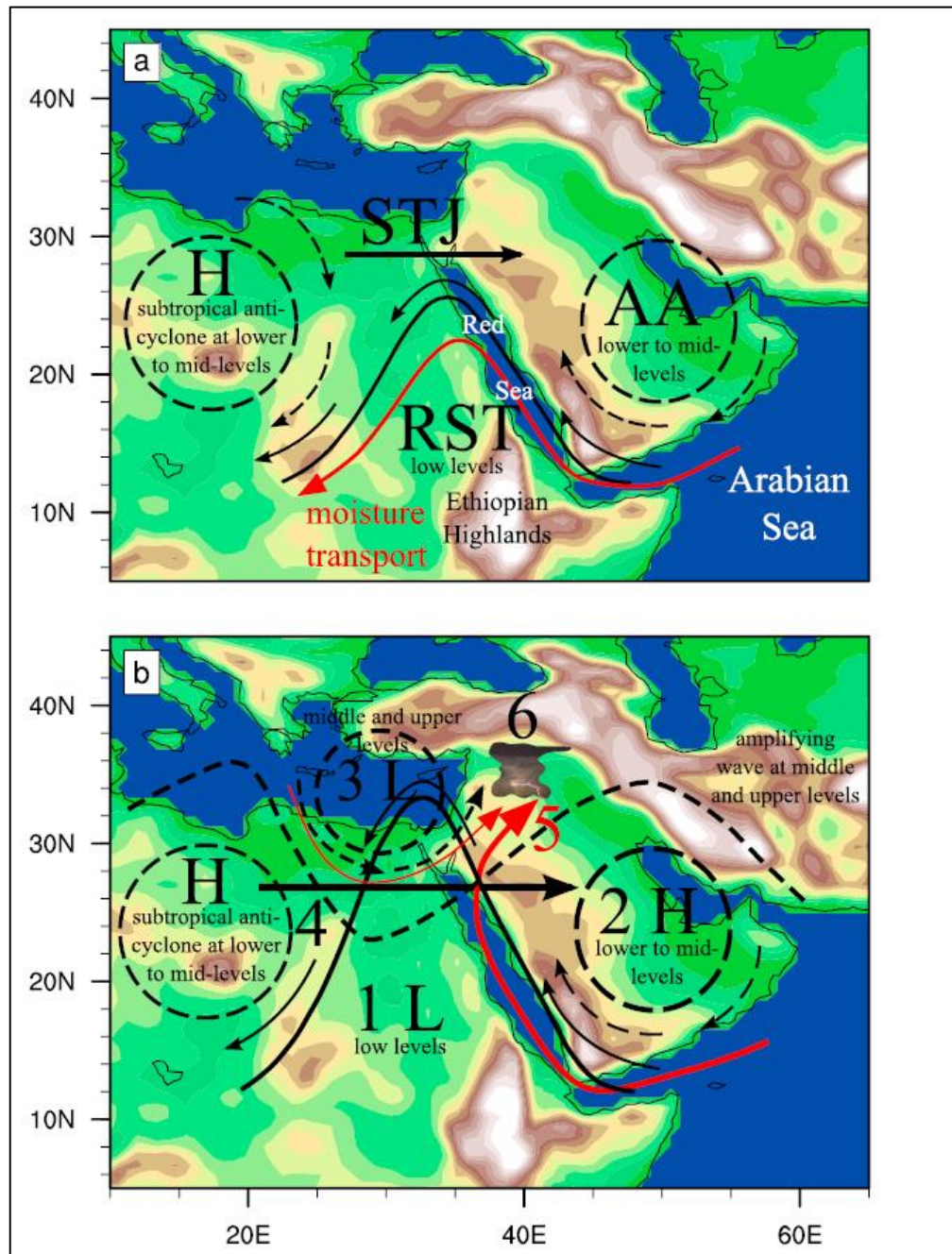
Figure 2.2. Schematic representation of (a) the low-level circulation climatology of ARST (b) the ARST associated dynamical factors; 1.RST, 2.AA, 3.UT, 4.STJ, 5.moisture transportation, 6.upward motions (from de Vries et al., 2013).

This brings low pressure systems over the Mediterranean Sea region to the AP in the winter (Kumar et al., 2016). These Mediterranean Lows (MLs) or the Mediterranean Depressions (MDs) travel from west to east (Hasanean et al., 2015), which are midlatitude extra-tropical

17

cold cyclones (Dayan and Morin, 2006). Sometimes these cyclones move eastwards, such as the Cyprus Low, which originates over the eastern Mediterranean, or in more intensive processes it goes eastward over the Levant and North Saudi Arabia (Lionello et al., 2006), termed the Levant Low (LL).

In addition, the extreme precipitation events in the Middle East (ME) can be triggered by tropical-extratropical interactions associated with large scale phenomena (de Vries et al., 2013), such as the extended cloud bands along the STJ from ITCZ, so called Tropical Plumes (Knippertz et al., 2003, Ziv, 2001).

2.5.   Teleconnection Patterns with precipitation over study area:

Large-scale climate teleconnection patterns are widely known in both hemispheres to influence regional and local weather and climate conditions. There are many climate variability indices available to use as diagnostics of large-scale climate variability. Some of these indices measure the change in the average value of a single atmospheric variable, such as Indian Ocean Dipole (IOD). The IOD index is based on sea surface temperature (SST) anomalies, such as when the SST is warmer or cooler than usual in the eastern or western Indian Ocean (Saji et al., 1999). In addition, some indices are based on variations in the strength of higher and lower pressure systems such as North Atlantic Oscillation (NAO). This index uses empirical orthogonal function analysis to determine the MSLP anomalies between two stations over the Northern Atlantic Ocean, one in Iceland and one in the Azores (Jones et al., 1997); it also measures anomalies between winters (Hurrell, 1995). Furthermore, some indices combine several observed fields. Such indices include the Multivariate ENSO Index (MEI), which uses six atmospheric variables: MSLP, zonal (u) and meridional (v) components of the surface wind, SST, surface air temperature and total cloudiness fraction of the sky

18

(Wolter and Timlin, 2011). This index is one of many indices that are used to monitor El Niño/Southern Oscillation (ENSO) variability such as the Nino1+2, Nino3.4 and Nino4 indices, which are derived from SST anomalies.

Several studies have investigated the relationship between large scale climate teleconnection patterns and precipitation. For example, Schubert et al. (2008) examined the impact of ENSO on intensity of extreme precipitation events in wintertime over the United States using the time series of the principal components associated with the leading 6 empirical orthogonal functions of precipitation. In a previous study, Price et al. (1998) found a link between the El Niño phenomenon and the precipitation over some parts of the Middle East. Furthermore, (Mariotti et al., 2005) found a relationship between precipitation and ENSO over some regions in Southwest Asia, Northern Africa and Southwest Europe in autumn. In addition, several studies have found a strong relationship between NAO and precipitation over Europe and some parts of the Mediterranean region and the Middle East in winter time (Hurrell et al., 2003, Yadav et al., 2009), for example, Krichak and Alpert (2005) found that the increase in precipitation over the western part of the Mediterranean region has been linked to the negative trend of the NAO.

However, very few studies have examined this relationship over the Arabian Peninsula, particularly in the context of extreme precipitation events. Many of these studies included the Arabian Peninsula as the part of large scale region, such as the Middle East (Hurrell et al., 2003, Price et al., 1998), Southwest Asia (Mariotti et al., 2005) or Arab regions (i.e. North Africa and Arabian Peninsula) (Donat et al., 2013). Some of these studies provided reasonably consistent evidence of the relationships between teleconnection patterns and extreme weather over the Arabian Peninsula, which will be discussed in the following section.

19

Results from one study indicate a strong statistical relationship between ENSO and the rainfall over Southwest Asia in autumn (Mariotti et al., 2005). In a study examining Arab regions, Donat et al. (2013) found that the relationship between ENSO and climate extremes indices (i.e. annual sum of daily precipitation>99th percentile and temperatures; warm day when maximum temperature >90th percentile and cold night when minimum temperature <10th percentile) are found to be stronger than those between NAO and the extremes in the Arabian Peninsula. They also found that these relationships were stronger for the temperature indices compared to the precipitation indices in general. Further, Krichak et al. (2014b) found positive correlations between ENSO and the moisture flux transport from tropical Africa and the Indian Ocean to Arabian Peninsula, and these were associated with Red Sea troughs during the October–November months. These results are similar to other studies that showed a strong relationship between net atmospheric moisture flux into AP from adjacent sea areas and the concurrent positive IOD and El Niño events (Chakraborty et al., 2006).

Kumar et al. (2016) also corroborated the findings of the previous studies of a strong relationship between ENSO and rainfall over the Arabian Peninsula and the transfer of moisture with the western winds of the adjacent seas that coincide with this phenomenon. They added that there is a clear change in the phase of the Rossby wave which affects the jet stream and shifts it over the Arabian Peninsula. In a recent study, Kang et al. (2015) used Global Climate Models to investigate the average Arabian Peninsula rainfall and link it to ENSO over 6 months from November to April during 60 years. They found that rainfall was negatively correlated with ENSO from 1950 to 1979 and positively correlated to ENSO from 1981 to 2010 and that this depended on the magnitude of the Indian Ocean and Pacific SST anomalies. In addition, the negative geopotential height anomalies at 200hPa, which is

accompanied with positive ENSO index (El Niño events), shifted subtropical jet streams over Arabian Peninsula, which then increased precipitation over the region.

2.6. Past and future changes in precipitation over study area:

The IPCC reports are significant publications in climatology, especially with regard to climate change. Their preparation is based on a significant number of government and independent researchers around the world. The IPCC's Fifth Assessment Report (AR5) is based on climate system observations, paleoclimate archives and theoretical studies of the Atmosphere-Ocean General Circulation Models (AOGCMs), also known as Global Circulation Models or Global Climate Models (GCMs). The IPCC's Fourth Assessment Report (AR4) and the IPCC Special Report on Managing the Risks of Extreme Events and Disasters to Advance Climate Change Adaptation (SREX) are also important sources for data on extreme climate events (Stocker et al., 2013). The IPCC SREX report shows that anthropogenic influences on climate extremes variables (temperature, precipitation and wind). For example, there has been an overall increase in both the number of heavy precipitation events and extreme daily maximum temperatures on the global scale, while having low confidence in observed trends in small spatial-scale phenomena (Field, 2012). However, responsibility for all climate extremes cannot be placed on anthropogenic climate change (Peterson et al., 2012).

Accordingly to one long-term study, Lee (2011) suggests that aerosols increase the frequency of precipitation events in convective clouds, which grow deeper than cleaner clouds (L'Ecuyer and Jiang, 2011, Tao et al., 2012); however, the direct and indirect effects of anthropogenic aerosols impact the microphysical, amount and lifetime of clouds (IPCC, 2007). Moreover, many studies have shown that land changes the impact of climate forcings at the local, regional and global scales (Ashley et al., 2012, Pielke et al., 2002). The evaporation rate

21

increases as the global temperature increases. For every 1°C increase in global temperatures, there is a 7% increase in the lower troposphere moisture, in accordance with the Clausius–Clapeyron equation (Trenberth et al., 2003).

However, due to the increased availability of moisture in the atmosphere because of global warming, medium-to-low confidence is expected for increased extreme precipitation events at the global level, despite a decrease in the mean total precipitation (Gershunov et al., 2013). Changes projected by the Coupled Model Intercomparison Project Phase 5 (CMIP5) confirm there is an increase in the global mean of heavy precipitation events by 5 to 10% per °C of warming, with substantial variations between the regions of the world. However, this projected change is more frequent and intense in warmer areas of the world (Stocker et al., 2013)

From this perspective, the eastern Red Sea coast region has rapidly growing urban areas, and this population and industrial growth contributes directly towards increasing greenhouse gas emission, as well as a hot spots of dust generation. This is notable particularly between 21°N and 27°N (Tao et al., 2013), which play important role in the thermal balance and affects air circulation over the Red Sea (Kalenderski et al., 2013). Furthermore, several studies have confirmed the warming of the Arabian Sea and Red Sea in the last decades (Nandkeolyar et al., 2013). According to Raitsos et al. (2011), the Red Sea temperature has increased sharply by 0.7°C since 1994, faster than the world average which shows increases of 0.5°C since the mid-1970s. Consequently, the moisture will increase as evaporation increases. Recent research has shown that the moisture over the Red Sea has increased from the late 1990s until the 2010s (Zolina et al., 2017), and the growing intensity of heavy precipitation events

over the Arabian Peninsula is the result of moisture brought from the Arabian Sea and the Red Sea (Kumar et al. 2015).

2.6.1. Recent past observed trends:

The first analysis study of climate extremes indices in Middle East was reported by Zhang et al. (2005), who found that trends in precipitation indices are negligible. Furthermore, no significant changes in rainfall over the Arabian Peninsula could be identified, except for heavy precipitation which decreased during 1986–2008 (AlSarmi and Washington, 2013). The recent past trends in precipitation and temperature over all parts of Saudi Arabia have been investigated by Athar (2014), who found that the precipitation in most stations in Saudi Arabia showed no significant trends as temperature with no statistically significant decadal trends in extreme precipitation indices such as extremely wet days when annual total precipitation amount from days (mm) > 99th percentile (R99p) and very wet days when annual total precipitation amount from days (mm) > 95th percentile (R95p).

A recent study focussing on southwest Saudi Arabia, found that wet day counts during the period between 1985 to 2011 was a significant declining trend in the majority of the region, especially the station on the Asir mountain, but also showed trend where it was increasing in the Gizan station on the Red Sea coastal plain (Furl et al. (2014). Almazroui et al. (2012b) also found that there has been a linear decrease (6.2 mm per decade) in the rainfall for Saudi Arabia from 1978-2009, while there is a notable increasing trend along the western coast of the Arabian Peninsula during the 2000–2009 decade, compared to 1980–1989.

In another study, Kenawy and McCabe (2015) evaluated the performance of GCM based rainfall products and gauge based rainfall products over Saudi Arabia and investigated annual and seasonal rainfall trends of observation and the different products. They found a

23

decreasing trend of annual rainfall from 1965 to 2005 in observation data and the majority of gauge-based products, whereas there was a slight increase in two of the gauge-based products and a significant increase in all three GCM-based products. In contrast, the increase of the observed and some of the gauge-based products rainfall are defined with just one GCM-based product, which is EC-Earth in winter season, while another gauge-based and GCM based products suggest a slight decrease (Kenawy and McCabe, 2015).

Another example of observed trends is the analysis of annual frequencies of the synoptic systems, such as RST, which is associated with extreme precipitation events over East Mediterranean regions and Arabian Peninsula. The frequencies of this synoptic system increased since the 1960s (Alpert et al., 2004). In another regional study, which compared two periods (1964–1985 and 1986–2007), Shentsis et al. (2012) found that the frequency and magnitude of RST events increased during this time period.

2.6.2. Future climate change projections:

On the other hand, Almazroui (2013) studied the probabilistic projections of future precipitation changes in Arabian Peninsula for period from 2021 to 2070 using low emissions scenario (A1B) and showed that these regions may experience more extreme rainfall events over the central and southern parts of WCSA. Another study by Almazroui et al. (2016b) used an ensemble combining of 20 GCMs data from the Couple Model Intercomparison Project 3 (CMIP3) for three projections of future climate change: low, intermediate and high emissions scenarios (A1B, A2 and B1). They showed that there is a strong decline in the precipitation in the northern part of the Arabian Peninsula during the winter, which is affected by the Mediterranean climate.

24

On the other hand, there is a strong increase in precipitation in the southern part during the summer. Overall, an increase in summer and a decrease in the winter precipitation is simulated in these models for the whole of the Arabian Peninsula. Nevertheless, the rate of mean annual rainfall is decreasing on the Arabian Peninsula by 1.35%, but has increased by 1.2% in the southern parts (Almazroui et al., 2016b).

A recently published article by Almazroui et al. (2017) used 22 GCMs of CMIP5 for high-emission scenarios (B1) to assess the projected changes in precipitation over the Arabian Peninsula. A large increase in the projected signal of the annual total precipitation over the southern part of Arabian Peninsula, including the coastline, was found. Further, this increasing rate gradually reduced from south to north and along the Red Sea coastline. In addition, the annual change in extreme precipitation amounts is projected to increase along the Red Sea coastline, with a low negative change over a portion of the northern region (Almazroui et al., 2017). This study partially contradicted the findings by Almazroui et al. (2016b) who used CMIP3.

2.6.3. Summary of past and future change:

Thus, in summary, the changes in observed precipitation indices trends are insignificant, with a notable increasing trend along the WCSA during the last decade. In addition, the overall findings of climate change projection suggest with considerable uncertainty that precipitation is increasing in the southern and central region of WCSA and decreasing in the northern part; it is increased in winter and decreased in summer.

However, these findings are based on only a few GCMs that offer partial, relatively coarse resolution and focus on a large area of the Arabian Peninsula without sufficient consideration of location and topography. The consequence of these few findings is that further research is

needed into climate projections over the Arabian Peninsula, particularly with focus on individual areas with similar topographic characteristics, such as WCSA, by the higher resolution of GCMs.

2.7.   High-resolution future climate projections:

Although GCMs have succeeded in assessing climate change in many studies, it is still difficult to deliver and interpret these results effectively on a regional scale (Giorgi et al., 2009). This is not surprising, given the difficulties encountered in assessing extreme events, especially in those with complex topography and coastlines (Giorgi and Gutowski, 2015). For these reasons, there is an obvious need for dynamic downscaling by Regional Climate Models (RCMs) to add further detail to the GCM analysis (Iqbal et al., 2016). This is especially true for the generation and analysis of extreme events in data-sparse regions.

The Coordinated Regional Climate Downscaling Experiment (CORDEX) is a framework designed for many different domains around the world (Giorgi et al., 2009). The Arabian Peninsula has been included in three of these domains, namely (CORDEX-Africa) for Africa and the Middle East (Hewitson et al., 2012, Kim et al., 2011), (CORDEX-WAS) for South Asia and Middle-East regions (Iqbal et al., 2016, Ghimire et al., 2015) and (CORDEX-MENA) for Arab regions, which covers Middle-East and North Africa regions (Bucchignani et al., 2015b, Bucchignani et al., 2015a, Almazroui et al., 2015b, Almazroui, 2016, Zittis et al., 2014). The Methodology and Data chapter provides a list of all RCMs and GCMs. It also details the model simulations that are available for the area being studied.

Nevertheless, only a few studies have analysed the climate projections for precipitation and climate extremes over the Arabian Peninsula made by CORDEX models, and there is a lack of regional climate downscaling experiments over the CORDEX-MENA domain (Bucchignani et

al., 2015b). However, Almazroui et al. (2016a) recommended the Regional Climate Model RegCM to study high-resolution climate change projection for the future period over the CORDEX-MENA. Moreover, Bucchignani et al. (2015b) showed that RCM COSMO-CLM is reasonably capable of reproducing the main climate features over the CORDEX-MENA domain at a spatial resolution of 0.44° and has low biases when compared to other state-of-the-art RCMs. The simulation of variability and change in extreme climates, such as extreme precipitation and strong wind, are more realistically described by RCMs than by GCMs (Christensen et al., 2001).

Chapter 3. DATA AND METHODOLOGY

3.1.   Overview:

This chapter of the dissertation is divided into two sections. The first section has described observational and modelling data which are collected from several sources. The second section has explained different methods that have been proposed to analysis the precipitation data, identify the extreme precipitation events, diagnostic manually the atmospheric dynamic processes which associate with extreme precipitation events and classify objectively the weather circulation patterns.

3.2.   Data:

3.2.1. Historical Precipitation Data:

The daily precipitation data used in this research was based on rain gauge observations from weather station data, archived at the General Authority of Meteorology & Environmental Protection (PME) for Saudi Arabia (PME, 2015). To measure precipitation differences across the region, this researcher selected stations located on the WCSA at Wajh, Yanbu, Jeddah and Gizan and a station in Makkah (which is 90 km inland from Jeddah) to use as sources of information. No stations located on mountaintops were included, because topographical effects are likely to have an important impact on the distribution of precipitation and therefore rainfall characteristics may be subject to complex regional and seasonal variations (Wheater et al., 1991). Since the variation in annual mean precipitation between the coastal regions and the mountains is too high (Subyani et al., 2010), the identification of homogeneous precipitation zones based on homogeneous precipitation distributions could

provide a better, more comprehensive picture of precipitation characteristics for the WCSA region.

Table 3-1 presents the information gathered for the 30-year study period (1985–2014) from all the weather stations used in this research, thus enabling this study to identify the most extreme precipitation events recorded. In addition to the precipitation, land data from the Global Precipitation Climatology Centre (GPCC) for the 19-year period from 1990–2008 are used. GPCC is the non-real-time Full Data Reanalysis product, which conducts a global analysis of monthly precipitation on the earth's land surface based on in-situ rain gauge data. It uses gauge-based gridded datasets over the land's surface at a 0.5° x 0.5° resolution (Schneider et al., 2014).

City	ICAO	WMO	Lat	Long	Elevation	Radiosonde	S.Date	E.Date	period	missing data
Wajh	OEWJ	40400	26-20N	036-48E	20 m		1978	2014	37 years	2.03%
Yanbu	OEYN	40439	24-13N	038-07E	8 m		1978	2014	37 years	1.71%
Jeddah	OEJN	41024	21-70N	039-18E	15 m	*	1977	2014	38 years	0.67%
Makkah	OEMK	41030	21-43N	039-77E	310 m		1985	2014	30 years	0.43%
Gizan	OEGN	41140	16-88N	042-58E	6 m		1977	2014	38 years	1.70%

Table 3-1. Station weather observation data along the western region of Saudi Arabia which was used in this research, during the period 1977–2014, and included WMO and ICAO code, longitude (°E), latitude (°N) and altitude (m), percentage of missing data (%), period (year). The asterisk (*) indicates that the station has upper air data.

3.2.2. ERA-Interim Reanalysis Data:

The reanalysis data that will be used in this study are the time series of daily meteorological variables ERA-Interim re-analysis data produced from the European Centre for Medium-Range Weather Forecasts during the 30 year period from 1979 to 2014. ERA-Interim re-analysis data is the latest global atmospheric reanalysis data produced by the European Centre for Medium-Range Weather Forecasts (ECMWF) which has a spatial resolution of the data set of approximately 80 km (T255 spectral), as a regular N128 Gaussian grids on regular

latitude-longitude grid resolution of 0.75˚ × 0.75˚ and 60 vertical levels (Dee et al., 2011). The reanalysis data consists of mean sea level pressure (MSLP), accumulated precipitation from the previous 24h from 06UTC to 06UTC, geopotential height (GPH), specific humidity (q) and horizontal wind components (u-eastward, v-northward) at nine isobaric levels from 1000hPa to 200hPa. This data was selected from the domain of study which extends from 0°S to 60°N and from 60°W to 80°E.

3.2.3. Regional Climate Downscaling Data:

RCMs and GCMs have been developed to investigate the impact of future climate change. However, RCMs produce coordinated sets in one Coordinated Regional Climate Downscaling Experiment (CORDEX) framework (Giorgi et al., 2009). This framework has 14 domains that cover across the whole earth. Two of these CORDEX domains cover the whole of the Arabian Peninsula, namely the African domain (CORDEX-Africa), which is evaluated by Kim et al. (2011), and the Middle East-North African domain (CORDEX-MENA), which covers the region from 7°S–45°N and 27°W–76°E (Almazroui, 2016). Figure 3.1 shows the CORDEX-Africa and CORDEX-MENA domains.

3.2.3.1. CORDEX model set up:

These experiments consist of different RCMs which are nested into different GCMs and evaluated by ERA-Interim re-analysis data. Table 3-2 shows the list of RCMs and GCMs used in this Thesis. 8 RCMs (HadGEM3-RA (Diallo et al., 2014), HadRM3P (Jones et al., 2004), CCLM4-8-17 (Rockel et al., 2008) , CRCM5 (Zadra et al., 2008), HIRHAM5 (Christensen et al., 2006), RACMO22T (Van Meijgaard et al., 2008), RCA4 (Samuelsson et al., 2011) and REMO2009 (Jacob et al., 2012)) were integrated over the CORDEX-Africa domain; just one

RCM (RCA4) was integrated over the CORDEX-MENA domain, recommended by CORDEX with a horizontal grid spacing of 0.44°.

These CORDEX-Africa and CORDEX-MENA RCM simulations were driven by the atmospheric lateral boundary conditions and SSTs from 12 GMCs (as shown in Table 3-2) for the historical period of 1951–2005 and for the future period of 2006–2100 under the effects of high greenhouse gas emission scenario (i.e., a representative concentration pathway RCP of 8.5 [RCP85]).

These RCMs were first run in evaluation mode, which was driven by the atmospheric lateral boundary conditions and SSTs from ERA-Interim reanalysis data (Dee et al., 2011), for various periods (1998–2008 for HadGEM3-RA, CCLM4-8-17 and REMO2009, 1990–2011 for HadRM3P, 1979–2012 for CRCM5 and RACMO22T, 1989–2010 for HIRHAM5 and 1980–2010 for RCA4).
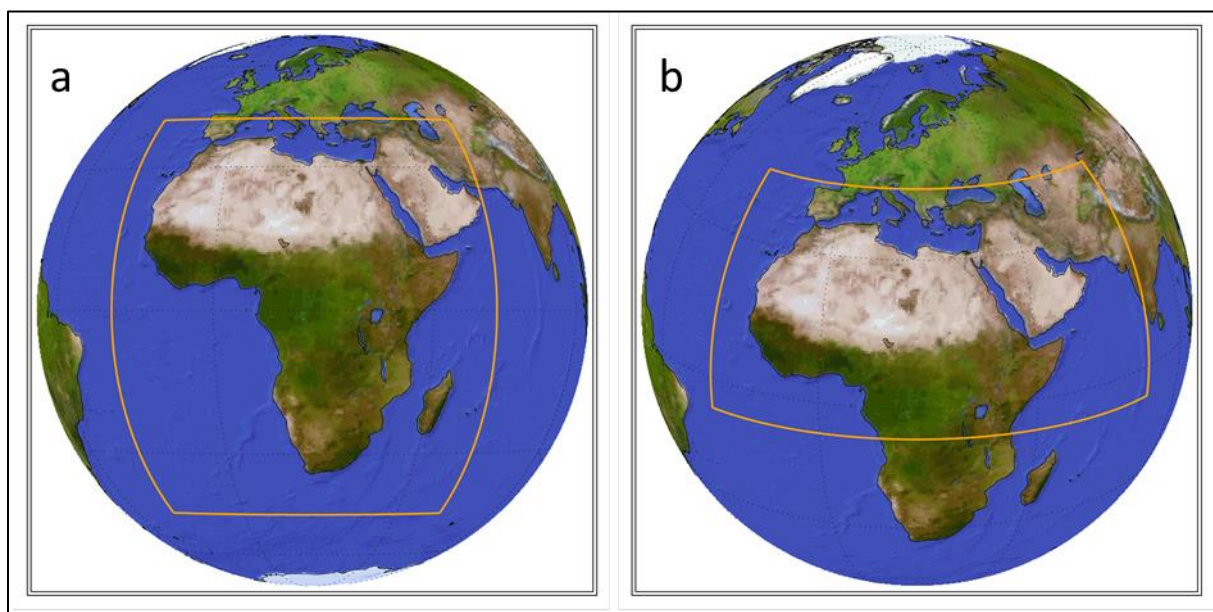
Figure 3.1. a) CORDEX-Africa domain b) CORDEX-MENA domain (from http://cordex.org)

No.	Domaine	Downscaling RCM	Driving Global Model	Evaluation	Historical	rcp85
1	CORDEX-AFR	CCLM4-8-17	MPI-M-MPI-ESM-LR	ERA-Interim	✓	✓
2	CORDEX-AFR	CCLM4-8-17	MOHC-HadGEM2-ES	=	✓	✓
3	CORDEX-AFR	CCLM4-8-17	ICHEC-EC-EARTH	=	✓	✓
4	CORDEX-AFR	CCLM4-8-17	CNRM-CERFACS-CNRM-CM5	=	✓	✓
5	CORDEX-AFR	CRCM5	MPI-M-MPI-ESM-LR	=	✓	✗
6	CORDEX-AFR	CRCM5	CCCma-CanESM2	=	✓	✗
7	CORDEX-AFR	HadGEM3-RA	✗	=	✗	✗
8	CORDEX-AFR	HadRM3P	✗	=	✗	✗
9	CORDEX-AFR	HIRHAM5	NCC-NorESM1-M	=	✓	✓
10	CORDEX-AFR	HIRHAM5	ICHEC-EC-EARTH	=	✓	✓
11	CORDEX-AFR	RACMO22T	MOHC-HadGEM2-ES	=	✓	✓
12	CORDEX-AFR	RACMO22T	ICHEC-EC-EARTH	=	✓	✓
13	CORDEX-AFR	RCA4	NOAA-GFDL-GFDL-ESM2M	=	✓	✓
14	CORDEX-AFR	RCA4	NCC-NorESM1-M	=	✓	✓
15	CORDEX-AFR	RCA4	MPI-M-MPI-ESM-LR	=	✓	✓
16	CORDEX-AFR	RCA4	MOHC-HadGEM2-ES	=	✓	✓
17	CORDEX-AFR	RCA4	MIROC-MIROC5	=	✓	✓
18	CORDEX-AFR	RCA4	IPSL-IPSL-CM5A-MR	=	✓	✓
19	CORDEX-AFR	RCA4	ICHEC-EC-EARTH	=	✓	✓
20	CORDEX-AFR	RCA4	CSIRO-QCCCE-CSIRO-Mk3-6-0	=	✓	✓
21	CORDEX-AFR	RCA4	CNRM-CERFACS-CNRM-CM5	=	✓	✓
22	CORDEX-AFR	RCA4	CCCma-CanESM2	=	✓	✓
23	CORDEX-AFR	REMO2009	NOAA-GFDL-GFDL-ESM2G	=	✓	✗
24	CORDEX-AFR	REMO2009	MPI-M-MPI-ESM-LR	=	✓	✓
25	CORDEX-AFR	REMO2009	MOHC-HadGEM2-ES	=	✓	✓
26	CORDEX-AFR	REMO2009	MIROC-MIROC5	=	✓	✓
27	CORDEX-AFR	REMO2009	IPSL-IPSL-CM5A-LR	=	✓	✓
28	CORDEX-AFR	REMO2009	ICHEC-EC-EARTH	=	✓	✓
29	CORDEX-MENA	RCA4	CNRM-CERFACS-CNRM-CM5	=	✓	✓
30	CORDEX-MENA	RCA4	ICHEC-EC-EARTH	=	✓	✓
31	CORDEX-MENA	RCA4	NOAA-GFDL-GFDL-ESM2M	=	✓	✓

Table 3-2. The list of regional climate models and global climate models used in this chapter.

3.2.3.1. CORDEX output data:

The output of the historical simulated data period (1976 to 2005) and the future period (2070-2099) of projected climate change under effect of RCP85 emission scenario for many climatic elements (e.g. precipitation, mean sea level pressure, GPH at 500hPa and wind speed at 200hPa) from CORDEX-Africa and CORDEX-MENA domains are used. The output data have a spatial resolution of the data set of approximately 50 km (T399 spectral) on a regular latitude-longitude grid resolution of $0.44° × 0.44°$.

The output data includes the availability of information for each experiment, which is evaluation data, historical data and prediction data under high greenhouse gas emission scenarios (i.e., in a representative concentration pathway RCP8.5 scenario). All the simulation datasets from CORDEX-Africa and CORDEX-MENA were obtained from the Earth System Grid Federation (ESGF) portal at the Centre for Environmental Data Analysis (CEDA), where it is hosted by the British Atmospheric Data Centre (BADC) and available online (https://esgf-index1.ceda.ac.uk/ search/cordex-ceda/).

3.2.4. The Teleconnection Indices:

This study used 10 climate variability data indices to examine the relationship between large-scale climate phenomenon and the extreme precipitation events over the WCSA during the wet season period. All climate variability indices are obtained from the Physical Sciences Division (PSD) of the Earth System Research Laboratory (ESRL) of the National Oceanic and Atmospheric Administration (NOAA) web site (https://www.esrl.noaa.gov/psd/data/climate-indices/), except one of NAO indices which is obtained from the Climate Prediction Center (CPC) at the National Oceanic and Atmospheric Administration (NOAA) websites

(/). All this monthly anomaly indices averaged to obtain the values for the wet season used in this study.

Five indices were extracted from El-Niño Southern Oscillation, which is one of the most important large atmospheric phenomena that affects interannual variability of the global climate. This ENSO phenomenon has been monitored by several teleconnection indices that are used in this thesis, such as Multivariate ENSO Index. These indices are based on unrotated principal component analysis and applied to six variables (MSLP, U and V components of the surface wind, sea surface temperature SST, surface air temperature , and total cloudiness fraction of the sky (Wolter and Timlin, 2011)). Furthermore, they use Nino1+2, Nino3.4 and Nino4 which are based on SST (where extreme eastern tropical pacific (0°-10°S, 90°W-80°W) for Nino1+2, east central tropical pacific (5°N-5°S, 170°W-120°W) for Nino3.4 and central tropical pacific (5°N-5°S, 160°E-150°W) for Nino4). Moreover, it also uses the ENSO precipitation index (ESPI), which is based on patterns of satellite-derived precipitation (Curtis and Adler, 2000).

In addition to ENSO indices, the NAO indices are also used. There are three NAO indices in this study: NAO-Jones, which is the time series of the leading empirical orthogonal function of MSLP anomalies over the North Atlantic (20°-80°N, 90°W-40°E) (Jones et al., 1997), NAO-station, which is based on the difference of normalised MSLP between two stations in the North Atlantic (Iceland and Portugal) (Hurrell, 2003) and NAO-CPC, which is obtained from the Climate Prediction Center (CPC) at the National Oceanic and Atmospheric Administration (NOAA). The procedure used to calculate the NAO-CPC index is the Rotated Principal Component Analysis (RPCA) (Barnston and Livezey, 1987). The RPCA is applied to the monthly

mean standardized 500hPa geopotential height anomalies over the North Atlantic region from 20°N to 90°N, between 1950 and 2000 (NOAA, 2008).

The IOD is defined by the Japan Agency for Marine–Earth Science Technology (JMASTEC) and is represented by the Dipole Mode Index (DMI). This index is obtained by computing anomalous SST differences between the western and southeastern equatorial Indian Ocean (Iizuka et al., 2000). The positive DMI events are associated with warm land-surface anomalies over regions that are affected by reduced rainfall (Saji and Yamagata, 2003). In addition, the Southern Oscillation Index (SOI) is used. This index is based on the difference in MSLP between Tahiti and Darwin (Allan et al., 1991) and is a measure of the Pacific Walker circulation changes (Price et al., 1998).

3.3. Methodologies:

3.3.1. Precipitation Analysis and Extreme Events Identification:

Because of the rarity of precipitation events over this region, a wet day is identified in this study when each station recorded greater than 0.1 mm precipitation during the course of one day. Although the majority of previous studies have identified a wet day as a day when precipitation equalled or was greater than 1 mm throughout the day, precipitation events in weather observation reports are defined by the World Meteorological Organisation (WMO) as precipitation in excess of 0.1 mm (WMO, 2015).

For the purposes of this study, extreme precipitation events are calculated by counting the number of events above the threshold of total precipitation amount for each station, during the defined the period. The threshold of precipitation amount is defined as being a percentile (e.g., 90th, 95th and 99th) of the daily precipitation amount out of the total precipitation of the

wet days during the examined period, from 1985 to 2014. These wet days are calculated from observational data when the total precipitation amount recorded was more than 0.1 mm per day. We calculated the fixed threshold (i.e., the mean threshold for all stations together) and the varied threshold for each station (Saidi et al., 2013).

3.3.2. Composite Mean and Anomaly analysis:

Diagnostic analysis of synoptic scale weather systems over AP was performed using ERA-Interim reanalysis data. MSLP, GPH and Wind were analysed at nine levels from 1000hPa to 200hPa together with surface weather elements, and accumulated precipitation from the previous 24h from 06UTC to 06UTC.

In addition, the 30 highest extreme precipitation events were chosen from among the 76 that had been identified to help understand relevant weather systems during these events. We used the daily mean for each meteorological variable, in addition to the daily standardised anomalies (Normalisation), which are calculated by dividing anomalies by the climatological standard deviation for each day in the long term of historical data;

$$N_s = \frac{X_{anomaly}}{S_x}$$

$$X_{anomaly} = X - \bar{X}$$

, where N_s is the normalization, S_x is the standard derivation, X is the daily meteorological variable and $\bar{X}$ the mean daily value of this parameter. The goal of the normalisation is to provide more information about the true magnitude of the anomalies and to clearly remove the influence of intra-annual variability on the results (Wilks, 2011).

3.3.3. Vertical Integrated Water Vapour Flux (VIWVF):

In addition to the diagnostics of MSLP, GPH and Wind, the reanalyses is performed daily during the period from 1985 to 2014 to calculate the vertically integrated horizontal water vapour flux (Kg m^{-1}s^{-1}). This was used by (Krichak et al., 2014a) to study the tropical moisture which enhances extreme precipitation events over the Mediterranean regions and also (de Vries et al., 2013) who investigated the dynamics of extreme precipitation events over the Middle East region. Thus, the vertically integrated horizontal water vapour flux is calculated by the following equation:

$$viwvf = \frac{1}{g} \int_{P\,mslp}^{P\,500} (q \cdot V_h)\,dp$$

, where g is the magnitude of gravitational acceleration, P is the air pressure from 500hPa to MSLP, V_h is the horizontal wind and q is the specific humidity.

3.3.4. Trajectory Analysis:

In order to identify air mass path, a trajectory analysis is applied. A trajectory tracks the path taken by an air parcel in a given period of time (Saha, 2008). There are many trajectory models used in atmospheric research. Examples of these trajectory models are; the Hybrid Single-Particle Lagrangian Integrated Trajectory model (HYSPLIT), which was developed by NOAA (Stein et al., 2015), FLEXTRA trajectory model (Stohl and Seibert, 1998), the LAGRANTO Lagrangian analysis tool – version 2.0 (Sprenger and Wernli, 2015) and the METeorological data EXplorer (METEX), which was developed by Japan Meteorological Agency (Zeng et al., 2010).

Although there is more than 20 % error in the air parcel pathway (Fuhrmann and II, 2013), especially for trajectories lasting longer than one day, it still gives a general idea of air route

and can be a way to deduce the moisture pathway (Alexander et al., 2015). However, this study uses the HYSPLIT model to identify the backward air parcel trajectories for 11 extreme events which will be defined in chapter 4. All the backward trajectories ending at 1200 UTC in each station that recorded the extreme precipitation event for 72 hrs backward duration at 6-h intervals and at different heights from 5000m to 1000m which are in the range between 450hPa-925hPa.

3.3.5. Objective Analysis:

This study used Empirical Orthogonal Function (EOF) analysis, also known as Principal Components Analysis (PCA) (Hannachi et al., 2007), to classify 30 years of daily winter MSLP data and identify the most relevant synoptic circulation patterns (Huth et al., 2008) associated with extreme precipitation days during the wet season. Based on this, we used composite circulation anomalies (Esteban et al., 2005) to identify the specific role of the respective classes (EOFs) in this study. We used six EOF retaining components, which were applied to the daily average MSLP by S-mode. We then used Varimax orthogonal rotation, as suggested by Almazroui et al. (2014), who classified the atmospheric circulation patterns during the wet season period (Oct–May) for the Saudi Arabian climate.

3.3.6. Validation data:

The Taylor diagram of the correlation coefficient (CORR) and the normalised standard deviation (NSD) analysis are used to evaluate ERA-Interim reanalysis precipitation data and the output of CORDEX multi-RCM hindcast data (precipitation, MSLP, GPH at 200 and 500hPa and wind speed at 200hPa) for the 19-year period from 1990–2008. This evaluation was applied over the area surrounding the western coast of the Arabian Peninsula from 12°S–30°N and 32°W–44°E in addition to the individual chosen grid cells. Therefore, it utilised a

comparison of 22 grid points from each evaluated data area with the corresponding grid point in the reference data. The average of these 22 grid points' values are used. Figure 3.2 illustrates the topography map of the study area (WCSA) and position of the meteorological stations and the 35 small boxes indicate a grid point with a 0.75° resolution. This included 22 green grid points over the land that are crosslinking GPCC grid points.
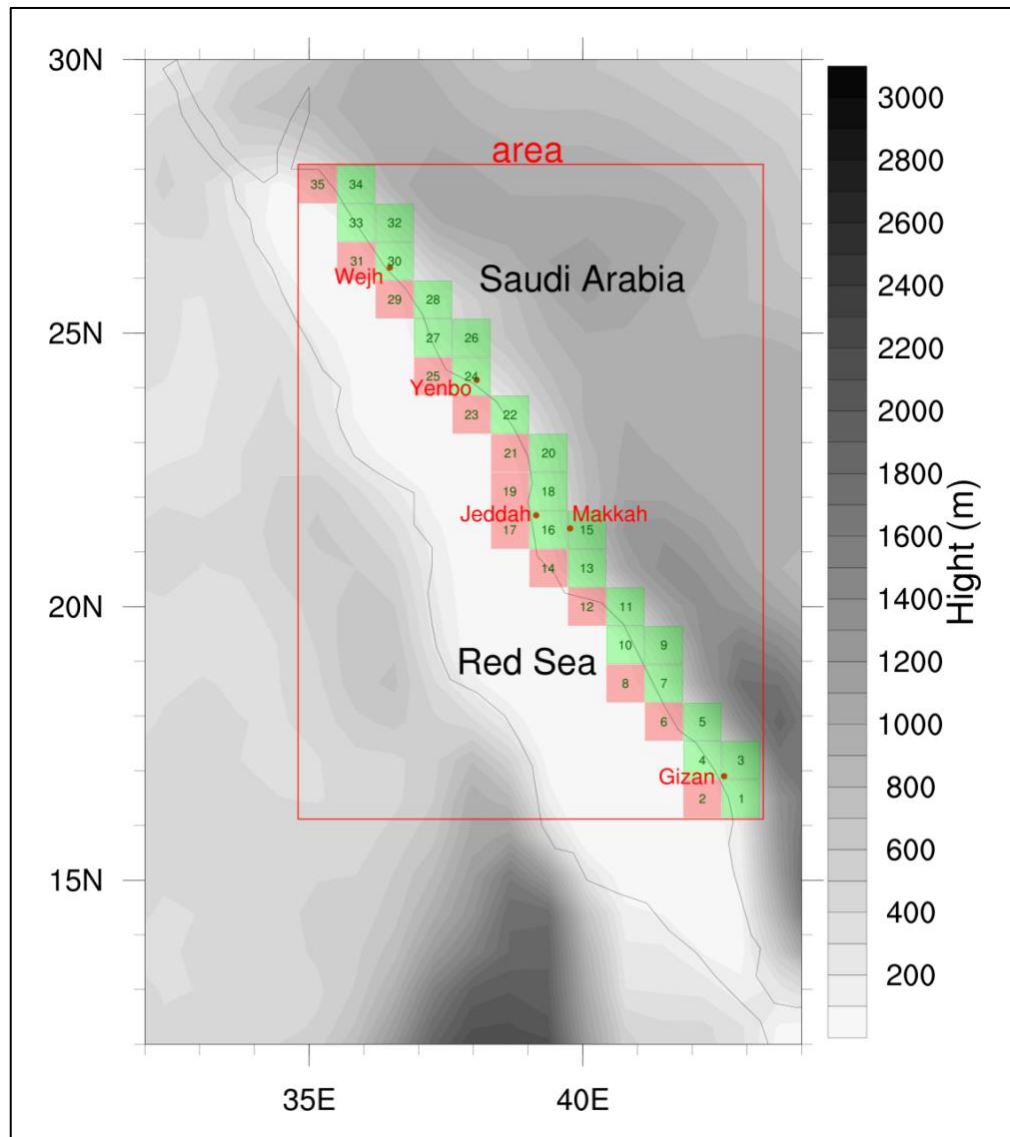
Figure 3.2. Location map of the study area (WCSA) with topography (in meters) and position of the meteorological stations (red circles); the large box indicates the subdomain (35°–43°E and 16°–28°N), and the 35 small boxes indicate a grid point with a 0.75° resolution from the ERA-Interim reanalysis data. Green 22 grid points over the land.

In addition to the spatial diversity, these comparisons were also applied in several temporal scales, including annual (year) and seasonal (wet_season, dry_season, sem1_season,

39

sem2_season) periods, which were calculated by monthly precipitation. Seasonal periods are defined in Chapter 4.

On the other hand, the four values of the precipitation indices that were calculated from 1990–2008 were based on wet days and the 90th percentile thresholds from the daily precipitation amounts during wet days (rain amount more than 0.1 mm). For the precipitation indices, we used monthly precipitation amount (RR), monthly wet-day frequency (RQ), monthly total precipitation from days > 90th percentile thresholds from the daily precipitation amounts at wet days (RR90) and monthly wet-day frequency from days > 90th percentile thresholds from the daily precipitation amounts at wet days (RQ90).

3.3.6.1.   Spatial Interpolation:

In order to evaluate the ERA-Interim reanalysis data and the output of CORDEX multi-RCM hindcast data, this data must be on the same horizontal grid size. The interpolation or regridded data processes are required to make different grid scale data transform to a uniform grid scale (Ma et al., 2009). In this study, the gauge-based gridded observational datasets from the GPCC dataset with 0.5° by 0.5° resolution and output of CORDEX multi-RCM hindcast data with 0.44° by 0.44° resolution are converted to the spatial resolution of ERA-Interim. This study used The Climate Data Operators (CDO) software to convert this data by commend (*remapbil, n128)* where n128 is mean the N128 Gaussian grids size (T255, nominally 0.703125 degrees).

3.3.6.2.   Evaluation of the ERA-Interim reanalysis precipitation data:

The CORR and NSD analysis are used to evaluate the validity and performance of ERA-Interim reanalysis precipitation data for monthly precipitation and each of the five meteorological

rain gauge stations. There are many studies that use this validation study to compare ERA-Interim with in situ observations (Diro et al., 2009, Worqlul et al., 2014, Nkiaka et al., 2017). In addition, in this study ERA-Interim reanalysis precipitation data are also compared with GPCC (Bosilovich et al., 2008), where GPCC shows good agreement with in situ measurement data in Iran (Raziei et al., 2011) and Saudi Arabia (Kenawy and McCabe, 2015)

3.3.6.3.   Evaluation of the CORDEX multi-RCM Hindcast data:

The CORR and NSD analysis between the CORDEX multi-RCM hindcast data (precipitation, MSLP, GPH at 200 and 500hPa and wind speed at 200hPa) and ERA-Interim reanalysis data have been applied to evaluate the performance of these RCM simulations from CORDEX-Africa and CORDEX-MENA domains. The hindcast is also called the evaluation data that is collected from CORDEX web site data. This is the RCM simulations in recent climate conditions, which is forced by the driving model ECMWF- ERA-Interim. This evaluation was applied for several RCMs over CORDEX-Africa domain (CCLM4-8-17, HIRHAM5, RACMO22T, CRCM5, REMO2009, HadGEM3-RA, HadRM3P, and RCA4) and just one RCM from CORDEX-MENA domain which is (RCA4).

In addition to this evaluation of precipitation, we evaluated the MSLP of this area. The main reason for this assessment was to know the capabilities of the RCMs that we would use in climate prediction in the next chapter. Therefore, when we evaluated the MSLP in this chapter, we scanned an area that covers the geographical window 20°–70°E and 05°–40°N, which we used to study atmospheric circulation patterns in chapters 4 and 5. Then, the RCMs in CORDEX-AFRICA domain were covered just to 60°E; thus, we used only hindcast simulation for CORDEX-MENA.

Chapter 4. EXTREME PRECIPITATION ANALYSIS

4.1.   Overview:

Based on the unique data source of sub-daily data of the West Coast of the Saudi-Arabian Peninsula (WCSA), this first results chapter will analyse in detail the climatological precipitation conditions from the station-based observations, as well as from the perspective of larger-scale hemispheric flow characteristics by state-of-the-art re-analysis data. Special focus is laid on the identification of extreme events. This detailed analysis has not been previously carried out and will help introduce the systematic classification analysis in Chapter 5 and, thus, contribute to the analysis and results achieved in Chapter 6 (Modelling and anthropogenic change signal).

4.2.   Primary Precipitation Characteristics for the WCSA:

The locations of five observation stations over the WCSA region and the significant differences in their amounts of mean annual precipitation during the period from 1985 to 2014 are shown in Figure 4.1. The total precipitation amount shows maximum values in the south which decrease towards the north, with Gizan (the southernmost station location) recording the highest amount of precipitation, followed by Makkah, Jeddah, Yanbu and finally, Wajh (the northernmost station).

Based on the rate-of-precipitation results, there is a slight gradual decrease in the annual precipitation amount from the south to the north along the WCSA, with annual average precipitation figures ranging from 58 mm, 38mm, and 34 mm in Jeddah, Yanbu and Wajh, respectively. Makkah, a short distance inland to the east of Jeddah, receives twice the amount

of precipitation, with Makkah receiving 105mm, which is still high compared to the precipitation at the nearby Jeddah station.
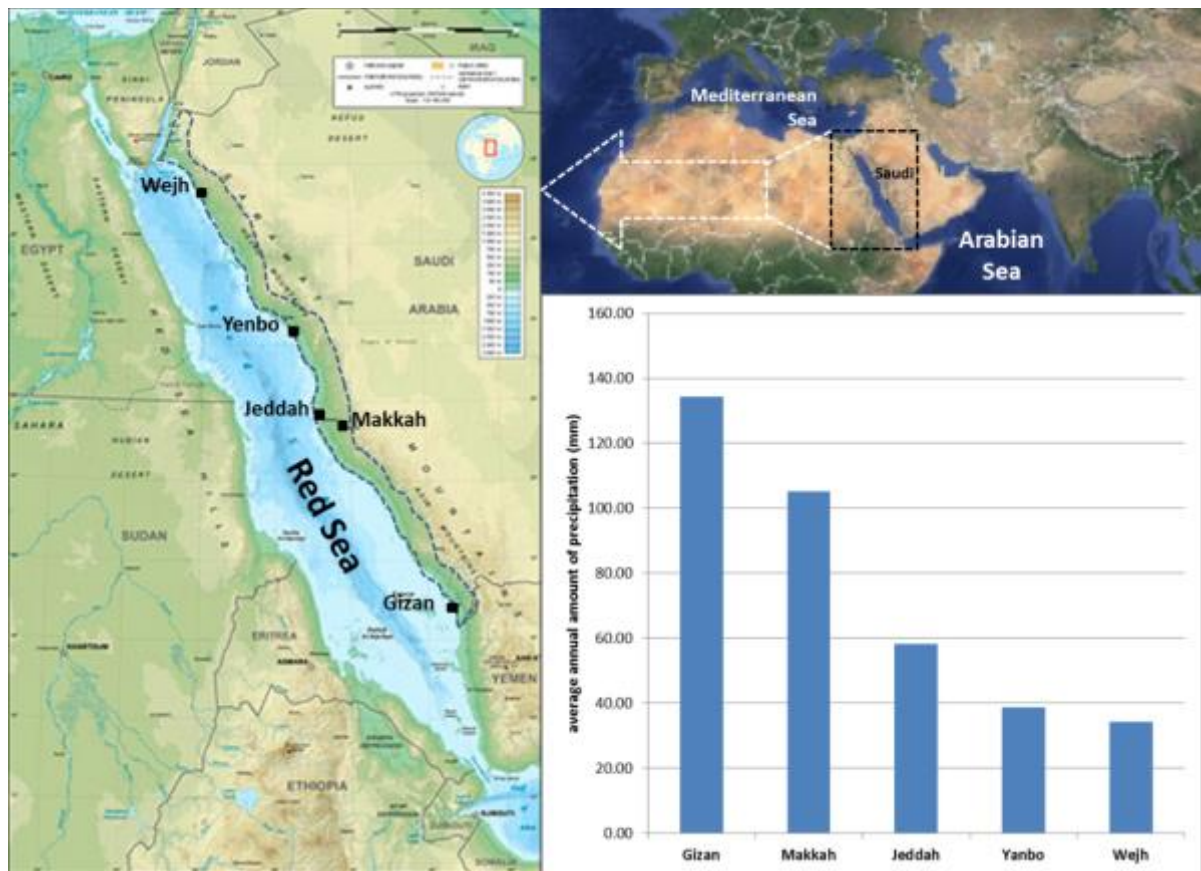
Figure 4.1. Saudi Arabian map showing the locations of the five weather stations and their annual mean precipitation (mm) from 1985 to 2014.

The rates of precipitation in Makkah and Jeddah are dramatically different, which may be attributed to the effect of thermodynamic and/or orographic conditions around Makkah. Makkah is bordered by mountains to the south and the east, which may influence the rain-productive processes in Makkah (e.g., orographic lifting). Thus, more mesoscale or convective-scale studies are required in order to further proof the factors for these mesoscale differences. However, these are beyond the scale of this investigation.

On the other hand, the highest amount of annual precipitation was recorded in Gizan, with a mean rate of 134 mm per year. This is a considerable amount in a semi-arid area such as the Arabian Peninsula and likely arises from two factors: (i) nearness to the equator and the effect

43

of the ITCZ, which can move north during the summer (Yan, 2005), and/or (ii) enhanced convective activity over the eastern mountains surrounding this station (de Vries et al., 2016).

In addition to annual precipitation, the mean monthly rainfall distribution was analysed. Figure 4.2 shows the mean monthly of precipitation amount data from five observation stations over the WCSA region during the period from 1985 to 2014. These spatial and temporal distributions of precipitation variation over this period shows that multiple climatic factors play important roles in the distribution of precipitation within this region, which will be analysed in this chapter.
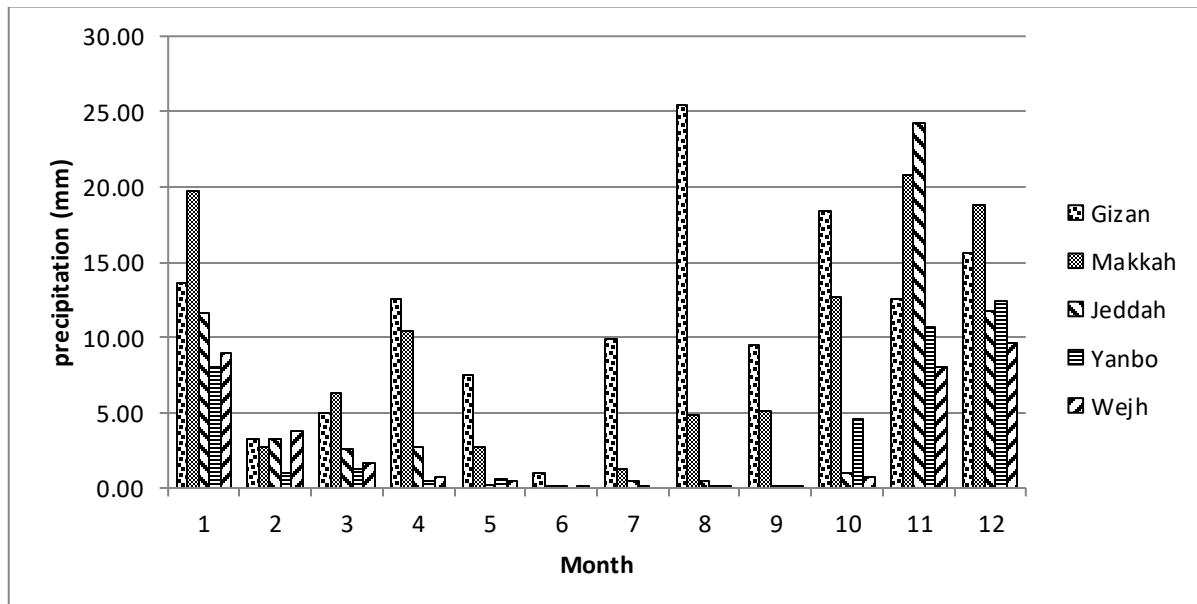
Figure 4.2. Mean monthly precipitation at each observation station for the period from 1985 to 2014

To analyse precipitation in more detail, two indices of precipitation were calculated for each station in the period from 1985 to 2014: the number of rain events, which is referred to as the precipitation frequency, and total precipitation, which is referred to as the precipitation amount (Haylock and Nicholls, 2000). Figure 4.3 and Figure 4.4 show the distributions of the percentages of mean monthly precipitation (amount) and the number of mean monthly

precipitation events (frequency), respectively, relative to the historical total precipitation averages for each station from 1985 to 2014.

The goal of considering the amount and frequency distributions of the precipitation data is to integrate them and thus explore all precipitation distribution properties. For example, Wajh recorded 18% and 10% precipitation days (frequency) over the studied 30-year period in February and November, respectively, while the percentages of total precipitation amount during these two months are 11% and 24%, respectively. In addition, at Yanbu, 13% of the rain days occurred in March, while the amount of precipitation is only about 3% of the total annual precipitation amount.
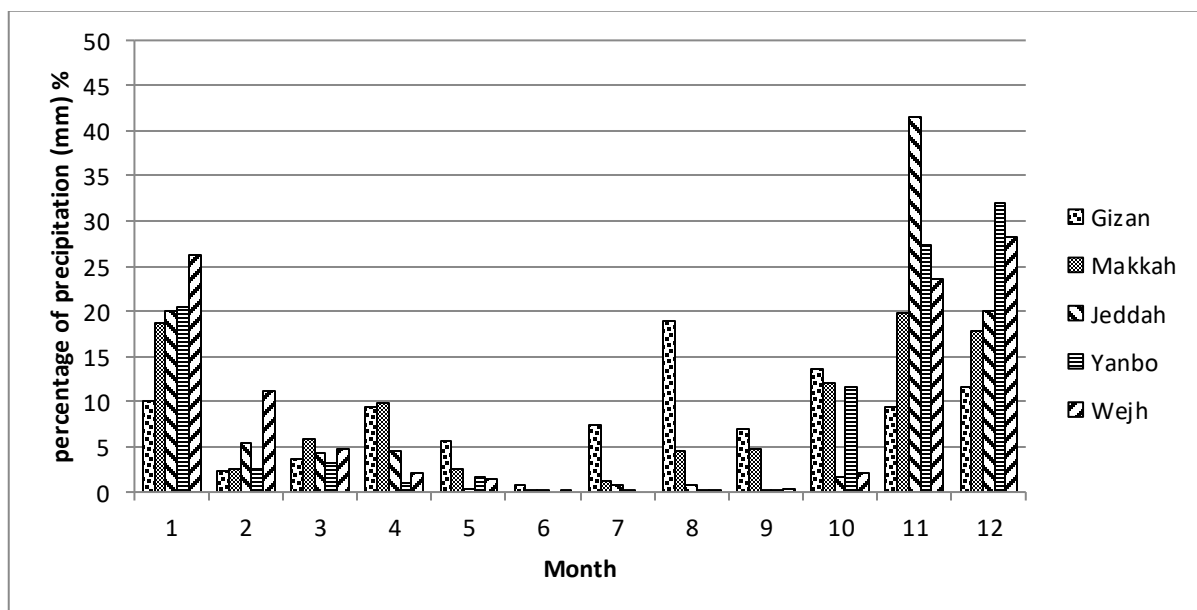
Figure 4.3. Mean monthly precipitation amount percentages (%) relative to annual precipitation amount for each station during the period from 1985 to 2014

In Jeddah, Yanbu and Wajh, rain mainly fell from October to February. The yearly precipitation distribution in Gizan is different because it is located in the southern part of the WCSA and is more affected by tropical precipitation characteristics. Consequently, Gizan has two primary precipitation seasons. The first season, similar to the AP, is the rainy period which takes place from November to April (Almazroui, 2011a). The second season is in

45

summer, from June to September, which is classified as the dry season in the AP, where the AP has a dry climate during summer except over the southern region (Almazroui, 2011a). In addition, Makkah has two peak precipitation seasons: a "dry" season in the summer, like Gizan in the south, and a wet season from October to May, like most stations in the AP.

During the dry season, there are some rare precipitation days in Jeddah, but no precipitation occurred in either Yanbu or Wajh. In some cases, Makkah shares this dry season with Gizan in terms of having very little precipitation, with only 20% precipitation days and an amount of precipitation that does not exceed 10% (Figure 4.3 and Figure 4.4).
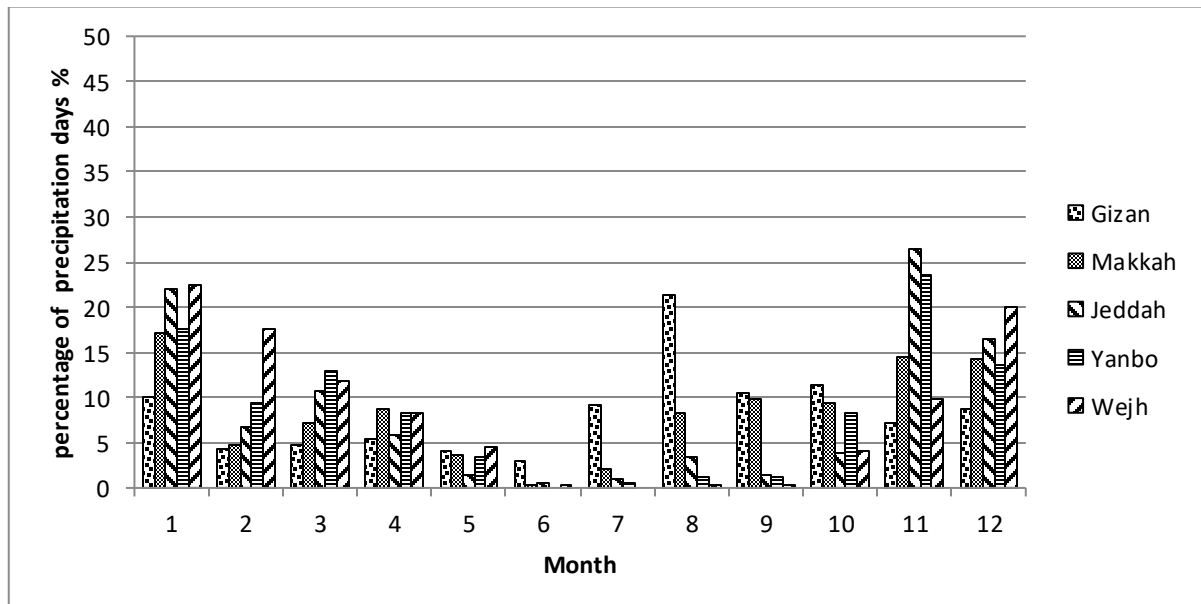
Figure 4.4. Mean monthly precipitation event percentages (%) relative to annual precipitation events for each station during the period from 1985 to 2014

The temporal distribution of precipitation at these five stations shows that the wet season starts in October for Makkah and Yanbu, with only a few precipitation events in Jeddah and Wajh that do not exceed 2% and 0.5% of total precipitation, respectively. All stations recorded high precipitation amount from November to January. This ran into February in Wajh, with only rare cases of rain at the other stations after January. The analysis shows several precipitation seasons along the west coast, with precipitation being distributed throughout

46

the year: first, in the southern regions, precipitation occurs in the summer, late autumn and early winter; secondly, in the central regions, precipitation occurs at the end of autumn and the beginning of winter and, finally, in the northern region, precipitation is concentrated in the winter.

Through this analysis, three precipitation seasons can be identified, namely the dry season, which occurs at only two stations, Makkah and Gizan, the semi-wet season, which is characterised by low precipitation amounts and occurs at several of the stations, and the wet season, which is characterised by significant precipitation events and occurs at all five stations. Many previous studies (Kang et al., 2015, Hasanean and Almazroui, 2015, Athar, 2015, Almazroui, 2013, Islam and Almazroui, 2012, Almazroui et al., 2012a) define the wet season as lasting from November to April and the dry as lasting from June to September, while May and October are the transition periods from the wet season to the dry season and from the dry season to the wet season, respectively (Almazroui, 2011a). In addition (Almazroui et al., 2015a) used the wet season (October to May) to study the relationships between atmospheric circulation patterns and surface climate over Saudi Arabia by principal component analysis.

4.3.   Extreme Events Identification:

For the purposes of this study, extreme events were identified by the Extreme Frequency Index, which is calculated by counting the number of events above the threshold precipitation amount for each station in the period. Table 4-1 shows the total extreme precipitation events from 1985–2014 for each station; the individual threshold is shown in the top table and the fixed threshold is shown in the bottom table. Considering only one of these factors (precipitation amount or precipitation frequency) does not provide a complete picture of

47

extreme precipitation distribution. An increased number of precipitation events in a certain month does not necessarily imply an increased number of extreme events in that month, especially if the total precipitation amount is low.

Threshold percentile (vary for each station)	Gizan	Makkah	Jeddah	Yanbu	Wajh	sum
extreme precipitation threshold above 99th percentile per event (mm)	65	60	54	70	54	
(frequency) the number of events above 99th percentile (day)	4	4	2	2	2	14
extreme precipitation threshold above 95th percentile (mm) per event	39	35	39	36	17	
(frequency) the number of events above 95th percentile (day)	21	20	11	9	13	67
extreme precipitation threshold above 90th percentile per event (mm)	24	23	24	19	10	
(frequency) the number of events above 90th percentile (day)	50	41	25	18	25	136
Threshold percentile (fixed threshold for all stations together)						
extreme precipitation threshold above 99th percentile => 61 mm (day)	5	4	1	2	1	13
extreme precipitation threshold above 95th percentile => 33 mm (day)	26	23	12	11	7	77
extreme precipitation threshold above 90th percentile => 20 mm (day)	64	46	36	17	10	161

Table 4-1. The total extreme precipitation events from 1985–2014 for each station by individual threshold in the top table. The fixed threshold for all stations in the bottom table.

A fixed threshold is impractical for significant variability in precipitation (Haylock and Nicholls, 2000). For example, the mean 90th percentile for the stations varied from 10–24 mm per day. In addition, the 99th and 95th percentiles had few extreme events, with 14 and 67 events, respectively, for all five stations throughout the data collection period. This study focuses on extreme precipitation above the 90th percentile, which varies for each station. In total, 136 events from all five stations were found in all seasons during the 30-year study period.

48

As discussed above, this study focuses on the analysis of extreme events and the principle understanding of causal processes. The study defines an extreme event relative to the background climatology of the respective station. While multiple extreme indices are, in principle, available (Alexander et al., 2006), this researcher decided to apply a threshold. This threshold can easily be transferred and applied to climate model simulation studies, taking into account possibly biased precipitation characteristics in respective model simulations.

4.4. Seasonal Precipitation Cycles:

In this section, the period of seasonal precipitation in the WCSA region is identified according to the monthly percentages (%) of extreme events (RR > 90th); characteristics of the seasonal totals and extreme precipitation are then described.

4.4.1. The Determination of Precipitation Seasons in WCSA:

Figure 4.5 shows the monthly percentages (%) of extreme events (RR > 90th) relative to historical precipitation events during the period of 1985–2014 for each station. Across all the stations, the highest percentages of extreme events occurred in November, December and January (NDJ). These months are therefore considered the wet season for the purposes of this study. This study defines the dry season from June to September (JJAS). Based on this detailed analysis of station data, the study defines the first semi-wet season from February to May (FMAM; hereafter referred to as sem1-season) and the second semi-wet season, which follows the dry season, in October (hereafter referred to as sem2-season).
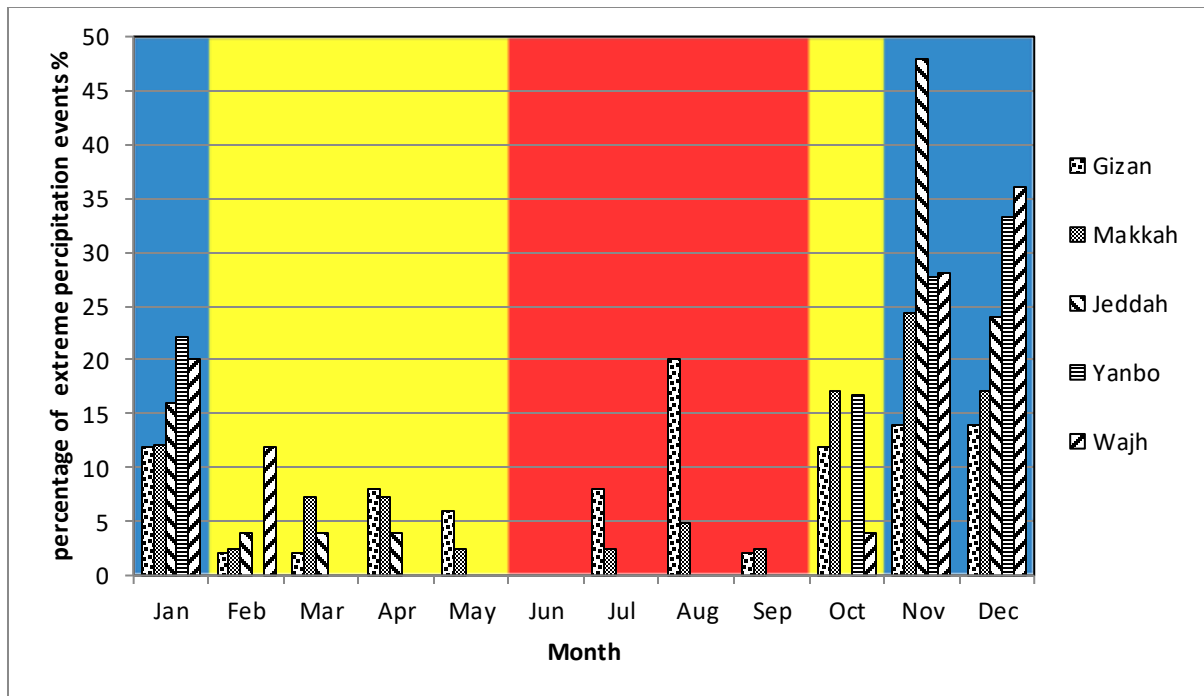
Figure 4.5. Monthly extreme precipitation events percentages (RR > 90th) for each station from 1985 to 2014, wet season (blue), dry season (red) and semi-wet season (yellow).

4.4.2. The Characteristics of Precipitation Seasonal Cycles in WCSA:

Figure 4.6 shows seasonal cycles with total precipitation amount and Figure 4.7 shows seasonal cycles with extreme precipitation amounts for each station from 1985 to 2014. All stations exhibited a strong intraseasonal variability and there were obvious patterns for each station. First, three stations (Jeddah, Yanbu and Wajh) had huge amounts of precipitation during the wet season, while the Makkah station had a large amount of precipitation in the wet season but also a considerable amount of precipitation in sem1_season. Finally, the Gizan station had two significant precipitation seasons – one in the dry season and one in the wet season – with a considerable amount of total precipitation in the other two seasons.

There was no significant difference between seasonal cycles in total precipitation amounts (Figure 4.6) and seasonal cycles with extreme precipitation amount (Figure 4.7) However, extreme precipitation amount in Gizan wet season was larger than that of the dry season; this is the opposite of what was observed in terms of the amount of total precipitation.
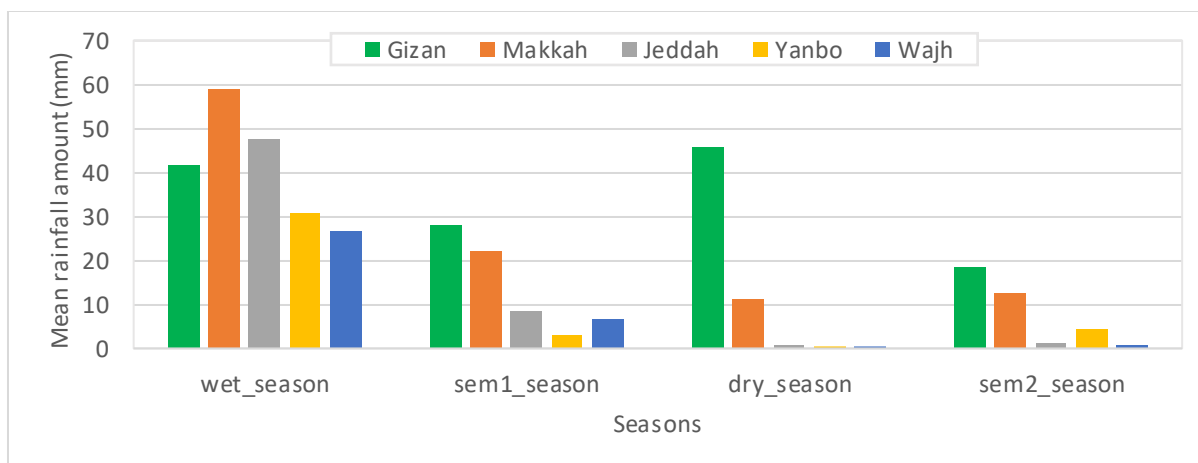
Figure 4.6. Seasonal cycles in total precipitation amount for each station from 1985 to 2014.
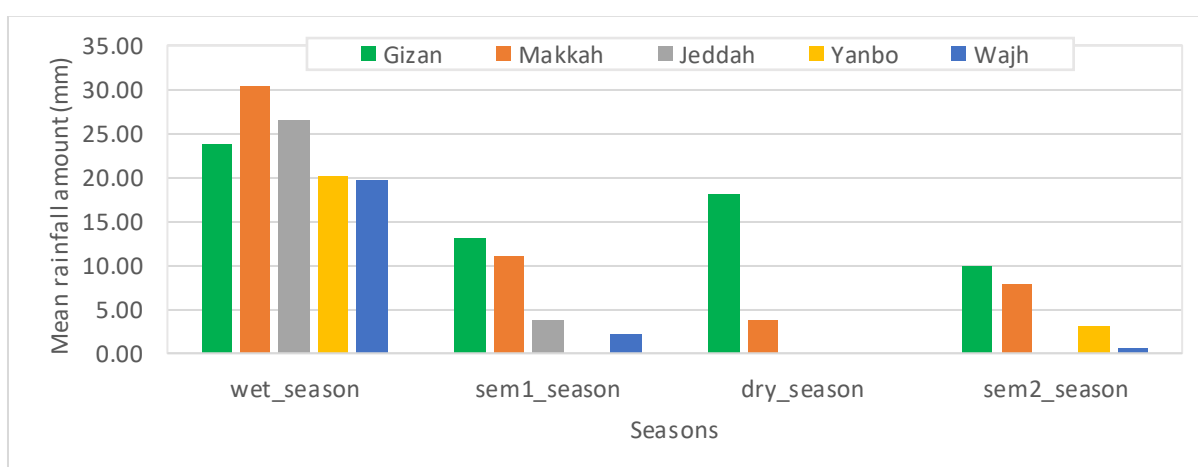
Figure 4.7. Seasonal cycles in extreme precipitation amount for each station from 1985 to 2014.

The significant precipitation amounts during the dry season in Gizan in the southern part of the WCAS were caused by the ITCZ, which mainly affects the southern part of the AP and sometimes extends further north over the AP to influence the Hejaz Mountains in the summer. All stations had large amounts of precipitation during the wet season because of the activation of the Red Sea trough, the effects of which run from late autumn to early spring.

In addition to the strong intraseasonal variability, there was significant interannual variability for all stations with no obvious pattern for any station in all seasons. This is illustrated in Figure 4.8, which shows the time series of total precipitation amounts for each station in each season, with the trend in each season for each station from 1985 to 2014. Regarding the trends of total precipitation, the wet season showed an increase in the northern region (e.g.,

51

Wajh and Yanbu) and a decrease in the central region (e.g., Jeddah and Makkah); there was

no change in Gizan, which is located in the southern region of WCSA.
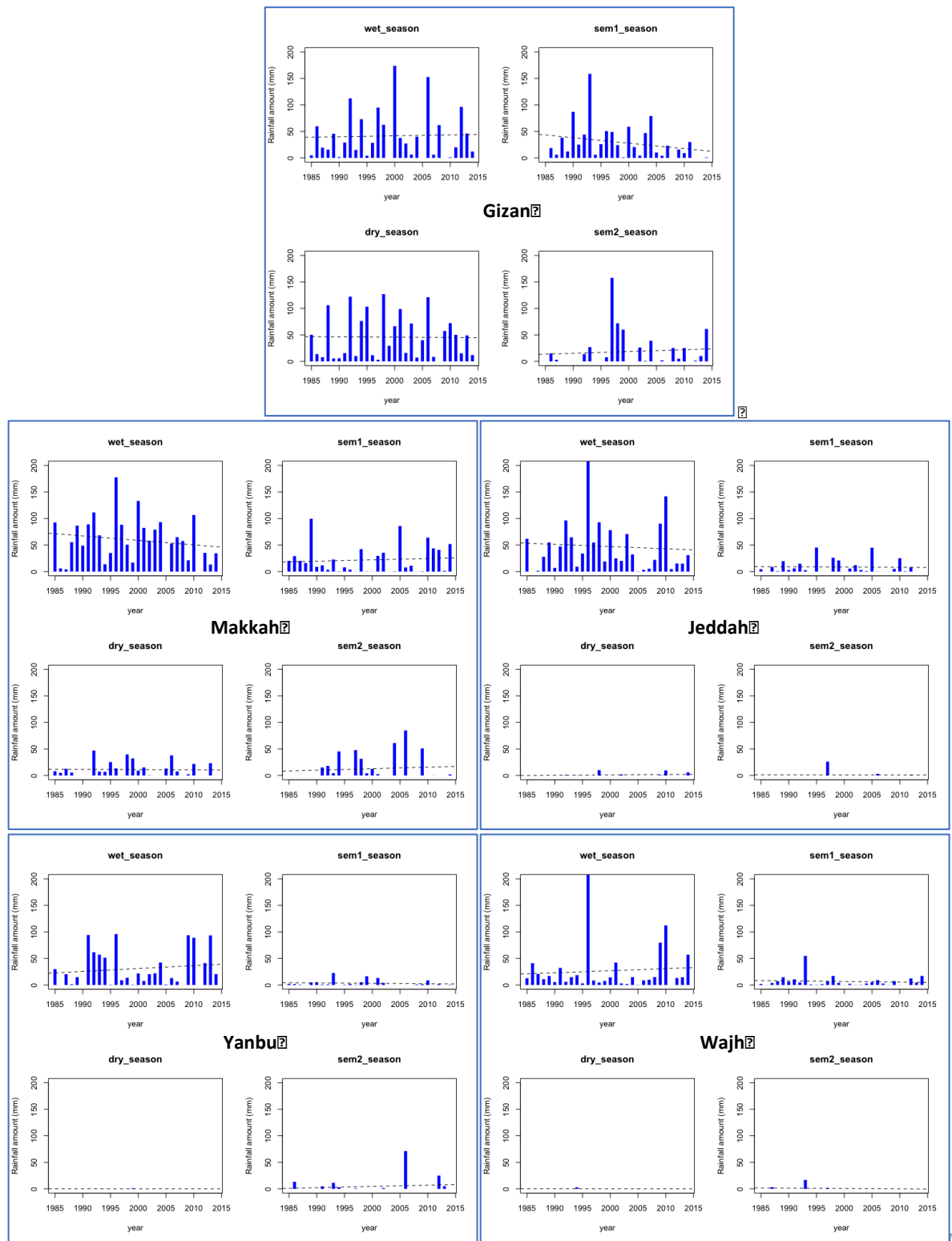
Figure 4.8. The time series of total precipitation amount for each station in each season.

Furthermore, Table 4-2 details the number of precipitation events and extreme precipitation events for each station over the studied 30 years, as well as the percentages of seasonal precipitation and extreme events for each station.

Time	Precipitation events						Extreme precipitation events					
	Gizan	Makkah	Jeddah	Yanbu	Wajh	Total	Gizan	Makkah	Jeddah	Yanbu	Wajh	Total
January	41 (10%)	71 (17%)	45 (22%)	30 (18%)	55 (23%)	169 (15%)	6 (12%)	5 (12%)	4 (16%)	4 (22%)	5 (20%)	20 (15%)
February	18 (4%)	20 (5%)	14 (7%)	16 (9%)	43 (18%)	89 (8%)	1 (2%)	1 (2%)	1 (4%)	-	3 (12%)	6 (4%)
March	19 (5%)	30 (7%)	22 (11%)	22 (13%)	29 (12%)	84 (8%)	1 (2%)	3 (7%)	1 (4%)	-	-	5 (4%)
April	22 (5%)	36 (9%)	12 (6%)	14 (8%)	20 (8%)	80 (7%)	4 (8%)	3 (7%)	1 (4%)	-	-	7 (5%)
May	17 (4%)	15 (4%)	3 (1%)	6 (4%)	11 (5%)	46 (4%)	3 (6%)	1 (2%)	-	-	-	4 (3%)
June	12 (3%)	1 (0.2%)	1 (0.5%)	-	1 (0.4%)	15 (1%)	-	-	-	-	-	0 (0%)
July	38 (9%)	9 (2%)	2 (1%)	1 (1%)	-	47 (4%)	4 (8%)	1 (2%)	-	-	-	5 (4%)
August	87 (21%)	34 (8%)	7 (3%)	2 (1%)	1 (0.4%)	118 (11%)	10 (20%)	2 (5%)	-	-	-	12 (9%)
September	43 (11%)	41 (10%)	3 (1%)	2 (1%)	1 (0.4%)	88 (8%)	1 (2%)	1 (2%)	-	-	-	2 (1%)
October	47 (11%)	39 (9%)	8 (4%)	14 (8%)	10 (4%)	100 (9%)	6 (12%)	7 (17%)	-	3 (17%)	1 (4%)	16 (12%)
November	29 (7%)	60 (14%)	54 (26%)	40 (24%)	24 (10%)	132 (12%)	7 (14%)	10 (24%)	12 (48%)	5 (28%)	7 (28%)	32 (24%)
December	36 (9%)	59 (14%)	34 (17%)	23 (14%)	49 (20%)	144 (13%)	7 (14%)	7 (17%)	6 (24%)	6 (33%)	9 (36%)	27 (20%)
wet-season	106 (26%)	190 (46%)	133 (65%)	93 (55%)	128 (52%)	445 (40%)	20 (40%)	22 (54%)	22 (88%)	15 (83%)	21 (84%)	79 (58%)
semi wet-season1	76 (19%)	101 (24%)	51 (25%)	58 (34%)	103 (42%)	299 (27%)	9 (18%)	8 (20%)	3 (12%)	-	3 (12%)	22 (16%)
dry season	180 (44%)	85 (20%)	13 (6%)	5 (3%)	3 (1%)	268 (24%)	15 (30%)	4 (10%)	-	-	-	19 (14%)
semi wet-season2	47 (11%)	39 (9%)	8 (4%)	14 (8%)	10 (4%)	100 (9%)	6 (12%)	7 (17%)	-	3 (17%)	1 (4%)	16 (12%)
Total	409 (100%)	415 (100%)	205 (100%)	170 (100%)	244 (100%)	1112 (100%)	50 (100%)	41 (100%)	25 (100%)	18 (100%)	25 (100%)	136 (100%)

Table 4-2. Number of precipitation and extreme precipitation (>90th) events for each station from 1985 to 2014; the numbers in parentheses are percentage values, which are given for each individual station.

Analysis of the total number of extreme precipitation events in the study period shows the percentage of extreme events in the dry season is about 14%, representing 19 events out of the total number of extreme precipitation events. These events occurred only in Makkah and Gizan, where Makkah experienced 10% of all its extreme precipitation events in the study period and Gizan experienced 30% of total extreme events in this period. Additionally, the first and second semi-wet seasons brought 28% of the total extreme events at all stations in the study period from 1985 to 2014 (as shown in Table 4-2).

In addition, during the wet season, Wajh, Yanbu, Jeddah, Makkah and Gizan recorded 88%, 84%, 83%, 50% and 40% of the total extreme events for each station, respectively. These

percentages are larger than the percentages in the total precipitation values. For example, these values have obvious differences in Gizan. Although the mean precipitation amount and the percentage of its frequency in the dry season in Gizan (i.e., 46 mm and 44%, respectively) are larger than in the wet season (41 mm and 26%, respectively), these values differ for extreme precipitation events, where the values in the wet season (24 mm, 40%) are larger than in the dry season (18 mm, 30%).

On average, the wet season comprises about 58% of all extreme events that occurred during the 30-year study period for all stations along the WCSA. Consequently, the number of extreme events during the dry and the transition periods cannot be neglected if we want to understand the reasons for extreme and damage-prone events. Nevertheless, the majority of extreme events occur from November to January; thus, this season is the focus of this study. It has been noted that the variability in the 90th percentile is significant, showing variations from 24 mm to 10 mm, depending on the station. The extreme wet season is homogeneous for all the stations not only in terms of precipitation occurrence and amount but also climatologically in terms of mean monthly sea-level pressure and geopotential height anomalies; these are described in the subsequent section.

4.5. Synoptic Dynamics of Extreme Events:

In order to investigate the synoptic factors favouring and leading to the generation of extreme precipitation events, the study will analyse the 3 dimension tropospheric conditions during these events by means of the most important meteorological variables based on ECMWF ERA-Interim re-analysis data. We will carry this out with the widely used standard pressure levels for the precipitation classifications derived in the previous section. Firstly, the average

seasonal conditions are presented, followed by a more targeted analysis focussing on the anomalies during the extreme event occurrence.

4.5.1. Average Circulation:

To more accurately understand the climatological background configuration, the seasonal averaged mean sea-level distribution is calculated and analysed with respect to the major modes of steering variability. Thus, Figure 4.9 represents the climatology of the seasonal mean sea level pressure (hPa) distribution over the Red Sea region from 1979 to 2014, using the precipitation season classifications developed for this study (i.e., *wet season, sem1-season, dry season and sem2-season*).
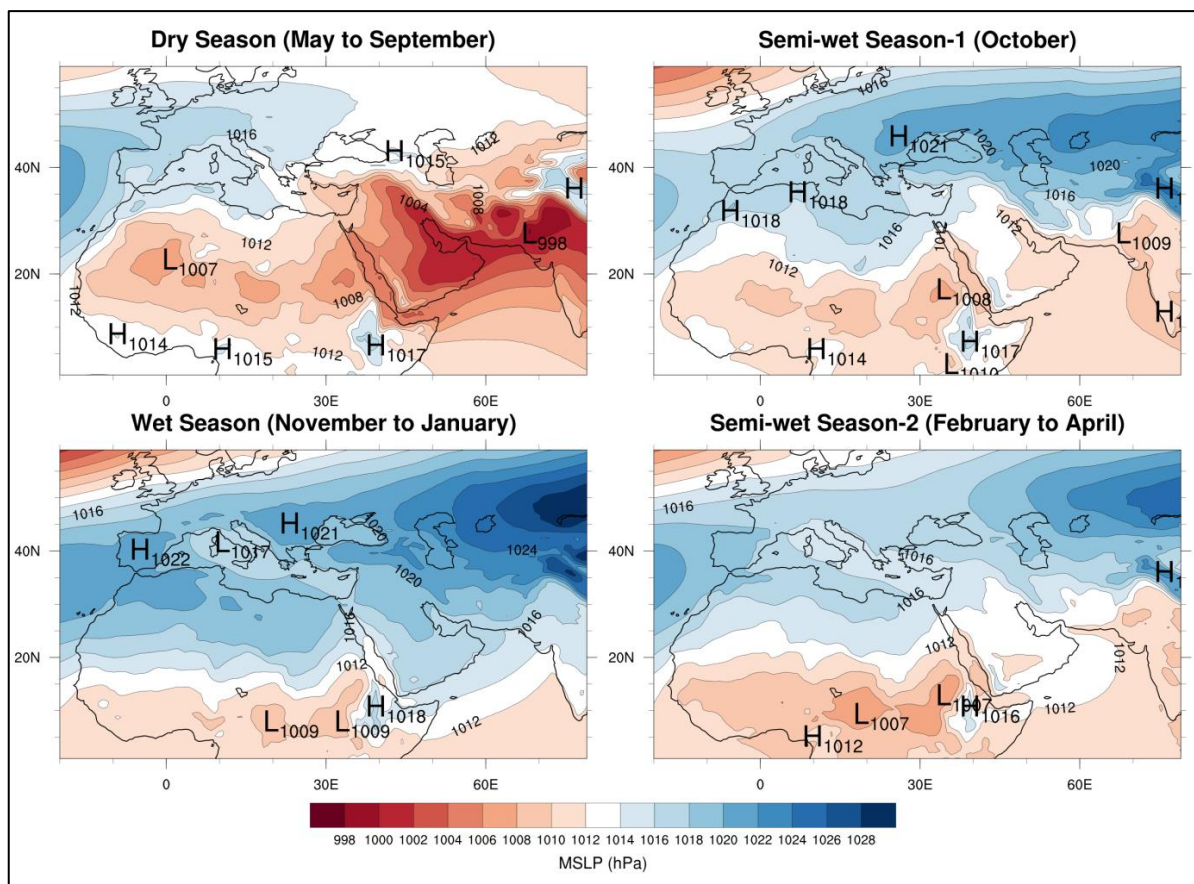
Figure 4.9. Climatology of seasonal mean sea level pressure (hPa) from 1979 to 2014. Based on ECMWF ERA-Interim reanalysis data.

In general, various surface pressure patterns dominate the climate in this region. In the dry season, the Indian summer monsoon dominates the weather in the AP, leading to heavy precipitation over nearby coastal high mountains in the southern part of the AP (Chakraborty et al., 2006). The westerly wind that is associated with the Indian summer monsoon carries moist air over the Asir Mountains (Abdullah and Al-Mazroui, 1998). The orographic effect then forces the moist air to ascend over nearby high coastal mountains and form convective precipitation (Axisa et al., 2011).

In the first *sem1-season* (Oct), the Siberian High extends to the northeast of the AP, and the Indian summer monsoon is forced to progressively fade away and is eventually replaced with Arabian or Persian Gulf Trough (Bitan and Sa'Aroni, 1992), abbreviated as AGT . This trough begins to occur in summer and remains until September and, in some cases, October (Dayan et al., 2012). In addition, the thermally driven SL begins to appear over east Africa and the Red Sea during this time of year.

During the wet season (Nov-Jan), the influence of the SH increases. It extends to central Saudi Arabia and is associated with the NAH. The SL retracts westwards, but the RST extends over the Red Sea as a trough from the SL. The RST extends northward towards the eastern Mediterranean between these two high-pressure systems (i.e., the NAH and SH), as shown in Figure 4.9.

4.5.2. Extreme Event dynamic analysis by means of anomaly composites for different Geopotential Heights:

In addition to providing a statistical analysis of precipitation, this study used the composites of normalised individual daily MSLP and GPH anomalies for each month. These correspond with subjectively selected events during extreme precipitation days (136 days) in order to

identify relevant steering factors for the extreme wet season events. The normalisation is done as follows: for each event-day, the anomaly for the respective long-term mean monthly was calculated. By this approach, it is assured that the relevant background climatology is considered and only the event anomaly for the long-term average climatic conditions is identified, which is ultimately the relevant synoptic situation we are interested in. The goal of the normalisation is to provide more information about the true magnitude of the anomalies and to clearly remove the influence of intra-annual variability on the results. Thus, the analysed anomalies are individual event specifications against the respective long-term average seasonal climatological conditions.

Consequently, this investigation is done individually per month: Figure 4.10 shows the anomaly composites of monthly normalised GPH at three atmospheric pressure levels, namely 1000hPa, 500hPa and 200hPa. The charts are produced based on extreme precipitation days. The charts show that the negative GPH anomaly at 1000hPa is beginning to appear in October over North Africa and associates with a negative GPH anomaly in the upper level. Subsequently, in November, December and January the negative GPH anomaly at 1000hPa are moved eastward to be a large over the Red Sea region, and this is associated with a highly negative GPH anomaly in the upper level.

A detailed analysis shows that the strong amplitude of the negative anomalies of geopotential height at 1000 hPa around WCSA are significant for all months from Oct to Feb. Thus, by including the core wet season as defined in this study. In addition, the negative anomalies of geopotential height at 1000 hPa are associated with large negative anomalies of 500 hPa and 200 hPa geopotential heights over the Red Sea; this supports the controlling of the strength of a trough along the Red Sea, which extends from the tropical regions. This is indicative for

a destabilisation of the entire subtropical air mass column especially above the Red Sea and Western Saudi-Arabia up to the 200hPa level. On the other hand, these negative gradients move into the AP in February. These results confirm that the months of November, December and January are the most representative periods of the extreme wet season along the western coast of Saudi Arabia.
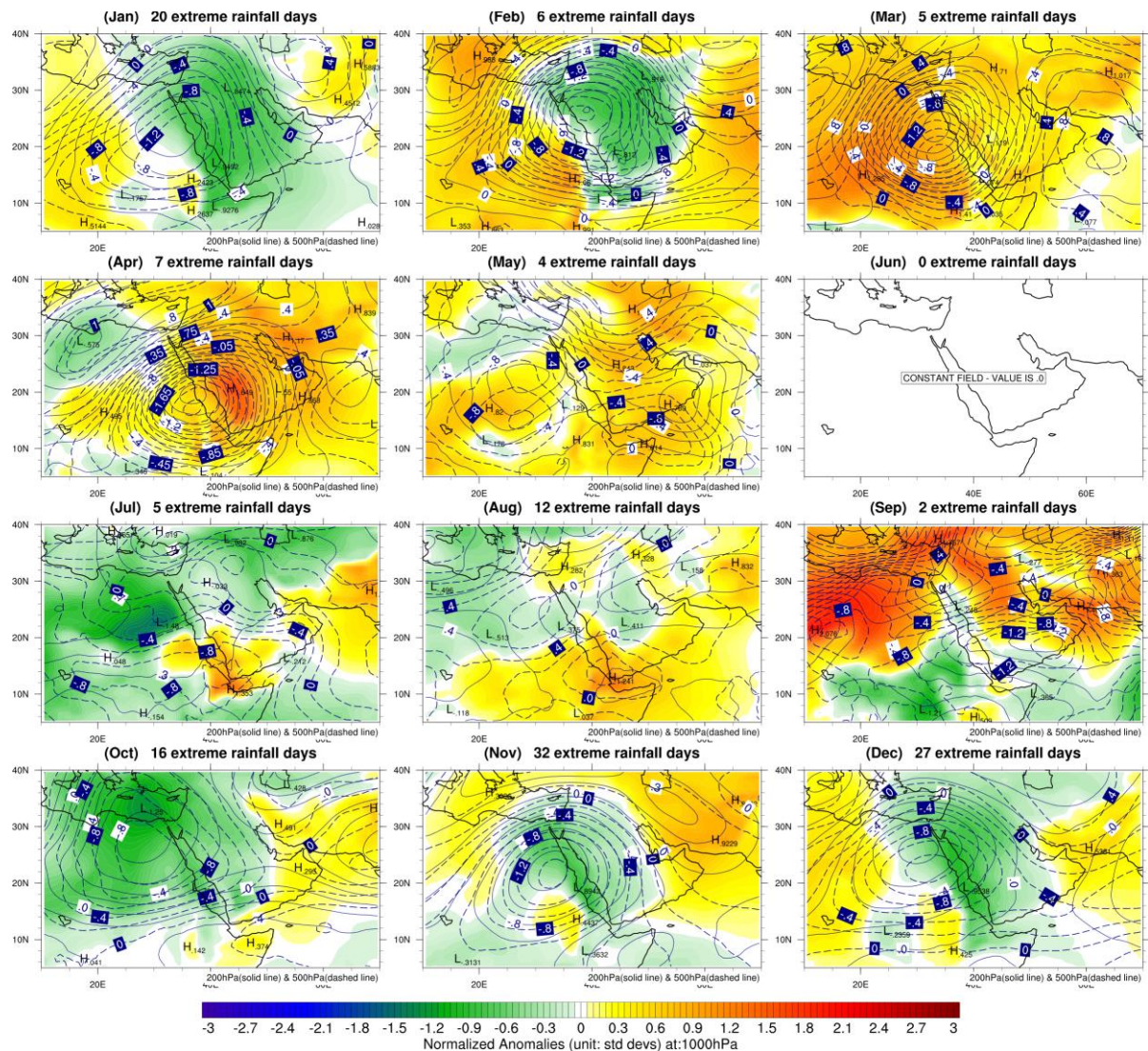
Figure 4.10. The composite of daily mean normalised GPH anomalies for extreme events (RR>90th percentile) in each month during the period from 1985 to 2014 at three GPH levels, 1000hPa (colour fill), 500hPa (dashed line) and 200hPa (solid line); anomalies are given in units of standard deviations.

To further investigate the specific dynamical situation important for individual stations, anomaly composites for the wet season most extreme values were conducted. Figure 4.11

illustrates the composites of the MSLP average and the normalised MSLP anomalies and GPH

anomalies at 850hPa and 500hPa for extreme precipitation days for each station during the

wet season. Figure 4.11 shows that the RST is very clear at the surface for all stations except

for Gizan. This is due to the strong NAH over North Africa and the SH over Saudi Arabia,

however, this only weakly affects Gizan events. The normalised MSLP anomaly composites in

Figure 4.11b show a strongly negative geopotential gradient over the Red Sea at all stations,

except Gizan. Also, there is a strong gradient that appears at the 850hPa level.
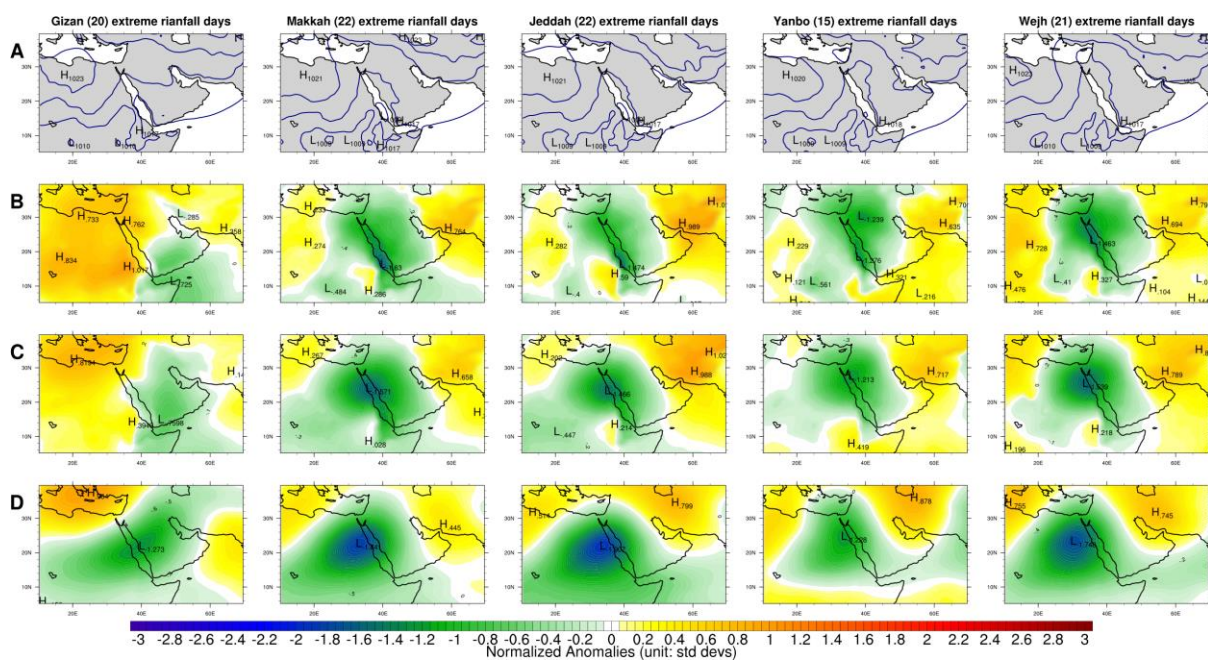
Figure 4.11. Composite mean for each station during the extreme wet season: A) MSLP average, B) normalised anomaly for MSLP, C) 850hPa and D) 500hPa

In addition, the areas surrounding the Red Sea, from the AP to the east to North Africa in the

west, have a positive geopotential gradient. This demonstrates the important role of the SH

and the NAH, although this is not true in Gizan, where the SH disappears. As Gizan is not

affected by the RST, the RST's effect likely extends only to the centre of the Red Sea region.

The main factor resulting in extreme events in Gizan is the interaction between the NAH and

the SL. Negative 500hPa geopotential height anomalies can be found over all stations across

the Red Sea region with the strongest anomalies found in Jeddah, Makkah and Wajh, then

Yanbu and finally Gizan. This supports the notion of an effect on the part of the Upper Atmospheric Level Trough, which extends toward the equator from the north of the Mediterranean Sea during the cold seasons.

4.6. Analyses of Subjective Selected Extreme Event Case Studies;

In order to increase our understanding of the dynamical forcing factors constituting an extreme precipitation event over the Western AP, the 30 most extreme events were identified and analysed in detail with respect to causing mechanisms. As it is a core aim of this study to identify major forcing factors and their potential changes under anthropogenic climate change conditions, out of these 30 events 11 cases were selected to be discussed in detail. This analysis will set the basis for the development of an objective classification approach specifically for the purpose of the analysis of extremes, which also can be applied to coarser resolution and high resolution climate model simulations. In Chapter 5 this approach will be presented in detail and linked to the extreme cases discussed in this chapter.

4.6.1. Thirty most extreme events:

The 30 most extreme events that occurred during the wet season at all five stations were identified and analysed. The 30 extreme precipitation events are the highest rate of total precipitation amount of 79 events for all five stations during the 30 years in wet season (NDJ). These cases were analysed and used to investigate the daily normalised mean sea-level pressure anomaly, geopotential height anomalies, the vertical integrated (1000-500hPa) moisture flux and wind speed and direction in the surface and the upper air (850hPa, 700hPa, 500hPa, 200hPa) during the wet season from 1985 to 2014. Furthermore, the two previous days before the day of each extreme event were analysed to investigate the set-up conditions

in more detail. A summary of the significant surface and upper air pressure systems that affect and support these 30 extreme events is presented in Table 4-3.

No.	city	date	Gizan	Makkah	Jeddah	Yanbo	Wejh	Surface	850 hPa	700 hPa	500 hPa	200 hPa
	Jeddah	18-Nov-1985		4.1	38	27		RST - SH - NAH	SH - NAH - RST	AA - RSL	AA - UT	-
1	Makkah	18-Dec-1985		63	22	0.6	12.1	NAH - LL - SL	AA - UT	AA - UT	AA - UT	SJ
	Wejh	29-Nov-1986					26	LL	LL	AA - CL	AA - UT	SJ
	Yanbo	29-Nov-1991				73.2		RST - SH - NAH - LL	SH - NAH - MD	AA - CL	CL	-
	Jeddah	10-Jan-1992		49.4	40.2	14.4	8.2	RST - SH - NAH	SH - NAH - RSL	CL	UT	SJ
2	Jeddah	2-Nov-1992		17.9	51.5	19.7		SH - SL	SH - RSL	SH - RSL	CL	-
	Gizan	11-Nov-1992	40.2	1.6	7			RST - SH - NAH - LL	SH - NAH - LL	UT	AA - UT	SJ
3	Yanbo	22-Dec-1993				48.5	1.7	RST - SH - NAH	SH - NAH - RSL	UT	UT	SJ
4	Gizan	9-Nov-1994	43					SL	SH - SL	AA - UT	AA	-
	Yanbo	29-Dec-1994				43		RST - SH - NAH	AA - NAH - LL	AA - CL	AA - CL	SJ
5	Wejh	17-Nov-1996	0.1	31.1	22.8	9.8	116.4	RST - SH	SH - RSL	AA - RSL	AA - CL	-
	Jeddah	25-Nov-1996		0.6	55	2		RST - SH - NAH - MD	AA - NAH - RSL	AA - UT	AA - UT	-
	Wejh	14-Jan-1997		4.2			46.9	RST - SH - LL	AA - LL	UT	UT	SJ
	Gizan	12-Nov-1997	59					NAH - AL - SL	AA - NAH - AL	AA - UT	AA - UT	SJ
6	Gizan	9-Jan-1999	61.6	0.1			4.1	NAH - LL - AL	AA - NAH - ML	AA - UT	UT	SJ
	Makkah	16-Nov-2000		53.7	40	1.6		SL	RSL	RSL	CL	-
	Gizan	15-Dec-2000	60.1					NAH - AL	NAH	NAH - UT	UT	SJ
	Makkah	30-Nov-2002		50		19.2		RST	LL	LL	CL	SJ
	Jeddah	10-Nov-2003			44.4	10.5		RST - SH - NAH - MD	SH - NAH - MD	UT - tm	UT	-
7	Makkah	22-Jan-2005		65.2	32	34.7	0.5	NAH - LL	AA - SH - NAH - UT	AA - UT	AA - UT	SJ
	Makkah	11-Jan-2008		61.1				AL - SL	LL	CL	UT	SJ
8	Makkah	6-Nov-2008		51				NAH - SL - AGT	NAH - SL	AA - UT	AA - UT	SJ
	Jeddah	25-Nov-2009		6.2	70			RST - SH - NAH	AA - LL	AA - UT	AA - UT	SJ
9	Yanbo	22-Dec-2009		9.9	6.3	92.5	11.2	RST - SH - NAH	AA - NAH - LL	UT	UT	-
	Wejh	18-Jan-2010				1.2	48	RST - SH - NAH - LL	SH - NAH - MD	AA - UT	AA - UT	SJ
10	Wejh	30-Dec-2010		41	41	36.7	41.7	RST - SH - NAH	SH - RSL	RSL	CL	SJ
	Yanbo	1-Jan-2011				36		RST - SH - NAH	AA	AA - UT	UT	SJ
11	Gizan	3-Jan-2013	47.8					NAH - SL	NAH - SL	AA		SJ
	Yanbo	29-Dec-2013				52	5.6	RST - SH - NAH - MD	SH - NAH - MD	MD	CL	SJ
	Wejh	9-Dec-2014					57	RST - SH - NAH - MD	SH - UT	AA - UT	UT	SJ

Table 4-3. Top 30 extreme precipitation events from 1985 to 2014 during the wet season.

However, Table 4-3 shows the overall results of subjective analysis for each extreme event of the top 30 extreme precipitation events during the wet season over the study area. The table shows the total precipitation amount for each event in each station and the date of occurrence event. The red filling reveal the amount of precipitation that goes beyond the

threshold (above the 90th percentile) in each station. In addition, the table summaries and explains the main synoptic weather circulation in the surface and three atmospheric levels (850hPa, 700hPa and 500hPa) and the subtropical jet stream at 200hPa. The bold text reveals the 11 cases which will be described in more detail in the next section.

Appendix 1 shows the surface and upper weather systems in the top 30 extreme precipitation events, specifically mean MSLP and GPH and normalised pressure and GPH anomaly at the 850hPa, 700hPa, 500hPa and 200hPa levels with wind speed and direction in each level. These are presented in Table 4-3. It has been noted that eleven case studies from these 30 extreme events are selected to cover the full range of possible steering mechanisms as will be shown in the next section. These eleven case studies are used to investigate the surface and upper air conditions, as well as the vertically integrated horizontal water vapour flux (VIWVF) and 3-day backward trajectories of the air parcels in different vertical levels involved in these extreme events.

4.6.2. Detailed Dynamics of representative case studies:

The dynamics of each case study are analysed using the following investigation method and variables: mean MSLP, GPH (850hPa, 500hPa and 200hPa) and wind speed and direction on the day of the extreme event. This is in addition to the normalised MSLP and GPH anomalies; the mean daily vertically integrated horizontal water vapour transport, which is calculated by integrating the zonal and meridional moisture fluxes through each atmospheric layer between 1000hPa and 500hPa, as described in Equation (3) in the methodology chapter; an ensemble of 3-day backward trajectories at three levels from 900hPa to 500hPa over the area that received the heavy precipitation. The figures from Figure 4.12 to Figure 4.22 present dynamic charts for the eleven extreme precipitation events.

4.6.2.1. Case 1; Extreme Event at Makkah on 18.12.1985:

On 18th December 1985, the MSLP anomaly (Figure 4.12 top row) reveals a strong low-pressure system over the Levant and the north of the AP, often also referred to as the LL. It is the steering synoptic-scale weather system during this episode and thus is mainly responsible for bringing heavy rain to the centre and north of the WCSA and the interior areas adjacent to the coast. This low-pressure system propagated from the west over the north of Africa on the 16th of December (not shown). When this low-pressure system passes over the Red Sea, the RST increases the strength of this low-pressure system, forming a strong low-pressure system over the north of the AP.

This system is associated with the strong positive normalisation of the NAH, which is located behind the LL and a weak SH. These conditions allow the LL to penetrate the Levant and reach up to the northern AP and Iraq. The main moisture transport is consequently anticlockwise over North Africa along the Mediterranean coast and converges directly over the central parts of the WCSA.

The UT dominates the mid- and high-upper air levels. The UT is located in the northern Mediterranean and extends to North Africa and the AP. It leads to cold advection from the pole and enhances upward motion when associated with the LL in the low air level over the northern Arabian Peninsula. In addition, the AA is located over the Arabian Sea, which brings warm moist air. Thus, water vapour is transported in large quantities (i.e. reaches more than 500 Kg m^{-1} s^{-1} over precipitation area) from the Mediterranean Sea to Egypt and from the Arabian Sea to the Red Sea. The water vapour density increases over the Red Sea because of the convergence zone between these two moist air masses, which is representative for the climatological feature of the RSCZ.

However, the trajectory maps in the bottom row of Figure 4.12 show that in the low and middle atmosphere, the air flow comes from the Arabian Sea and Red Sea, while in the mid-upper atmosphere, the air flow comes from the Mediterranean Sea through Africa. Obviously, this involves the ARST phenomena, in which moist air masses are transported throughout the low and middle atmosphere by the AA and from the Mediterranean Sea in the mid-upper air by the UT. Additionally, the destabilisation of the air column over the central WCSA is supported by the upper-troposphere trough approaching this reaching at the same time.
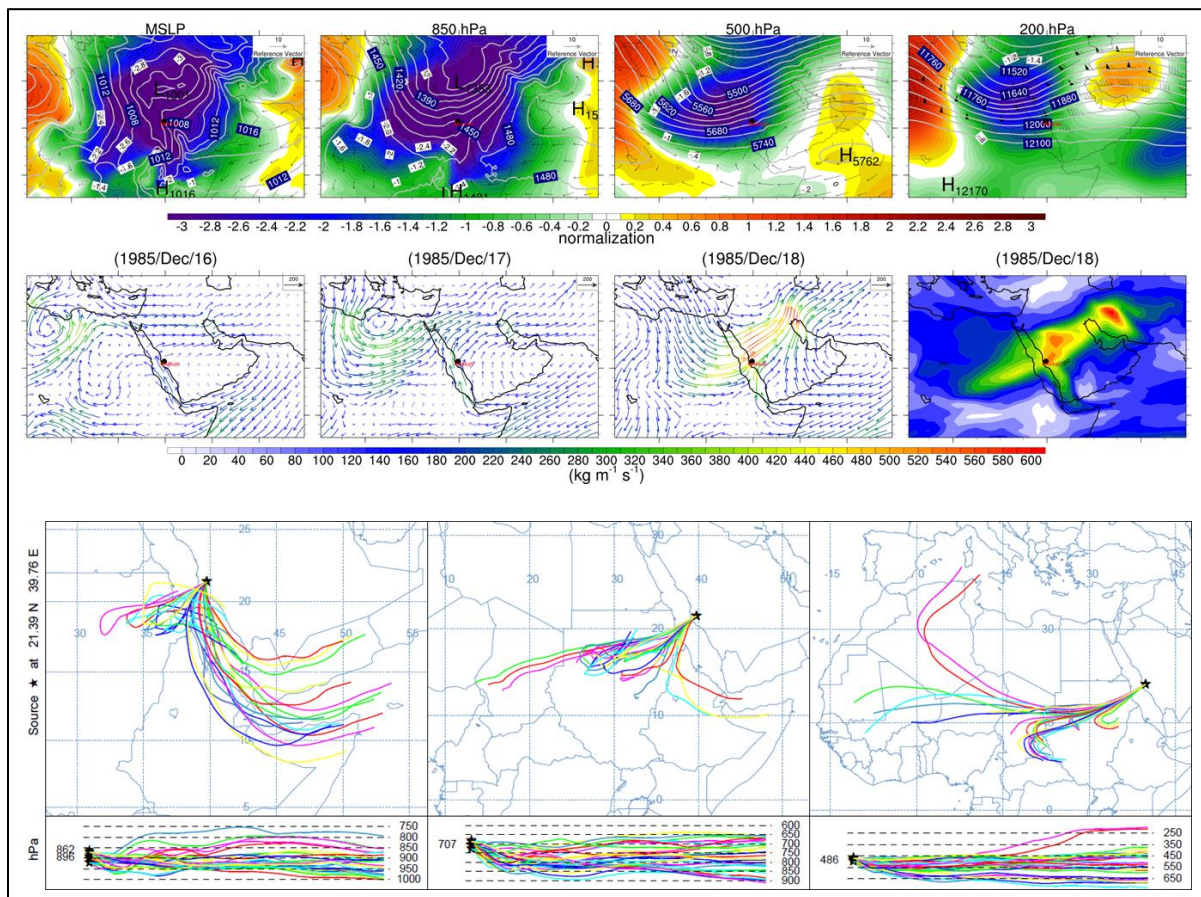
Figure 4.12. Top panel: four charts show the surface and upper weather systems on December 18, 1985, specifically wind (vector), mean MSLP and GPH (contour line) and normalised pressure and GPH anomaly (fill colour) at the 850hPa, 500hPa and 200hPa levels. Middle panel: the mean daily vertically integrated horizontal (1000hPa to 500hPa) water vapour flux (colour and arrows, in Kg m-1 s-1) appear in the first two charts from the left, which show the data for two days before the extreme event. Right = Moisture Flux convergence. Bottom panel: 3-day backward trajectories of an air mass reaching Makkah, starting at 1200 UTC December 18, 1985, at the 900hPa, 700hPa and 500hPa levels.

4.6.2.2. Case 2; Jeddah, 2nd November 1992:

Heavy precipitation (51.5 mm/day; Jeddah station) occurred over the central area of the WCSA on November 2, 1992. The synoptic situation is characterised by a SL extending from Central Africa towards the Northeast of Africa along the Red Sea, without penetrating further into the AP (Figure 4.13). A strong negative normalised anomaly for the SL is associated with a large positive normalised anomaly for the SH, which dominates the Arabian Peninsula and the Eastern Mediterranean. The STJ at 200haP disappears in this extreme event.
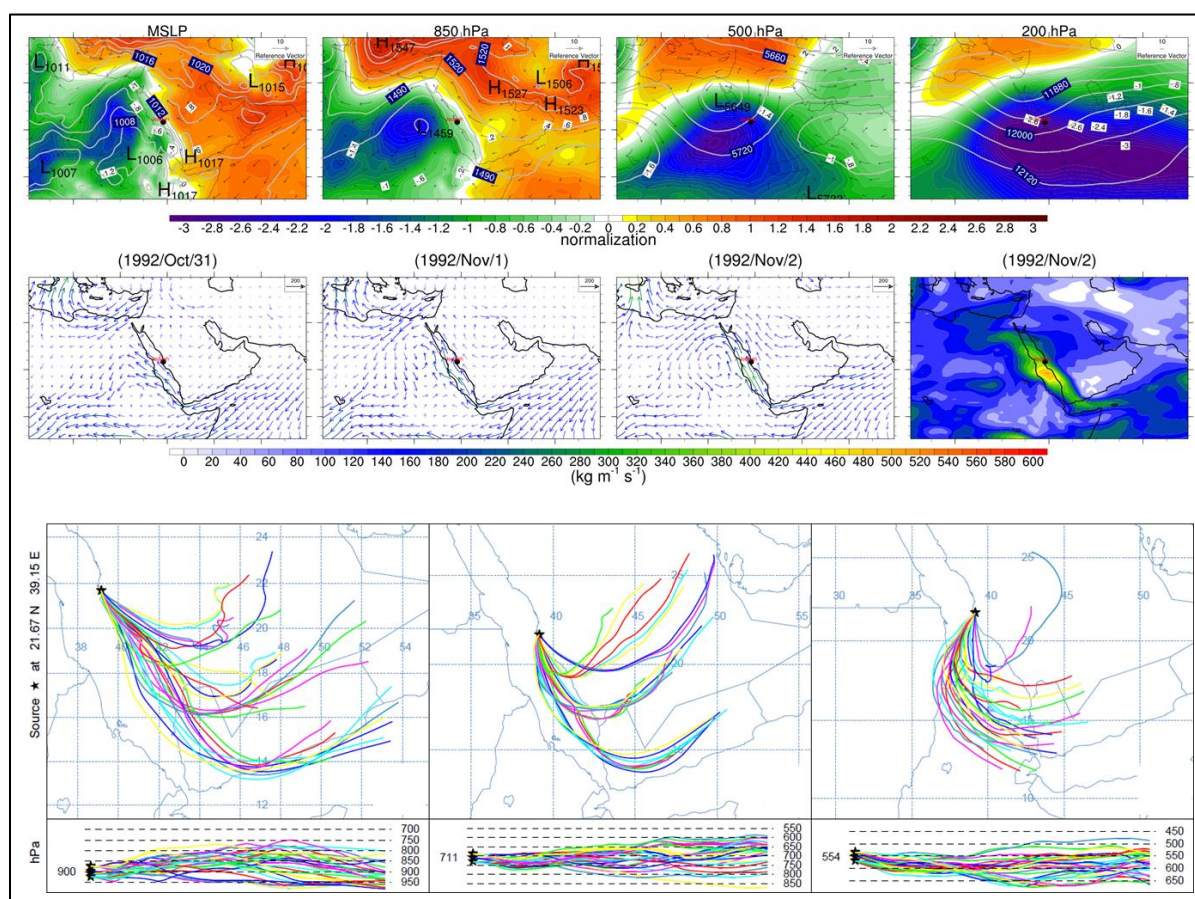
Figure 4.13. as in Figure 4.12 but for Jeddah on November 2, 1992.

This pattern continues vertically over 850hPa, and the deepening of the low forms a cut-off low (CL) over Egypt. This area of developing low pressure is associated with a UT at 500hPa to shift the CL to the northwest of Egypt. The VIWVF charts in the middle row of Figure 4.13 show the AA over the AP and cyclone circulation over Egypt.

65

The AA leads to strong cold advection from the AP, while the water vapour remains quite low. These two circulation patterns enhance the transport of moisture over the WCSA. The water vapour flux is transported from the Arabian Sea through the Red Sea, as is illustrated by the VIWVF and confirmed by the trajectory at all atmospheric levels, as shown in the bottom row of Figure 4.13. Thus, the main source of moisture air is the southern Red Sea and the Arabian Sea, with nearly no interaction to e.g., mid-latitude streamflow conditions.

4.6.2.3. Case 3; Yanbu, 22nd December 1993:

The heavy precipitation on December 22, 1993 in Yanbu was influenced by three pressure systems: the RST, the SH and a strong NAH. These three systems appear most obviously at 850hPa, where the sharp RST extends along the Red Sea between two huge ridges of high pressure over the central AP and North Africa. The result of the RST developing is a cut-off low over the Red Sea on the surface as cyclone. It develops over the northern Red Sea which is called the Red Sea Low (RSL). This RSL extends to the upper air levels at 850hPa. At 500hPa, the UT is displaced to the south and supports the CL in tilting towards the north.

The STJ flows west-to-east through the Red Sea, which enhances the upward motion and instability (because the location of the CL's centre is within the left exit of the STJ), while a frontal wave forms in the right entrance of the STJ. Figure 4.14 shows large amounts of water vapour coming from the Arabian Sea and east Africa. These are similar to the results obtained via the trajectory method, but Figure 4.14 shows the air masses coming from the Arabian Sea in low and middle altitudes and from east Africa in the middle- and high-upper atmosphere in more detail.
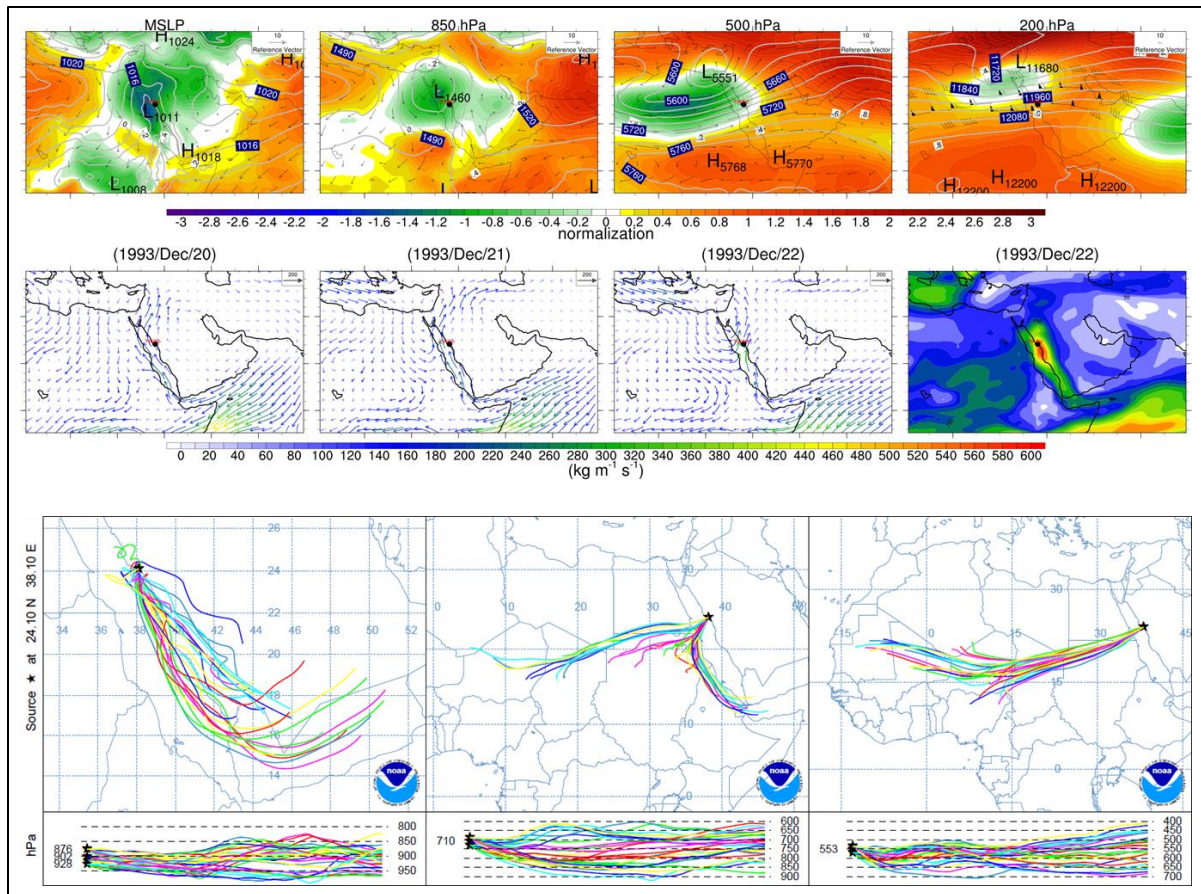
Figure 4.14. as in Figure 4.12 but for Yanbu on December 22, 1993.

4.6.2.4. Case 4; Gizan, 9th November 1994:

A heavy precipitation event occurred over the southern part of the WCSA on November 9, 1994, as shown in Figure 4.15. The RST was weak and did not extend far enough north to influence the Central Red Sea because of the huge high-pressure system that dominates AP.

This case mentions for the RST as a mere trough of the SL because the real shape of the RST is unclear. The central point of this high-pressure system, which has a strong positive normalised anomaly, is located over Turkey, and the system extends to North Africa and the AP. The intensive high-pressure system over central Saudi Arabia is at 850hPa (AA), and it dominates the synoptic conditions over the southern part of the AP and Arabian Sea at the 500hPa level. The AA moves the total flux of the water vapour transported from the Arabian Sea and through the Red Sea to the precipitation area. This is due to the influence of SL, as is

67

shown in the VIWVF charts in the middle row in Figure 4.15. The air mass trajectory figures also confirm the findings of the VIWVF charts.
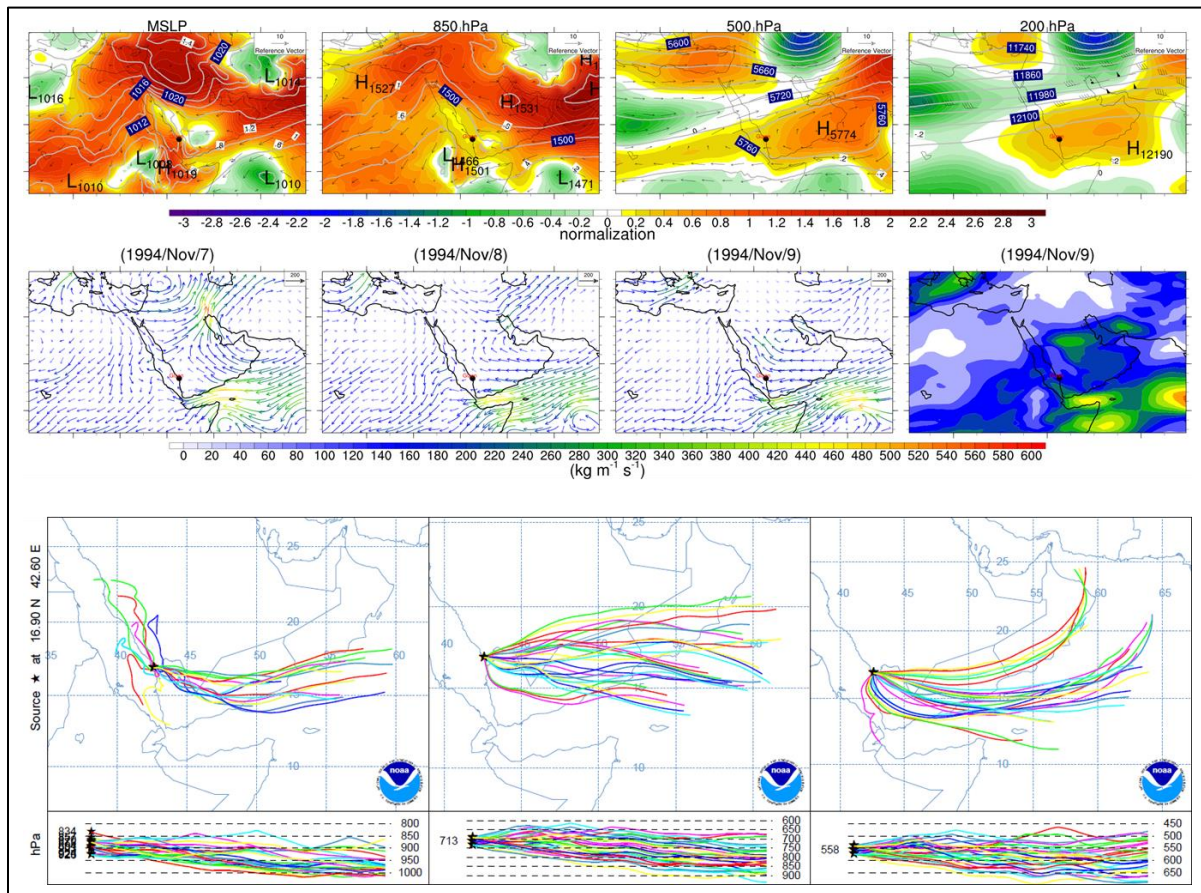
Figure 4.15. as Figure 4.12 but for Gizan on November 9, 1994.

4.6.2.5. Case 5; Wajh, 15-22nd November 1996:

A sequence of heavy precipitation events from November 15 to 22, 1996 resulted in one of the wettest weeks in Western Saudi Arabia in the last four decades. Heavy precipitation was recorded in Wajh. In fact, it was the heaviest precipitation recorded at any station in the WCSA since records began being kept in 1979, with a total of 116mm of precipitation on November 17, 1996. As the Figure 4.16 shows, this case is similar to Case 2. However, in this case, the SH is stronger, while in Case 2 the SL is stronger. In addition, in this case, the RST is more obvious and forms over land in east Africa. The strong SH extends to the southern part of the Red Sea and Mediterranean Sea. This means, in effect, that the RST is surrounded by anomalous high

68

pressure. Thus, strong cyclonic circulation establishes over Egypt and the northern part of the Red Sea.
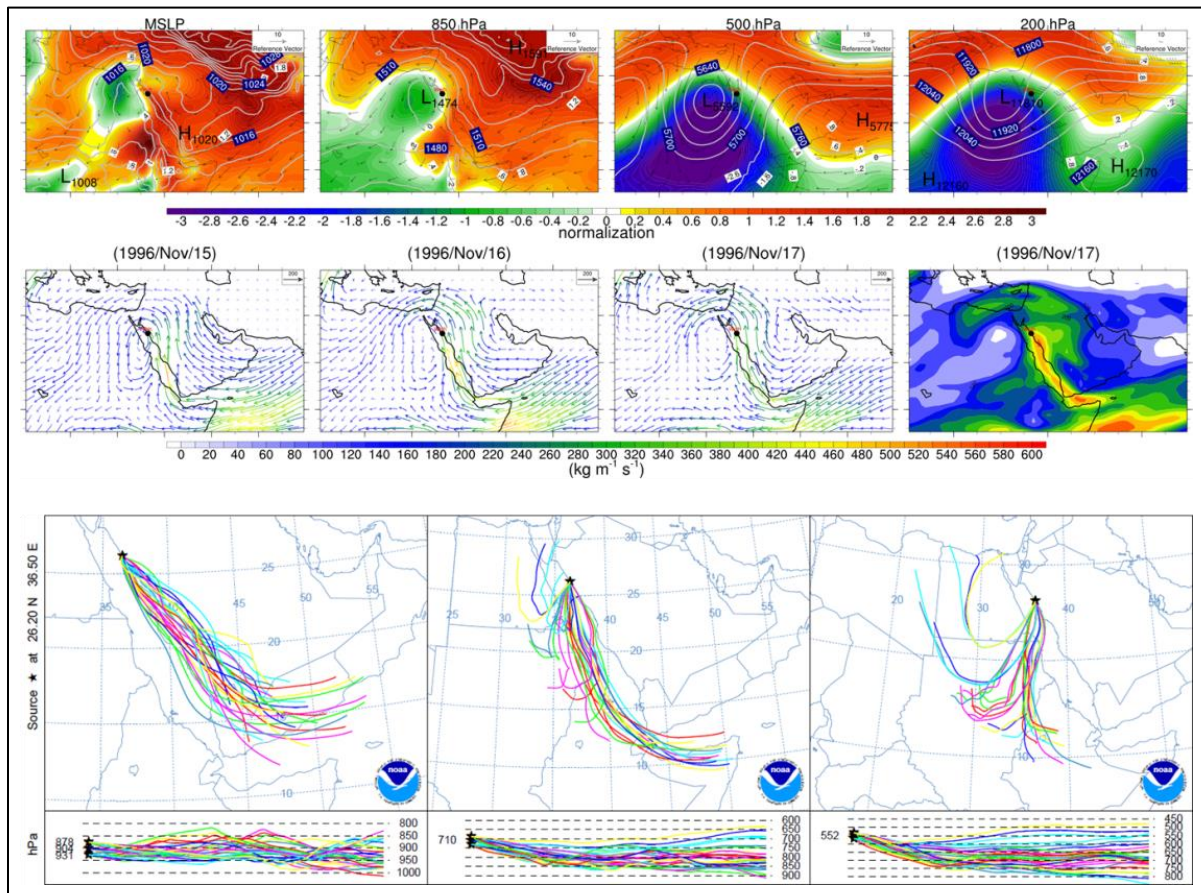
Figure 4.16. as in Figure 4.12 but for Wajh on November 17, 1996.

In addition to the water vapour transport, the source of the water vapour is mainly derived from the Arabian Sea and moisture is transported in the low atmospheric levels across the Red Sea. Also, there is a great deal of evaporation transported from the Red Sea because of the RST. The trajectory analyses show that air masses come from the low altitudes over the Arabian Sea. Other air masses come from Egypt and Sudan and may be formed due to a cut-off low over Egypt at the middle altitudes. This moisture transport is thus strongly linked to persistent cyclonic flow because of the length (one week) of this configuration in this case.

4.6.2.6.   Case 6; Gizan, 9th January 1999:

This event occurred on January 9, 1999 in the southern part of the Red Sea. A strong positive NAH anomaly dominates over North Africa, extending into central Africa and the northern part of the AP (top row in Figure 4.17).
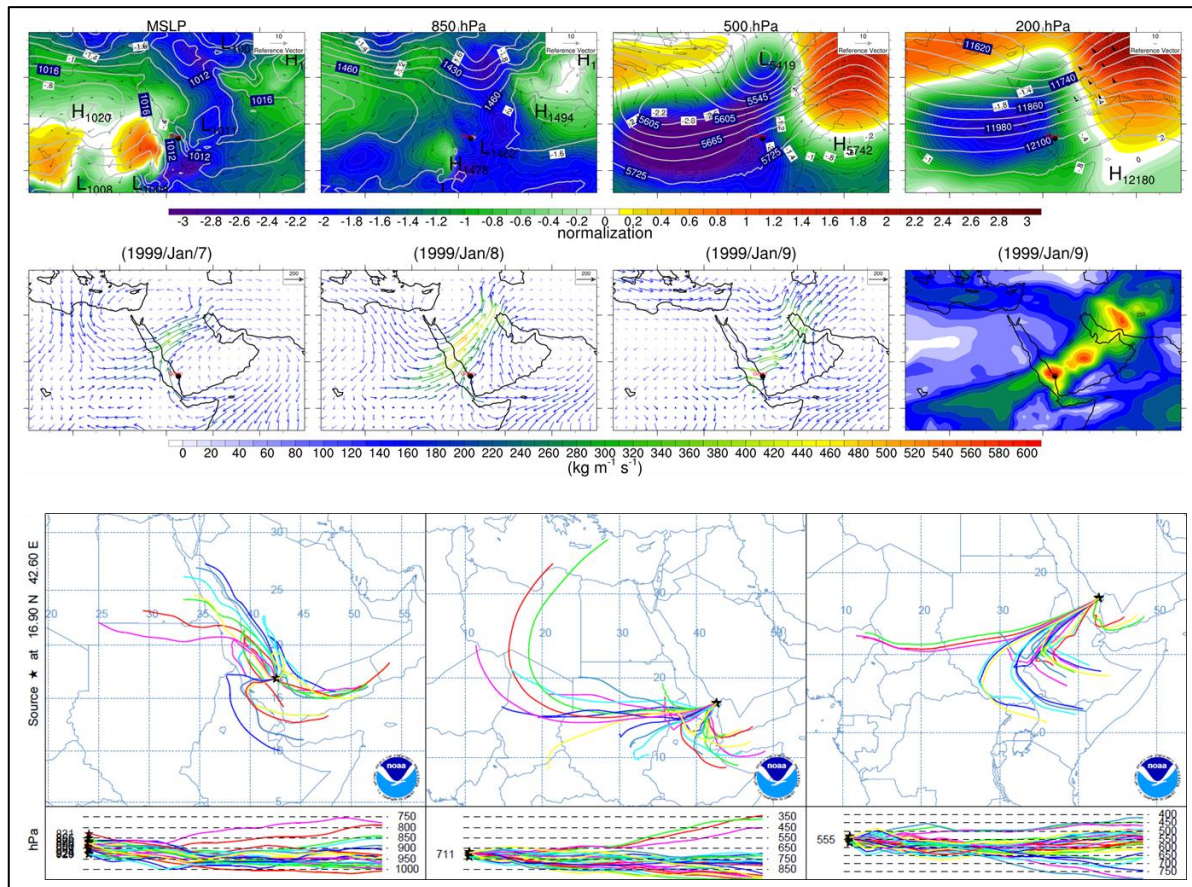
Figure 4.17; as in Figure 4.12 but for Gizan on January 9, 1999.

A low-pressure system is generated over the southwest coast of the AP and then moves into the southern part of the AP. The AL may have originally been part of the RST, but it has been displaced into the Arabian Peninsula by the strength of the NAH and the decline of the Siberian high. This low-pressure system is a good example of the so called climatological Arabian low (AL), and it is linked with the MLs that reach Turkey. The AA forms in the mid-troposphere over the Arabian Sea. This helps to advect warm humid air that is saturated when

it meets with the cold air mass coming from the Mediterranean across the Red Sea and Central Africa.

The axis of the UT extends to the southern part of the Red Sea. Water vapour arrives from East Africa and the North Red Sea, in addition to that coming from the Arabian Sea, as the VIWVF shows in Figure 4.17. Moreover, the trajectory shows that the moisture comes from the Arabian Sea and the northern Red Sea in the low altitudes and cooler air destabilises coming from Central Africa in the middle and high altitudes.

4.6.2.7. Case 7; Makkah, 22nd January 2005:

Heavy precipitation affected the northern and central parts of the Red Sea Coast on January 22, 2005. Figure 4.11 shows that four synoptic pressure systems converged in this region, namely the SH, NAH, RST and ML and are steering the general configuration.

The ML displaces the SH and NAH and extends to meet the RST over the AP. The development of a low-pressure system occurred, allowing the LL to form over the northern part of the AP. This represents the same situation as in Case 6, but here, the SH is stronger. Hence, the low-pressure system was stalled over the Red Sea region. These surface pressure systems are associated with the UT and AA in the upper air, in addition to the SJ, which flows over the AP. These upper-air pressure systems enable the transfer of water vapour from several areas.

Water vapour comes from the Arabian Sea and the Red Sea in the lower layers, while in the middle and upper layers, water vapour comes from the Mediterranean and Central Africa. The water vapour located in Central Africa probably comes from the Arabian Sea due to the strong AA or the fact that an extremely strong westerly STJ stream produces a cloud band that stretches across the Red Sea from Africa. This is one of the two type of Tropical Plumes

moisture pathways over the Middle East where the STJ works with AA to bring moisture from the from Central and Eastern Africa (Tubi and Dayan, 2014).
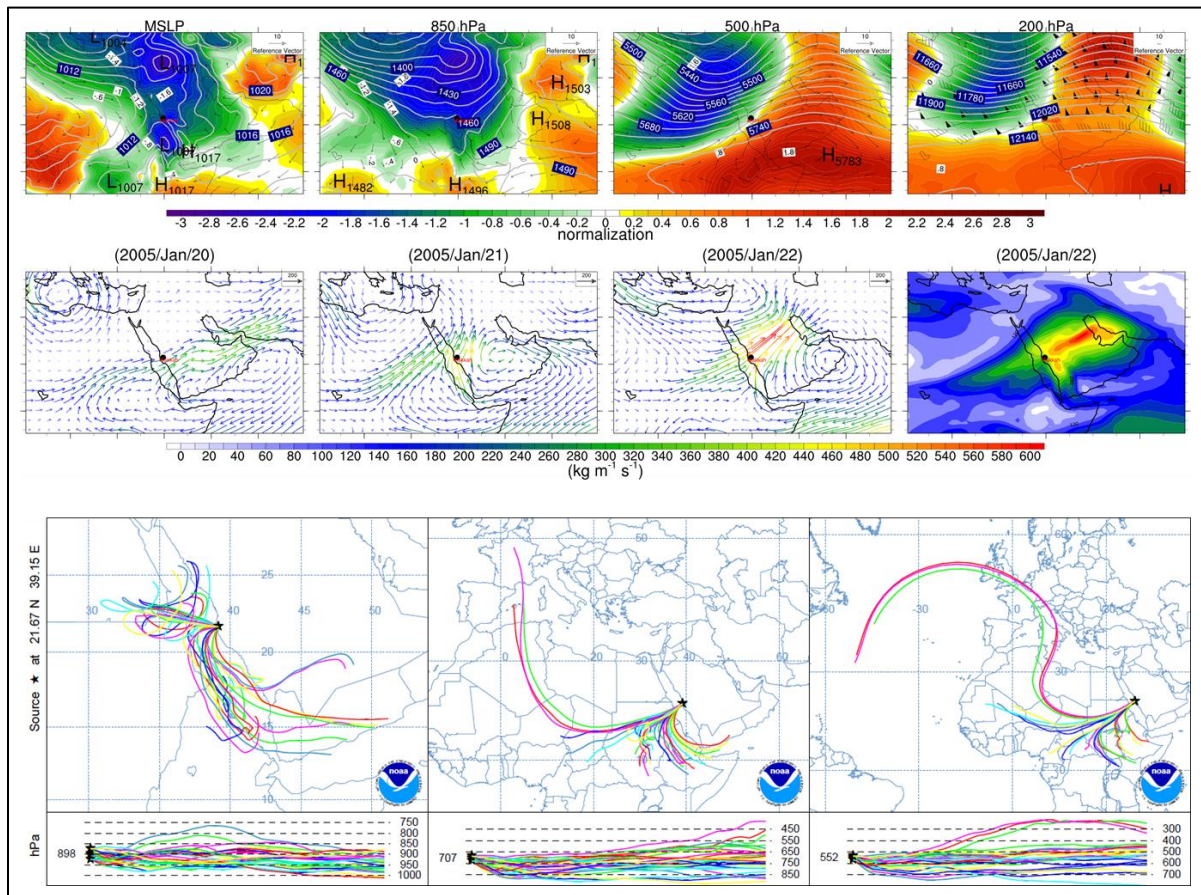
Figure 4.18. as in Figure 4.12 but for Makkah on January 22, 2005.

4.6.2.8.   Case 8; Makkah, 6th November 2008:

Heavy precipitation occurred on November 6, 2008 within the city of Makkah. The basic synoptic conditions are generated by the weakening of the NAH. Then, the SL spreading and stretching into the Arabian Peninsula and the Mediterranean and extending into the northern AP through the Levant region (Figure 4.19).

The result is a high-pressure system that forms over northern Saudi Arabia called the NSH. This high-pressure system brings cold, dry air into the AP, which meets with the moist air that comes from the Red Sea. Further, the air mass from the Arabian Gulf due to the AGT, which

forms over the Arabian Gulf. This circulation pattern is similar to the synoptic pattern observed in *sem1-eason*, in October, as shown in Figure 4.9. In addition, the VIWVF charts in the middle row in Figure 4.19 shows that, two days before the event occurred, the main moisture source was the Arabian Sea. The trajectory analysis also shows the entry of this air mass from inside the AP and Red Sea at low levels, while at the middle and high altitudes, the air mass came from Africa and the Mediterranean.
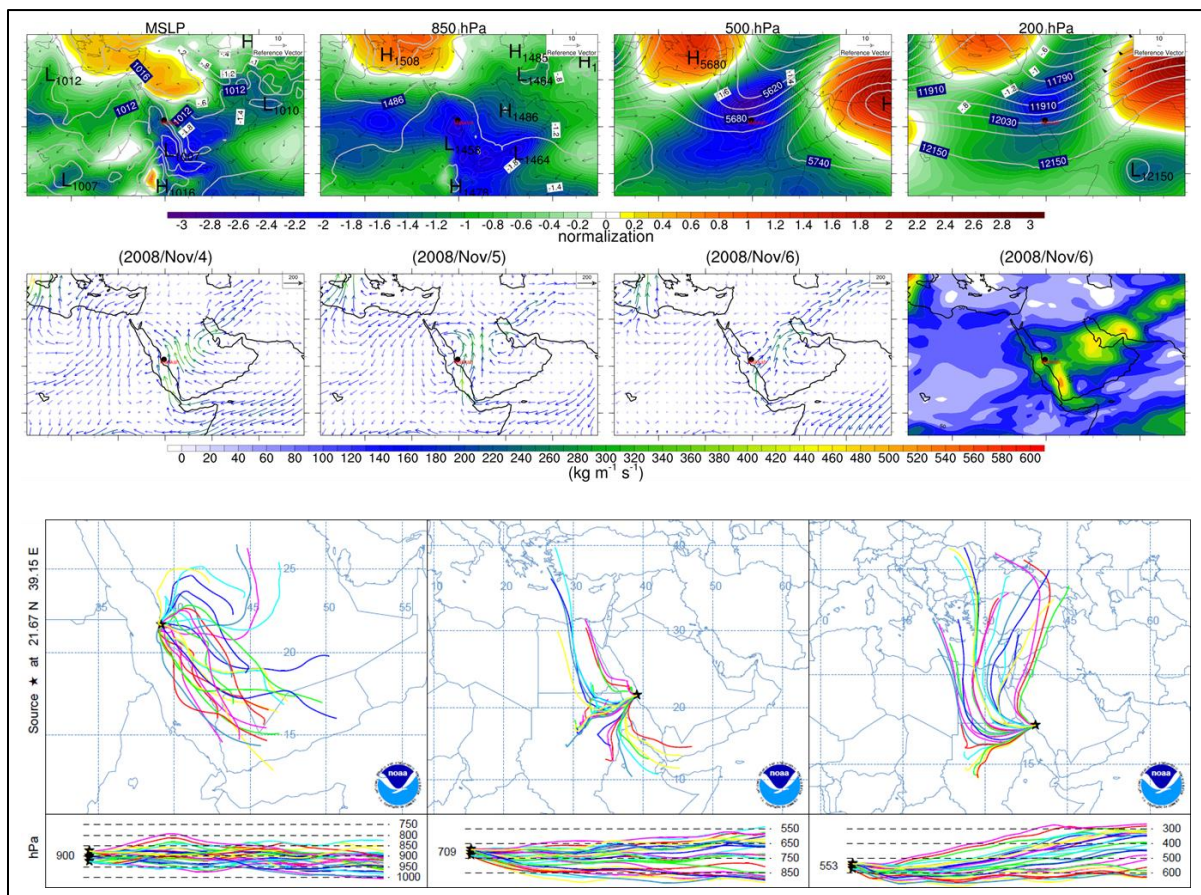
Figure 4.19. as in Figure 4.12, but for Makkah on November 6, 2008.

4.6.2.9. Case 9; Yanbu, 22th December 2009:

Exceptionally prolonged and heavy precipitation across most of the north and central Red Sea coast on 25th November of 2009 led to severe flooding in Jeddah, which is analysed in many previous studies (e.g. Alkhalaf and Basset, 2013, Almazroui, 2011b, Almazroui, 2012, de Vries et al., 2016, de Vries et al., 2013, Haggag and El-Badry, 2013, Yesubabu et al., 2015). Figure

4.20 shows the dynamic systems which play the important role in heavy precipitation occurred on December 22, 2009 within the city of Yanbu.
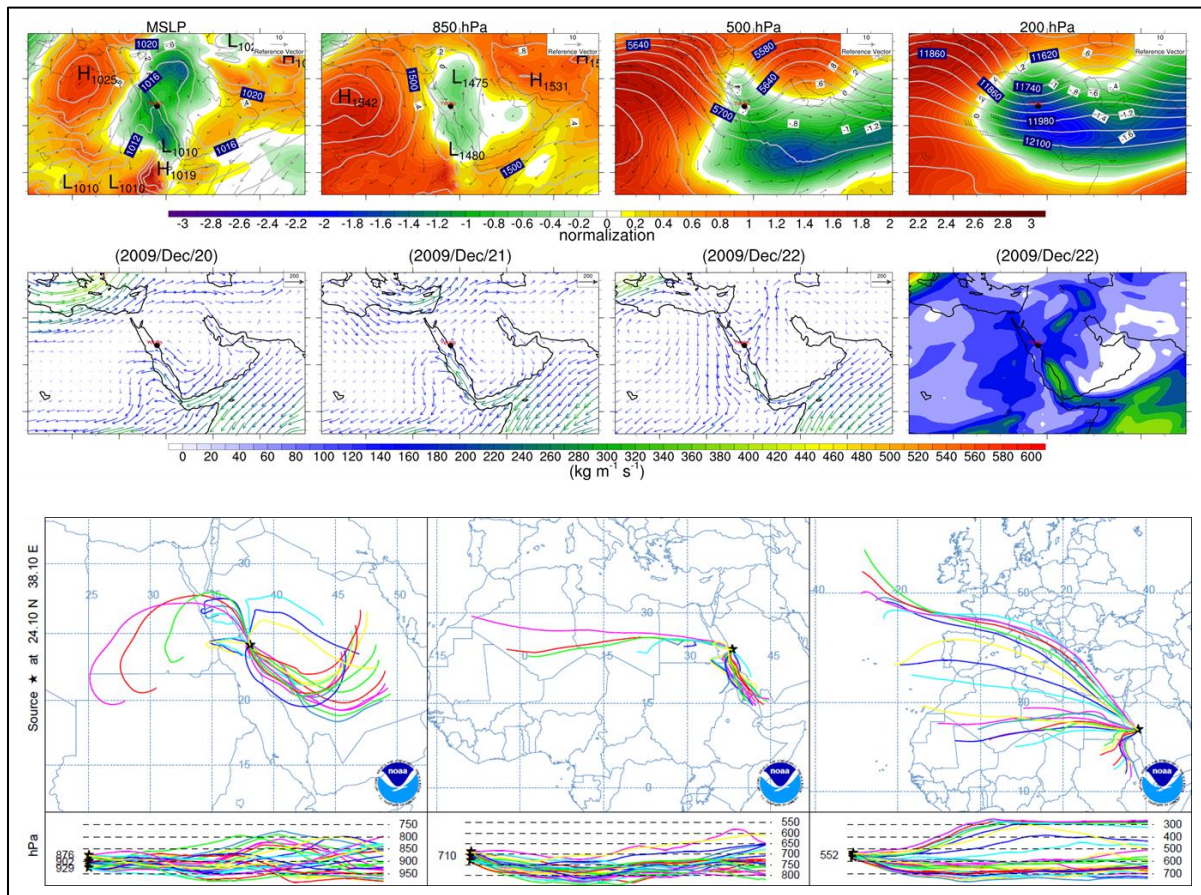
Figure 4.20. as in Figure 4.12 but for Yanbu on December 22, 2009.

The RST extends into the AP toward Iraq because a strong NAH with a positive normalised anomaly controls North Africa and the Mediterranean Sea. At 850hPa, the AA forms over Iran. This consists of a strong LL over the northern AP, which meets with the RST over the Central Red Sea. The VIWVF depicted in the middle row in Figure 4.20 indicates that one day before the event occurred, two anticyclonic circulations existed: one over the Mediterranean Sea which is ML and the other over the Red Sea as RST shape. Hence, they met over the north Red Sea coast region.

In addition, the above figure shows that a saturated air mass came from the Mediterranean and Arabian Sea and moved through the Red Sea. The trajectory shows that this mass had

three components: one dry, cold component coming from the central of the AP; a second component coming from Africa and the Red Sea and, in the high altitudes, a third component coming from the Atlantic Ocean through Central Africa and the Mediterranean region.

4.6.2.10. Case 10; Wajh, 30th December 2010:

This case includes the central and northern parts of the coast on December 30, 2010. This case is similar to Case 3. However, for this case, the NAH was weaker and did not extend across the Red Sea. Therefore, the RST extended over the Red Sea (Figure 4.21).
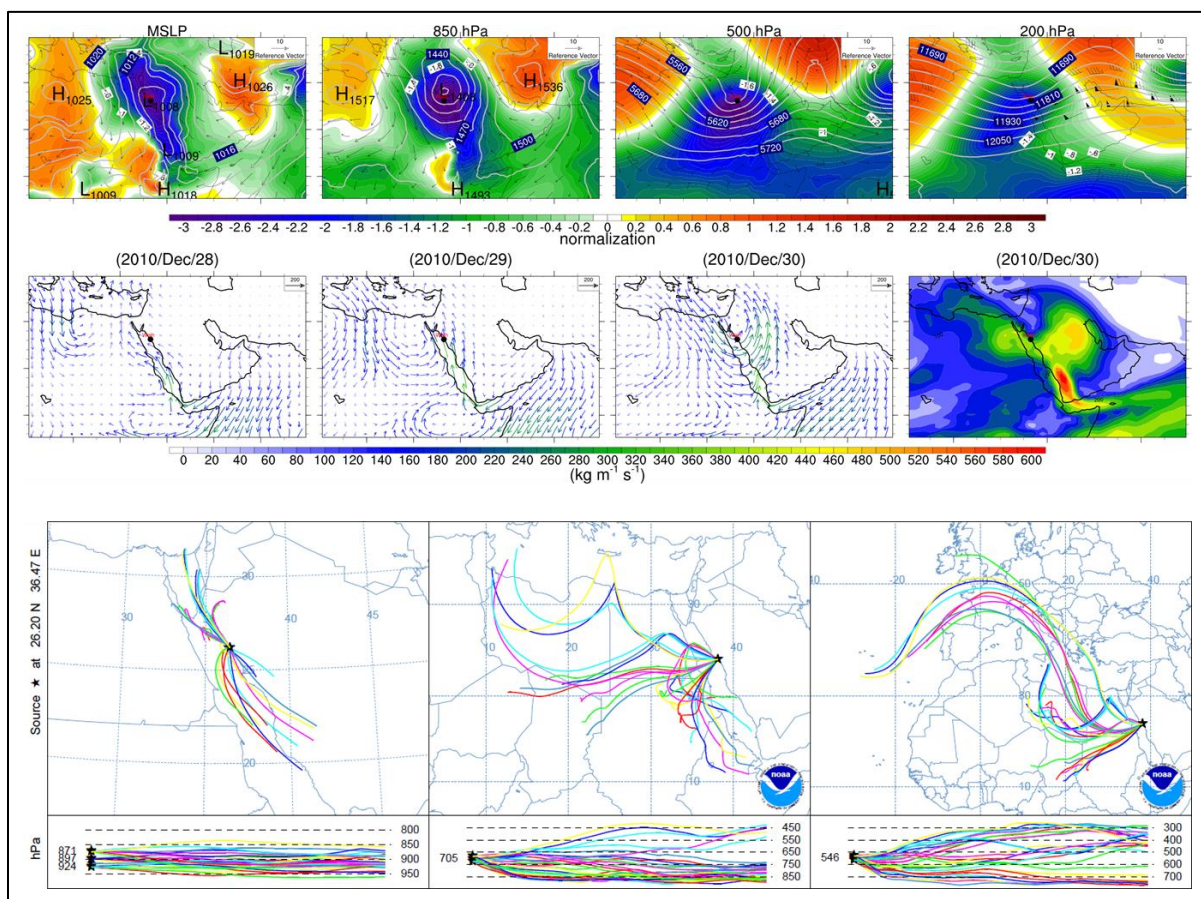
Figure 4.21, as in Figure 4.12 but for Wajh on December 30, 2010.

The RST was deep and has a strong normalised anomaly. In addition, it extended from the Mediterranean Sea to the Arabian Sea. A strong RSL was created over the Red Sea, which was associated with the STJ and UT in the upper air. The term 'RSL' refers to strong cyclonic wind

circulation. Thus, moist air is transported from the Mediterranean and Arabian Sea, as is the rising moist air from the Red Sea. In addition to the VIWVF, the trajectory shows that the air mass entered the precipitation area from the Mediterranean and Arabian Sea through the Red Sea. Also, an additional air mass was picked up by westerly winds from the Atlantic Ocean and moved across Africa.

4.6.2.11.   Case 11; Gizan, 3th January 2013:

On January 3, 2013, a heavy precipitation event occurred in the southern part of the coast. This case is very similar to Case 4, which also occurred in Gizan, but in this case, the central part of the high-pressure system was displaced to the east of the Mediterranean. This pattern continues vertically for the AA over the AP at 850hPa and over the Arabian Sea at 500hPa, as Figure 4.22 shows. Due to the AA over the Arabian Sea, water vapour is transported from the Arabian Sea as the VIWVF chart shows. In addition, the trajectory charts show that some air mass comes from the internal part of the Arabian Peninsula and Africa at the middle atmospheric level and from Arabian Sea in higher.

4.7.   Summary:

In summary, it has been shown from the precipitation analysis of five meteorological stations along the WCSA during 30-years (1985-2014) that the annual total precipitation amount shows a slight gradual decrease from the south to the north. The annual average precipitation values in order from large to small are 134mm, 105mm, 85mm, 38mm and 34mm in Gizan, Makkah, Jeddah, Yanbu and Wajh, respectively. Further analysis showed that the distributions of percentages of the mean monthly total and extreme precipitation (frequency and amount) showed a large month to month and station to station variability.
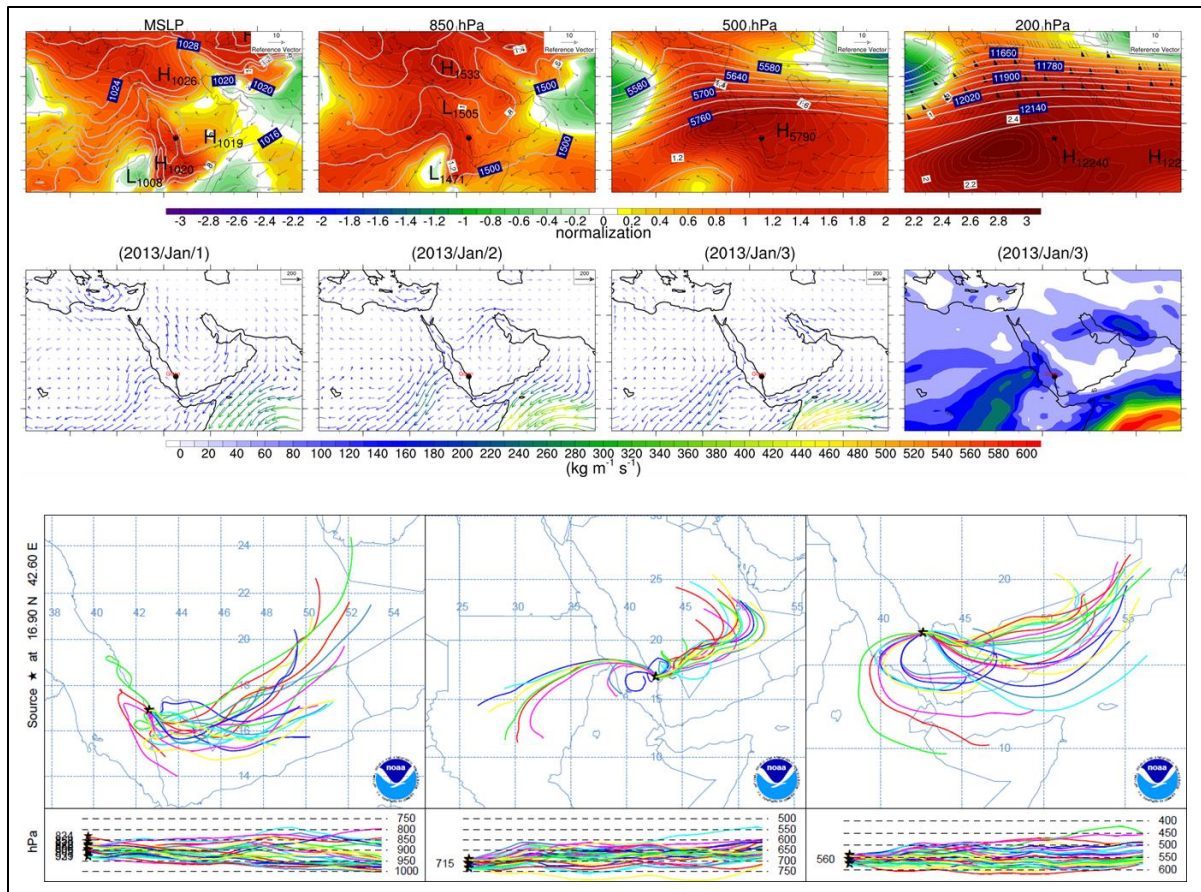
Figure 4.22. as in Figure 4.12 but for over Gizan on January 3, 2013.

The spatial and temporal distributions of precipitation throughout the year along the WCSA have been divided into three main sub-regions. In the southern regions, precipitation occurs in the summer, late autumn and early winter, whereas in the central regions, precipitation occurs at the end of autumn and the beginning of winter and in the northern region, precipitation occurs in the winter.

In addition, these results show that several precipitation seasons along the WCSA with two peak precipitation periods of winter and summer occurring just in two stations (Makkah and Gizan). All stations recorded high total and extreme precipitation amount and frequency from November to January. This period from November to January is one of the two peak precipitation periods throughout the year and is considered as the wet season. Another peak precipitation occurs over the southern region and in some inland areas from June to

77

September and is known as the dry season. The other two seasons are depicted as the transfer seasons between dry and wet season, these two transition seasons have a small amount and frequency of total and extreme precipitation events. This study defines these two seasons as the first semi-wet season from February to May (FMAM) and the second semi-wet season in October, which follows the dry season.

The investigation of extreme precipitation events has shown that 136 extreme events had been recorded from all five observation stations in all seasons during the 30 years by 90th percentile of threshold. 79 of these extreme events are in the wet season from November to January. These 79 events accounted for 58% of all extreme events that occurred during the 30-year period. The percentages of total extreme events for each individual station are 40%, 50%, 83%, 84% and 88% for Gizan, Makkah, Jeddah, Yanbu and Wajh, respectively.

This extreme wet season is homogeneous for all the stations not only in terms of precipitation but also in dynamic climatology factors. Regarding this concept, means monthly of average and anomaly composites for MSLP and different Geopotential Heights for the all days and all extreme event days throughout the year and also for each station extreme days. It shows that in November, December and January the negative MSLP anomaly is moved eastward over the Red Sea region, and this is associated with highly negative GPH anomalies in the upper levels.

The results from individual stations were similar between stations but there are some different dynamic climates in Gizan where the RST is very clear at the surface for all stations except Gizan. In general, the surface and upper GPH charts show that multiple climatic factors play important roles in the distribution of precipitation during the wet season. The main factor of dynamic climatological factors is RST, which extends over the Red Sea as a trough from the

SL and the two high-pressure systems NAH and SH in addition to UT in the upper atmospheric level.

These dynamic climatic factors were further investigated by a subjective study that looked at the 30 highest rates of total precipitation amount out of 79 extreme events. These case analyses concluded that the high and low pressure systems on the surface play an important role by interacting with the STJ. These STJ appear in most of the events, along with UT, which exists in almost all events (the exceptions were some events that occurred in Gizan). Furthermore, the vertically integrated horizontal water vapour flux results are noteworthy as they are present in all extreme precipitation events; they are relatively comparable to the precipitation observation data regarding location and amount of precipitation in most extreme events. In addition, the vertically integrated horizontal water vapour flux results are confirmed by the trajectory air mass.

In order to link these events with objective analysis, 11 events were selected and investigated in more detail. The results show that many of pressure synoptic systems which are investigated have been discussed in previous studies but some of them did not such as RSL. In addition, some of these systems have been investigated in more detail, such as RST and MLs. MLs in this study have been categorised to two type one is LL which is located east of eastern Mediterranean region and extend to the Levant and, the second which is remain over the Mediterranean sea and called in this study Mediterranean depressions MDs as Capris low.

In some cases the MLs meet with RST and then it is classified as ARST. RSL is the cut off low which is created when the extreme RST extends between strong two high pressures (i.e. SH and NAH) and in some cases this cut off low is over Egypt. RST exist in most of the events but with different location of its axis and sometimes does not extend to the north of Red Sea.

When the RST do not appear this mane the SL system extend to inside the AP and acting with SH. In this situation SL affects the southern part of WCSA, in addition, in the rare case, the AGT extends inside the AP from the eastern AP. Also in this situation the moisture air mass which is derived by AGT affects the southern and the inland in central region of WCSA.

In addition to the low pressure systems, the high pressure systems play a very important role in the extreme precipitation events over the WCSA. For some of the cases this occurred over the northern part of WCSA, SH shifts RST axis to be over the western Red Sea in Africa land and the cot off low is crated over Egypt. Conversely, in precipitation events which occurred over the southern part of WCSA, NAH shift RST axis to be over inside the AP and crates Arabian low. Also in rare case when a strong SL extends to northern Africa and shifts the high pressure system to inside the AP, the high pressure system is created over AP and helps the AGT to bring the air moisture mass from the Arabian Gulf and interacts with SL over the AP. This satiation is similar to the semi wet season in the second semi-wet season in October.

Chapter 5. PERFORMANCE EVALUATION OF MODELS DATA

5.1. Overview:

In this section, the study evaluates the performance of ERA-Interim reanalysis precipitation products using WCSA observations and GPCC data. This is in addition to the performance of regional climate evaluation simulations (hindcast data) from CORDEX-Africa and CORDEX-MENA, which use ERA-Interim reanalysis data and GPCC data over the WCSA region. Finally, the study compares GCMs historical data with RCMs hindcast data in order to use GCMs to assess future climate change in Chapter 7.
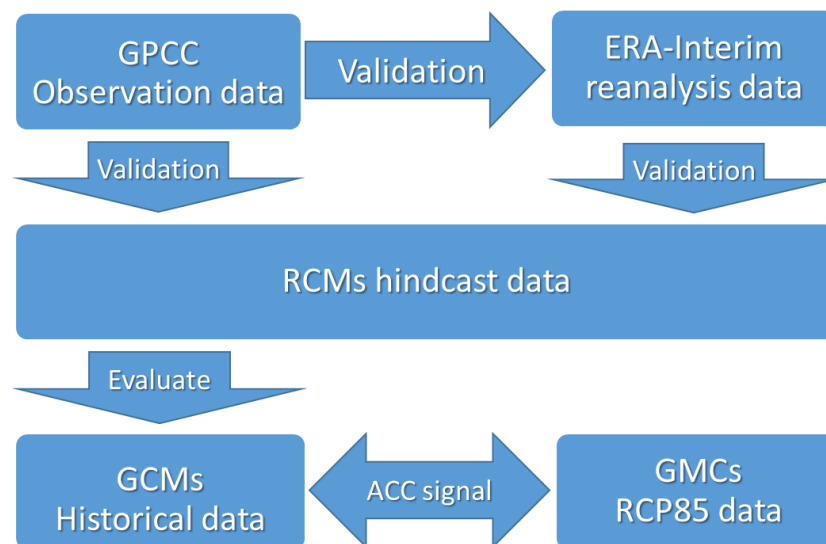
Figure 5.1 Flowchart of the evaluation of models data

Figure 5.1 shows the flowchart that was used to evaluate model products. First, monthly GPCC data and observed precipitation records in the WCSA were used to evaluate the performance of ERA-Interim reanalysis data and RCMs hindcast data and assess the validity of these data. Second, the RCMs' hindcasts were evaluated by ERA-Interim reanalysis, taking the validation of these data into account in the first step, to determine the best performance for RCMs. In fact, RCM validation by direct comparison with observed data was difficult due to many

challenging aspects: the errors in the model formulation, the errors that were imported from driving data and the lack of time and space in a high-resolution observations dataset (Caya and Biner, 2004).

5.2. Validation of ERA-Interim reanalysis derived precipitation for the WCSA area:

5.2.1. ERA-Interim versus observed precipitation dataset:

For the purpose of ERA-Interim reanalysis precipitation validation over the WCSA region in the wet season period from 1985 to 2014, the evaluation was made to investigate the reliability of the daily precipitation field from 35 ERA-Interim reanalysis grid points along the WCSA. ERA-Interim reanalysis precipitation is compared with the observed precipitation dataset from five meteorological stations along the WCSA region: Gizan, Makkah, Jeddah, Yanbu and Wajh, as shown in Figure 5.2.

Therefore, serial correlation coefficients were carried out to determine the relationship between several reanalysis grid points (6, 17, 19, 23, and 27) and the corresponding observation at each chosen station (Gizan, Makkah, Jeddah, Yanbu and Wajh, respectively). The daily total precipitation from the five observed stations and the five corresponding grid points selected and between the daily total precipitation from the five observed stations and all 35 grid points along the WCSA were used. The results of this correlation coefficient are less than 0.3 in the south of the region, which represents the station at Gizan and the points around it. The correlation coefficient increases northward; between 0.3 and 0.4.

However, this relationship remains difficult to determine because of several factors that affect the accuracy of the reanalysis data. For example, these areas are located on the

coastline and are bounded by the mountains in the east and the impact of a tropical climate as ITCZ, especially on the southern regions. Therefore, the assessment of this relationship remains difficult, especially with the lack of rainfall information because of sparsely distributed rainfall gauges and the short duration of monitoring, which does not exceed 30 years at some stations.
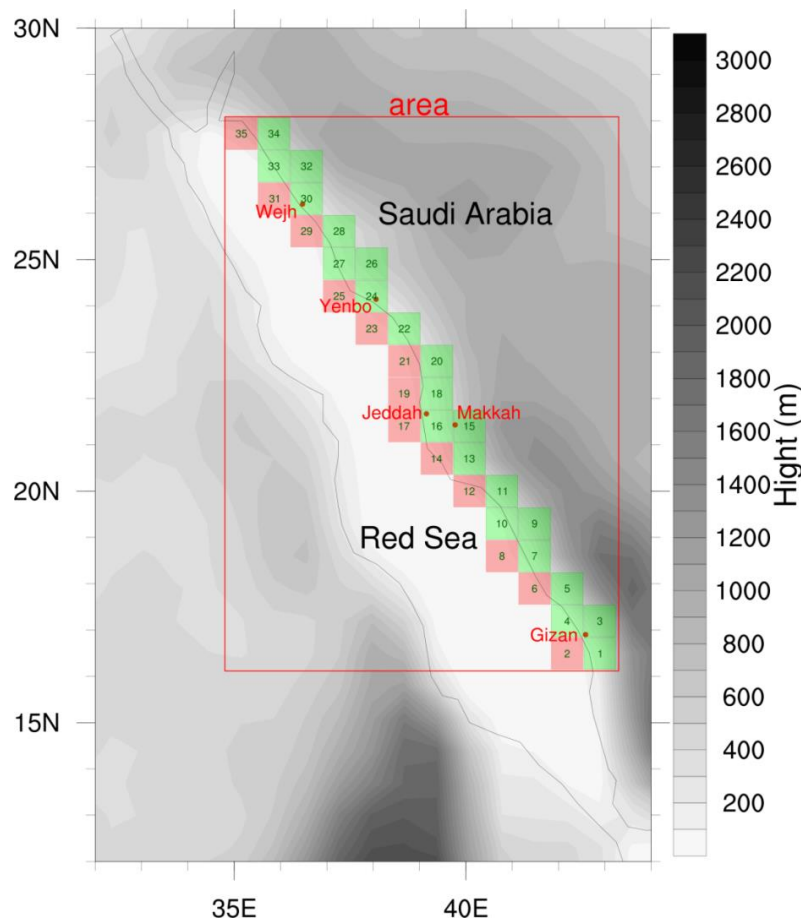
Figure 5.2. Location map of the study area (WCSA) with topography (in meters) and position of the meteorological stations (red circles); the large box indicates the subdomain (35°–43°E and 16°–28°N), and the 35 small boxes indicate a grid point with a 0.75° resolution from the ERA-Interim reanalysis data. Green 22 grid points over the land.

Because of this, the study investigated the number of observed extreme events that were not produced in the reanalysis data at the 90th percentile for each station. The current study found four events in Gizan, four events in Makkah, one event in Jeddah, two events in Yanbu and four events in Wajh. This suggests that the reanalysis underestimates the observations by an

83

average of 19%. The total events that did not appear in the reanalysis data were 15 of 79 extreme events during the wet season during the period from 1985 to 2014.

5.2.2. ERA-Interim versus GPCC:

In this section, the ERA-Interim reanalysis precipitation data are compared with GPCC data to determine the ability of ERA-Interim to assess the precipitation amount and wet-day frequency over the chosen grid cells. Figure 5.3 shows the Taylor diagram results of the CORR and NSD analysis between GPCC and ERA-Interim for values of the total precipitation that is calculated from 1990–2008 of the daily precipitation amounts at wet days (RR). Then, the monthly mean of the precipitation amount is calculated for these values and used. The frequency of precipitation daily data is not used in this part of the evaluation because the data from the GPCC are created monthly and not able to count the number of precipitation events.

All the results are obtained for wet season and whole year, and the annual values (whole year) are better than those found for the seasonal values (wet season). The best results were obtained for the monthly mean precipitation RR reflected by overall positive correlations for all grid cells, with most correlations exceeding 0.5. Most of the NSD values suggest an overestimation of approximately 1.3 for the average year values and above 1.5 for the average wet season values. On the other hand, there was high correlation found between GPCC and ERA-Interim in the individual grid points, which are located over the northern part of the Red Sea coastal region specifically during the wet season. The correlation values in these northern grid points was approximately 0.8 whilst the majority of grid points in year values were between 0.5 and 0.7.
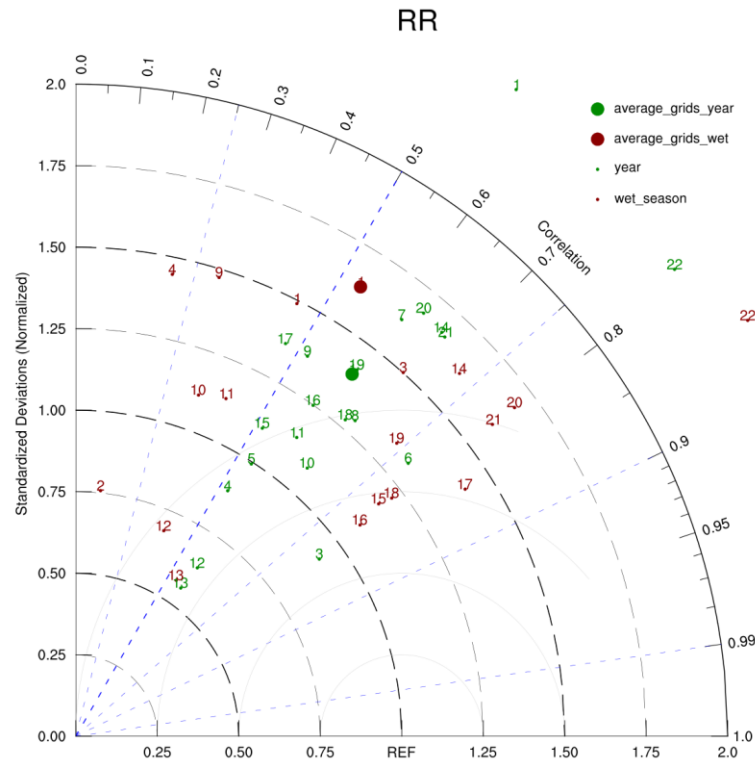
Figure 5.3. Taylor diagram of precipitation in the wet season and annually averaged over WCSA; average for all grid points for the whole year (green), average for all grid points in the wet season (red), grid points for the year (number green), grid points for the year (number red), showing normalised standard deviation and pattern correlation (ERA-Interim reanalysis versus GPCC) for just total precipitation indices (RR).

5.3. Validation regional climate hindcast simulations from CORDEX:

5.3.1. Overview:

The issue of climate change and its future impact is one of the most important issues in the world today because it has both direct and indirect impacts on humans and the land they live on. Therefore, climate centres worldwide develop models to simulate future climate conditions in order to investigate the impact of greenhouse gas emissions on global warming and assess the impact on societies and economies with regard to energy, economy, agriculture and population growth.

Another important goal is to inform policy-makers about changes in extreme weather events; this requires knowledge of how climate states are linked to the amount or frequency of

extreme precipitation events. Therefore, an extension of the current study on extreme weather would be to investigate the extent to which global warming will affect the behaviour of extreme precipitation in the future in this vital part of the Arabian Peninsula. This information of how the climate might change under future climate conditions is provided by many large-scale global climate models, but to provide climate change information on much smaller spatial scales, such as regional scales, regional climate downscaling methods (RCD) are used. One such method is the dynamic downscaling method, which uses RCMs forced by GCMs at its lateral boundaries.

RCMs and GCMs have been developed to investigate the impact of future climate change. However, unlike GCMs, RCMs produce coordinated sets in one CORDEX framework (Giorgi et al., 2009). This framework has 14 domains that cover the entire Earth. Two of these CORDEX domains cover the entire Arabian Peninsula, namely the African domain (CORDEX-Africa), which was evaluated by Kim et al. (2011), and the Middle East–North African domain (CORDEX-MENA), which approximately covers the region from 7°S–45°N and 27°W–76°E (Almazroui, 2016). Figure 3.1 shows the CORDEX-Africa and CORDEX-MENA domains.

To analyse future projections of the CORDEX-Africa and CORDEX-MENA domains, it was necessary to evaluate the performance of RCMs that are used to downscale the GMCs. The specific objective of this section is to evaluate the performance of the available RCMs from CORDEX-Africa and CORDEX-MENA to simulate mean and extreme precipitation over the western coast of Saudi Arabia. However, to evaluate these RCMs, this study uses the respective evaluation simulations (hindcast data) from each RCM, which are driven by ERA-Interim reanalysis data at their lateral boundaries. The dynamic downscaling of RCM simulations are driven at the lateral boundaries by several GCMs or reanalysis data (Giorgi

and Lionello, 2008). It is best to situate the lateral boundaries of RCM domains as far as possible from the study area (Giorgi, 2006). Despite lateral boundary constraints on RCMs, many studies have shown that the internal variability values are exhibited as different solutions by the capacity of RCM with the same set of lateral boundaries (Alexandru et al., 2007). This variability depends on a function of season, domain size, synoptic regime and geographical location (Giorgi and Gutowski, 2015). For example, on a seasonal scale, the maximum of the internal variability for precipitation in the warm season is computed according to the variance between the individual member seasonal averages (Alexandru et al., 2007).

5.3.2. Hindcast simulations data and methodology:

Only the SMHI simulations were available through the Earth System Grid Federation (ESGF), even though more RCMs have been run for the CORDES-MENA domain (such as, the Danish Meteorological Institute (DMI), University du Quebec a Montreal (UQAM), Swedish Meteorological and Hydrological Institute (SMHI), Climate Limited-area Modelling Community (CLMcom) (Bucchignani et al., 2015a) and King Abdulaziz University (KAU) (Almazroui et al., 2016a)). In addition to these data CORDEX-MENA simulations for the CORDEX-Africa domain was used. Simulation output from the SMHI RCM (RCA4) used for the CORDEX-MENA domain is also available for CORDEX-Africa. Table 5-1 shows the information of the list of evaluation simulations forced by the driving model ECMWF-ERAINT. All simulations have been run in a horizontal resolution of 0.44°.

To evaluate the performance of these models for precipitation, the correlation coefficient (CORR) and the normalised standard deviation (NSD) are calculated for monthly precipitation rates between the RCMs hindcast and GPCC data for the 16-year period from 1990–2005 and

87

between the RCMs hindcast and ERA-Interim reanalysis data for the 19-year period from 1990–2008. This evaluation was applied over the area surrounding the western coast of the Arabian Peninsula from 12°S–30°N and 32°W–44°E (Figure 5.2).

No	Institute name	Institute ID	CORDEX Domain	RCM name	RCM ID	Period run
1	Danish Meteorological Institute	DMI	Africa	HIRHAM5	HIRHAM5	1989–2010
2	Royal Netherlands Meteorological Institute	KNMI	Africa	RACMO22T	RACMO22T	1979–2012
3	Universite du Quebec a Montreal	UQAM	Africa	CRCM5	CRCM5	1979–2012
4	Climate Limited-area Modelling Community	CLMcom	Africa	CCLM4-8-17	CCLM4	1989–2008
5	Max Planck Institute for Meteorology	MPI-CSC	Africa	REMO2009	REMO2009	1989–2008
6	Met Office Hadley Centre	MOHC	Africa	HadGEM3-RA	HadGEM3	1990–2008
7	Met Office Hadley Centre	MOHC	Africa	HadRM3P	HadRM3P	1990–2011
8	Swedish Meteorological and Hydrological Institute	SMHI	Africa	RCA4	RCA4	1980–2010
9	Swedish Meteorological and Hydrological Institute	SMHI	MENA	RCA4	RCA4	1980–2010

Table 5-1. The list of regional climate models used in the evaluation.

This area includes the whole Red Sea region with its complex topographical terrain in the southern part of the eastern coast of the Red Sea, which is affected by many climatic factors; orographic lifting and convective processes (ITCZ). The representation of these factors within the model might heavily affect their performance, especially with respect to the estimates of local precipitation rates. Therefore, another step was taken to avoid geographical factors; by

comparing the 22 grid points from each hindcast simulation with the corresponding grid point in the GPCC data. Figure 5.2 illustrates these grid points in a green colour. They were chosen based on the location over the coastal area which are corresponding to the gauge-based gridded observational data from the GPCC dataset.

In addition to the spatial diversity, these comparisons were also applied in several temporal scales, including annual (year) and seasonal (*wet_season, dry_season, sem1_season, sem2_season*) periods, which were calculated by monthly precipitation. Seasonal periods are defined in Chapter 4. On the other hand, the four values of the precipitation indices that were calculated from 1990–2008 were based on wet days and the 90th percentile thresholds from the daily precipitation amounts at wet days (rain amount more than 1 mm). These four values of the precipitation indices are based on monthly mean, namely RR, RQ, RR90, and RQ90 which are described in Chapter 3.

In addition to the evaluation of precipitation values in this chapter, the MSLP will be evaluated as well. It will be evaluated over the area that covers the geographical window 20°–70°E and 05°–40°N, which was used to study atmospheric circulation patterns in Chapter 4. The RCMs in the CORDEX-Africa domain have covered just to 60°E, because that the area which will selected of this domain will not be equal to the geographical window which was used in Chapter 4. Thus, the hindcast simulation from CORDEX-MENA is only used because it covers the whole geographical window 20°–70°E and 05°–40°N.

The main reason for this assessment of MSLP is to know the capabilities of the RCMs that will be used to investigate the climate prediction in the next chapter. However, the RCMs in CORDEX-Africa are generally able to reproduce a good value of MSLP when compared to the

ERA-Interim reanalysis data, with a small bias. For example, the value bias of CCLM hindcast in CORDEX-Africa over all areas averaged by approximately 2 hPa (Panitz et al., 2014).

5.3.3. Regional climate evaluation simulations versus GPCC data:

To review the overall evaluation of the hindcast experiment models, the results from the preliminary analysis of the CORR and NSD were obtained for these models, which assumed GPCC data as the reference dataset in all seasons and annual average, as well as the bias of wet season and annual mean precipitation (mm/month) between GPCC and CORDEX-AFRICA hindcast simulations. All these results are based on the 1990–2005 period.Figure 5.4 shows the taylor diagrams for RR over the subdomain target area used in this study for the 9 hindcast experiment models.
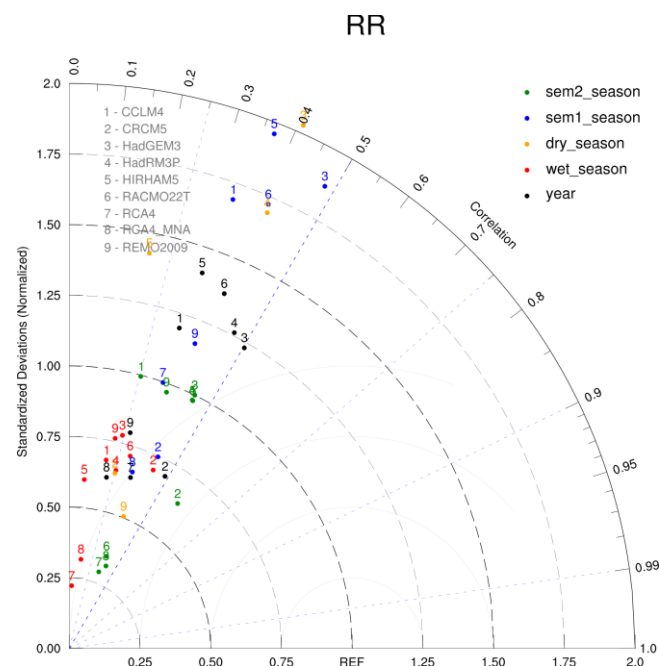
Figure 5.4 Taylor diagram of total precipitation (RR) in all seasons and annual average (Sem2_season (green), Sem1_season (blue), dry_season (yellow), wet_season (red), annual (black)), showing normalised standard deviations and pattern correlations (9 hindcast experiment RCMs versus GPCC).

In the dry_season period, it was found that in RR, the correlation coefficient values are low, less than 0.5 for most of the simulations, and most of these models show a large NSD (some of them not shown in the diagrams because it is greater than 2.0). However, the best

correlations are in HadGEM3 and HadRM3P of about 0.4 with high values of NSD which exceeds 1.75.

In the sem1_season period, the correlation coefficient values in this season for total precipitation amount index in most RCMs are between 0.3 and 0.5. The normalised standard deviation for most of the models is between 2.0 and 0.6. The HadGEM3 and CRCM5 show a relatively good correlation of around 0.45. However, the HadGEM3 model records a high overestimation of around 1.8 for the normalised standard deviation, while the CRCM5 model record an underestimation around 0.75 of normalised standard deviation.

In the sem2_season period, the correlation coefficient values of total precipitation amount index for most models are between 0.4 and 0.5 except in CRCM5, where its correlation was around .0.6. In addition, the correlation coefficient value in HadGEM3 and HadRM3P is close to 0.5. These tow model perform better in respect to NSD with a value close to 1, while CRCM5 model had a small underestimation at around 0.6.

In the wet_season, the results of the CORR and NSD were more homogeneous compared to the other seasons and has a small internal variability. The NSD in all models has a small underestimation at around 0.75 and the CORR in most models are recorded as around 0.25 except in CRCM5, where its correlation was approximately 0.4.

For a whole year average, the best model with respect to CORR was CRCM5 which reached 0.5, then follow by three models (HadGEM3, HadRM3P and RACMO22T), which recorded around 0.4. these models record a small overestimation of around 1.25 for the normalised standard deviation, while the CRCM5 model record an underestimation around 0.75 of normalised standard deviation. The values of CORR and NSD in CRCM5 model are similar in all seasons and annual average.

91

Figure 5.5 shows the bias of annual mean precipitation between GPCC and CORDEX-Africa hindcast simulations based on the 1990–2005 period. In central part of the WCSA, most model performances are reasonable with small underestimates, while the precipitation pattern in northern and southern WCSA is overestimations. In some models such as HadGEM3 the observed pattern of precipitation is reasonably represented, with small precipitation overestimation along Red Sea coast. However, the best representation of the precipitation pattern along Red Sea coast in the whole year was found in with CRCM5 and REMO2009 models.
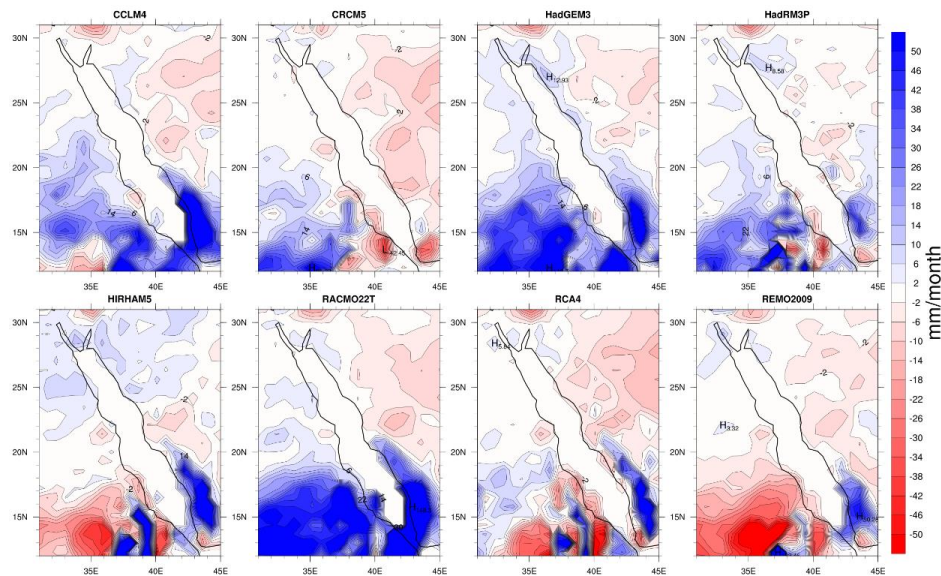
Figure 5.5. The bias of annual mean precipitation (mm/month) between GPCC and CORDEX-Africa hindcast simulations based on the 1990–2005 period.

Figure 5.6 shows the bias of wet season mean precipitation (mm/month) between GPCC and CORDEX-Africa hindcast simulations based on the 1990–2005 period. In the northern and central parts of the Red Sea coast, the observed pattern of precipitation is reasonably represented as the results in annual mean precipitation in Figure 5.5, while there is change in the result over the southern part where there is a small underestimation in most models.
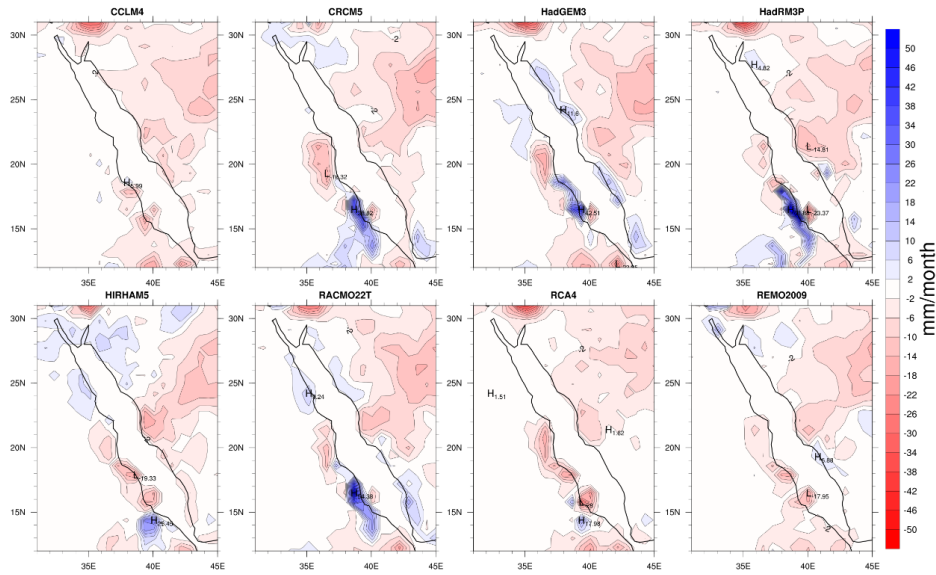
Figure 5.6. The bias of wet season mean precipitation ((mm/month) between GPCC and CORDEX-Africa hindcast simulations based on the 1990–2005 period.

On the other hand, Figure 5.7 shows the same values in Figure 5.6 but with the amount of extreme precipitation events which is indicated as RR90. Generally, a reasonable representation of the rainfall pattern is shown over all the coast areas with small underestimations over the central parts. The best representation is found for CCLM4, HIRHAM5 and RCA4, where they represent the lowest of bias values.
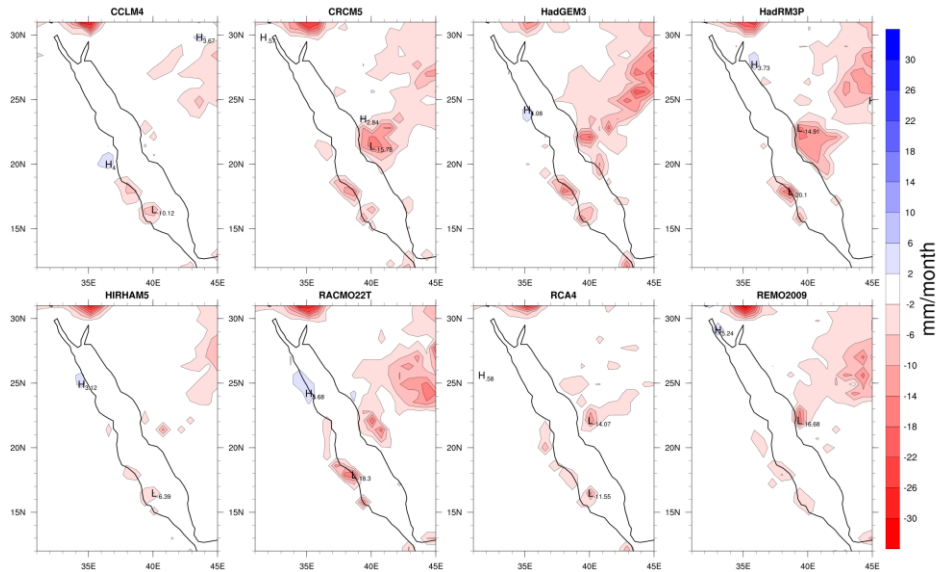
Figure 5.7. Same as Figure 5.6 but for monthly total precipitation from days > 90th percentile thresholds from the daily precipitation amounts for the wet days (RR90).

5.3.4. Regional climate evaluation simulations versus ERA-Interim reanalysis data:

To review the overall evaluation of the nine hindcast experiment models, the results from the preliminary analysis of the CORR and NSD were obtained for these models, which assumed ERA-Interim reanalysis as the reference dataset in the following five periods: year, wet_season, dry_season, sem1_season and sem2_season. Figure 5.8 shows the Taylor diagrams for RR, RQ, RR90, and RQ90 over the subdomain target area used in this study for the 9 hindcast experiment models;

5.3.4.1. Dry season:

In the dry_season period, it was found that in RR and RQ, the CORR is low, less than 0.5 for most of the simulations, and most of these models show a large NSD (not shown in the diagrams because it is greater than 2.0). However, this was not the case for CRCM5 and REMO2009 in RQ, where the NSD is 1.4 and 1.1, respectively, and has a good correlation of about 0.55. On the other hand, in RQ90 most models recorded a good CORR ranging between 0.5–0.7, but the NSD mostly exceeds values of 1.5. However, looking at the results for CRCM5, REMO2009 are similar to those for RQ being close to 1.2. The CORR in RR90 was higher than the CORR in RQ90; many models recorded values between 0.75–0.85, and the CRCM5 model still maintains a good ratio of NSD (1.25), whereas most models record values higher than 1.75. The REMO2009 model shows a large value of more than 2.0.

5.3.4.1. Sem1_season:

In the sem1_season period, the correlation coefficient values in this season for all four precipitation indices are between 0.3 and 0.5. In more detail, the correlation coefficient values are between 0.4–0.5 for RR and RQ and between 0.3–0.4 for RR90 and RQ90. The

normalised standard deviation for most of the models is between 1.3 and 0.6 for RQ. The HORHAM5, RACMO22T, and REMO2009 show a relatively good correlation of around 0.45, while the HadGEM3 model simulates a higher value of about 0.55. However, the HadGEM3 model records a high overestimation of around 1.4 for the normalised standard deviation, while the HORHAM5 and REMO2009 models record an underestimation around 0.75 of normalised standard deviation. The best value was found for the RACMO22T model, with a small error of around 1.1 with respect to normalised standard deviation.
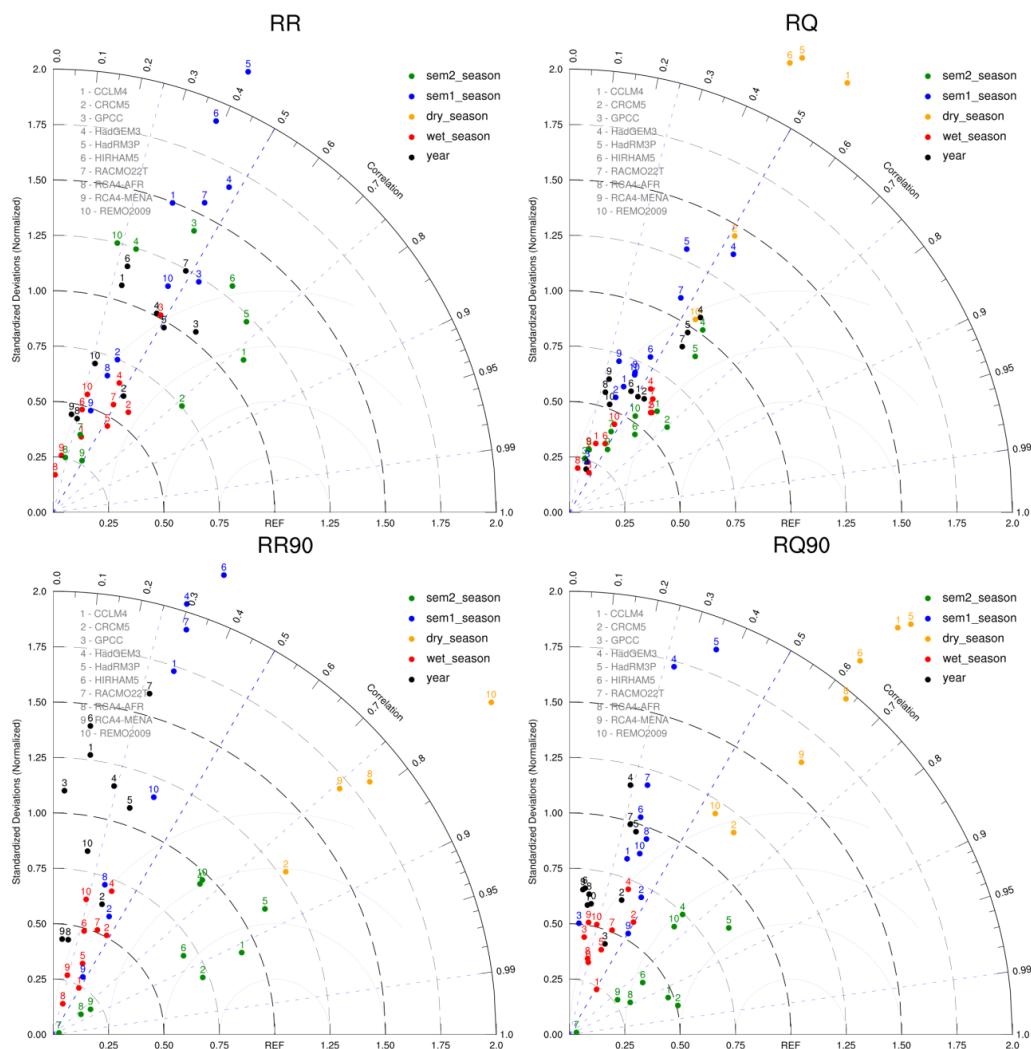
Figure 5.8. Taylor diagram of precipitation in all seasons and annual average (Sem2_season (green), Sem1_season (blue), dry_season (yellow), wet_season (red), annual (black)), showing normalised standard deviations and pattern correlations (nine hindcast experiment RCMs versus ERA-Interim reanalysis), for each precipitation index (RR, RQ, RR90 and RQ90).

The same CORR results were almost noted in RR but with larger errors in respect to normalised standard deviations. For example, HadGEM3 recorded 1.6 while REMO2009 recorded approximately 1.2. The analysis also found that the correlation coefficient in the RQ90 values was between 0.3–0.4, except in CRCM5, where the CORR was close to 0.5 and close to 0.4 in REMO2009. The NSD recorded ideal values and was close to 1 in REMO2009 while the CRCM5 recorded a small error of around 0.75. Overall, the same values were recorded in RQ90, but the best models that had a correlation coefficient of close to 0.5 were RCA4_MENA, CRCM5 and REMO2009, which had 0.5, 0.45 and 0.4, respectively. Also, the NSD values were greatly underestimated in CRCM5 and RCA4_MENA while the REMO2009 model's value was closer to 1.

5.3.4.2.   Sem2_season:

In the sem2_season period, the correlation coefficient recorded the highest values among the four seasons, which were between 0.5–0.85 in most models except in RCA4_AFR, where its correlation was very small. For RR, the highest correlations were found for CRC5 and CCLM4 with a correlation coefficient of 0.76 and 0.78 respectively. These were followed by HIRHAM5 and HadRM3P, which were approximately 0.62 and 0.72 respectively. The CCLM4 model performs better in respect to NSD with a value close to 1, followed by HadRM3P and HIRHAM5, which had small overestimations at around 1.25, and CRCM5 which had a small underestimation at 0.75.

The same distributions of the correlation coefficient values were also recorded in RQ but with slightly lower values, except in the HadRM3P model, which recorded a very high correlation close to 0.9. In RR90, the correlation coefficient was high in most models at around 0.7–0.9, which was especially true for the CCLM4 and CRCM5 models, where the CORR value was

96

above 0.9. In addition, the normalised standard deviation shows values below 1 for all models; it was between 0.25–0.85 in RQ90. These values increased in RR90 to be between 0.5–1.2. For example, in RQ90, CCLM4 showed a normalised standard deviation of about 0.5, and HadRM3P was 0.8. However, in RR90, CCLM4 showed a normalised standard deviation of 0.9 and HadRM3P of 1.2.

5.3.4.3.   Wet season:

In the wet_season, the results of the CORR and NSD were more homogeneous compared to the other seasons. The CORR was recorded as between 0.5–0.7 in RR and RQ while the value of the CORR in RR90 and RQ90 was between 0.3–0.5 in most models. The best models in RR and RQ were CRCM5, HadGEM3, HadRM3P and RACMO22T, where the CORR was close to 0.6 and the NSD was between 0.5–0.75. In RR90 and RQ90, CCLM4 and CCRCM5 had the best correlation, but the NSD of the CCLM4 model had a large underestimation (0.25), while in CCRCM5, it was around 0.75.

Figure 5.9 shows the bias of wet season mean precipitation (mm/month) between ERA-Interim reanalysis and CORDEX-AFRICA hindcast simulations based on the 1990–2008 period. In addition, the two figures in the bottom panel show the mean monthly (mm/month) and seasonal (mm/wet season) total precipitation calculated using ERA-Interim reanalysis data for wet season. The figures in the top two rows show the precipitation bias (mm/month) between ERA-Interim reanalysis data and CORDEX-Africa hindcast simulations. In the northern part of the Red Sea coast, the observed pattern of precipitation is reasonably represented, with small precipitation overestimation in some models, such as HIRHAM5 and HadGEM3, and small precipitation underestimation in CCLM4, HadRM3P and RCA4. Rainfall over the central and southern Red Sea coast is underestimated by all models; the best representation of the

97

precipitation pattern in central and south Red Sea coast was in HadGEM3 models then RACMO22T, RCA4 and REMO2009.
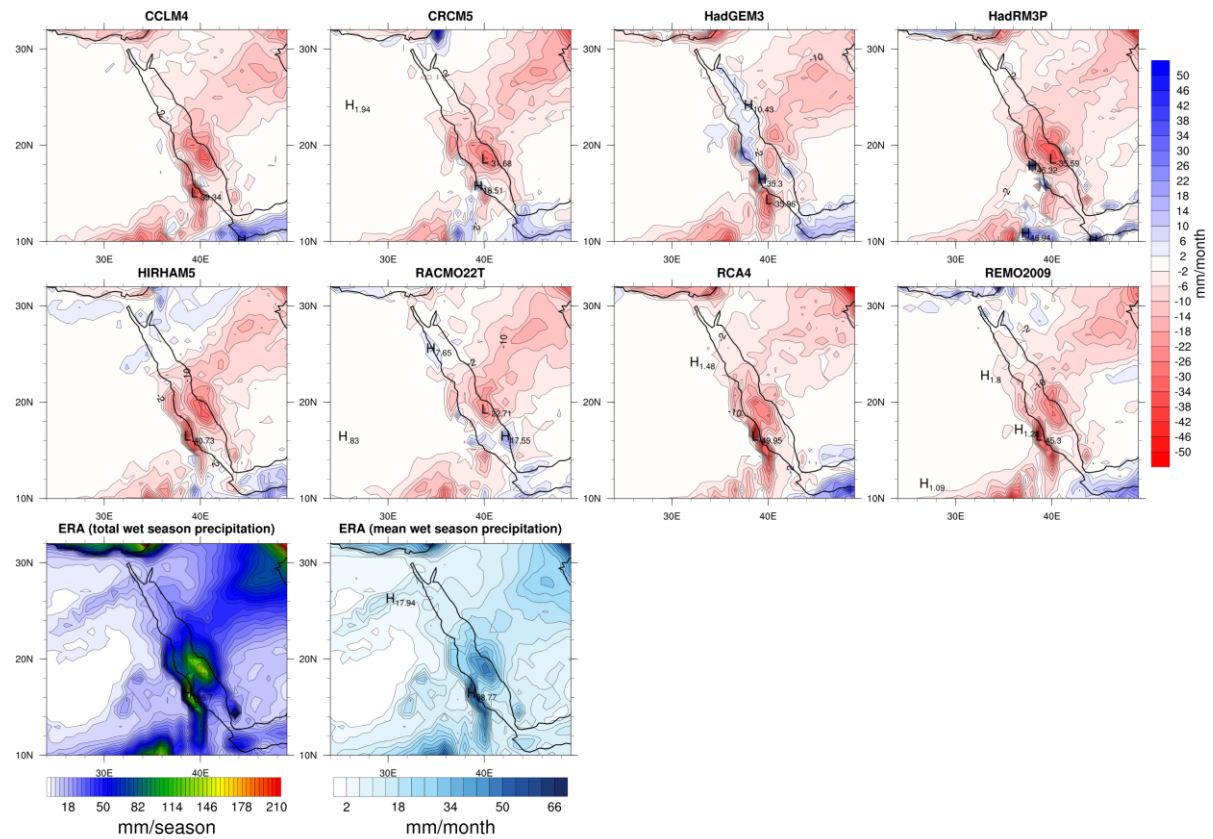
Figure 5.9. Total wet season precipitation (mm/season) (left bottom panel), the mean of wet season precipitation per month (mm/month) (right bottom panel) provided by ERA-Interim reanalysis data and bias of wet season mean precipitation (mm/month) between ERA-Interim and CORDEX-Africa hindcast simulations (two top lines of panel), based on the 1990–2008 period.

On the other hand, Figure 5.10 shows the same values in Figure 5.9 but with the amount of extreme precipitation events which is indicated as RR90, in addition to the figure of 90th percentile thresholds in the right bottom panel. Generally, a reasonable representation of the rainfall pattern is shown over all the coast areas with small underestimations over the central parts. The central part of WCSA has a high percentile value and amount of extreme precipitation in this time of year (wet season) as the figure in middle bottom panel reveals. The best representation is found for CCLM4 and RCA4, where they represent the lowest of bias values.
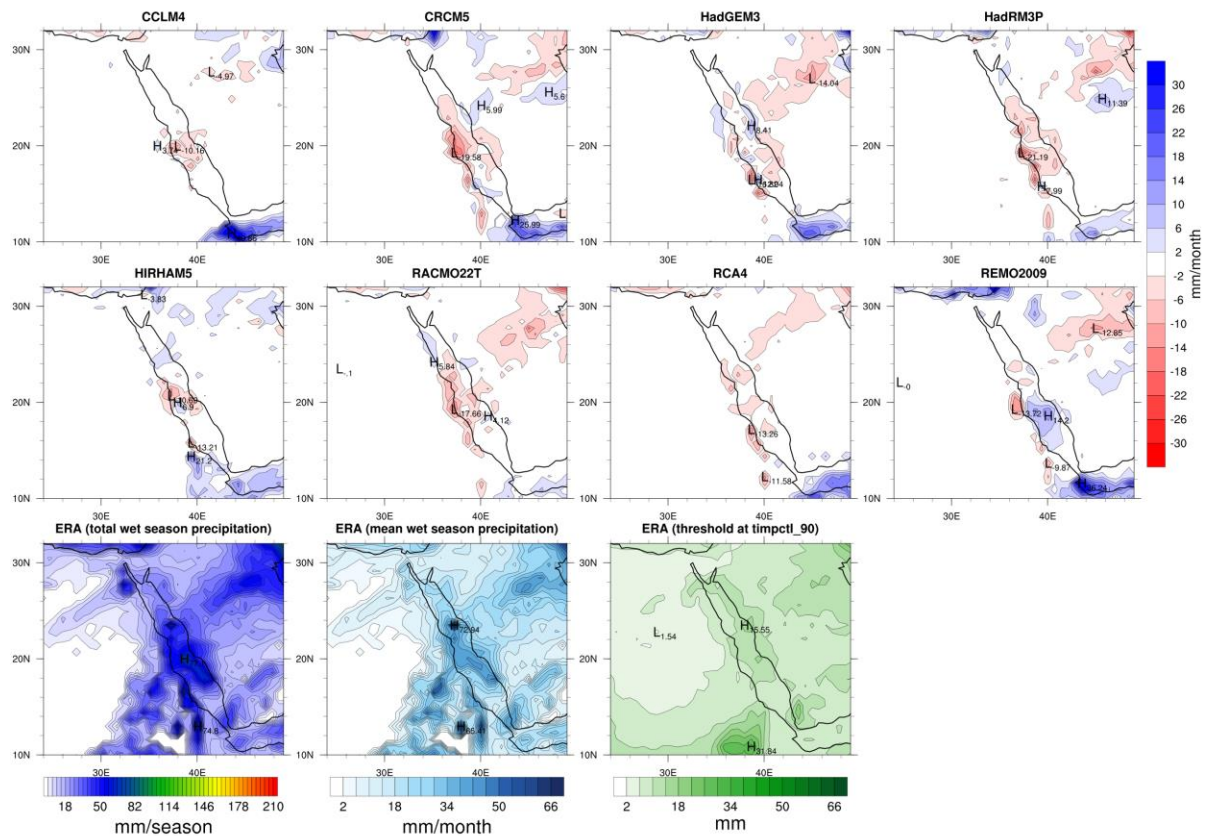
Figure 5.10. Same as for Figure 5.9 but for monthly total precipitation from days > 90th percentile thresholds from the daily precipitation amounts for the wet days (RR90), in addition to map of 90th percentile thresholds (mm) at right bottom panel.

5.3.4.1.   Whole Year:

For a whole year average, the results were similar to the results found for the wet_season, where in RR and RQ, the best models with respect to CORR were CRCM5, HadGEM3, HadRM3P and RACMO22T, reaching 0.5. The NSD for these models were close to 1, except for CRCM5, which was approximately 0.6. RR90 and RQ90 had low values of CORR between 0.2–0.3. However, the best values were still obtained in these four models; CRCM5, HadGEM3, HadRM3P and RACMO22T, while RCA4_MENA and RCA4_AFR had the poorest values in the CORR and NSD.

Figure 5.11 shows the mean monthly (mm/month) and annual (mm/year) total precipitation calculated from ERA-Interim reanalysis data in the whole year. This is shown in the two figures

in the bottom panel, while figures in the top two rows show the precipitation bias (mm/month) between ERA-Interim reanalysis data and CORDEX-Africa hindcast simulations in the annual values. Firstly, the mean annual precipitation pattern is different compared to the previous Figure 5.9 for the wet season. This is where the mean rainfall amount is increased over the southern part of domain because of the rainfall season during summer which is affected by Indian monsoons.

Figure 5.11. Total annual precipitation (mm/year) (left bottom panel), the mean of annual precipitation per month (mm/month) (right bottom panel) provided by ERA-Interim reanalysis and bias of annual mean precipitation (mm/month) between ERA-Interim reanalysis and CORDEX-Africa hindcast simulations (two top lines of panel), based on the 1990–2008 period.

In the northern and central part of the Red Sea coast, model performances are reasonable with small underestimates, while the precipitation pattern in south Red Sea coast is underestimated in some models such as CRCM5 or overestimations such as RACMO22T. However, the best representation of the precipitation pattern along Red Sea coast in the

100

whole year was found in the CRCM5, RCA4 and HadGEM3 models, despite a majority of models continuing to have small overestimations and underestimation of precipitation.

Figure 5.12 shows the same values in Figure 5.11 but for the amount of extreme precipitation events which is indicated as RR90 for whole year, in addition to figure of 90th percentile thresholds in the right bottom panel. Generally, the bias error is increased compared to the one found for the wet season. Model performances are still having reasonable estimations aside from the southern coastal parts, especially for CCLM4, REMO2009, HIRHAM5 and RACMO22T which recorded large precipitation overestimation over this area. However, the best models with respect to the observed annual extreme precipitation pattern along the Red Sea coast are the same as for the wet season, which are CRCM5, RCA4 and HadGEM3.
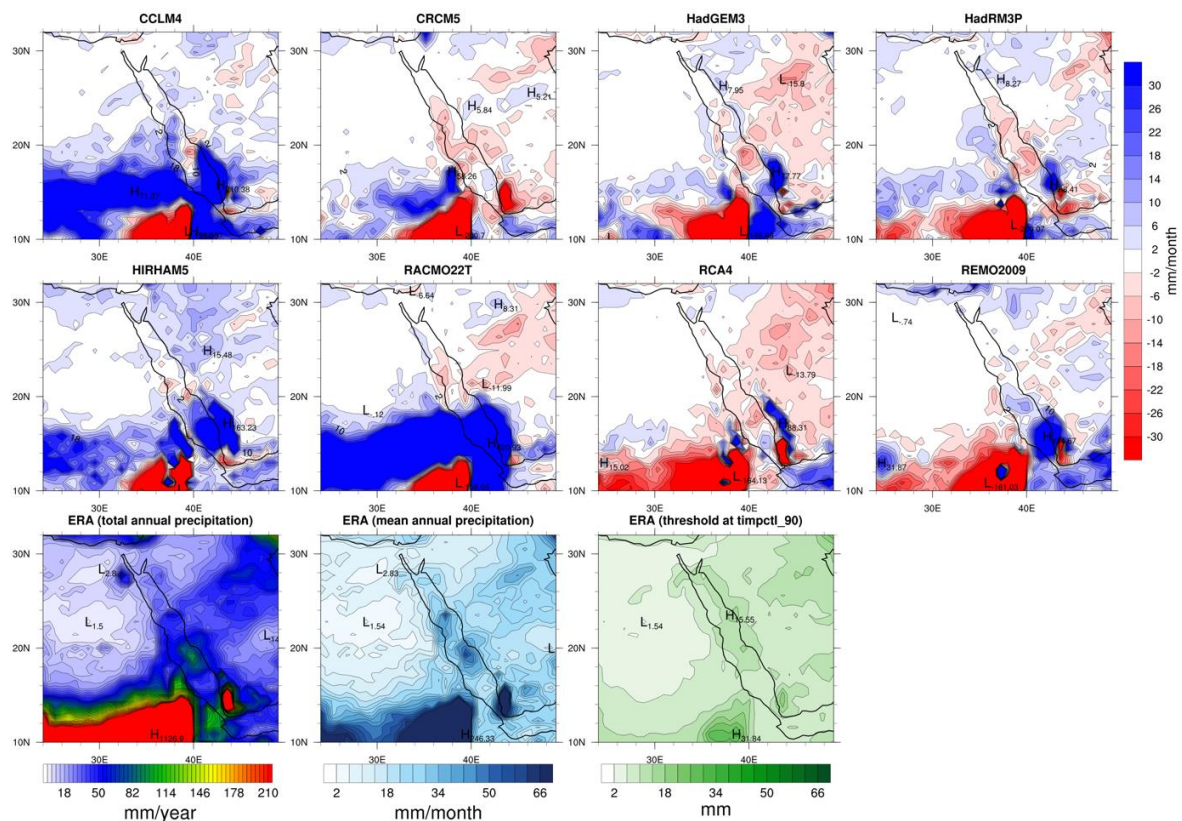
Figure 5.12. The same as Figure 5.11 but for monthly total precipitation from days > 90th percentile thresholds from the daily precipitation amounts for the wet days (RR90), in addition to map of 90th percentile thresholds (mm) at right bottom pane.

5.3.4.2. The evaluation of the best performing RCMs:

From the previous results, the study found that the best performing models, especially for the wet_season and whole year, were CRCM5, HadGEM3, HadRM3P and RACMO22T. So, in the next section, which examines the spatial distribution of these values, the study focuses on the results of these four models in the wet_season and whole year only. Three spatial variables were used in this investigation: the values for the individual 22 grid cells, the total average of all these points and the average of the subdomain's target area.

5.3.4.2.1. Monthly precipitation amount (RR):

Figure 5.13 shows the distribution of the RR values over 22 grid points and the average of the subdomain target area for the best four hindcast simulation models (CRCM5, HadGEM3, HadRM3P and RACMO22T) during the wet season and their annual values. In addition, the best values came from CRCM5, showing values between 0.5 and 0.75 in the CORR and a small underestimation of 0.65 in the NSD. The second model was HadRM3P, where the CORR was around 0.5–0.6, but the NSD is superior being close to 1.

The CORR in the CRCM5 model was better than for the HadRM3P model overall, but some grid point values were better in HadRM3P than CRCM5, particularly for the wet season. Although there were good results for HadRM3P, these values were more dispersed, compared to CRCM5. In addition, it was found that the grid point values in the northern coastal areas recorded higher rates for the CORR compared to the southern regions. This was because of the terrain which plays an important role in the weather in southern region.

102
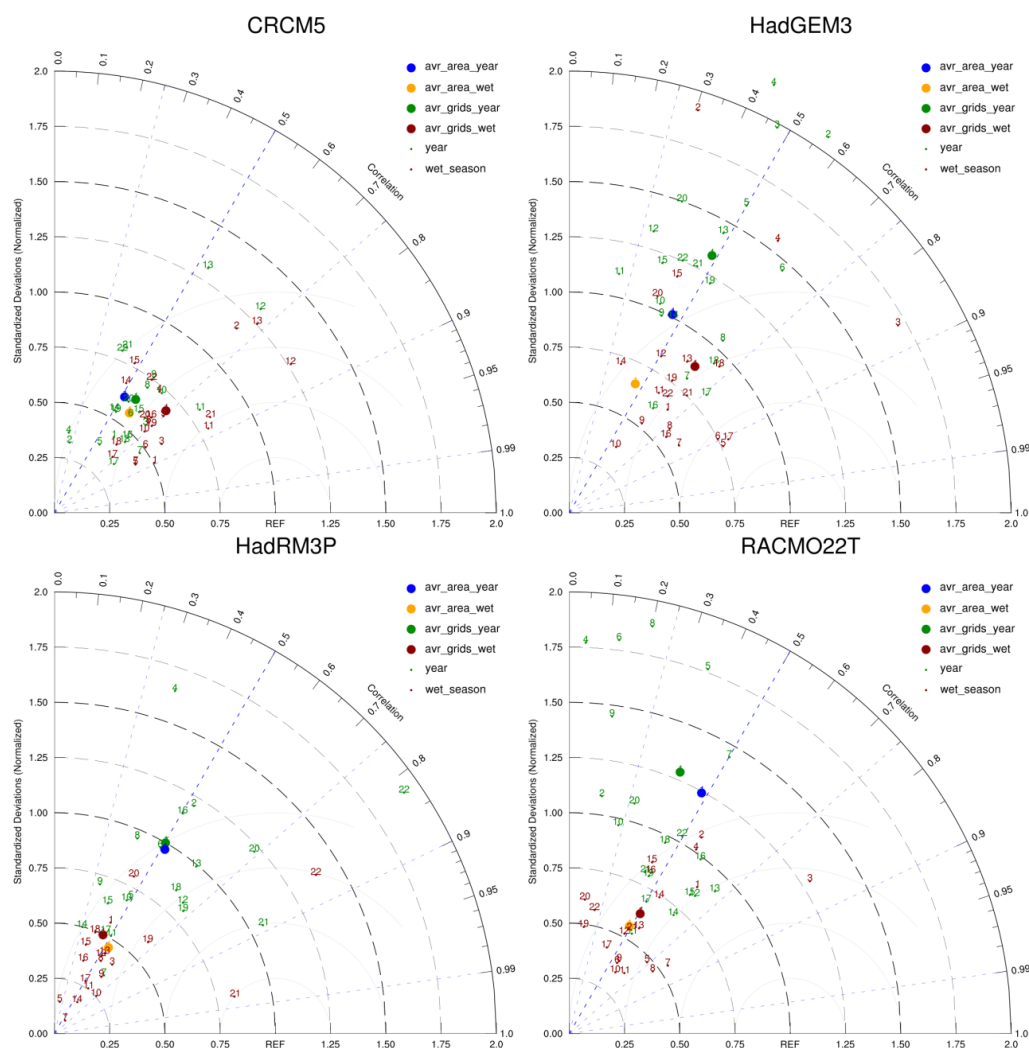
Figure 5.13. Taylor diagram of monthly precipitation amount (RR) in the wet season and annually averaged over the area and grids (average area for the whole year (blue), average area in the wet season (yellow), average of all grid points for the whole year (green), average of all grid points in the wet season (red), grid points for the year (number green), grid points for the year (number red)), showing the normalised standard deviation and pattern correlation (hindcast experiment RCMs versus ERA-Interim reanalysis) for four RCMs (CRCM5, HadGEM3, HadRM3P and RACMO22T).

5.3.4.2.1. Monthly wet-day frequency (RQ):

Figure 5.14 shows the distribution of the RQ values over 22 grid points and the average over the subdomain target area for the best four hindcast simulation models (CRCM5, HadGEM3, HadRM3P and RACMO22T) for the wet season and for the annual value. These values in the RQ were better than the previous data (RR), and most results of the NSD were a small underestimation and limited to between 0.05–1.

103

HadGEM3 had the best NSD values at 0.75–1.25 with the correlation being the highest; the average for the CORR in the wet season is approximately 0.75, and in the whole year is approximately 0.65. The CRCM5 model represented the value in the south and middle better than in the northern coastal area, while HadRM3P represented the northern regions better. RACMO22T model represented the middle areas better than the northern and middle ones.
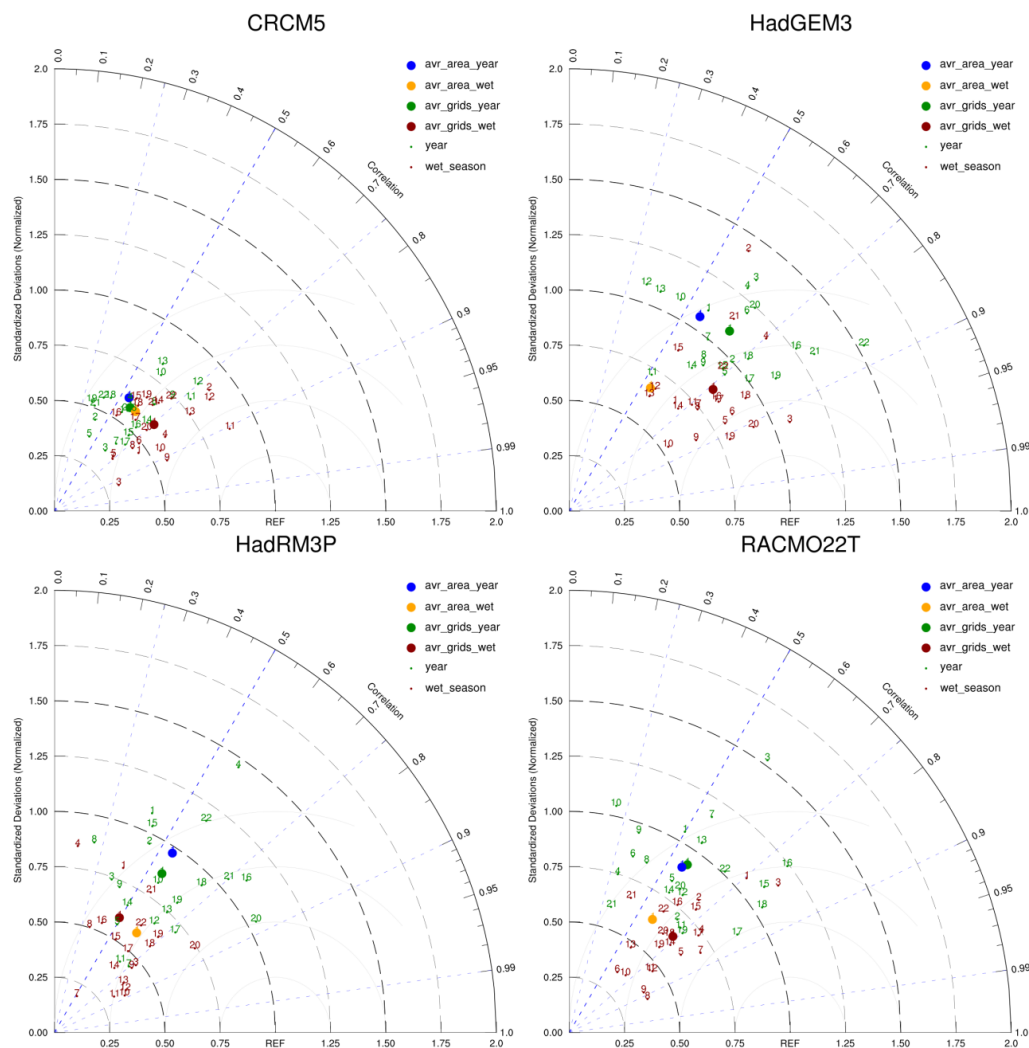
Figure 5.14. The same as Figure 5.13 but for monthly wet-day frequency (RQ).

5.3.4.2.1. Monthly 90th percentile precipitation amount (RR90):

Figure 5.15 shows the distribution of the RR90 values over 22 grid points and the average of the subdomain target area for the four simulation models (CRCM5, HadGEM3, HadRM3P and RACMO22T) in the wet season and whole year period.
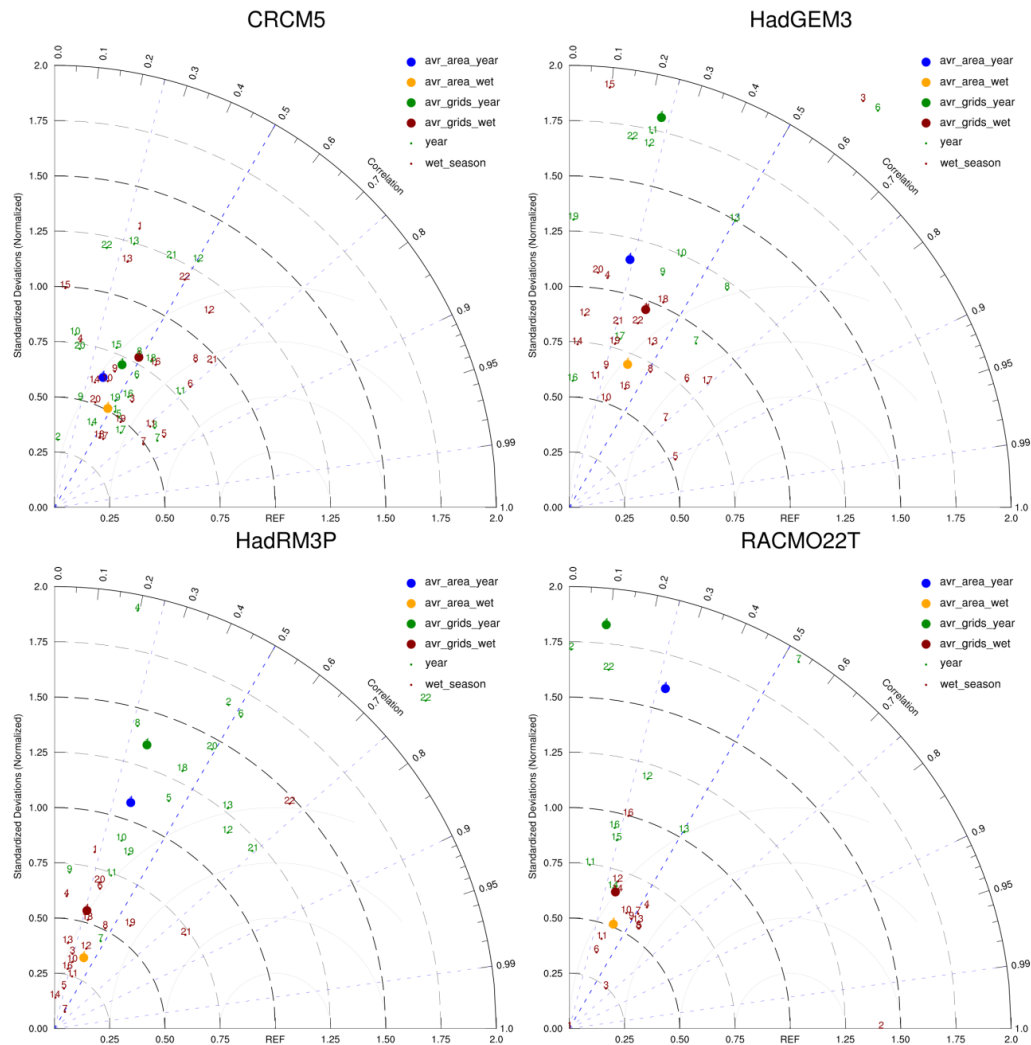
Figure 5.15. The same as Figure 5.13 but for monthly total precipitation from days > 90th percentile thresholds from the daily precipitation amounts for the wet days (RR90).

Overall, the models showed relatively poor performance; most of the average values of the correlation confections were limited to between 0.5–0.4. The best results were recorded in the CRCM5 model, especially in wet_season, where it reached a CORR of 0.5. For some grid points using the CRCM5 and RACMO22T models, the CORR exceeds 0.5 with a small underestimation for the NSD values, particularly in the wet season. There was no distinctive place from north to south over the coastal region that has been confirmed by the CRCM5 model. However, the RACMO22T model was better in the central region and the HadRM3P model was superior in the northern region.

5.3.4.2.2. Monthly 90th percentile wet-day frequency (RQ90);

Figure 5.16 shows the distribution of the RQ90 values over 22 grid points and the average of the subdomain target area for the four models (CRCM5, HadGEM3, HadRM3P and RACMO22T) in the wet season and over a whole year period.
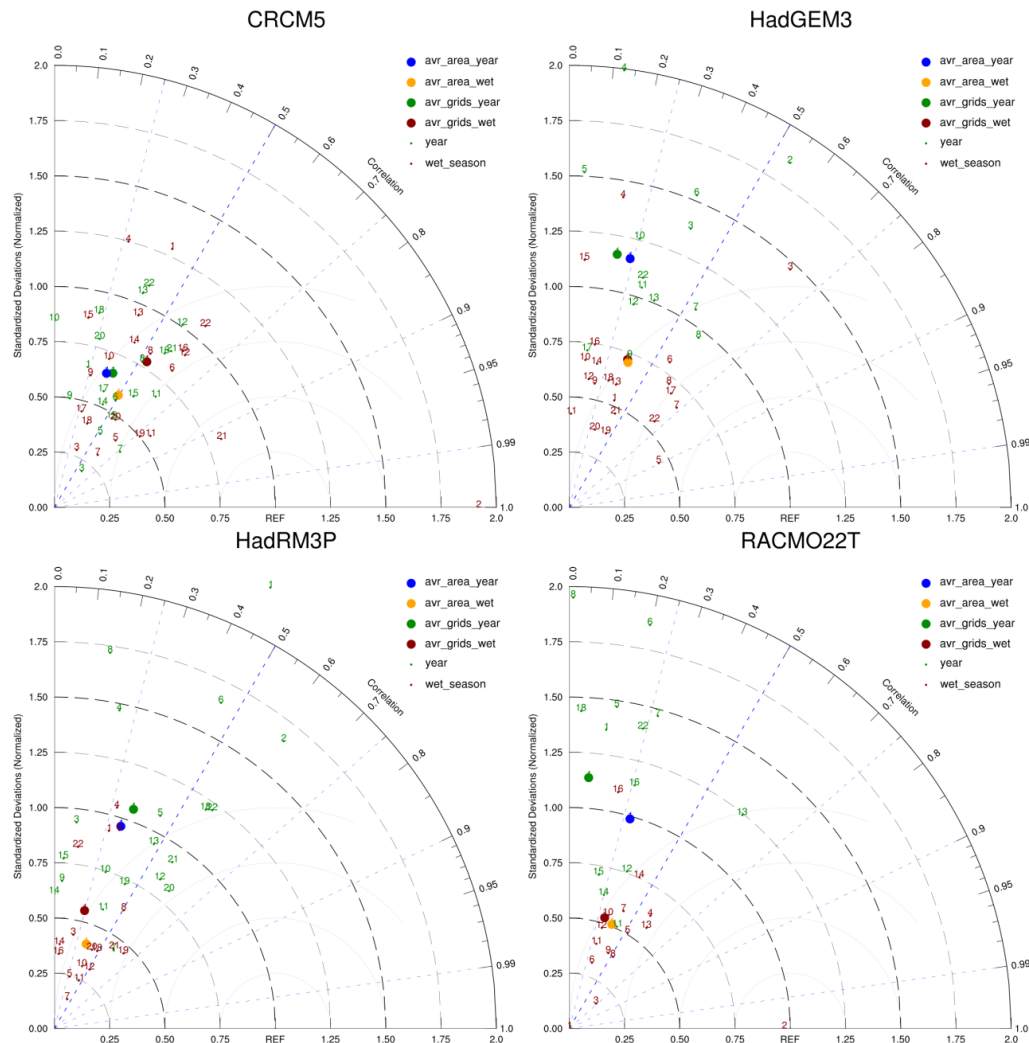
Figure 5.16. The same as Figure 5.13 but shows the monthly wet-day frequency from the days > 90th percentile thresholds from the daily precipitation amounts during the wet days (RQ90).

The results here are similar (extreme precipitation amounts, RR90) but show a relatively larger CORR; the correlation in CRCM5 was about 0.5 for the wet_season average while most the correlation value of grids were still between 0.4–0.5. NSD values of grids are less spaced than the previous data. HadRM3P also had a good distribution record for the average values

for the one-year period. In addition, this model represented the values of some grids in the northern regions better than in the southern region. However, the results were mostly poor, except for in the CRCM5 model.

5.3.5. GCMs historical data versus RCMs evaluation data:

Figure 5.17 shows the difference in total precipitation amounts between a GCM historical simulations (1990 to 2005) and CORDEX-MENA hindcast simulations (1990 to 2005) for the 3 individual experiments from CORDEX-Africa domain. The best result is in NAOO-RCA4. However, the bias errors are close to zero in northern and central part of Red sea coast in all three experiments but the overestimation is existing over the southern region in first two experiment.
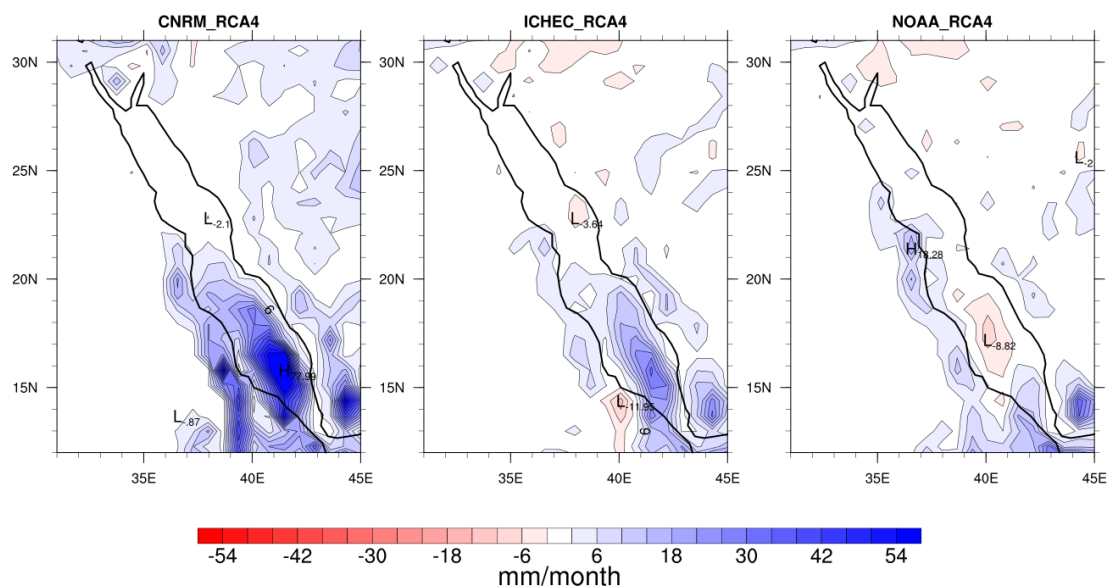
Figure 5.17. The difference for the amount of total precipitation (mm/month) between GCM historical simulations (1990 to 2005) and CORDEX-MENA hindcast simulations (1990 to 2005) in the wet season for 3 experimental models.

In addition, Figure 5.18 shows the difference in total precipitation amounts between a GCM historical simulations (1990 to 2005) and CORDEX-Africa hindcast simulations (1990 to 2005) for the 23 individual experiments from CORDEX-Africa domain. Some of the model simulates a large overestimation in precipitation over the Red Sea region (e.g., CNRM-CCLM4, ICHEC-

107

RACMO22T and MOHC-REMO2009) while the model simulations which used RCA4 have better estimation with small overestimation in precipitation such as CNRM-RCA4, ICHEC-RCA4 and MOHC-RCA4 or good estimation without significant bias errors such as CCCam-RCA4, IPSL-RCA4 and NCC-RCA4.
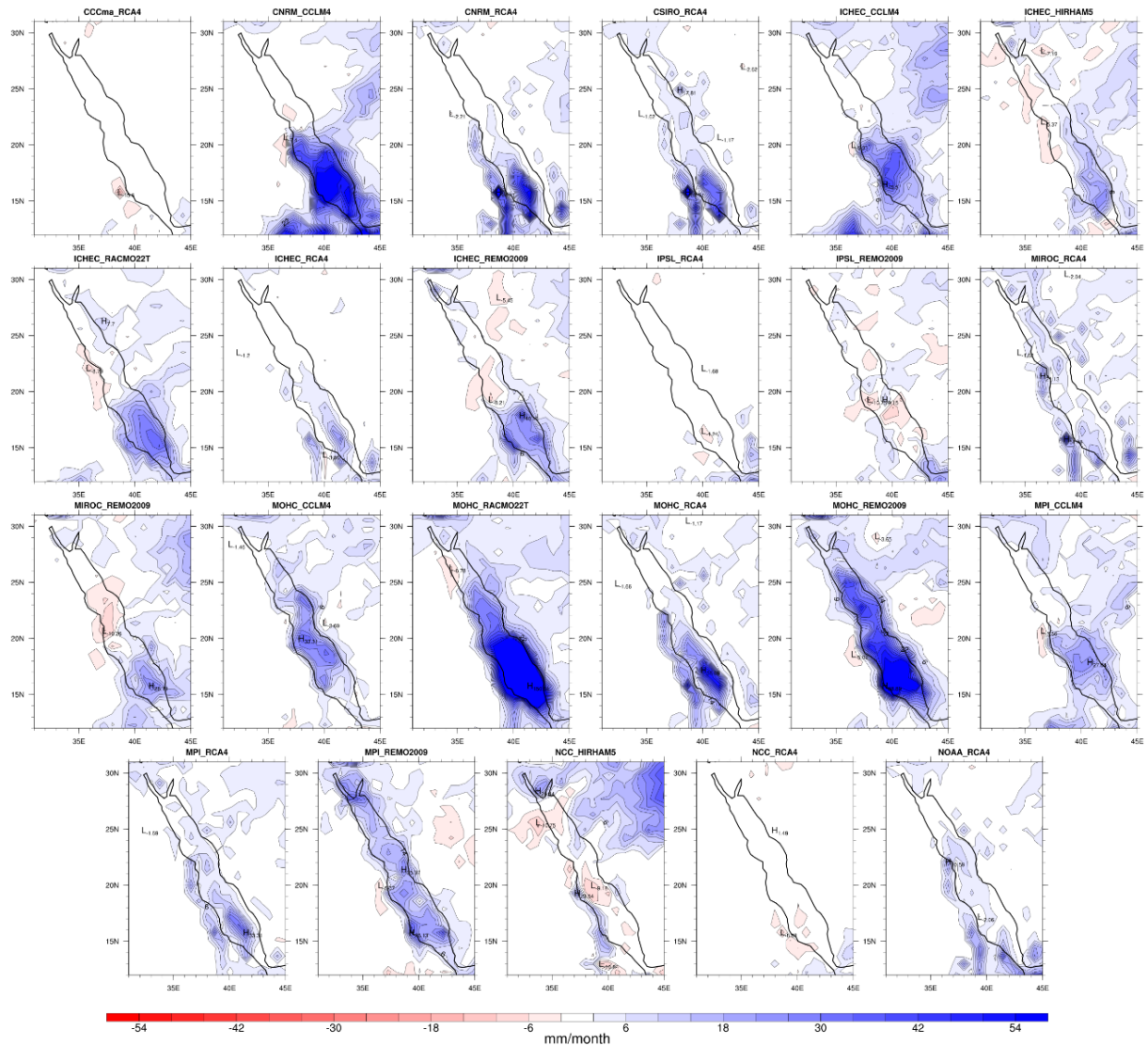
Figure 5.18. The difference for the amount of total precipitation (mm/month) between GCM historical simulations (1990 to 2005) and CORDEX-Africa hindcast simulations (1990 to 2005) in the wet season for 23 experimental models.

5.3.6. CORDEX-MENA evaluation:

The geographical region within 20°–70°E and 05°–40°N, which is used in this study and defined in Chapter 4, is not entirely covered by CORDEX-Africa but is in CORDEX-MENA. Due

to this, the available atmospheric variables in the CORDEX-MENA domain are used in this section. These atmospheric variables are the same as those that were used in the dynamic study in Chapter 4. Table 5-2 summarises the seasonal and annual CORR, NSTD and mean absolute error MAE of RR total amount precipitation (mm/month), RQ wet-day frequency (days), RR90 total amount extreme precipitation (mm/month), RQ90 extreme event frequency (days), MSLP mean sea level pressure (hPa), wind speed at 200hPa (m/s) and GPH at 500hPa and 200hPa (m) selected from RCA4 hindcast simulations (CORDEX-MENA) using ERA-Interim as reference.

Overall, a reasonable representation of the MSLP, GPH at 200 and 500hPa and wind speed at 200hPa is registered, while the correlations for precipitation indices are relatively poor. The mean absolute error in the precipitation was 19 (mm/month) in the year averaged and 21 (mm/month) in the wet season, which compares well to results using the regional climate model COSMO-CLM over CORDEX-MENA domain by Bucchignani et al. (2015a). They found that MAE values of precipitation of around 15 mm/month over the whole CORDEX-MENA domain (27W–76E, 7S–45N).

5.3.6.1. MSLP evaluation:

RCA4 (CORDEX-MENA) is generally able to reproduce the seasonal and annual MSLP over the study area if using ERA-Interim reanalysis data as reference. The value of the correlation coefficient was close to 1 with an overestimation of the normalised standard deviation, which was generally smaller than 1.25. Figure 5.19 shows the bias of the MSLP of RCA4 compared to ERA-Interim reanalysis data for the annual and season's averages. Over the whole year and in the wet season, the distribution of MSLP's bias showed the highest overestimation around the Red Sea regions and the largest underestimation over the Ethiopian Highlands. In

109

addition, looking at a seasonal time scale, the lowest bias was in the dry season while the

highest bias was in the wet season.

		year	wet season	sem1 season	sem2 season	dry season
MSLP	CORR	0.92	0.81	0.83	0.71	0.76
	MAE	1.33	1.98	1.34	1.39	0.86
	NSTD	1.10	1.02	0.89	1.03	0.87
Windspeed at 200hPa	CORR	0.89	0.83	0.83	0.79	0.82
	MAE	1.33	1.64	2.17	2.05	1.21
	NSTD	1.07	1.06	1.13	1.07	1.08
GPH 500hPa	CORR	0.92	0.89	0.89	0.81	0.85
	MAE	110.09	103.12	111.73	99.85	105.20
	NSTD	0.99	1.04	1.01	1.09	1.05
GPH 200hPa	CORR	0.98	0.94	0.94	0.93	0.94
	MAE	234.45	225.89	224.82	228.51	229.26
	NSTD	1.03	1.03	1.01	1.05	1.04
RR	CORR	0.18	0.24	0.27	0.36	0.22
	MAE	19.71	20.94	14.58	26.90	22.95
	NSTD	1.36	1.39	1.57	4.29	2.70
RQ	CORR	0.30	0.46	0.38	0.40	0.29
	MAE	2.04	2.47	2.20	3.99	1.99
	NSTD	0.73	0.47	0.85	0.83	1.74
RR90	CORR	0.16	0.46	0.34	0.58	0.55
	MAE	6.33	7.87	5.58	10.31	9.31
	NSTD	1.09	1.25	0.97	1.49	0.74
RQ90	CORR	0.13	0.31	0.34	0.53	0.47
	MAE	0.44	0.46	0.37	0.52	0.53
	NSTD	0.90	0.88	0.99	0.73	0.63

Table 5-2. Seasonal and annual CORR, MAE and NSTD of RR total amount precipitation (mm/month), RQ wet-day frequency (days), RR90 total amount extreme precipitation (mm/month), RQ90 extreme event frequency (days), MSLP mean sea level pressure (hPa), wind speed at 200hPa (m/s) and GPH at 500hPa and 200hPa (m) compared to the ERA-Interim reanalysis dataset, averaged over the whole our studt domain (20°–70°E and 05°–40°N).
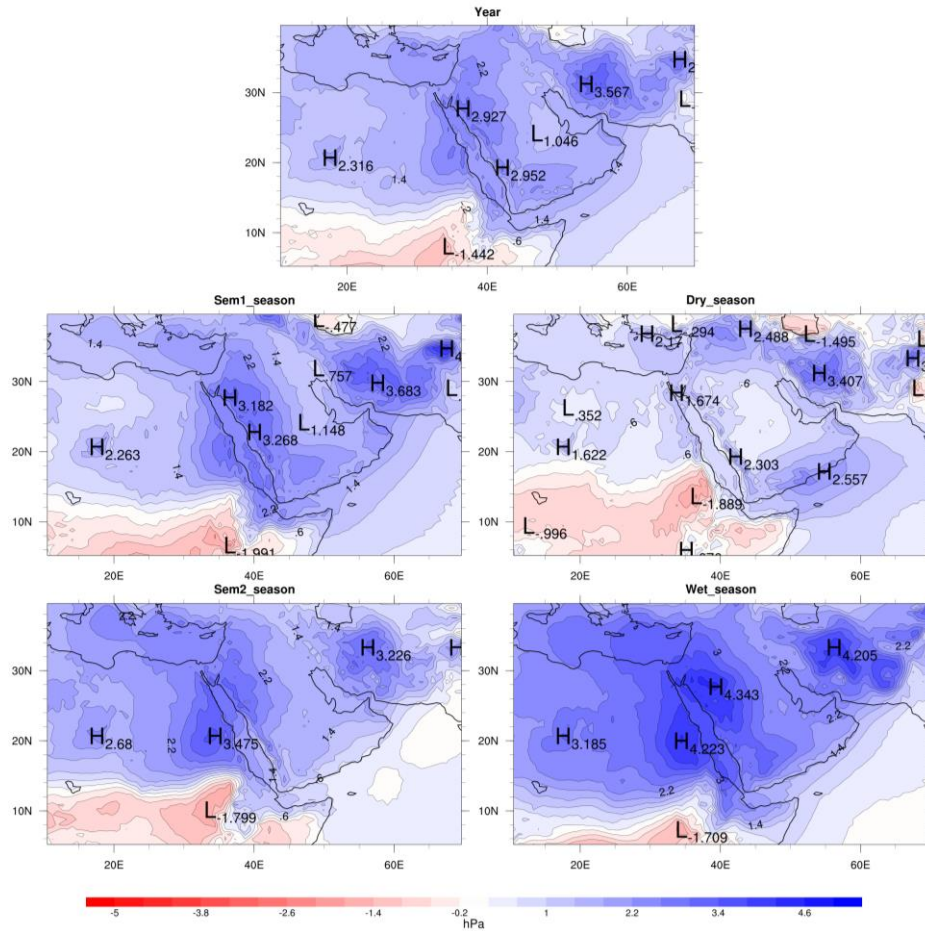
Figure 5.19. The bias of the MSLP of RCA4 compared to ERA-Interim reanalysis data for annual (top) and seasonal time scales (second and third row).

5.4.   Discussion and Conclusion:

Evaluation of precipitation from the ERA-Interim reanalysis data are applied by comparing it versus GPCC and observed precipitation dataset. Despite the complex topography and few rain gauges on the WCSA, the evaluation of the ERA-Interim reanalysis data with GPCC data remained relatively good, with correlation values exceeding 0.5 in most grid points at total precipitation, while these values are reduced for extreme precipitation events. On the other hand, the correlation coefficient between the ERA-Interim and observed precipitation dataset was less than 0.3 in the south of the region and increases northward to be around 0.4.

For these events, the ERA-Interim reanalysis data are used as a reference to evaluate the assessment of precipitation data of nine regional climate model simulations for the CORDEX-

111

MENA and CORDEX-Africa domains. Overall, the best results were in the following models: CRCM5 (Laprise et al., 2013), HadGEM3-RA (Hewitt et al., 2011), HadRM3P (Jones et al., 2004) and RACMO22T (Van Meijgaard et al., 2008).

These four models have a correlation coefficient above 0.5 for most precipitation events (RR and RQ), and most of their normalised standard deviation values were underestimated, compared to ERA-Interim reanalysis. Because for extreme precipitation events (RR90 and RQ90) the correlation values showed a relatively poor performance, the study divided the performance models according to their grid point values. This was where the best model overall was CRCM5, HadRM3P for the northern region and RACMO22T for the middle and western coastal areas. In addition, for all precipitation indices, the normalised standard deviation values were overestimated in the annual data and underestimated in the wet season data.

Typically, there are errors in precipitation in climate models, and the proportion of these errors increase when the events are caused by small-scale processes or affected by complex orography or coastlines. These factors cannot be resolved by a 0.44° climate model and need to increase the resolution to 0.11° in order to improve precipitation simulations in climate models (Prein et al., 2016). However, the precipitation results from four RCMs (CRCM5, HadGEM3-RA, HadRM3P and RACMO22T) from CORDEX-Africa were still reasonable in order to investigate future climate change. The same is the case for the RCA4 model from CORDEX-MENA, which was also used to analyse the MSLP.

These findings of evolution reanalysis grid point model data and regional climate models are relatively reasonable. It would be of benefit to do further analysis in light of objective classification and climate change studies, which will be discussed in the next chapters.

Chapter 6. OBJECTIVE CLASSIFICATIONS

6.1.   Overview:

In order to derive objective weather circulation pattern classifications, this study employs the method of EOF analysis to identify the variability of weather circulation patterns (WCPs) during the wet season (November through January). This is done to establish the link between local and regional extremes and the synoptic to large-scale meteorological conditions in a systematic way. A very common and comprehensive tool to do so is the analysis of EOFs, which are used to identify the major modes of variability in the atmospheric circulation affecting the region of interest. This classification is then related to the identified extreme events in Chapter 4 and the relevance of specific circulation situations for the occurrence of extremes evaluated. This is in addition to investigating the link between large scale modes and the weather circulation patterns which are associated with extreme rainfall.

6.2.   Generation of Weather Circulation Patterns WCPs:

Six EOFs were derived from mean sea level pressure (MSLP) gridded reanalysis data, using Varimax Rotated Principal Components analysis for the chosen geographical window (05°N–40°N; 10°E–70°E) after the area weight was computed as the square root of the cosine of the latitude and degrees were converted to radians. Figure 6.1 shows the six Varimax rotated EOFs for the wet season and gives a percentage for each one. These six EOFs account for about 88% of the total variance. However, from EOF 1 to EOF 6, they contribute about 18.7%, 18.2%, 16.0%, 13.0%, 12.9% and 9.8%, respectively.

Each EOF for each day has either a negative or a positive principal component (PC) factor score that is calculated from the principal component analysis (PCA) (Esteban et al., 2005). In fact, each EOF contributes to each day by a zero or negative or positive PC factor score. A day with maximum positive PC scores will tend to be one of the six EOFs, and a day with negative PC scores will tend to be the inverse of one of the six EOFs, whereas a PC score of zero means that it does not play any role in explaining the variation on EOF. In this case, these six EOFs generate 12 mean sea-level WCPs. These WCPs are constructed by anomaly composite of MSLP fields, assuming a largely geostrophic flow on the scale of this investigation.
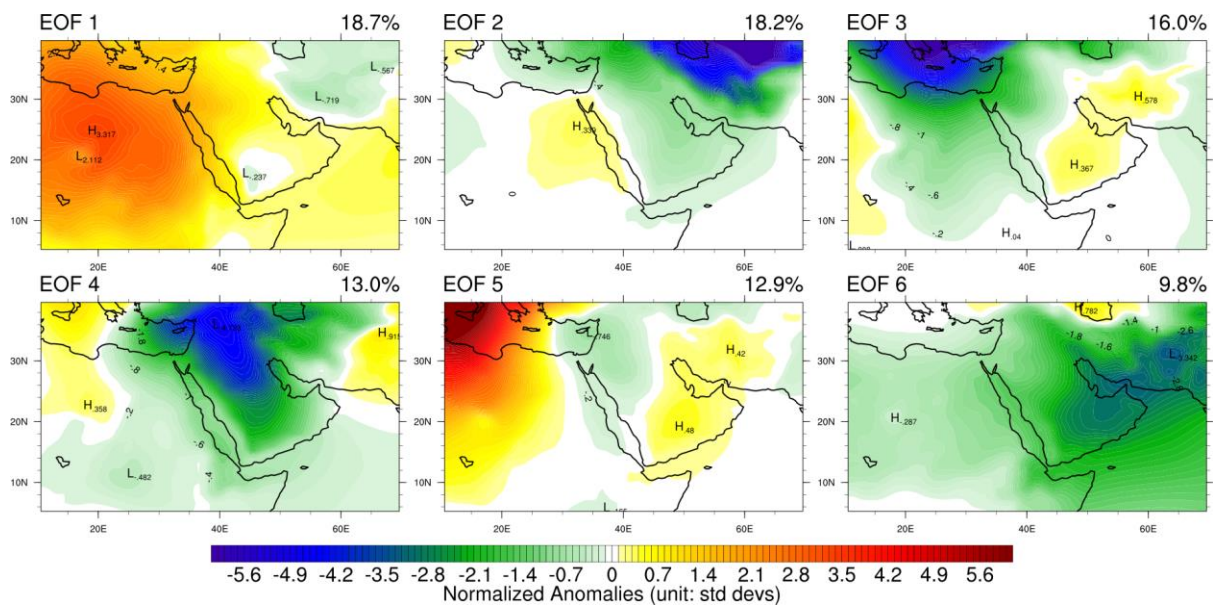
Figure 6.1. The leading six Varimax rotated EOF patterns for the wet season (Nov./Dec./Jan.) from the daily mean sea level pressure (MSLP) in units of normalised standard deviations.

The anomaly composite map is created for each WCP by gathering similar PC scores days by a threshold factor of the highest component score for each day. Four thresholds were tested, ±2.0, ±1.5, ±1.0, ±0.75 and ±0.5. The total number of classified days out of the overall days are 27%, 52.6%, 82%, 93.3% and 98.6%, respectively. The use of above ±0.5 was suggested because it classifies 98.6% of all days in the wet season as well as 97.5% of both the

114

precipitation days and the extreme event days. These percentages of classified days are sufficient for this study.

Consequently, 12 WCPs were identified. These were obtained from classified wet season days for the period from 1985 to 2014, and they correspond to the six EOF patterns. The first six types (1–6) correspond to the positive component scores and the next six (7–12) correspond to the negative component scores. Figure 6.2 displays the 12 WCPs for all days in the wet season by the composite of daily MSLP averages and normalised MSLP anomalies Figure 6.3 does the same for precipitation days, and Figure 6.4 illustrates 11 WCPs that are related to extreme precipitation days. The normalisation of the MSLP is achieved by using the same standard deviation, i.e., the calculation is done by daily normalisation of all wet season days (Nov., Dec. and Jan.) over 30 years. The three subsets are composited as selected days, depending on the type of group: 79 extreme days in one group (extreme precipitation events), 445 wet days in the second group (precipitation days) and all days (2760 days) in the third group (all wet season days).

These three figures have been derived from the composite of daily MSLP average and normalised MSLP anomalies for the chosen geographical window (0°S–60°N; 60°W–80°E). This large-scale domain size, which extends from the North Atlantic to the Arabian Sea, can provide a comprehensive description of WCPs and the possibility of linking WCPs with some teleconnection patterns (e.g. North Atlantic Oscillation (NAO), El Niño Southern Oscillation (ENSO) or Southern Oscillation Index (SOI)). For example, these figures show the real extent of certain pressure systems, where it finds that the NAH is originally the extension of the North Atlantic Subtropical High (Azores High), as shown in WCP1, WCP5 and WCP9 in all three

figures. In addition, it shows how the Red Sea Trough extends in some patterns northward linking to the Icelandic Low, as seen in WCP3.

Twelve WCPs for all days in the wet season, 12 WCPs for precipitation days and 11 WCPs for extreme precipitation days were compared to find out the extent to which the differences among them form patterns. For this purpose, pattern correlation coefficients were applied among these three WCPs. The pattern correlation coefficients correlate all grid points of two WCPs (i.e., WCPs for all wet season days, WCPs for precipitation days and WCPs for extreme precipitation days) for each time step (i.e., WCP1, WCP2,…WCP12) where there was no WCP11 in the WCPs based on extreme precipitation days. Pattern correlation coefficients among each of these 12 WCPs on all wet season days, precipitation days and extreme event days show a high positive correlation that was very close to 1 between extreme event days and all wet season days (the exceptions were WCP2 and WCP12, which were 0.91 and 0.92, respectively). This reveals a striking feature of this analysis. During precipitation, and especially during extreme precipitation events, the similar large scale modes of variability were important and no new circulation features emerged. The difference was not in the pattern itself, but in the value of MSLP and its normalised anomalies. Of special interest was how much these values changed between each WCP on all wet season days and precipitation days, and between each WCP in all wet season days and extreme event days.

The frequency distribution of the 12 WCPs in wet season days does not have a significant variance, and the distribution percentage ranges between 5% and 11%. The dominating WCPs in the wet season are the classes WCP1, WCP3, and WCP7, WCP8, WCP9, and WCP11, with highest frequency of the classes WCP1, WCP3, WCP7, and WCP8 with values above 10% (Figure 6.2).

116

On the other hand, the distribution percentage of the 12 WCPs on precipitation days and extreme event days is relatively similar; for wet days, this principle distribution is preserved, but with higher contributions from classes WCP1, WCP3, WCP8, and WCP4 with values above 10% (Figure 6.3). For the latter, an increase of about 16% has to be noted in class WCP4. For extreme events, the distributions of the most five important patterns (WCP4, WCP8, WCP1, WCP7 and WCP3) have the highest recorded incidence, which were 16.5%, 16.5%, 12.7%, 11.4% and 11.4%, respectively, while WCP11 does not occur in extreme events (Figure 6.4). However, in some important classes of WCPs, such as WCP7 and WCP8, the percentage has more frequency in extreme event days than in precipitation days.
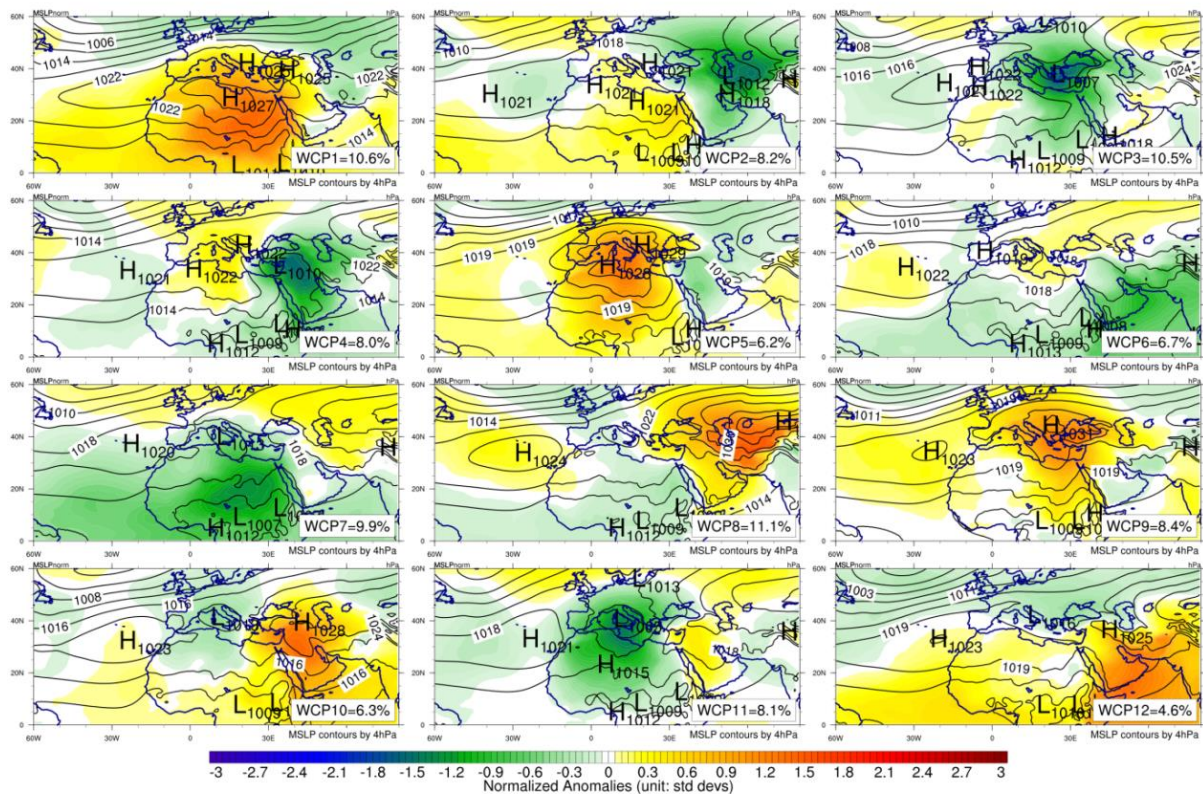
Figure 6.2. Composite of the daily MSLP average (dashed line) and normalised MSLP anomalies (colour fill) for all days in the wet season (Nov./Dec./Jan.) over 30 years (2760 days), The percentage (%) in rectangles represent the distribution percentage of each WCP.
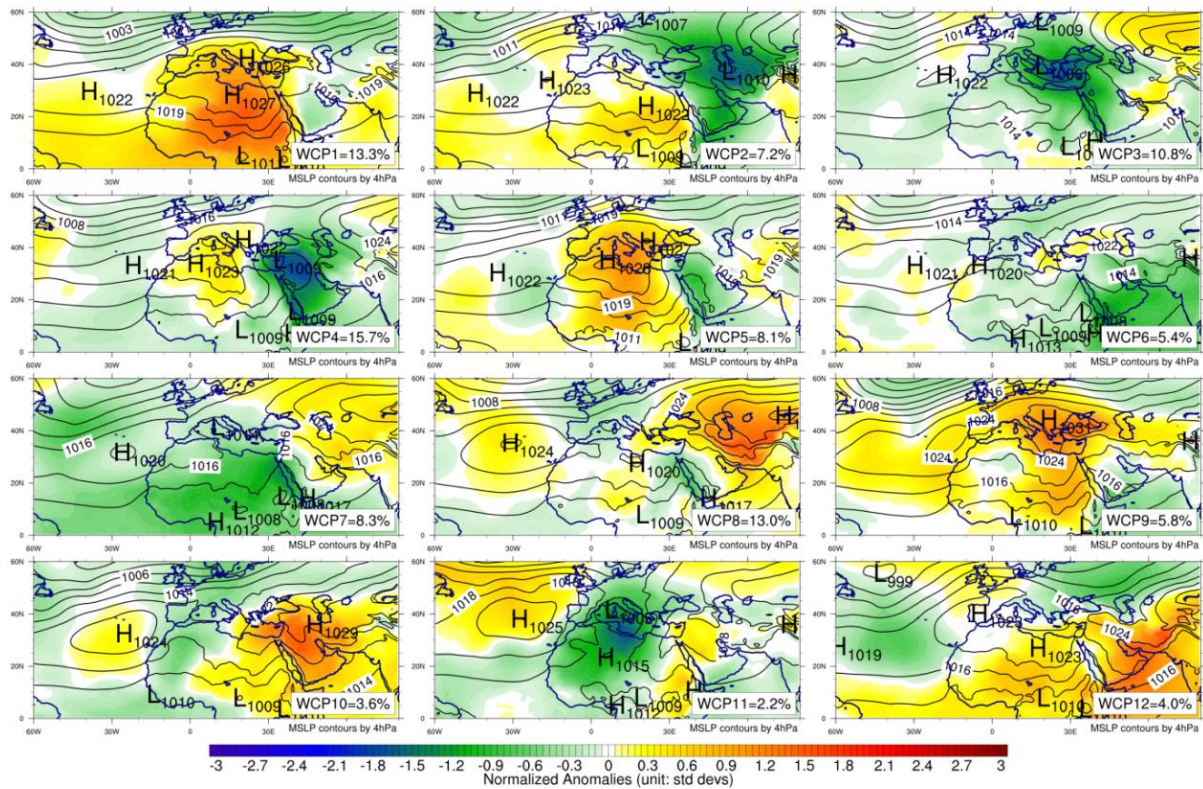
Figure 6.3. As Figure 6.2, but for precipitation days (445 days) in 30 wet seasos.
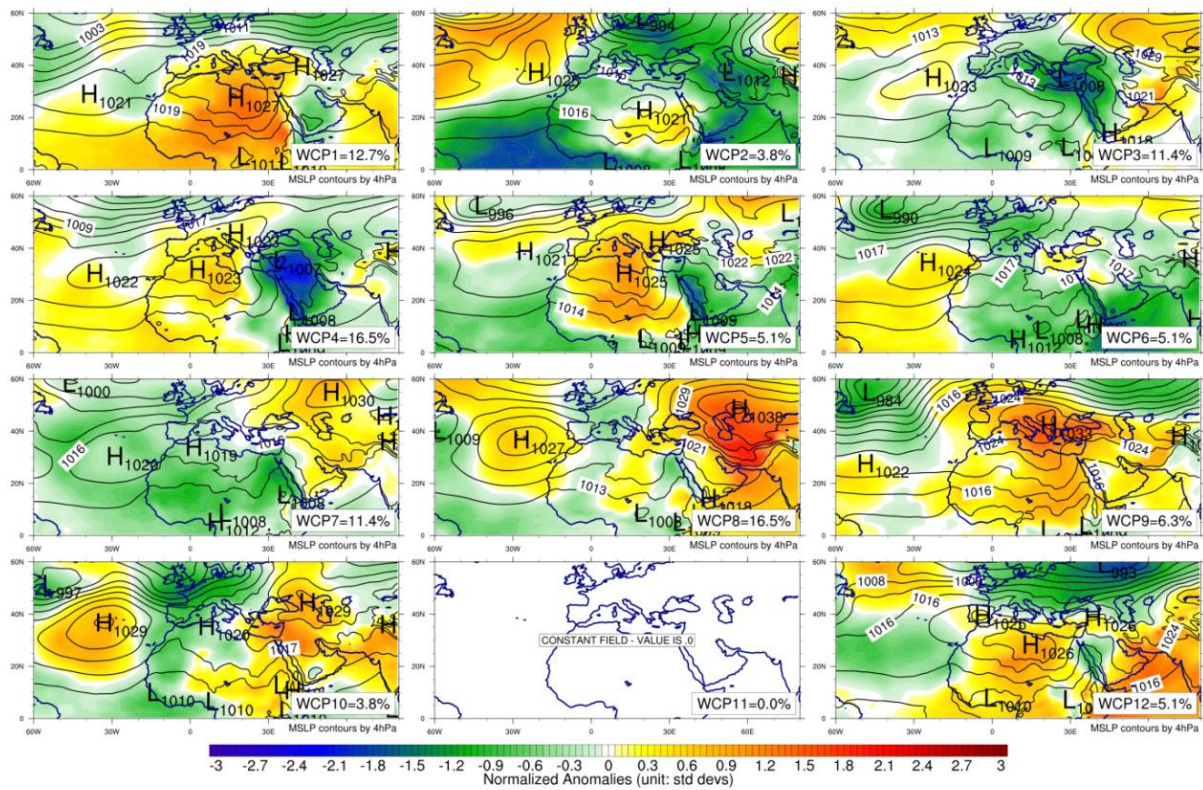
Figure 6.4. As Figure 6.2, but for extreme events (79 events) in 30 wet seasos.

To clearly understand about the nature of anomalies during extreme precipitation events, the difference between the normalised MSLP anomalies of precipitation days and the normalised MSLP anomalies of all wet season days for each WCP are calculated (Figure 6.5). Figure 6.6 shows the difference between the extreme event days and all wet season days; these two figures are a useful indicator of the strength of the pressure systems that contribute to each WCP. The anomaly value of low pressure decreases from all wet season days to extreme event days, while the value of the high pressure increases, which is a sign of the severity of these pressure systems during extreme events.
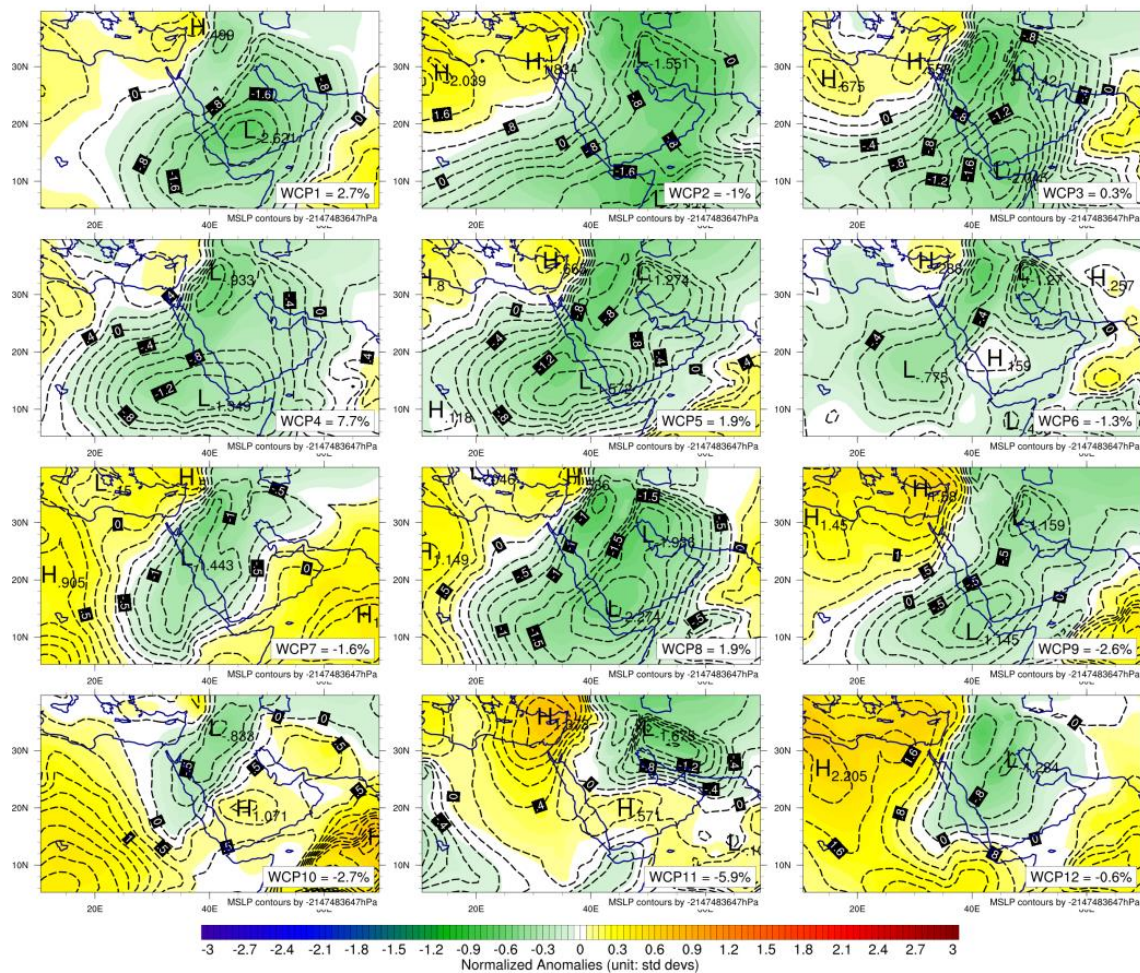
Figure 6.5. The difference between the normalised MSLP anomalies of the precipitation days and all wet season days (colour fill) and the difference between the daily MSLP average of the precipitation days and all wet season days (dashed line) for each WCP. The percentage (%) in rectangles represent the different distribution percentage of each WCP.

On the other hand, the percentage distribution for individual WCP is changed from all wet season days and both precipitation days and extreme events. Figure 6.5 represents the difference of distribution percentage for each WCP between the precipitation days and all wet season days and found that the significant increase in the percentage was in WCP4 by 7.7% more occurrence with the precipitation days, as well as the slight increasing change in WCP1, WCP3, WCP5 and WCP8 by 2.7%, 0.3%, 1.9% and 1.9%, respectively. In all these WCPs, the strong negative normalised MSLP anomaly is centred over the south of Red Sea. Furthermore, the significant decrease in the percentage occurrence of WCP which associates with precipitation days was in WCP11 where recorded -5.9%.
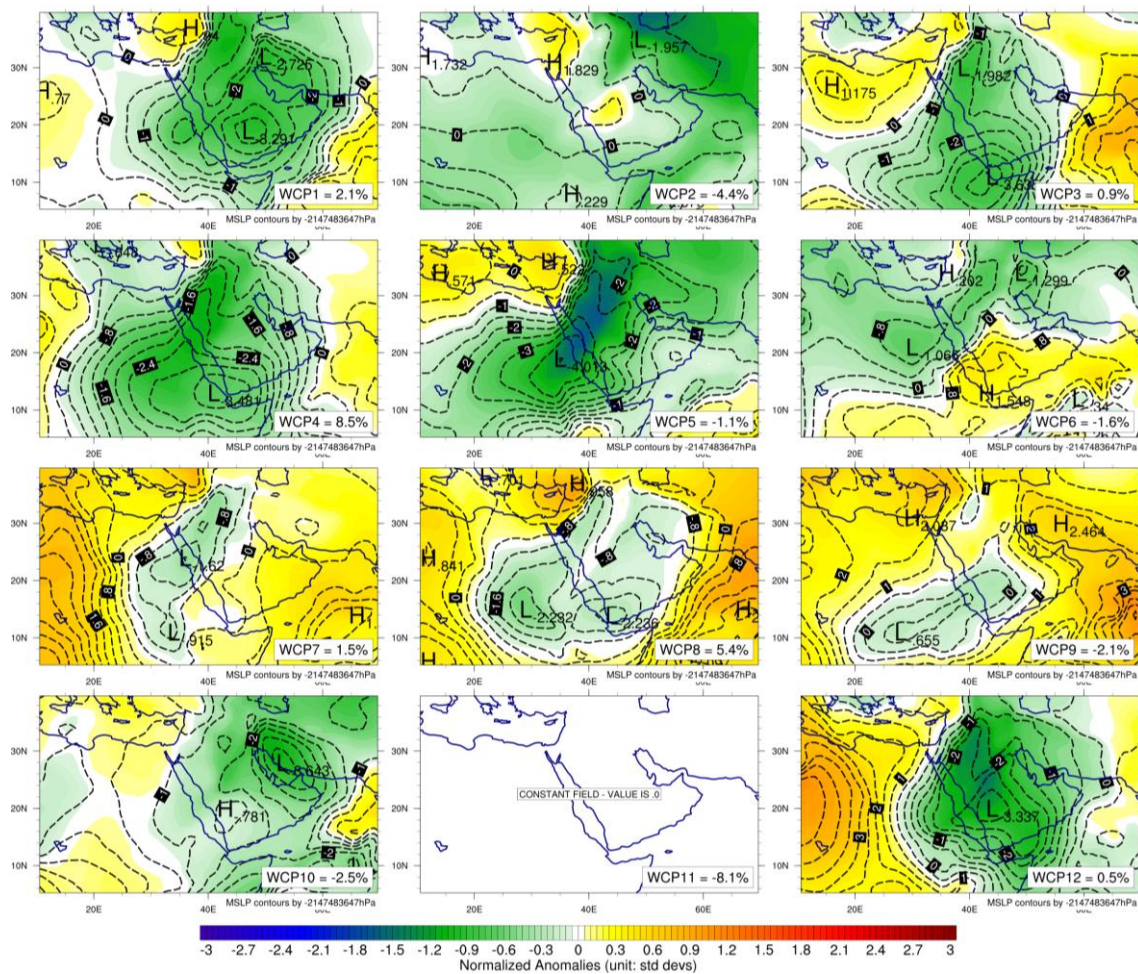
Figure 6.6. As Figure 6.5, but between the extreme event days and all wet season days.

In addition, Figure 6.6 represents the difference of distribution percentage for each WCP between the extreme events and all wet season days and found that the percentage was slightly different with what was found in precipitation days. The significant increase in the percentage occurrence was in WCP4 and WCP8 by 8.5% and 5.4% with the extreme events, as well as the slight increasing change in WCP1, WCP3, WCP7 and WCP12 by 2.1%, 0.9%, 1.5% and 0.5%, respectively. In most of these WCPs, the strong negative normalised MSLP anomaly is centred over the south of Red Sea except in WCP7, which is located over the central of Red Sea. In addition, WCP5 is decreased by -1.1% but with a stronger negative normalised MSLP anomaly over the Red Sea and north AP.

6.3.   Spatial and temporal WCPs distributions:

This section has attempted to provide a brief summary of the monthly frequency distribution of WCPs. Figure 6.7 illustrates the frequency distribution of WCPs over 30 years for all wet season days, precipitation days and extreme evens, in addition to the difference between the percentages of these frequency distribution (precipitation days minus all wet season days, extreme event days minus all wet season days, extreme event days minus precipitation days). It shows that only 1.4% of the wet season days are unclassified, and this percentage is slightly increased for extreme event days (2.5%). The monthly distribution percentage of WCPs during the extreme event days, precipitation days and wet season days shows a slight difference between December and January, but November is an exception. Class WCP4 and WCP8 reveal remarkably more influence for the generation of extreme precipitation, especially in November, which has relative increases up to 100% in class WCP8. In addition, the most extreme events which are associated with class WCP7 occur in November. On the other hand,

the extreme events which regularly occur in January and December are associated with class WCP1 and WCP3.

Figure 6.7: The mean monthly distribution percentage of WCPs during all wet season days (Top-left panels), during all precipitation days (top-right panel) and during all extreme event days (bottom-left panel), bottom-right panel; the difference between the percentage of precipitation days and all wet season days (blue), between the percentage of extreme event days and all wet season days (red) and between extreme event days and precipitation days(green). (Unit: % of all)

Moreover, the bottom-right panel in Figure 6.7 shows significant changes in class WCP4 and WCP8 from their percentages in all wet season days to extreme event days and pronounced differences are visible for the frequency distribution of extreme wet days. On the contrary, class WCP1 shows a slight change and WCP3 does not record any important changes.

Figure 6.8 illustrates the monthly percentage distribution of frequency and amount for each WCP in extreme events at each station. In general, there was no significant difference between the percentage distribution of frequency and amount of extreme precipitation events, except in WCP8, where there is a clear trend of increasing the cumulative amount percentage by 21.4% while the cumulative frequency percentage does not exceed 16.5%. This means that WCP8 is characterised by a higher amount of extreme event days, while WCP4

has a slight decrease in the amount and increase in the number of extreme events. This shows that the extreme rain associated with this pattern is less severe than for WCP8.
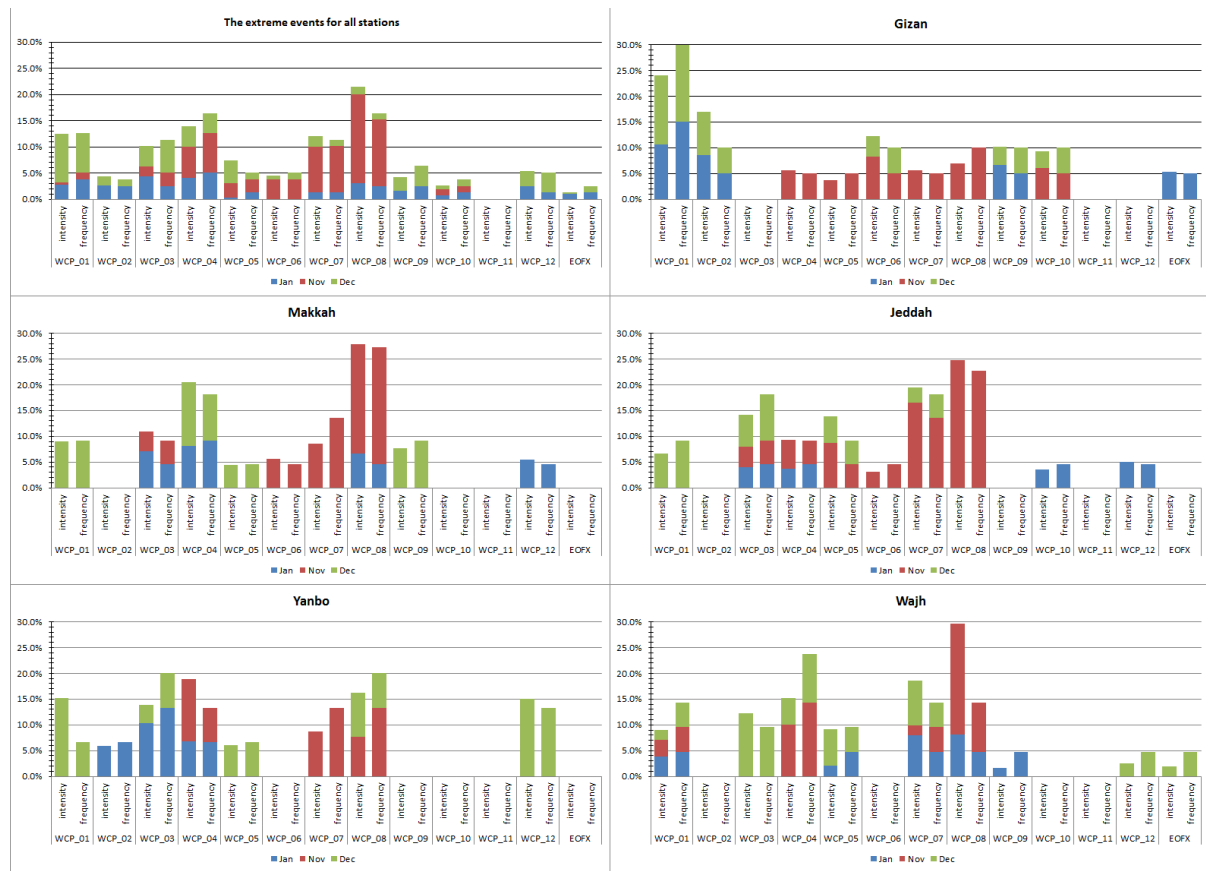
Figure 6.8. The stacked column chart of the monthly percentage distribution of frequency and amount of extreme precipitation events for each WCP. The top left figure shows the percentage summation of all 5 stations together and the other five charts show the percentage of each station.

Furthermore, the distribution of these five most important patterns on the cities are as follows: WCP4 in Makkah, Yanbu and Wajh; WCP8 in all cities; WCP1 in Gizan and Wajh; WCP7 is an important occurrence with the extreme events in Jeddah, Makkah and Yanbu; and WCP3 in Jeddah and Yanbu. Moreover, for the monthly distribution of these patterns, the study find that the WCP4 and WCP3 are distributed relatively evenly between three months, while WCP8 and WCP7 regularly occur in November and WCP1 occurs only in December and January. On the other hand, the occurrence of extreme events is associated with WCP8, WCP7 and WCP6 in November in all cities, while WCP1 and WCP2 affect only Gizan in December and

123

January. This is in contrast with WCP3 and WCP4, which occur equally in all months except in Gizan.

6.4. Characteristics of WCPs:

This study investigates the characteristics of WCPs that are responsible for extreme precipitation events in more detail. Figure 6.9 illustrates the WCPs that occur around the west coast of Saudi Arabia area, while the extension of these patterns is shown in Figure 6.4. The patterns are discussed below in order of importance for the generation of extreme precipitation.
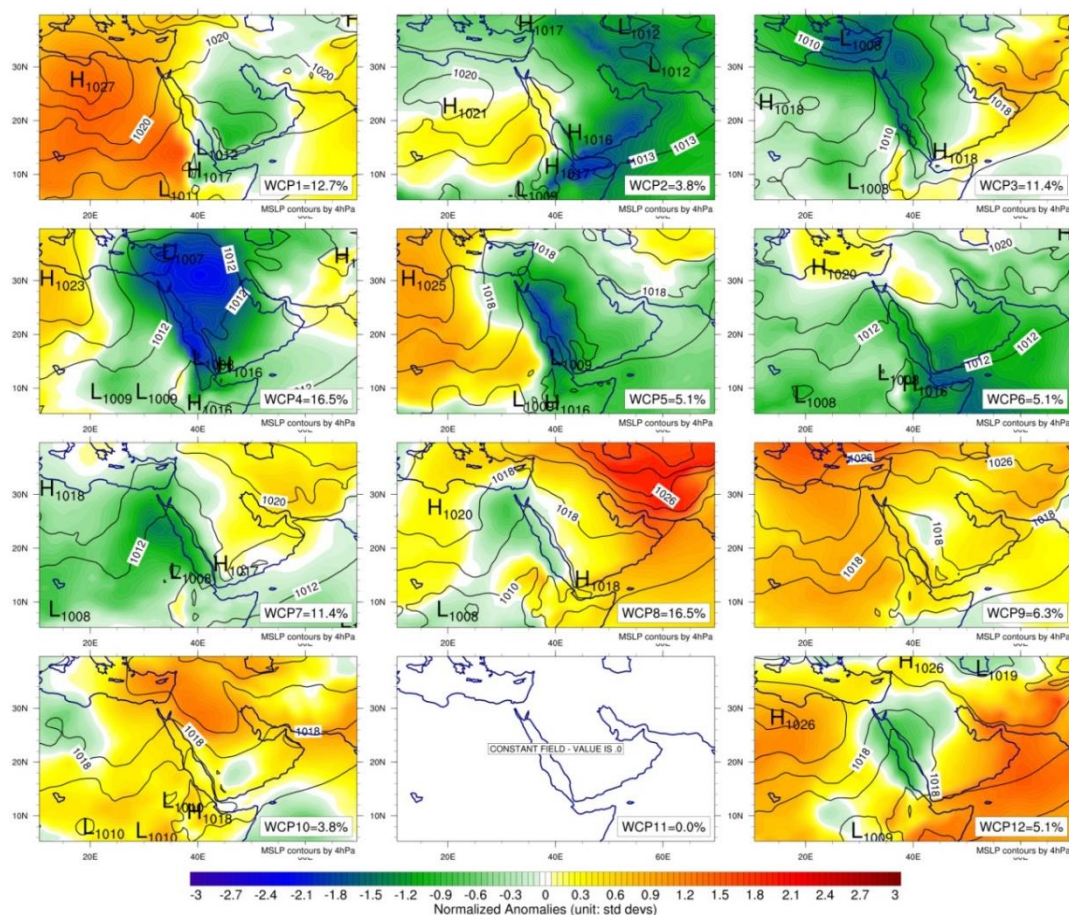
Figure 6.9. Composite of the daily MSLP average and normalised MSLP anomalies for extreme events (79 events) in the wet season (Nov./Dec./Jan.) over 30 years, (same as for Figure 6.4) but the geographical window (05°N–40°N; 10°E–70°E). The percentage (%) in rectangles represent the distribution percentage of each WCP.

6.4.1. WCP4:

This circulation pattern has a major influence on the occurrence of extreme events at stations on the central and northern west coast of Saudi Arabia as about 16.5% of extreme events occur during this class. The NAH has a strong positive anomaly which strengthens and moves northward over the Mediterranean Sea, and is associated with a weak SH. The SH is replaced to the east by MLs, which extend from the Mediterranean Sea to Levant. The strong negative anomaly of the intense RST extends northward over the Red Sea and north-eastward to pass the AP and approach Levant, Iraq and southern Turkey. These two low pressure systems combine to create the LL over Levant. It is also classified as the Active Red Sea Trough.

6.4.2. WCP8:

This circulation pattern is responsible for the occurrences of 16.5% of the extreme events overall. The Azores High is stationed on the ocean with a positive anomaly, but the SH monopolises the systems over Saudi Arabia with a high positive anomaly and moves westward to the Mediterranean Sea and northern Egypt. The NAH is formed here by SH, which is supportive but not strong. The SL cannot extend deeper into the AP because of the strong SH, and the RST extends over Red Sea between these high pressure systems. The eastern border of the RST is included in our study area, whereas the western side covers part of Egypt.

6.4.3. WCP1:

This circulation pattern corresponds to positive EOF 1. It is the third most common circulation pattern and is linked to cases of extreme precipitation in this area, where nearly 12.7% of all extreme events occur. Significantly, 30% of the extreme events occur in Gizan, as shown in Figure 6.8. A weak SH extends to the west to confluence with the Azores High over the

Mediterranean to support and increase the strength of the NAH. The normalised anomaly of the NAH is intensely positive. This illustrates the important role played by the NAH in this weather pattern; it is, in fact, the main factor. The NAH limits the RST expansion northward, however, the RST extends toward the northeast and spreads into the AP.

6.4.4. WCP7:

This weather pattern constitutes 11.4% with significant accrual in the central and northern west coast of Saudi Arabia by approximately 18.2%, 14.3%, 13.6% and 13.3% of extreme day events in Jeddah, Wajh, Makkah and Yanbu, respectively. The significantly intense precipitation in Wajh is associated with this pattern, especially in December and January. The SL extends from Central Africa toward north-eastern Africa along the Red Sea without stretching inside the AP. The strong negative normalised anomaly of the SL is associated with the large positive normalised anomaly of the SH, which dominates the AP and the Eastern Mediterranean. The Azores High and the NAH are very weak with a positive normalised anomaly.

6.4.5. WCP3:

This pattern accounts for 11.4% of extreme events along the Red Sea Coast. During this situation, the SH extends to the southwest of Saudi Arabia with a high positive anomaly that increases its strength. The NAH is weak, making it possible for the MLs to form in the Mediterranean Sea Centre. The SH limits the extension of the SL to the AP, which generates a strong RST along with the eastern Red Sea, and extends toward the Mediterranean from North Africa. Where the MLs run the RST from northwest of the Red Sea, it is the ARST. All the stations are affected by these situations, particularly in the central and north Red Sea region.

126

6.4.6. WCP5:

This circulation pattern is rare and although it is similar to WCP1, the RST here is deeper and located directly over the Red Sea. It extends more northward and continues to approach the Mediterranean Sea. In addition, it is affected by a weak SH from the east, intensifying the RST. This makes it possible to produce or create small cyclones over which the Red Sea Low (RSL) develops. As it can be seen in Figure 6.9, a small cyclone has appeared in the southern WCSA.

6.4.7. WCP9:

This circulation pattern affects Gizan and Makkah. The MSLP in this pattern is similar to WCP8, but the normalised anomaly is different. A strong positive normalised high pressure anomaly over the Mediterranean extends to Levant and the northern AP. In addition, the RST has a positive normalised anomaly that weakens its role. It is smaller than WCP1, however, the NAH, which is part of the Azores High, has shifted north.

6.4.8. WCP6:

This pattern occurs in the early part of the wet season and accounts for just 5% of the events, as Figure 6.4 shows. The SH extends westward into Saudi Arabia and the Azores High declines. The high pressure with a high positive anomaly is located over the AP. Two troughs surround this high pressure system. These two troughs are the RST and the AGT. This finding is consistent with results from Chapter 4 that show the AGT occurs in the late dry season because it is a trough from the Indian monsoon. In addition, this pattern affects the southwest coast of Saudi Arabia with rare events in Makkah and Jeddah, and its effects do not extend further than the central WCSA.

6.4.9. WCP2:

Three extreme events have been recorded with this circulation pattern: one in in the central Red Sea region and two over Gizan, corresponding only to about 3.8% of extreme events overall. Although it is a significant circulation pattern in the wet season, extreme events are rare with this WCP, accounting for only 3.8% of extreme events but 10% of all events in the southern Red Sea region. The SH is weak and the NAH is strong with a positive anomaly located over Egypt. This limits the SL from extending to the north over the Red Sea. The RST is not clearly present in this WCP. However, the strong SL has a negative anomaly. It extends into the centre of Saudi Arabia and deepens northeastwardly until it reaches the south of Turkey with a declining SH. In some cases, an AL is generated over the southern WCSA.

6.4.10. WCP12:

This weather circulation pattern corresponds to negative EOF 6 because the negative stage of EOF 5 (WCP11) does not have any extreme precipitation events associated with it. However, it is an infrequent WCP. Only around 5.1% of extreme events over the central and northern west coast of Saudi Arabia are associated with this pattern. The NAH extends north to the AP and the SH pushes to the southeast; the result is an AA over the AP. This associates with the RST, which extends along the WCSA. The RSL occurs because the RST is surrounded by many high pressure systems.

6.4.11. WCP10:

This is a very rare circulation pattern accounting for only 3.8% of events. However, 10% of the extreme events in Gizan occur due to this pattern. It is similar to WCP8, but the SH and the RST are weaker. In addition, the SL extends through Libya between the SH and Azores High, which is stationary over the Atlantic.

128

6.5. Linking WCPs with individual cases:

Table 6-1 contains values of factor scores for the top 30 extreme precipitation events from 1985 to 2014. It includes values for the wet season as well, since it extends to Table 4-3 in Chapter 4 (that table shows dynamics of these 30 extreme precipitation events). The WCP for each extreme event is classified by the highest factor scores, which are shown in Table 6-1 in the Type column. This classification does not discriminate between days with extreme precipitation and non-extreme precipitation; however, the same surface synoptic dynamic days are grouped together.

Case 1 represents a paradigmatic example of an ARST process, where the study found that the strong RST coincides with a UT and an AA in the upper and middle troposphere; these upper level systems support the RST to deepen northward into the northern AP. This case is classified as WCP4, which represents the most important pattern and one that is responsible for extreme events. The second most important pattern is WCP8; in this pattern, the SH dominates the AP. A wide RST extends along the Red Sea, which is also bordered by a strong NAH from the north and east. Perhaps the best illustration of this pattern is Case 5.

Case 9 represents the third most important pattern frequency and the most frequent pattern for all days in the wet season, which is WCP1. The RST is present between the NAH and the SH, but it expands inside the AP to the east because of the weakness of SH and the deep NAH.

The heavy rain in WCP7 and WCP3 occurred most often in the central and northern WCSA. However, Case 2 represents WCP7, where the SH has control over the AP. This high pressure system does not allow for the SL to go deeper into the AP. As a result, the SL stretches over the Red Sea and Egypt. This case is similar to case 5, which represents WCP8; however, due to the presence of the NAH and the strong influence of the SH, the RST becomes deeper and

129

more intense than in Case 5. In contrast, Case 7 represents WCP3. This case has the same

dynamic characteristics as WCP4; however, the RST in WCP3 extends to the northwest of the

AP. Due to the weakness of the NAH in the WCP3, the RST extends to the northwest of the AP

and meets the ML over the Mediterranean Sea to form the ARST. In WCP4, the SH is weak

and the RST shifts east to meet the LL over the Levant.

Case	City	Date	EOF01	EOF02	EOF03	EOF04	EOF05	EOF06	EOF07	EOF08	EOF09	EOF10	EOF11	EOF12	max	TYPE1
	Jeddah	18-Nov-1985	0.0	0.0	0.0	0.0	0.0	0.0	0.0	1.1	0.7	0.9	0.3	0.3	1.1	WCP08
1	Makkah	18-Dec-1985	0.0	2.7	1.9	4.0	0.4	1.8	1.2	0.0	0.0	0.0	0.0	0.0	4.0	WCP04
	Wejh	29-Nov-1986	0.0	0.0	0.0	1.5	1.2	0.1	0.1	0.0	0.4	0.0	0.0	0.0	1.5	WCP04
	Yanbo	29-Nov-1991	0.0	0.0	0.3	1.4	0.8	0.2	0.3	0.1	0.0	0.0	0.0	0.0	1.4	WCP04
	Jeddah	10-Jan-1992	2.6	0.0	0.0	0.0	1.7	0.0	0.0	2.7	1.8	2.2	0.0	3.0	3.0	WCP12
2	Jeddah	2-Nov-1992	0.0	0.3	0.3	0.4	0.0	0.8	1.6	0.0	0.0	0.0	0.8	0.0	1.6	WCP07
	Gizan	11-Nov-1992	0.1	0.2	0.0	0.7	0.6	0.5	0.0	0.0	0.1	0.0	0.0	0.0	0.7	WCP04
3	Yanbo	22-Dec-1993	0.4	0.2	0.2	0.2	0.4	0.0	0.0	0.0	0.0	0.0	0.0	0.6	0.6	WCP12
4	Gizan	9-Nov-1994	0.1	0.1	0.0	0.0	0.0	0.1	0.0	0.0	0.4	0.8	0.3	0.0	0.8	WCP10
	Yanbo	29-Dec-1994	1.3	0.0	0.0	0.0	1.3	0.0	0.0	0.7	0.6	0.2	0.0	1.6	1.6	WCP12
5	Wejh	17-Nov-1996	0.0	0.0	0.0	0.0	0.0	0.0	0.2	2.6	0.8	1.5	0.0	1.0	2.6	WCP08
	Jeddah	25-Nov-1996	0.0	0.0	0.5	0.1	0.0	0.4	0.6	0.4	0.0	0.0	0.0	0.0	0.6	WCP07
	Wejh	14-Jan-1997	0.0	0.0	0.4	0.2	0.1	0.0	0.7	0.7	0.0	0.0	0.0	0.2	0.7	WCP07
	Gizan	12-Nov-1997	0.0	0.6	0.1	0.4	0.0	1.1	0.6	0.0	0.0	0.0	1.0	0.0	1.1	WCP06
6	Gizan	9-Jan-1999	0.0	2.2	1.7	2.1	0.0	1.1	0.4	0.0	0.0	0.0	0.9	0.0	2.2	WCP02
	Makkah	16-Nov-2000	0.0	0.0	0.0	0.0	0.0	0.8	0.8	1.7	0.3	0.1	0.2	0.0	1.7	WCP08
	Gizan	15-Dec-2000	1.0	1.6	0.1	0.7	0.2	0.7	0.0	0.0	0.0	0.0	0.0	0.0	1.6	WCP02
	Makkah	30-Nov-2002	0.0	0.0	0.3	0.3	0.0	0.0	0.4	0.6	0.0	0.0	0.1	0.1	0.6	WCP08
	Jeddah	10-Nov-2003	0.0	1.4	1.7	3.0	0.0	1.6	1.8	0.0	0.0	0.0	0.4	0.0	3.0	WCP04
7	Makkah	22-Jan-2005	0.0	0.5	2.4	1.8	0.0	0.3	1.0	0.0	0.0	0.0	1.0	0.0	2.4	WCP03
	Makkah	11-Jan-2008	0.4	0.0	0.0	0.0	1.0	0.0	0.0	1.8	1.7	0.6	0.0	0.2	1.8	WCP08
8	Makkah	6-Nov-2008	0.0	1.1	0.5	1.0	0.0	2.1	1.4	0.0	0.0	0.0	0.9	0.0	2.1	WCP06
	Jeddah	25-Nov-2009	0.1	0.0	0.2	0.6	0.7	0.0	0.0	0.4	0.0	0.0	0.0	0.1	0.7	WCP05
9	Yanbo	22-Dec-2009	0.8	0.0	0.0	0.0	0.5	0.0	0.0	0.4	0.7	0.2	0.0	0.7	0.8	WCP01
	Wejh	18-Jan-2010	0.1	0.0	0.7	0.4	0.5	0.0	0.0	1.6	0.0	0.0	0.0	1.3	1.6	WCP08
10	Wejh	30-Dec-2010	0.4	0.0	0.0	0.4	1.0	0.0	0.0	0.5	0.0	0.0	0.0	0.3	1.0	WCP05
	Yanbo	1-Jan-2011	0.0	1.3	0.1	0.5	0.0	0.6	0.1	0.0	0.0	0.0	0.2	0.0	1.3	WCP02
11	Gizan	3-Jan-2013	1.9	0.0	0.0	0.0	1.5	0.0	0.0	1.9	2.3	1.9	0.0	1.4	2.3	WCP09
	Yanbo	29-Dec-2013	0.0	0.0	0.2	0.0	0.3	0.0	0.1	2.7	0.0	0.8	0.0	1.4	2.7	WCP08
	Wejh	9-Dec-2014	0.0	0.0	2.4	0.2	0.0	0.0	2.0	1.4	0.0	0.0	1.6	0.6	2.4	WCP03

Table 6-1. Top 30 extreme precipitation events from 1985 to 2014 during the wet season with values of factor scores for each event.

Case 10 represent WCP5. In this case, the cyclone pattern (RSL) forms over the Red Sea

because the deep RST over the Red Sea is located between two strong high pressure systems

(NAH and SH). In addition to case 10, the most important extreme event that hit Jeddah in

November 2009 is also classified as WCP5 and has the same synoptic dynamic characteristics, as Table 6-1 shows. In the same situation, case 3, which represents WCP12, is also produced by the RSL. These patterns are similar to WCP1, but the UT is deeper and forms a CL over the Red Sea as well as the strong SJ in the upper air in WCP5 and WCP12.

Several patterns (WCP2, WCP6, WCP9 and WCP10) occur particularly on the south coast as well as affect Makkah in some cases, such as case 8, which is classified as WCP6. The UT does not have any role in this case. In contrast, the UT extends significantly toward the southern AP in case 6, which is classified as WCP2. In this case, a low system forms over the southern AP. WCP9 and WCP10 are comparable to WCP8, but the RST is weak and has no effect in these two patterns. The RST is absent in WCP9 because of the high pressure system that controls the weather over the AP, such as in case 11. While in WCP10, the RST axis did not exceed further than the central WCSA, so its impact was on Gizan, as in case 4. In some cases, its impact reaches Makkah.

6.6. WCPs distribution based on ERA-Interim precipitation days:

In order to use the grid data to predict future data and climate change studies that rely on numerical models, there must be some sort of approximate relationship between observation data and some assimilation data product such as the ERA-Interim reanalysis grid point data. The work here should check if the WCP from ERA-Interim reanalysis grid point data lead to a similar distribution of precipitation as from observations. The study showed a change in precipitation data between ERA-Interim reanalysis and observation data as this was shown in Chapter 5, but hopefully this section would expect a similar WCP distribution. Thus, if this is changing under ACC, as it will be investigated in the next chapter, then it may expect to see changed precipitation and extreme events as well.

In this section, the EOF is applied to MSLP according to the ERA-Interim reanalysis precipitation grid point data. Several precipitation elements of the percentile precipitation values were selected (99th, 98th, 95th, 90th, 85th, 80th and 75th percentiles of all wet days), in addition to all wet days that were known to have more than 0.1 mm rainfall. The result was then applied to percentages of the occurrence of individual WCPs in each precipitation element. The correlation coefficient was applied to measure the degree of the relationship between the percentages of the occurrence of individual WCPs of extreme observed events and the percentages of the occurrence of individual WCPs of each (99th, 98th, 95th, 90th, 85th, 80th and 75th percentiles of all wet days) of ERA-Interim reanalysis precipitation data. It was also applied between the percentages of the occurrence of individual WCPs of precipitation observed days and the percentages of the occurrence of individual WCPs of ERA-Interim reanalysis precipitation days (>0.1mm).

The results of the correlational analysis are shown in Table 6-2. A positive correlation was found between the distribution of WCPs occurrence for observed precipitation days and gridded ERA-Interim reanalysis precipitation days, as shown in table H in Table 6-2. The lowest positive correlation was in the south, where correlation values were recorded 0.96, 0.95, 0.90, 0.80 and 0.76 in Wajh, Yanbu, Jeddah, Makkah and Gizan, respectively. To analyse a more robust pattern instead of only grid point perspective, another correlation in precipitation days was calculated between the total distribution of the five observation stations (spatial average) and the five grid points spatial average, the value also had a high positive correlation of 0.81.

For the purpose of the best WCPs distribution based on ERA-Interim reanalysis extreme precipitation days which are corresponding WCPs distribution based on observed extreme precipitation days, the correlation coefficients are applied between WCPs distribution of

132

seven ERA-Interim reanalysis extreme precipitation percentiles (99th, 98th, 95th, 90th, 85th, 80th and 75th) days and observed extreme days.

(A)	Ext_G	Ext_M	Ext_J	Ext_Y	Ext_W	Ext_sum
99_all_grids						0.73
99_G	-0.06					
99_M		0.31				
99_J			0.51			
99_Y				0.39		
99_W					0.30	
99_all_C						0.45

(E)	Ext_G	Ext_M	Ext_J	Ext_Y	Ext_W	Ext_sum
85_all_grids						0.75
85_G	0.77					
85_M		0.62				
85_J			0.55			
85_Y				0.82		
85_W					0.77	
85_all_C						0.86

(B)	Ext_G	Ext_M	Ext_J	Ext_Y	Ext_W	Ext_sum
98_all_grids						0.81
98_G	0.20					
98_M		0.49				
98_J			0.44			
98_Y				0.46		
98_W					0.70	
98_all_C						0.69

(F)	Ext_G	Ext_M	Ext_J	Ext_Y	Ext_W	Ext_sum
80_all_grids						0.72
80_G	0.76					
80_M		0.57				
80_J			0.53			
80_Y				0.81		
80_W					0.76	
80_all_C						0.82

(C)	Ext_G	Ext_M	Ext_J	Ext_Y	Ext_W	Ext_sum
95_all_grids						0.83
95_G	0.37					
95_M		0.42				
95_J			0.41			
95_Y				0.46		
95_W					0.63	
95_all_C						0.68

(G)	Ext_G	Ext_M	Ext_J	Ext_Y	Ext_W	Ext_sum
75_all_grids						0.72
75_G	0.75					
75_M		0.61				
75_J			0.53			
75_Y				0.80		
75_W					0.83	
75_all_C						0.82

(D)	Ext_G	Ext_M	Ext_J	Ext_Y	Ext_W	Ext_sum
90_all_grids						0.84
90_G	0.76					
90_M		0.56				
90_J			0.55			
90_Y				0.76		
90_W					0.79	
90_all_C						0.81

(H)	Wet_G	Wet_M	Wet_J	Wet_Y	Wet_W	Wet_sum
rr_all_grids						0.72
rr_G	0.76					
rr_M		0.78				
rr_J			0.89			
rr_Y				0.95		
rr_W					0.96	
rr_all_C						0.81

Table 6-2. (A, B ,C ,D, E, F, G tables) show the correlation coefficient between the percentages of individual WCPs of extreme observed events and the percentages of individual WCPs of each ERA-Interim reanalysis extreme precipitation percentiles (99th , 98th , 95th , 90th , 85th , 80th and 75th) days, while (table H) shows the correlation between the percentages of individual WCPs of precipitation days observed and the percentages of individual WCPs of ERA-Interim reanalysis precipitation days (>0.1mm).

The results of these correlation coefficients are displayed in tables (A, B, C, D, E, F and G) in Table 6-2. The best results of these correlations were with 90th and 85th percentiles, as shown in tables D and E. However, the current study chose the 90th percentile as the threshold for extreme precipitation. The lowest positive correlation was in the central region of the WCSA, where correlation values of 0.55 in Jeddah and Makkah were recorded, while in other stations, values of approximately 0.76 were recorded. Another correlation in extreme events

was between the total of distribution of the five observation stations and the five grid points, there was also a high positive correlation value of 0.81.

Figure 6.10 shows the percentages of difference between WCP distributions for ERA-Interim total precipitation days and WCP distributions for observed total precipitation days in six values (*rr_Wajh, rr_Yanbu, rr_Jeddah, rr_Makkah, rr_Gizan, rr_5_city_grids* and *rr_all_grids*). These values represent the 5 cities in addition to *rr_5_city_grids* which is calculated between the total distribution of the five observation stations (spatial average) and the five grid points (approximately near the observation station) spatial average, as well as *rr_all_grids* which is calculated as rr_5_city_grids but used a spatial average of all 35 grid points along the WCSA against the spatial average of five observation stations.
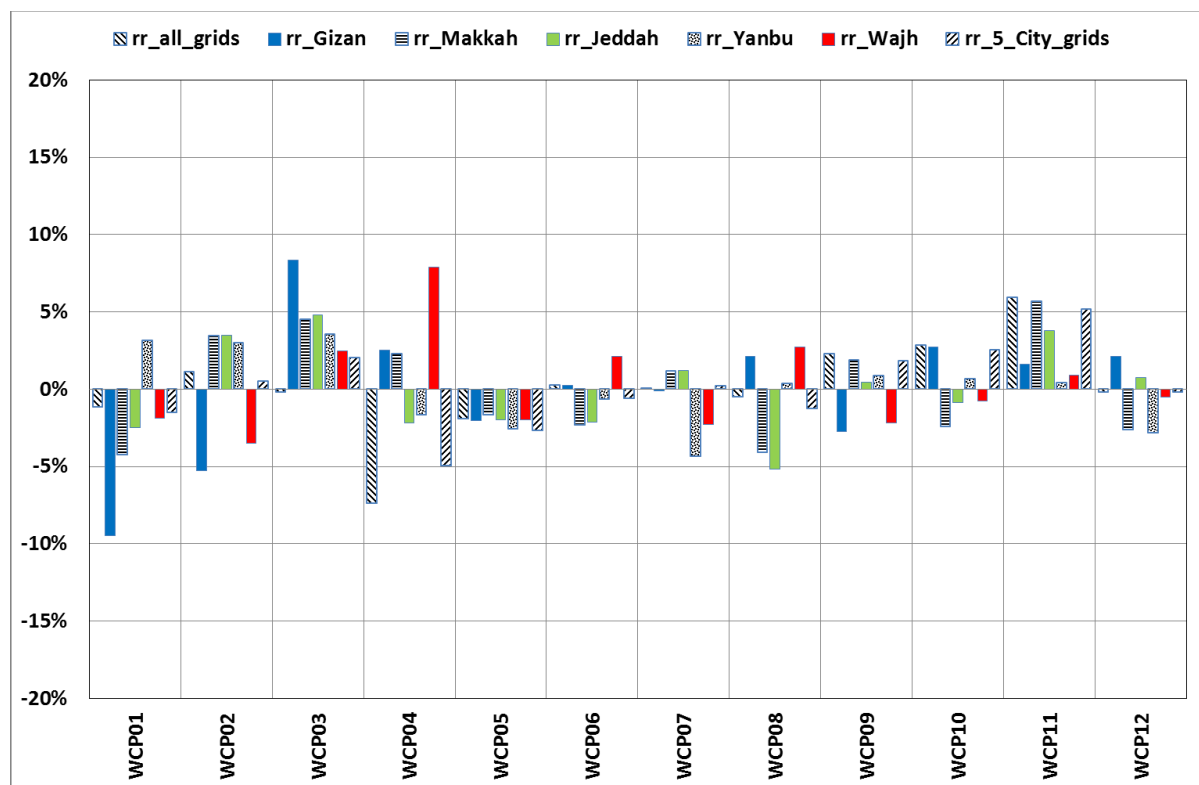
Figure 6.10. The difference percentages of WCP occurrence for total precipitation days between ERA-Interim precipitation days versus observed precipitation days (ERA − Obs) per WCP.

However, examining the differences of precipitation days per WCP it can be concluded that differences are small, not exceeding 9% for all WCPs and all the grid points. Furthermore,

134

comparing the results of all grid points along the west coast of Saudi Arabia (*rr_all_grids)* and of 5 grid points (*rr_5_city_grids)*, the study find inconsiderable deference between these two values. However, a significant decrease was found in the percentage of differences in WCP4 by 7% with *rr_all_grids* and 5% with *rr_5_city_grids* and a significant increase in the percentage of differences in WCP11 by 6% with *rr_all_grids* and 5% with *rr_5_city_grids.*

For extreme events, Figure 6.11 shows the percentages of difference between WCP distributions for ERA-Interim extreme precipitation days and WCP distributions for observed extreme precipitation days in six values (90_Wajh, 90_Yanbu, 90_Jeddah, 90_Makkah, 90_Gizan, 90_5_city_grids and 90_all_grids).
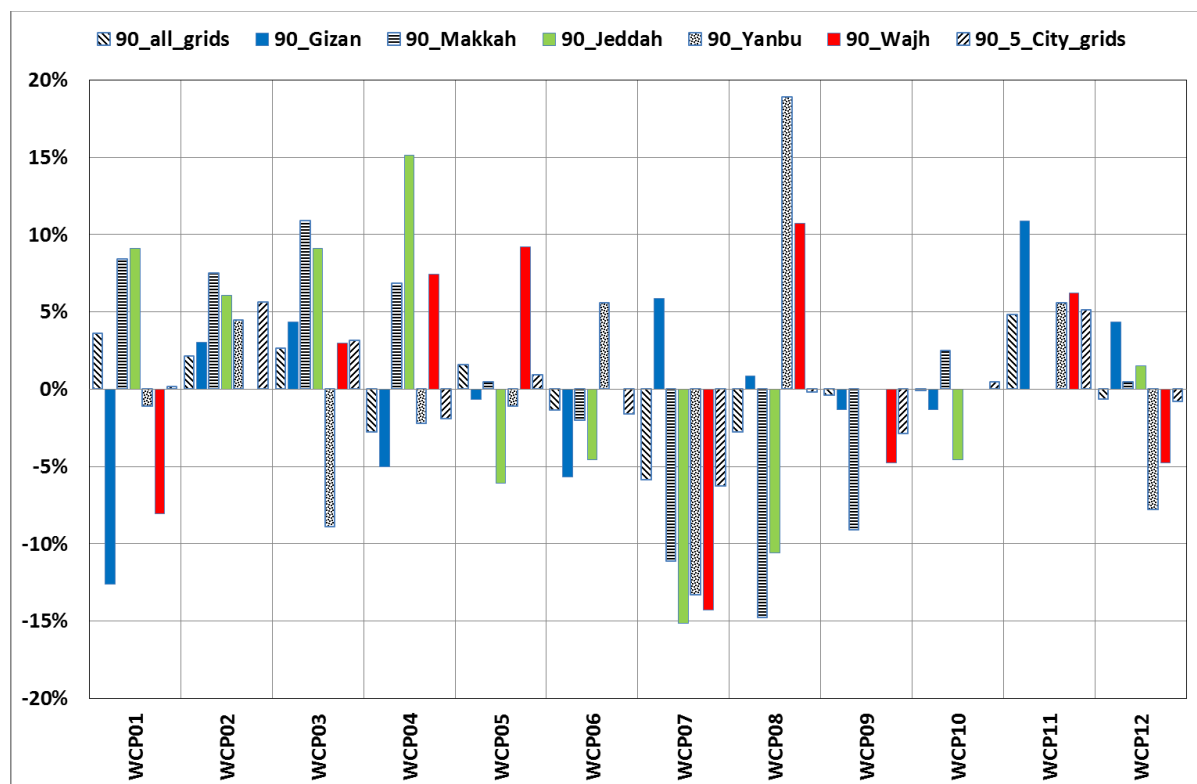
Figure 6.11. The difference percentages of WCP occurrence for extreme events (90th percentile) days between ERA-Interim extreme precipitation days versus observed extreme precipitation days (ERA – Obs) per WCP.

The percentages of difference values for extreme events are increased in comparison to total precipitation values: the percentages of difference exceed 15% in many WCPs and in several

stations and grid points, whether decreasing or increasing. The difference percentages of WCP8 occurrence is increased during extreme precipitation by more than 15% in Yanbu and decreased by 10% in Jeddah, while the difference percentages of WCP4 occurrence by 15% in Jeddah. In addition, the difference percentages of WCP7 occurrence are decreased during the extreme precipitation at all stations and the difference percentages of WCP11 occurrence are decreased in the northern and southern part of the west coast of Saudi Arabia is found. Moreover, comparing the results of all grid points along the west coast of Saudi Arabia (90_all_grids) and the sum of observed extreme events in all five observation stations, the study found a decrease in the percentage of WCP7 by 6% in the re-analysis data.

Figure 6.12 illustrates the mean monthly frequency distribution (in percentage) of WCP occurrences from ERA-Interim for precipitation days and extreme event days over all grid points along the WCSA, and the difference to the frequency distribution derived from observed data (shown in Figure 6.7). For all precipitation days, it shows that the frequency of WCP4, a relevant circulation type for precipitation decreased by about 7%, while WCP11 increased roughly by 6% in ERA-Interim. For extreme event days, the frequency of relevant classes has significantly changed: especially the frequencies of WCP7 and WCP8 which have significantly decreased by approximately 6% and about 5%. This is equivalent to a relative underestimation of these classes in ERA-Interim of about 50%. While for WCP4 no large differences are found (about 2%), WCP11 is overestimated in ERA-Interim. Although there was no extreme event associated with WCP11 according to the result in section 5.2, this class significantly increased where roughly 5% of extreme events are associated with WCP11 in all grid points along the WCSA.

In summary, according to the extreme precipitation events which were based on precipitation gridded data (ERA-Interim reanalysis data), the most important WCP patterns that have the highest recorded incidence of WCP distribution are WCP4, WCP8, WCP1 and WCP3. All these patterns have more than 10% of WCP distributions and have increasing frequency percentage from precipitation days to extreme event days, while the other eight WCPs have decreasing frequency percentage from precipitation days to extreme event days.
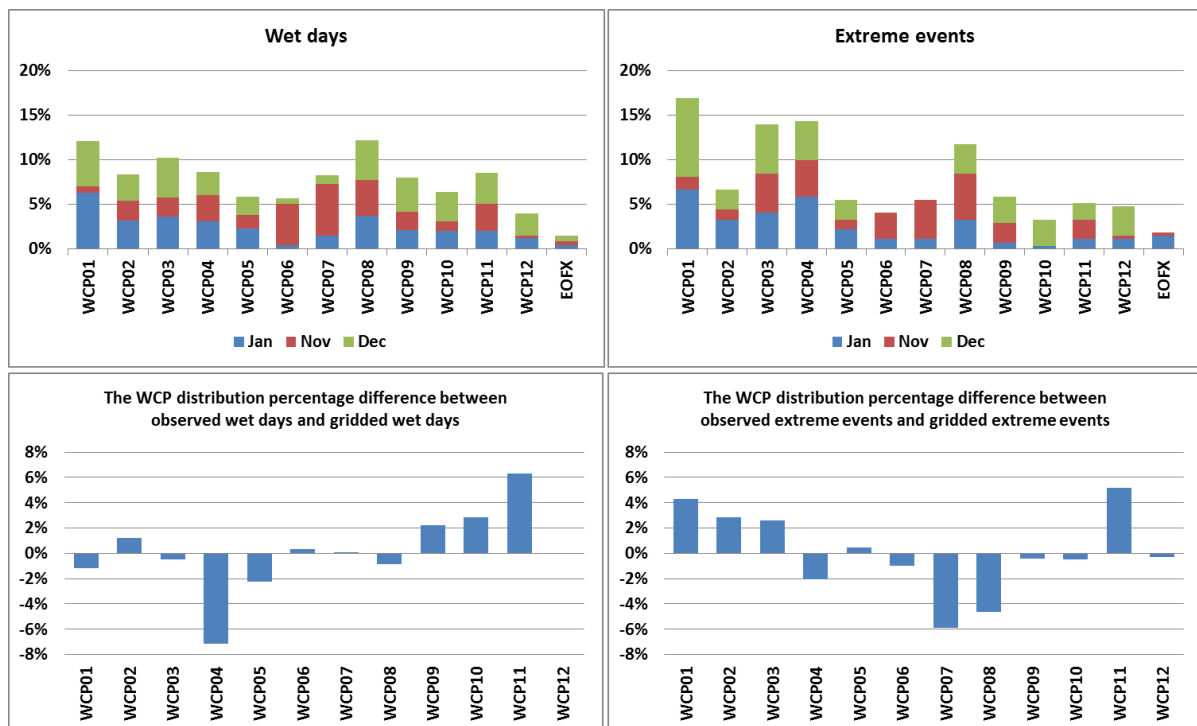
Figure 6.12. The mean monthly distribution percentage of WCPs over 30 years for precipitation days (top left) and extreme event days (top right) over all grid points along the west coast of Saudi Arabia from ERA-Interim; bottom figures show the WCP distribution difference between gridded ERA-Interim precipitation days and observed precipitation days (ERA – Obs) for (bottom left) and extreme event days (bottom right).

6.7.   Linking Extreme Rainfall with Large Scale Modes:

In this section, the linking between several large-scale climate variability modes and the total and extreme precipitation events over the eastern Red sea coastal regions has been established. The results for the statistically significant linear correlation coefficient teleconnections between 10 climate variability indices (NAO-Jones, NAO-station, NAO-CPC,

SOI, ESPI, Nino1+2, Nino3.4, Nino4, MEI and DMI) and the precipitation values for 9 grading areas and 5 meteorological stations are presented in the wet season period for 30 years. Figure 6.13 shows the location of five meteorological stations and nine areas along the Red Sea coast. The nine areas along the Red Sea coast comprise 35 grid points. Each area is defined by four grid points (2 × 2) with a horizontal resolution of 0.75° as the ERA-Interim reanalysis data resolution.
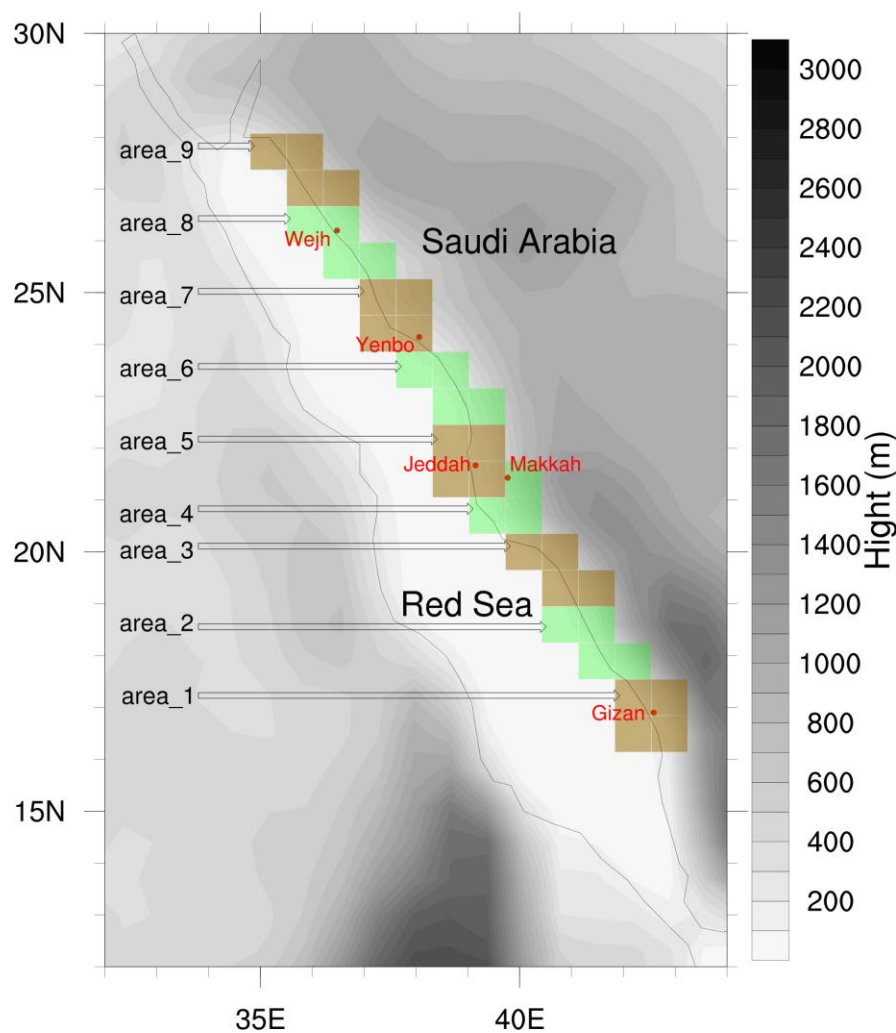
Figure 6.13. Location map of the study area (WCSA) with topography (in meters) and position of the meteorological stations (red circles). The nine areas along the Red Sea coast are each defined by four grid points (2 × 2) with a horizontal resolution of 0.75° for each grid point. Note: there are no differences between green and brown areas; the colouring is only used to distinguish between the nine areas in the map.

6.7.1. Teleconnection between precipitation and large scale climate variability:

Before investigating the correlation between 10 climate variability indices and each individual grid model area and observation station precipitation anomalies, the average of all 5 stations observation and the average of all 35 grid points for frequency and amount of total and extreme precipitation are collected. Figure 6.14 shows these correlations with 8 precipitation anomaly values; the averaged of total precipitation amount in 5 observation stations (*observation_wet_amount*), the averaged of extreme precipitation amount in 5 observation stations (*observation_extreme_amount*), the averaged of total precipitation days in 5 observation stations (*observation_wet_days*), the averaged of extreme precipitation days in 5 observation stations (*observation_extreme_days*), the averaged of total precipitation amount in all model grid points (*grid_wet_amount*), the averaged of extreme precipitation amount in all model grid points (*grid_extreme_amount*), the averaged of total precipitation days in all model grid points (*grid_wet_days*), and the averaged of extreme precipitation days in all model grid points (*grid_extreme_days*).

First, it was shown that the anomaly values based on model grid point averages were relatively similar. It recorded positive correlations (i.e., between 2 and 4) with the ESPI, Nino1+2, Nino3.4, Nino4, MEI and DMI indices and negative correlations (i.e., between -2 and -4) with the NAO-Jones, NAO-station, NAO-CPC and SOI indices. The highest positive correlations were between Nino1+2 and the precipitation values in *grid_extreme_amount* and *grid_extreme_days*, which was above 0.5.

On the other hand, the correlation values of observation averages have large variability from value to value except with NAO indices, where they are similar in correlation values to grid point averages. In addition, the correlation values between all the 10 climate variability

139

indices and *observation_wet_amount* values are relatively similar with results in grid point

average values but with a smaller correlation.
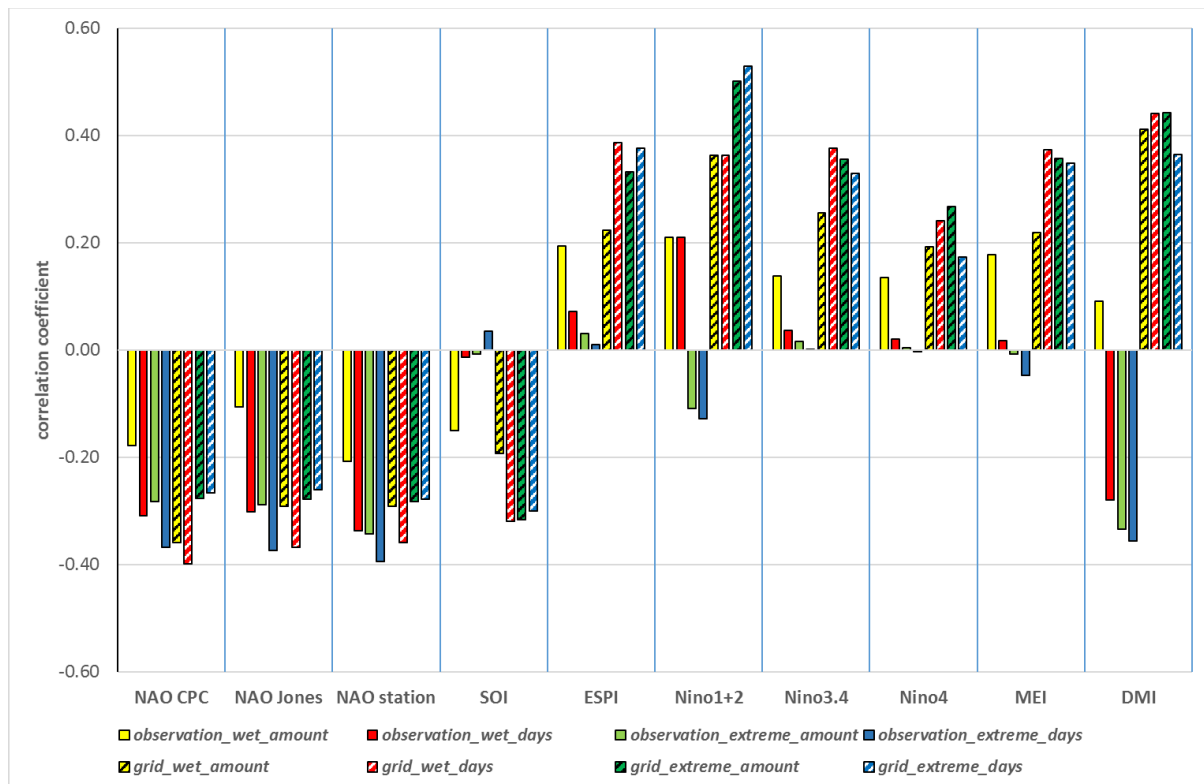
Figure 6.14. The correlation coefficients of the 10 indices with the total and extreme precipitation events based wet seasonal for; the average of 5 observation stations of total precipitation amount (observation_wet_amount), total precipitation days (observation_wet_days), extreme precipitation amount (observation_extreme_amount), extreme precipitation days (observation_extreme_days) and average of all model grid points of total precipitation amount (grid_wet_amount), total precipitation days (grid_wet_days), extreme precipitation amount (grid_extreme_amount), extreme precipitation days (grid_extreme_days).

In the following section, further analysis is proposed to investigate the correlations between

the large-scale patterns and the precipitation anomaly values of each station and individual

areas in more detail. Table 6-3 shows the correlation coefficients for the 10 indices with the

anomaly of total precipitation days and extreme precipitation events for each station and

individual area in the wet season period over 30 years. Firstly, the table shows that the

correlation values are quite similar between the total precipitation and extreme precipitation.

Secondly, the correlation values between the precipitation values based on observational

data from weather stations and SOI, ESPI, Nino1+2, Nino3.4, Nino3.4 and MEI are not

140

significant. Nevertheless, some findings, also based on observational data, refer to a noteworthy correlation of NAO measures with the total and extreme precipitation values, such as Jeddah and Wajh.

total precipitation days	wet_days	NAO-CPC	NAO-Jones	NAO-station	SOI	ESPI	Nino1+2	Nino3.4	Nino4	MEI	DMI
	Gizan	0.16	0.26	0.15	-0.11	0.20	0.19	0.16	0.14	0.19	0.15
	Makkah	-0.26	-0.26	-0.32	-0.01	0.03	0.04	-0.03	-0.04	0.00	-0.12
	Jeddah	-0.30	-0.33	-0.26	0.10	-0.07	-0.06	-0.10	-0.08	-0.08	-0.18
	yanbu	-0.21	-0.20	-0.23	-0.03	0.02	-0.03	-0.02	0.01	0.02	-0.23
	Wajh	-0.29	-0.27	-0.37	-0.18	0.21	0.08	0.16	0.17	0.17	-0.09
	all_cities	-0.18	-0.11	-0.21	-0.15	0.19	0.21	0.14	0.13	0.18	0.09
	area_1	-0.08	-0.01	-0.11	-0.31	0.42	0.59	0.36	0.20	0.38	0.51
	area_2	-0.22	-0.15	-0.20	-0.27	0.38	0.55	0.36	0.22	0.34	0.49
	area_3	-0.36	-0.29	-0.32	-0.24	0.34	0.50	0.32	0.21	0.28	0.57
	area_4	-0.54	-0.45	-0.44	-0.36	0.39	0.55	0.42	0.33	0.39	0.49
	area_5	-0.60	-0.57	-0.45	-0.17	0.14	0.29	0.23	0.20	0.17	0.25
	area_6	-0.58	-0.54	-0.40	-0.16	0.13	0.32	0.22	0.15	0.19	0.20
	area_7	-0.31	-0.29	-0.22	-0.18	0.00	0.01	0.08	0.16	0.10	-0.16
	area_8	-0.11	-0.15	-0.09	-0.16	0.06	-0.07	0.11	0.23	0.15	-0.26
	area_9	-0.21	-0.22	-0.16	-0.11	0.06	0.00	0.12	0.20	0.15	-0.05
	all_areas	-0.36	-0.29	-0.29	-0.19	0.22	0.36	0.25	0.19	0.22	0.41

extreme precipitation events	ext_days	NAO-CPC	NAO-Jones	NAO-station	SOI	ESPI	Nino1+2	Nino3.4	Nino4	MEI	DMI
	Gizan	0.13	0.30	0.14	-0.11	0.17	0.17	0.09	-0.01	0.17	-0.01
	Makkah	-0.20	-0.28	-0.26	0.21	-0.10	-0.15	-0.19	-0.23	-0.20	-0.38
	Jeddah	-0.42	-0.50	-0.49	0.09	-0.12	-0.24	-0.10	-0.05	-0.15	-0.44
	yanbu	-0.24	-0.17	-0.15	-0.13	0.18	0.00	0.22	0.23	0.12	-0.04
	Wajh	-0.42	-0.50	-0.46	0.05	-0.04	-0.16	0.01	0.04	-0.08	-0.26
	all_cities	-0.37	-0.37	-0.39	0.03	0.01	-0.13	0.00	0.00	-0.05	-0.36
	area_1	0.13	0.08	0.02	-0.26	0.39	0.48	0.34	0.18	0.30	0.49
	area_2	0.04	0.10	0.02	-0.32	0.44	0.65	0.40	0.23	0.41	0.60
	area_3	-0.05	-0.04	-0.08	-0.26	0.29	0.51	0.25	0.12	0.29	0.45
	area_4	-0.26	-0.28	-0.25	-0.16	0.18	0.41	0.15	-0.02	0.18	0.37
	area_5	-0.43	-0.41	-0.43	-0.22	0.28	0.42	0.24	0.07	0.24	0.33
	area_6	-0.01	0.02	-0.08	-0.33	0.36	0.25	0.24	0.16	0.29	-0.05
	area_7	-0.14	-0.11	-0.03	-0.07	0.02	-0.04	0.08	0.18	0.08	-0.23
	area_8	-0.34	-0.41	-0.32	0.05	-0.01	-0.11	0.03	0.09	0.01	-0.24
	area_9	-0.42	-0.50	-0.43	0.17	-0.13	-0.19	-0.09	-0.04	-0.13	-0.30
	all_areas	-0.27	-0.26	-0.28	-0.30	0.38	0.53	0.33	0.17	0.35	0.36

Table 6-3. The correlation coefficients of the 10 indices with total precipitation days (Table -A), total precipitation amount (Table-B), extreme precipitation events (Table-C) and extreme precipitation amount (Table-D) for each station and individual area in wet season.

The results of correlation between the 10 climate variability indices and the anomaly precipitation on 9 model grid point areas are as follows; the first three areas are located over the south of Red Sea coast, which are not significantly correlated with the majority of the indices except with some of the ENSO measures, such as Nino1+2 and MEI. The positive correlation between these three areas and Nino1+2 are strongly significant where it reaches up to 0.65 in some areas. DMI index has a non-significant correlation with all northern areas but it recorded a strong positive correlation with the southern area.

In addition, the anomaly precipitation in *area_4* has a strong positive correlation with Nino1+2 but the anomaly precipitation in this area also has a negative correlation observed with NAO indices. This area contains Makkah station which is affected by two rainfall season as was shown in Chapter 4. A negative correlation between the NAO indices and the northern Red Sea coastal areas has been observed, but did show a weak correlation with anomaly extreme precipitation in *area_6* and *area_7* and a strong negative correlation in *area_5*, *area_9* and *area_8*. Further, regarding anomaly extreme precipitation, the correlation in *area_6* are a strongly negative and weakly in *area_8* and *area_9*. All precipitation anomaly values in *area_7* have not recorded any significant correlation with any climate variability indices.

However, results from Table 6-3 show the most important three climate variability indices (i.e. Nino1+2, DMI and NAO-Jones), where Nion1+2 is noteworthy example to present the ENSO measures and also NAO-Jones is good to present NOA measures. Moreover, DMI index is one of the important climate variability index in the Arabian Peninsula regions. The regression coefficient for 9 model grid point areas with these three indices is investigated.

Table 6-4 shows the values of the regression coefficient for each grid point area with Nino1+2, DMI and NAO-Jones indices in total and extreme precipitation days in the wet season period during the 30 years. Negative values of regression coefficient indicate decrease of precipitation events with increasing climate variability index value and positive values of regression coefficient mean increase of precipitation event with increases of index value.

Index Nino1+2 show that, in northern parts of WCSA, there are no significant values, but the central and southern parts show a positive regression. This suggests that total and extreme precipitation increases with "El Niño". Furthermore, Index DMI shows the same situation in

index Nino1+2 but with a considerable positive regression. These values of positive regression are larger in the southern region, compared to the central region of WCSA. Finally, Index NAO-Jones shows relatively reversed results where it in the central and some parts of the southern regions has negative regression values. The negative values in the northern region are present but are relatively small with respect to the central region.

Indices	area_1	area_2	area_3	area_4	area_5	area_6	area_7	area_8	area_9	all areas	
NAO-Jones	-0.04	-1.21	-2.36	-2.75	-3.09	-2.10	-0.72	-0.34	-0.48	-1.45	total precipitation
Nino1+2	6.53	6.70	6.00	5.06	2.36	1.86	0.04	-0.22	0.00	3.15	
DMI	26.09	27.94	26.57	17.84	7.33	4.11	-0.55	-1.94	-1.47	11.77	
	area_1	area_2	area_3	area_4	area_5	area_6	area_7	area_8	area_9	all areas	
NAO-Jones	0.11	0.23	-0.32	-0.78	-0.95	-0.36	0.00	-0.27	-0.27	-0.29	extreme events
Nino1+2	1.06	2.06	1.78	1.56	1.01	0.48	-0.04	-0.07	-0.14	0.86	
DMI	4.33	8.19	7.78	5.97	3.53	1.24	-0.51	-0.67	-0.98	3.21	

Table 6-4. The regression coefficient for 9 model grid point areas with Nino1+2, DMI and NAO-Jones indices in total and extreme precipitation days in wet season during the 30 years.

6.7.2. Teleconnection between WCPs and large scale climate variability modes:

In order to investigate the relationships between large scale atmospheric phenomena and the weather circulation patterns which play an important role in extreme precipitation events, the most important three climate variability indices (Nino1+2, DMI and NAO-Jones) were examined. These were extracted from Table 6-3 findings and applied this investigation. Table 6-5 shows the values of the regression coefficient for the anomaly of each WCP occurrence with Nino1+2, DMI and NAO-Jones indices in total and extreme precipitation days in the wet season period during the 30 years.

Indices	WCP01	WCP02	WCP03	WCP04	WCP05	WCP06	WCP07	WCP08	WCP09	WCP10	WCP11	WCP12	
NAO-Jones	0.27	-0.02	-0.27	-0.08	0.06	-0.07	-0.17	-0.20	0.04	-0.15	-0.30	0.02	
Nino1+2	0.14	0.25	0.50	0.13	0.05	-0.11	0.24	-0.20	-0.01	0.15	0.30	0.28	total precepitation
DMI	0.97	0.34	1.36	0.44	0.82	0.06	0.99	-0.27	0.76	0.74	0.62	1.02	
	WCP01	WCP02	WCP03	WCP04	WCP05	WCP06	WCP07	WCP08	WCP09	WCP10	WCP11	WCP12	
NAO-Jones	0.07	-0.12	-0.27	-0.15	-0.06	-0.08	-0.07	-0.18	0.10	-0.09	0.00	-0.21	
Nino1+2	0.20	0.27	0.48	0.36	0.27	-0.13	0.68	-0.22	0.10	-0.01	0.00	0.05	extreme events
DMI	1.13	0.22	1.34	0.73	1.38	-0.30	1.67	-0.26	1.10	0.54	0.00	0.67	

Table 6-5. The regression coefficient for the anomaly of WCPs occurrence with Nino1+2, DMI and NAO-Jones indices in total and extreme precipitation days in wet season during the 30 years.

Overall, the results are similar between total precipitation days and extreme days. WCP8 and WCP6 have a small negative regression values with all indices. These values are not significant but are still relatively reasonable. Conversely, the result of the regression coefficient with WCP1 is positive with a positive significant value in DMI index. This positive significant value of DMI index is also associated with WCP7, WCP3 and WCP5. In addition, WCP7 and WCP3 have positive significant with Nino1+2 index.

In addition to the regression coefficient between the WCPs and these three indices, the influence of these indices phases (negative and positive) on the distribution of WCPs occurrence have been investigated, as shown in Table 6-6. Positive NAO index is associated with high percentage of occurrence of WCP1, WCP10 and WCP12, while negative NAO index is associated with WCP8, WCP6 and WCP3. In Nino index, WCP1, WCP4 and WCP12 is associated with a positive phase of ENSO and conversely, negative Nino1+2 index is associated with WCP2, WCP3, WCP7, WCP8 and WCP9. These percentage distributions, in ENSO, remain the same with the majority of WCPs in positive and negative DMI index, but the opposite it true in WCP1 and WCP12, in addition WCP3 and WCP9 have the same percentage.

		WCP01	WCP02	WCP03	WCP04	WCP05	WCP06	WCP07	WCP08	WCP09	WCP10	WCP11	WCP12	
+	NAO-Jones	10%	1%	4%	9%	1%	0%	5%	3%	4%	4%	0%	5%	
-	NAO-Jones	3%	3%	8%	8%	4%	5%	6%	14%	3%	0%	0%	0%	
+	Nino1+2	10%	0%	4%	12%	3%	1%	4%	3%	0%	3%	0%	4%	extreme events
-	Nino1+2	3%	4%	8%	5%	3%	4%	8%	14%	6%	1%	0%	1%	
+	DMI	8%	0%	5%	4%	3%	1%	4%	3%	3%	3%	0%	4%	
-	DMI	4%	4%	5%	10%	3%	3%	8%	14%	3%	1%	0%	1%	

Table 6-6. The distribution of WCPs occurrence with Nino1+2, DMI and NAO-Jones indices for extreme precipitation days in wet season during the 30 years.

6.8.   Summary:

In this chapter, EOF analysis of MSLP fields was used for daily ERA-Interim reanalyses data to classify synoptic circulation patterns conducive to extreme precipitation events along the west coast of Saudi Arabia. This was done for the wet season from 1985 to 2014. Moreover, daily precipitation observations were used to identify the individual extreme events for each station. In addition, ERA-Interim reanalysis precipitation was used to identify extreme event days for respective grid points along the west coast of Saudi Arabia to be compared with observation data.

In addition to the subjective analysis undertaken in the previous chapter, the objective classification of weather circulation pattern based on six EOFs of daily mean sea level pressure used for this study produced 12 WCPs for all days during the wet season. The distribution of these 12 WCPs are categorised to three distribution groups; one for all wet season days (2700 days), second for total precipitation days (441 days) and third for extreme precipitation days (79 days). The pattern of all WCPs which were based on all wet season days, precipitation days and extreme event days are similar and the difference is in the value of MSLP and its normalised anomalies. Where the result of the difference between all wet season days to extreme events show that the anomaly value of low pressure decreases and the value of the

high pressure increases in the WCPs which are associated with extreme event days. Furthermore, in most of these WCPs, the strong negative normalised MSLP anomaly is centred over the south of Red Sea, except in WCP7, which is located over the centre of Red Sea.

Extreme precipitation events occur during 11 WCPs. Five patterns (WCP4, WCP8, WCP1, WCP7 and WCP3) constituted the largest percentage of weather patterns associated with extreme events when WCPs are classified by precipitation dataset, based on observed station data. On the other hand, when WCPs are identified based on the ERA-Interim reanalysis precipitation dataset, the highest frequency of these classes were just in four weather patterns associated with extreme precipitation events (WCP4, WCP8, WCP1 and WCP3). Although there are no extreme events associated with WCP11 in data which is based on observed data, WCP11 was found in the analysis of extreme event days that refer to the ERA-Interim reanalysis precipitation dataset. However, WCP4, WCP8, WCP1 and WCP3 occur more frequently and are the most important, while the other eight patterns (WCP2, WCP5, WCP6, WCP7, WCP9, WCP10, WCP11 and WCP12) have a lower percentage of occurrence that are around or do not exceed 5% of the total days of extreme precipitation for each pattern. However, these eight WCPs are important because some of these patterns have a rare synoptic dynamic, such as WCP5 which represents the RSL. In addition, all of these 12 WCPs were represented by individual extreme events and some of them have similar characteristics.

In addition, the most extreme events, which are associated with class WCP6, WCP7 and WCP8, occur in November, and class WCP1, WCP2, WCP9 and WCP12 occur in January and December, while extreme events which are associated with class WCP3, WCP4, WCP5 and

WCP10 occur in all three months equally. Moreover, the percentage distribution of frequency and amount for each WCP in extreme events at each station show that the extreme rain associated with WCP4 is less severe than for WCP8. Furthermore, the most extreme events in the central and northern regions of WCSA are associated with WCP3, WCP4, WCP7 and WCP12, in the southern region with WCP2, WCP6, WCP9 and WCP10, while WCP1, WCP5 and WCP8 are associated with extreme events in all regions along the WCSA, but the WCP8 more in northern and central regions and WCP1 with more in southern region.

Therefore, 11 cases of subjective analysis, which are investigated in the previous chapter (Chapter 4), are taken as examples for each one of these 11 WCPs to evaluate this objective classification in order to assess the work of EOF with individual extreme events. Each of the 11 case studies is classified in one of the WCPs. The subjective comparing between the each synoptic chart of WCP and each synoptic chart of the case study show that the classifications are relatively reasonable and useful. For this concept, the 11 cases were classified as follows; Case 1 represents a paradigmatic example of an ARST process, where the study found that the strong RST shifts east to meet the LL over the Levant is classified as WCP4. Case 2 represents WCP7, where the SH has control over the AP and SL stretches over the Red Sea and Egypt. Case 3 represents WCP12, where RSL is produced over the Red Sea. Case 4 is classified as WCP10, the RST axis did not exceed further than the central WCSA. Case 5 is categorised as WCP8, a wide RST extends along the Red Sea between a strong NAH and SH. Case 6 is classified as WCP2, a low system AL forms over the southern AP. Case 7 represents WCP3, this pattern is categorised as ARST and is similar to WCP4 but RST here extends to the northwest of the AP and meets the ML over the Mediterranean Sea to form the ARST. Case 8 is classified as WCP6. In Case 9, RST is present between the NAH and the SH, but it expands inside the AP to the east because of the weakness of SH and the deep NAH, and this case is

147

classified as WCP1. Case 10 represents WCP5, where RSL is also produced over the Red Sea as WCP12, but here it is more intensive. In Case 11, which is classified as WCP9, the RST is absent because of the high pressure system that controls the weather over the AP.

Teleconnection between the total and extreme precipitation values and the large scale climate modes (ENSO, NAO and IOD) has been investigated by 10 climate variability indices (NAO-Jones, NAO-station, NAO-CPC, SOI, ESPI, Nino1+2, Nino3.4, Nino4, MEI and DMI). Study of the correlation between the precipitation values and the large scale climate modes has slightly changed between the observation data and model grid point data along whole WCSA, and also between the total precipitation and extreme events values.

However, the correlations between El-Nino and ODI and extreme precipitation events have a strong positive correlation over the southern and some parts of central WCSA areas, while a weak correlation appears over the northern part specifically with Nino1+2 index where the negative correlation between ODI and northern areas was observed. Conversely, the correlation between ENSO and extreme precipitation events has a strong positive correlation over the northern and some parts of central WCSA areas while a weak correlation appears over the northern region. This distribution of correlation results were also similar to the regression coefficient values.

Furthermore, relations between the large scale climate modes (ENSO, NAO and IOD) and the WCPs, which are associated with extreme precipitation, were investigated. WCP8, WCP2 and WCP6 are associated with a negative correlation to all these three indices, while WCP1, WCP10 and WCP12 are associated with a positive phase of these indices. WCP3 is associated with negative NAO and Nino and WCP7 is associated with negative DMI and Nino, while WCP4

is associated with negative DMI and positive Nino. WCP5 is associated with negative NAO and WCP9 with negative Nino.

These classifications and findings should help to improve predictions of the impact of climate change on extreme precipitation events over this area. Further studies should be undertaken to investigate climate change on extreme events over the West Coast of Saudi Arabia.

Chapter 7. ASSESSMENT OF FUTURE PROJECTIONS

7.1.   Overview:

In this chapter, the output of regional climate change projections from CORDEX-Africa and CORDEX-MENA domains are used to investigate the impact of high greenhouse gas emission scenarios (RCP8.5 scenario) on the behaviour of future precipitation over the Red Sea coast. This is specifically with respect to extreme events in the wet season. In this section, monthly averages of daily precipitation on wet days are used to compare the historical simulated data reference period (1976 to 2005) with a future period (2070-2099), following climate change projections. Additionally, the difference between the historical simulated data and the future projected climate change for other meteorological variables (mean sea level pressure MSLP, GPH at 500hPa and wind speed at 200hPa) will be investigated.

First, the precipitation change is investigated by means of 23 climate change experiments from the CORDEX-Africa domain and three climate change experiments over CORDEX-MENA domain. These 26 climate change experiments consist of different regional climate models which are nested into different GCMs. These investigations are conducted for individual experiments in addition to a Multi Model Ensemble Mean perspective. The latter is achieved by averaging over all individual precipitation change signals for all experiments in each domain.

Second, variables from the CORDEX-MENA domain were analysed and the mean changes investigated. These variables play an important role in the dynamics of the atmosphere (i.e., MSLP, GPH at 500hPa and wind speed at 200hPa, etc.). Again, the analysis was performed for individual experimental models as well as for Multi-Model Ensemble Mean (MMEM) changes.

In general, the MMEM method outperformed the individual models (Nikulin et al., 2012) because it is a reliable method for decreasing the uncertainties in climate change studies (Reichler and Kim, 2008). It was carried out by reducing the biases in climate change simulations to increase the creditability of future projections of precipitation (Li et al., 2016). This method is very important in this study because just four RCM simulations of nine RCMs had reasonable correlation values with ERA-Interim reanalysis data (around 0.5) in total precipitation events and the correlation values showed relatively poor performance in extreme precipitation events, as shown in Chapter 5.

Finally, an empirical orthogonal function (EOF) analysis is performed for MSLP to identify the variations in weather circulation patterns (WCPs) during the wet season (November through January) over the CORDEX-MENA domain. The difference between WCPs in the historical simulation scenario and WCPs in the RCP8.5 scenario is calculated and documented in this analysis and conclusions will be drawn in contrast to objective and subjective results presented in Chapters 4 and 6.

In the previous chapter (Chapter 5), an evaluation of the output of the RCMs from CORDEX-Africa and CORDEX-MENA domains was performed. The evaluation determined that the outputs of 4 RCMs (CRCM5, HadGEM3-RA, HadRM3P and RACMO22T) from CORDEX-Africa are the best models of precipitation simulations, and the outputs of RCA4 regional climate model from CORDEX-MENA were the best models of MSLP simulation over the area of study. Unfortunately, when extracting the RCP8.5 experiments from CORDEX-Africa, the data were not available for some of these models. Therefore, the individual experiments and an ensemble average of all 23 experiments, which are available for this study will be used to calculate the percentage changes in the amounts of rainfall.

Table 7-1 shows the list of RCMs and GCMs used in this chapter. It includes the availability of information for each experiment (evaluation data, historical data and prediction data) and the shortened name of each experiment used in this chapter. It also shows that the RCP8.5 and historical data from experiments which have been downscaled by RCMs (CRCM5, HadGEM3-RI and HadRM3P) are not available, although their results were the best when they were evaluated in the previous Chapter (Chapter5).

7.2. Future Precipitation Projections by CORDEX-Africa data:

At first, focus is laid on mean average changes in precipitation: Figure 7.1 shows climate change signal (RCP8.5) of the multi model ensemble mean percentage changes over the west coast of the Arabian Peninsula in the number of total precipitation days, amount of total precipitation and amount of extreme precipitation events between future simulations (2070–2099) and historical period simulations (1976–2005) annually and for the wet season.

Based on the multi model ensemble mean annual perspective, the number of rainy days is simulated to decrease in the future climate scenario (RCP8.5). However, the amount of total precipitation will increase, as well as the amount of extreme precipitation. The northern regions show the greatest reduction in annual precipitation occurrences (25 to 35 percent), with slightly lower percentage changes in the southern regions. When focusing on the southern regions, the ensemble average change in the number of annual precipitation events indicates an increase in precipitation events, along with increasing amounts of precipitation over the narrow coastal area along the southern and central west coastline of the Red Sea. Conversely, the increase in the amount of maximum annual precipitation in the southern regions is around 35 to 45 percent. In the northern regions, this percentage decreased slightly (5 to 15 percent).

152

no.	RCM	Driving Global Model			
		Evaluation	Historical	rcp85	Experiment name
1	RCA4	ERAINT	NOAA-GFDL-GFDL-ESM2M	NOAA-GFDL-GFDL-ESM2M	NOAA-RCA4
2	REMO2009	ERAINT	NOAA-GFDL-GFDL-ESM2G	no data	----
3	HIRHAM5	ERAINT	NCC-NorESM1-M	NCC-NorESM1-M	NCC-HIRHAM5
4	RCA4	ERAINT	NCC-NorESM1-M	NCC-NorESM1-M	NCC-RCA4
5	CCLM4-8-17	ERAINT	MPI-M-MPI-ESM-LR	MPI-M-MPI-ESM-LR	MPI-CCLM4
6	RCA4	ERAINT	MPI-M-MPI-ESM-LR	MPI-M-MPI-ESM-LR	MPI-RCA4
7	REMO2009	ERAINT	MPI-M-MPI-ESM-LR	MPI-M-MPI-ESM-LR	MPI-REMO2009
8	CRCM5	ERAINT	MPI-M-MPI-ESM-LR	no data	----
9	CCLM4-8-17	ERAINT	MOHC-HadGEM2-ES	MOHC-HadGEM2-ES	MOHC-CCLM4
10	RACMO22T	ERAINT	MOHC-HadGEM2-ES	MOHC-HadGEM2-ES	MOHC-RACMO22T
11	RCA4	ERAINT	MOHC-HadGEM2-ES	MOHC-HadGEM2-ES	MOHC-RCA4
12	REMO2009	ERAINT	MOHC-HadGEM2-ES	MOHC-HadGEM2-ES	MOHC-REMO2009
13	RCA4	ERAINT	MIROC-MIROC5	MIROC-MIROC5	MIROC-RCA4
14	REMO2009	ERAINT	MIROC-MIROC5	MIROC-MIROC5	MIROC-REMO2009
15	RCA4	ERAINT	IPSL-IPSL-CM5A-MR	IPSL-IPSL-CM5A-MR	IPSL-RCA4
16	REMO2009	ERAINT	IPSL-IPSL-CM5A-LR	IPSL-IPSL-CM5A-LR	IPSL-REMO2009
17	CCLM4-8-17	ERAINT	ICHEC-EC-EARTH	ICHEC-EC-EARTH	ICHEC-CCLM4
18	HIRHAM5	ERAINT	ICHEC-EC-EARTH	ICHEC-EC-EARTH	ICHEC-HIRHAM5
19	RACMO22T	ERAINT	ICHEC-EC-EARTH	ICHEC-EC-EARTH	ICHEC-RACMO22T
20	REMO2009	ERAINT	ICHEC-EC-EARTH	ICHEC-EC-EARTH	ICHEC-REMO2009
21	RCA4	ERAINT	ICHEC-EC-EARTH	ICHEC-EC-EARTH	ICHEC-RCA4
22	RCA4	ERAINT	CSIRO-QCCCE-CSIRO-Mk3-6-0	CSIRO-QCCCE-CSIRO-Mk3-6-0	CSIRO-RCA4
23	CCLM4-8-17	ERAINT	CNRM-CERFACS-CNRM-CM5	CNRM-CERFACS-CNRM-CM5	CNRM-CCLM4
24	RCA4	ERAINT	CNRM-CERFACS-CNRM-CM5	CNRM-CERFACS-CNRM-CM5	CNRM-RCA4
25	RCA4	ERAINT	CCCma-CanESM2	CCCma-CanESM2	CCCma-RCA4
26	CRCM5	ERAINT	CCCma-CanESM2	no data	----
27	HadGEM3-RA	ERAINT	no data	no data	----
28	HadRM3P	ERAINT	no data	no data	----

Table 7-1. The list of regional climate models and global climate models used in this chapter.
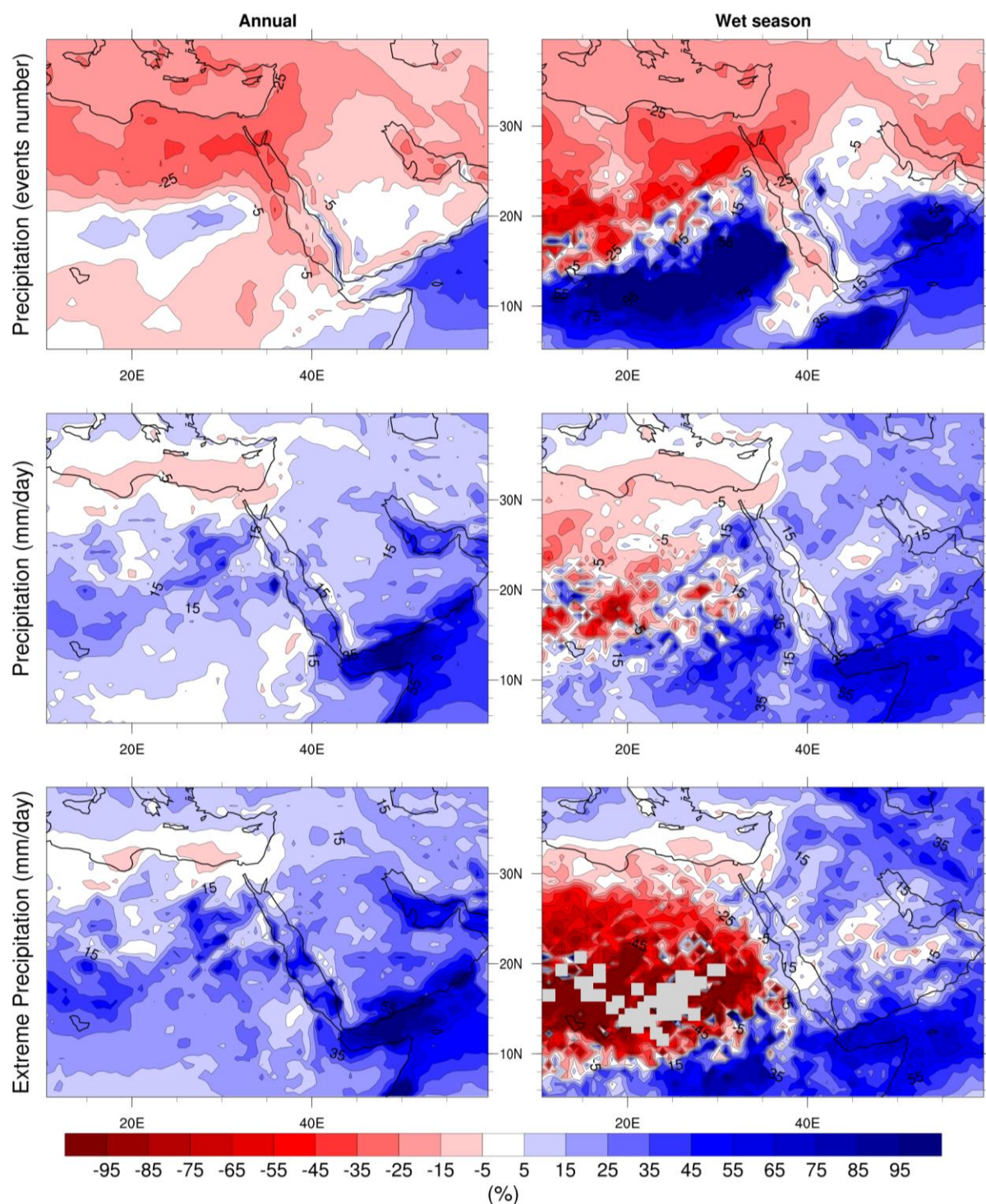
Figure 7.1. Climate Change signal (RCP8.5) of the multi model ensemble mean between the number of precipitation events (top two), mean precipitation amounts (middle two) and mean extreme precipitation amounts (bottom two) in future simulations (2070–2099) and historical period simulations (1976–2005) annually (left) and for the wet season (right). Units are percentages of present mm/day values. Grey areas indicate that the amount of rain is less than 0.1 mm/day.

A further analysis with a greater focus on the wet season revealed further interesting findings:

the number of rainy days are decreased in the northern regions and increased in the South.

154

Findings for the future time period also show that the amount of precipitation increased in some regions, especially in many northern and central coastal areas (around 5 to 15 percent) and decreased in parts of the southern region (around 5 to 15 percent). Additionally, the amount of precipitation in the southernmost portion of the Arabian Peninsula was increased by around 20 percent. However, this number is still less than the annual percentage change.

When comparing the total precipitation changes of wet season to changes of the annual total precipitation amounts, this is a small positive change in the amount of precipitation during the wet season. This is because of the main rainfall season over this region during the summer (dry season), which is affected by Indian monsoons. The extreme precipitation events in the dry season are not included in this study.

Focussing on extreme precipitation only (here again defined as the amount of precipitation above the 90th percentile, bottom two panels of Figure 7.1), this illustrates that annually, an increase of approximately 15 to 35% in the amounts of extreme precipitation along the southern and central coastline is projected. This positive change is slightly reduced (around 0 to 15 percent) in the northern regions along the coastline, while there is no significant impact on extreme precipitation amount in small parts of the northern region.

Further analysis of extreme precipitation shows that a slight decrease in the estimated positive changes from the northern to the southern regions along the coastline is evident in the wet season. Large positive changes in extreme precipitation occur over the northern region with increased values up to nearly 25%, while in some parts of the central and southern coastal areas this increased between 5 to 15 percent. Furthermore, there are two small areas that obtain some small negative changes in extreme precipitation amounts. One of these two

areas is between the northern and central regions and the second is between the central and southern regions.

7.2.1. Model-To-Model Variability in Wet Season (Spread in the Ensemble):

In order to focus on projected precipitation amounts in the wet season of the CORDEX-Africa domain, this section of the study investigates the percentage of change in total precipitation and the extreme precipitation amounts for individual models of 23 experiments in the CORDEX-Africa domain. The percentages of precipitation changes in the wet season are discussed individually and in detail for each experiment. The main sources of uncertainty in climate change projections are the coarse resolution of GCM, uncertainty of emissions scenarios, the formulation of the RCMs and the natural variability (Fronzek et al., 2012). However the uncertainty of natural variability and RCMs can be addressed by employing a multi-model ensemble approach (Jacob et al., 2014).Figure 7.2 shows the difference (in percentage) in total precipitation amounts between a future prediction (2070–2099) and historical simulations (1976–2005) for the 23 individual experiments in CORDEX-Africa. It also shows the change in the multi-model ensemble mean percentage.

The ensemble is characterised by a remarkable model-to-model variability leading to a large spread in the projected precipitation amounts in the 23 experimental simulations. Some of the models simulate a strong decrease in precipitation in all parts of the Red Sea region (e.g., CSIRO-RCA4, ICHEC-HIRHAM5, MIROC-RCA4 and MPI-REMO2009). Some other models project an increase in precipitation in the northern regions and a decrease in the southern regions (e.g., CNRM-CCLM4, ICHEC-RACMO22T and MOHC-REMO2009). However, the ICHEC-CCLM4 and MOHC-RACMO22T experiments are more comparable to ensemble mean changes in these models, as indicated in the bottom right corner of Figure 7.2.

156

For extreme precipitation events (Figure 7.3), most experiments simulate the percentage changes in the amounts of extreme precipitation as the percentage changes in the amounts of total precipitation in previous results, shown in Figure 7.2, but with more missing data and also intensified change in the precipitation signal. This means that the positive change in extreme precipitation amounts are higher than the positive change in total precipitation amounts. Similarly, it also shows that the negative change in extreme precipitation amounts are lower than the negative change in total precipitation amounts.
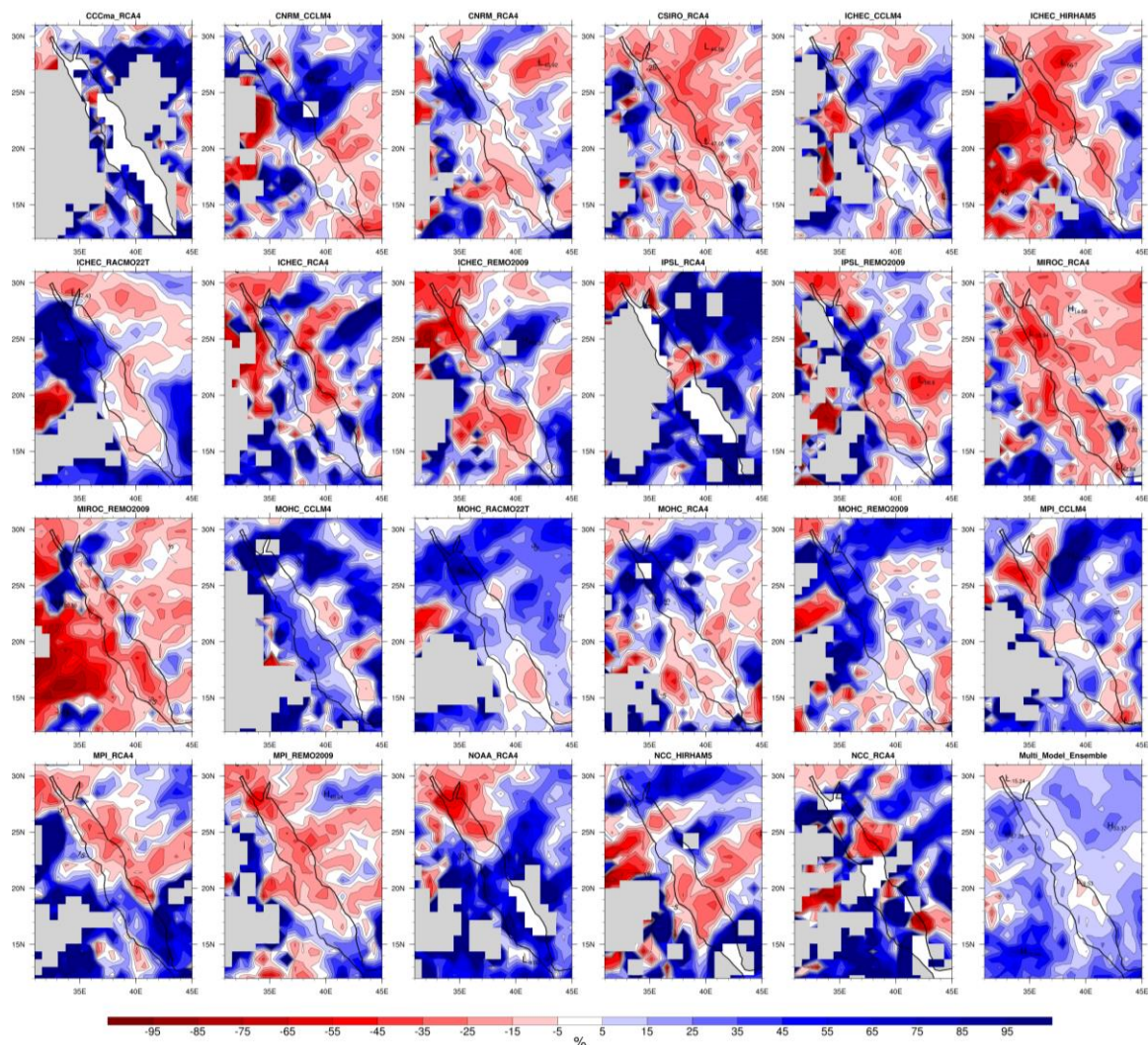
Figure 7.2. The difference (in %) for the amount of total precipitation between future prediction (2070 to 2099) and historical simulations (1976 to 2005) in the wet season for 23 experimental models and the multi model ensemble mean (right bottom corner). Units are percentages of present-day values. Grey areas mean that the amount of rain is less than 0.1 mm/day.

However, the MOHC-RACMO22T experiment is the closest and the most comparable one to the ensemble mean (bottom right corner of Figure 7-3). The ensemble mean percentage change in these models indicates a marked increase in the amount of extreme rainfall in most regions along the west coast. However, there is a decrease in some areas between the central and northern and the central and southern portions of the coastline.
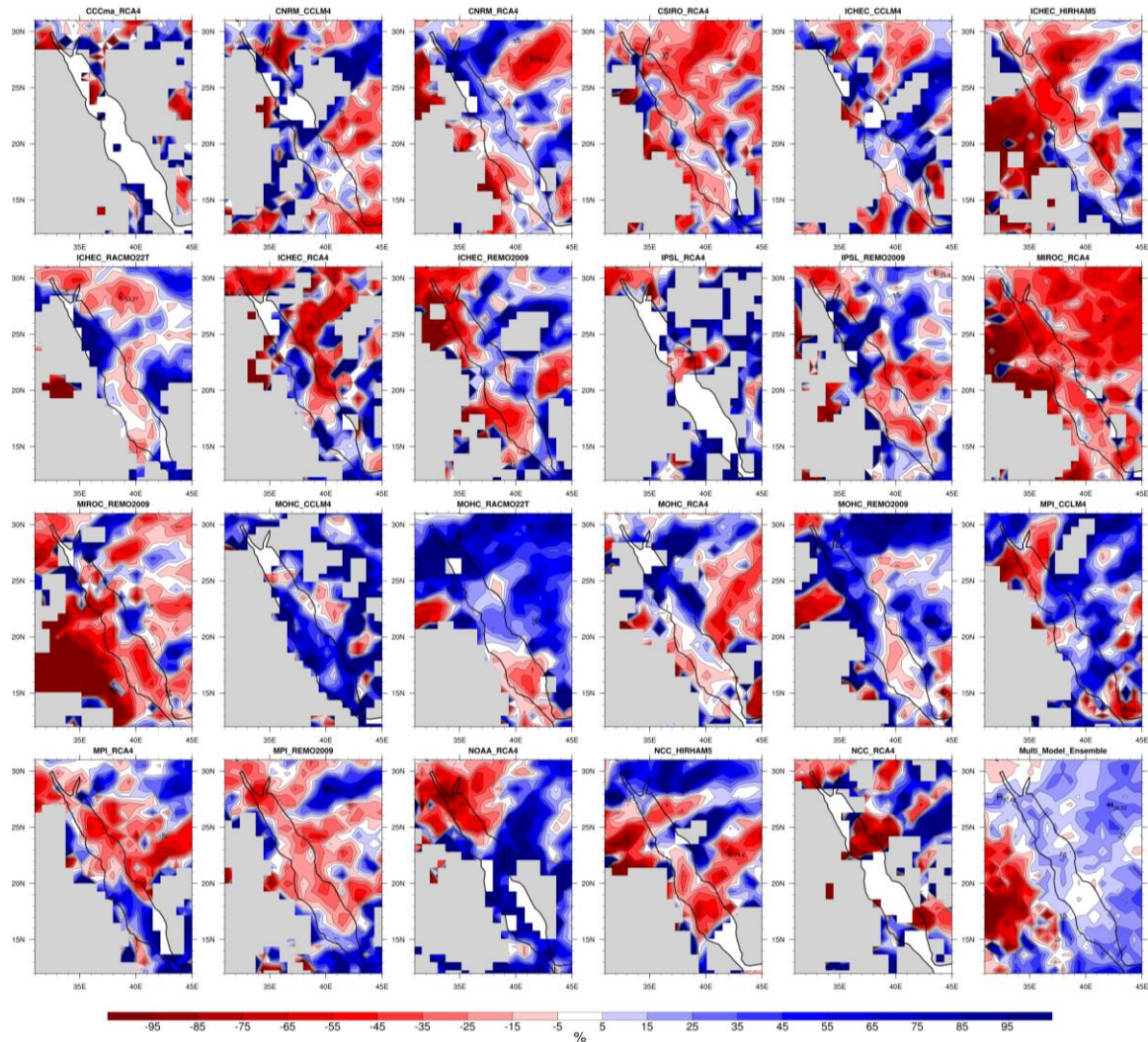
Figure 7.3. The difference (in %) for the amount of extreme precipitation events between future prediction (2070 to 2099) and historical simulations (1976 to 2005) in the wet season for 23 experimental models and the multi model ensemble mean (right bottom corner). Units are percentages of present-day values. Grey areas indicate that the amount of rain is less than 0.1 mm/day.

In order to determine the uncertainty between the values of total and extreme precipitation change of 23 regional climate models which were shown in Figure 7.2 and Figure 7.3, the

158

boxplot is used. This boxplot is produced by calculating minimum (10^{th}percentile), first quartile (25th percentile), median (50th percentile), third quartile (75th percentile) and maximum (90th percentile) for each point of 35 model grid points along the WCSA. Figure 7.4 and Figure 7.5 illustrate the uncertainty of total and extreme precipitation change in wet season over 9 areas along the WCSA (Figure 6.13), in addition to the average of whole areas along the WCSA under the climate change signal RCP8.5 scenario.
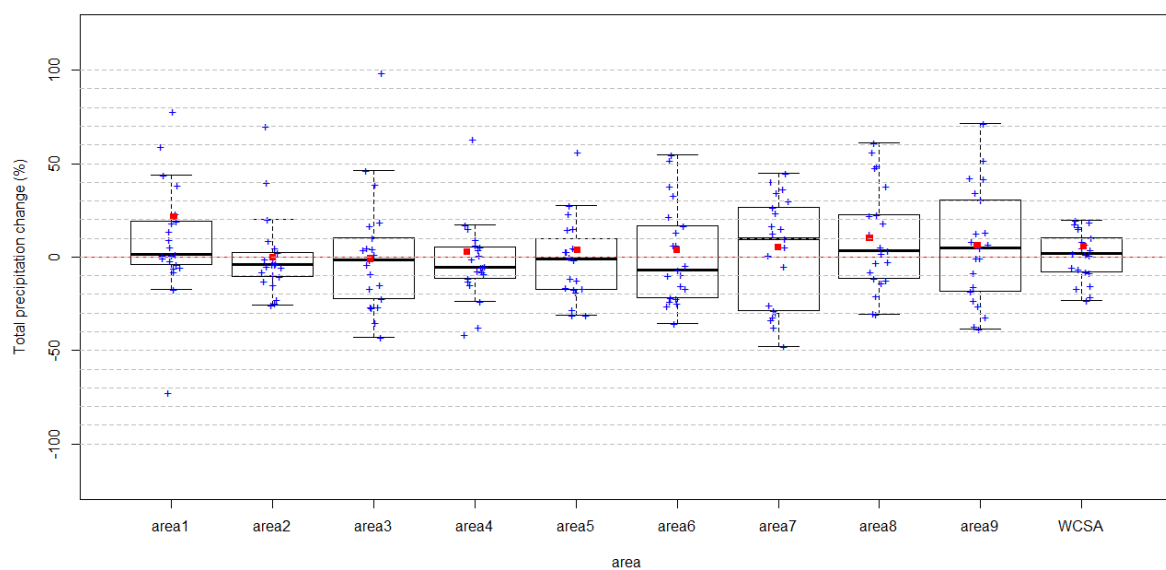
Figure 7.4. Uncertainty of total precipitation change in wet season over 9 areas along the WCSA in addition to the whole area of WCSA under the future climate scenario RCP8.5 scenario for the future periods 2070-2099 relative to reference historical simulation periods 1976 - 2005. Blue circles illustrate values of 23 experimental and red squares illustrates the value of the multi model ensemble mean.

The results show that the uncertainty in extreme precipitation change values is greater than total precipitation change values. The uncertainty in the total precipitation change values in the northern areas is larger than in the southern areas. The best result is in *area_2* and *area_4*. This result is relatively similar to the extreme precipitation change values but with a large uncertainty in all areas. However the uncertainty of these results of total and extreme precipitation change is large between these models, but when looking at the whole area along the WCSA the uncertainty is small.

159
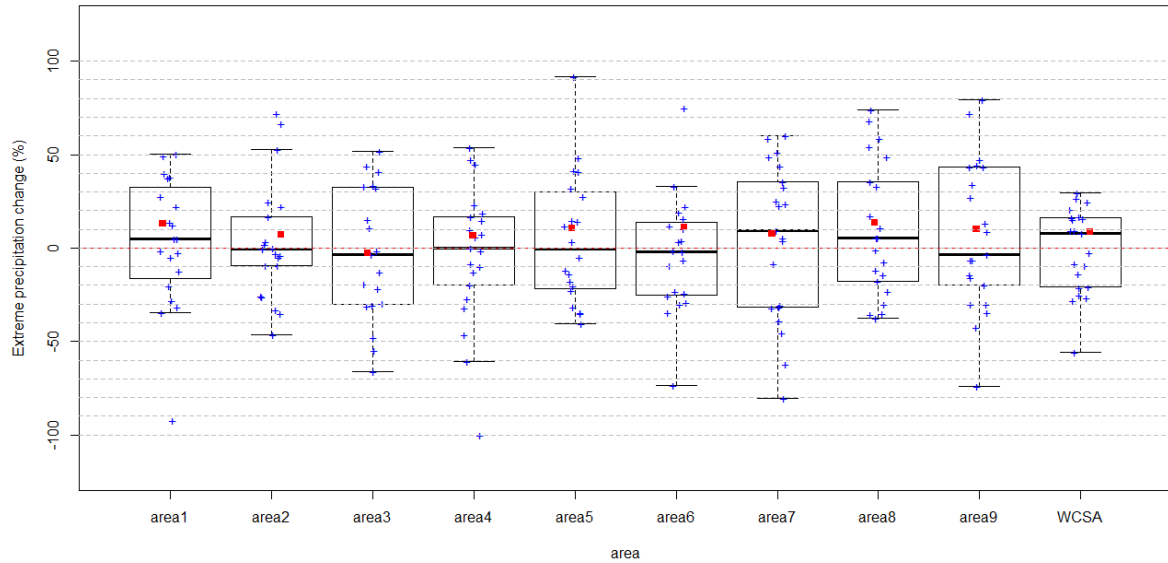
Figure 7.5 Uncertainty of extreme precipitation change in the wet season over 9 areas along the WCSA in addition to the whole area of WCSA under the future climate scenario RCP8.5 scenario for the future periods 2070-2099 relative to reference historical simulation periods 1976 - 2005. Blue circles illustrate values of 23 experimental and red squares illustrate the value of the multi model ensemble mean.

7.3.   Climate change projections from 3 experiments CORDEX-MENA:

A further analysis of projected precipitation in the wet season is investigated from CORDEX-MENA domain experiments. This domain covers the whole study area better than CORDEX-Africa. However, there are few experiments in CORDEX-MENA, so the previous section used CORDEX-Africa to estimate the future change in precipitation and it will also be used to assess the few results of projected precipitation that can be obtained from CORDEX-MENA. Projected precipitation results of individual model from CORDEX-MENA will be cambered with ensemble average of projected precipitation from CORDEX-Africa and with individual model from CORDEX-Africa to identify the best model of the three experiments in CORDEX-MENA.

The mean change of precipitation results will be examined in the three experiments available on the CORDEX-MENA domain, and the output of these three experiments are also used to study the mean changes of other atmospheric elements (Wind speed at 200hPa, GPH at

160

500hPa, MSLP). In addition, it carries out an empirical orthogonal function analysis of daily MSLP for individual experiments. The importance of using the CORDEX-MENA domain is that it covers the whole geographical window which was used to investigate dynamic processes of extreme precipitation events over WCSA in Chapter 4 and an EOF analysis in Chapter 6, thus making it easier to compare them. In addition to applying qualitative analysis on the same scale in the previous chapter this gives the result in this chapter more credibility.

7.3.1. Future changes in precipitation projected by CORDEX-MENA experiments:

Figure 7.6 shows the differences (in percentages) in total precipitation and extreme precipitation amounts between a future prediction (2070 to 2099) and historical simulations (1976 to 2005) annually and in the wet season for 3 experimental models from the CORDEX-MENA domain and the multi model ensemble mean percentage changes of these three models. In the annual results, the percentage changes of total precipitation amount are negative along the west coast of Arabian Peninsula in the CNRM-RCA4 experiments. This negative change shows a slight decrease from the northern to the southern regions along the coastline. Another noteworthy finding is that the percentage of precipitation change is negative in some parts of the northern region and positive in the southern region in the NOAA-RCA4 experiments. Additionally, the percentage of precipitation change is negative in the southern region and positive in the northern regions in the ICHEC-RCA4 experiments.

The ensemble average of the percentage changes of total precipitation amount of these experiments shows positive changes in almost all parts of the coastal regions, especially in the central region. However, there are small negative changes in some parts of the southern and northern regions, as shown in the ensemble average result of the 23 experiments in the CORDEX-Africa domain.

161
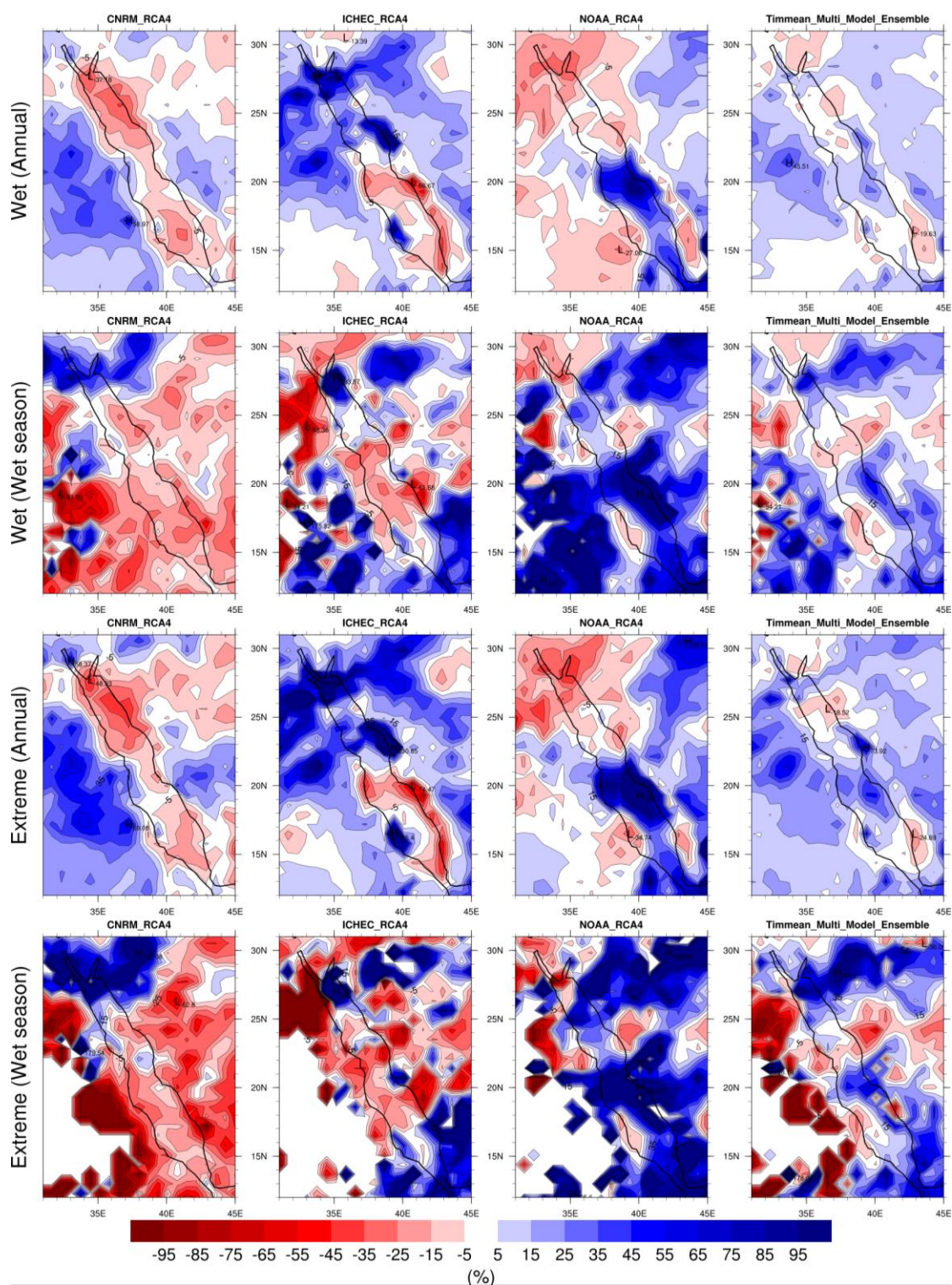
Figure 7.6. The difference (in %) between future prediction (2070 to 2099) and historical simulations (1976 to 2005) of the annual amount of total precipitation (top row), the amount of total precipitation in wet season (first middle row), the annual amount of extreme precipitation (second middle row) and the amount of extreme precipitation in wet season (bottom row) for 3 experimental models from the CORDEX-MENA domain (three column from left) and the multi model ensemble mean (rightmost column). Units are percentages of present-day values. Grey areas indicate that the amount of rain is less than 0.1 mm/day.

In the wet season, the results are quite similar to the annual values in all three experiments, but the negative change in the northern region did shift southwards. This area showed a negative change and produced the gap between the central and northern regions. However, the ensemble average of the future precipitation amount changes in these experiments increased in central, southern and northernmost of the coastal regions. This result is very similar to the ensemble average result of the 23 experiments in the CORDEX-Africa domain.

Similarly, the results between the experiments are different for extreme rainfall. An increase in the ensemble average change in these three models is projected over most regions along the west coast. However, there is a slight decrease in the area between the central and northern regions, in addition to the appearance of the other negative change gap between the central and southern regions. These two negative changes are similar to results that are projected in the ensemble average of CORDEX-Africa domain.

There is a large model-to-model variability of the future changes in projected total and extreme precipitation amounts in the 26 experimental simulations for the CORDEX-Africa and CORDEX-MENA domains, but the ensemble average of these experiments in the two domains showed more similarities. Regarding the average change of total ensemble models, the NOAA-RCA4 experiment from the CORDEX-MENA domain is the closest of any other experiment from either the CORDEX-Africa or CORDEX-MENA domains. Thus, in the next sections, other atmospheric elements (Wind speed at 200hPa, GPH at 500hPa, MSLP) will be investigated and obtained from CORDEX-MENA experiments data.

7.3.2. Future changes in wind speed projected at 200hPa by CORDEX-MENA:

The subtropical jet stream plays an important role to enhance precipitation especially in the middle east (de Vries et al., 2016) and South Asia (Iqbal et al., 2016). The extension of the

strengthening STJ from the Arabian Peninsula was found in band between 17° and 40° latitude which effects the Afghanistan and western Pakistan and has good a correlation with the wet winters by the regional climate model RCA4 which derived by ERA-Interim winds at 200hPa. In addition, (Abish et al., 2015) showed that the STJ has a noteworthy positive change in winter due to the warming as a result of climate change over South Asia. Figure 7.7 shows the percentage difference between a future prediction and historical simulations of mean wind speed change at 200hPa in the annual and wet seasons for the three experimental models from the CORDEX-MENA domain, along with the MMEM change.
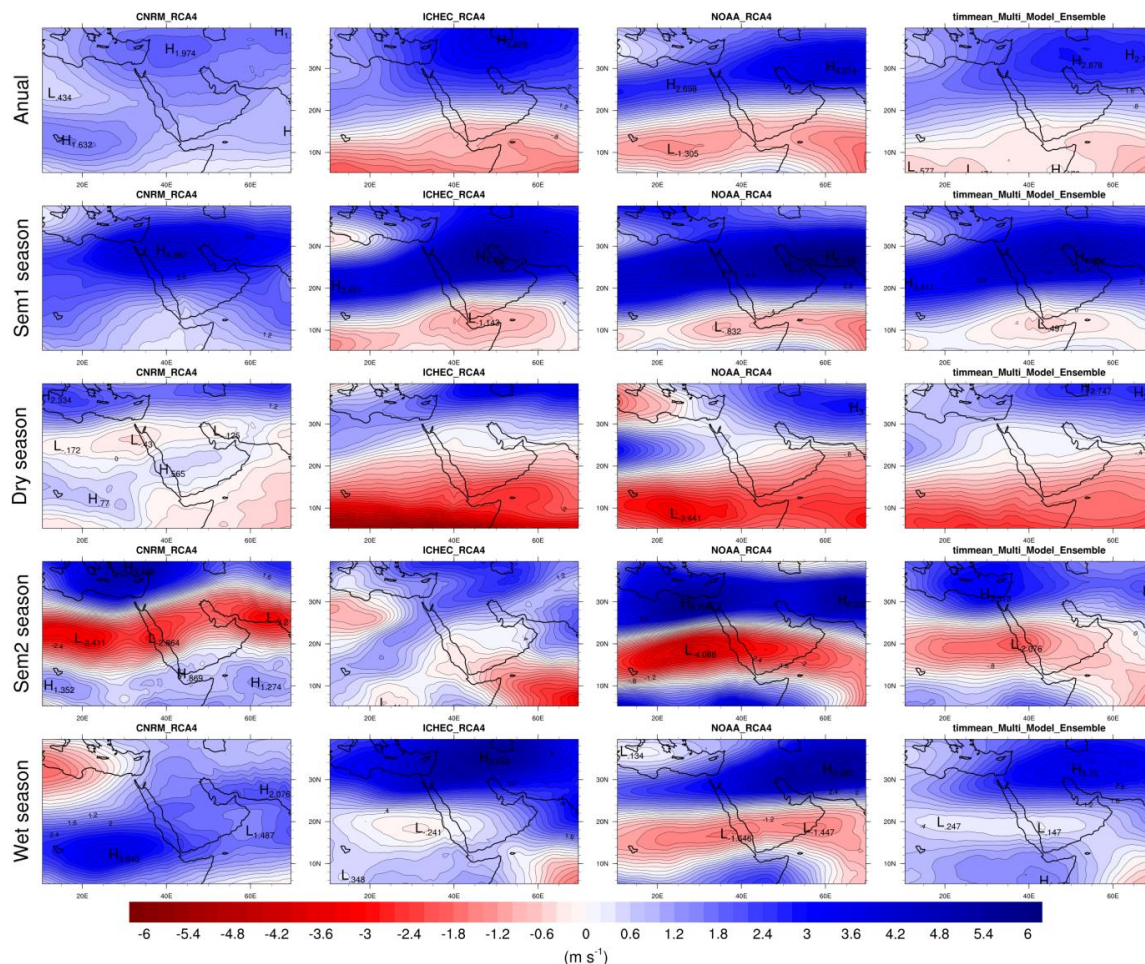
Figure 7.7. The difference between future data simulation (2070 to 2099) and historical data simulations (1976 to 2005) of annual and seasonal (wet season, sem1 season, sem2 season and dry season) mean wind speed changes at 200hPa for three experimental models from CORDEX-MENA domain, along with the multi model ensemble for each line. Units are in (m/s).

The NOAA-RCA4 and ICHEC-RCA4 experiments are similar and display the positive change of mean western wind speed at 200hPa in the upper atmosphere, especially in the northern part of the Red Sea. Additionally, the positive change in wind speed was also increased in all seasons. The most notable increases are in the Sem1 and Sem2 seasons, which occur before and after the wet season (for definition see Chapter 4). In the results, the MMEM change of wind speed shows an increase over the northern Red Sea region and Arabian Peninsula in the wet season.

7.3.3. Future changes in GPH projected at 500hPa by CORDEX-MENA:

Figure 7.8 shows the percentage of difference between the mean geopotential height at 500hPa in a future data simulation (2070 to 2099) and historical data simulations (1976 to 2005), both annually and in the wet season for three experimental models from the CORDEX-MENA domain, along with the average change of experiments ensemble.

The ensemble mean changes in geopotential height at 500hPa in climate change projections are constantly positive in these findings. This is caused by climate warming, which is expected in the future climate scenarios, this warming makes the atmosphere thicker, below 500hPa geopotential height. For a review of assessment of global climate change model simulations see (Giorgi and Lionello, 2008).

In the wet season, as represented by MMEM change, the low geopotential is pronounced above Turkey and the Levant as a trough, and it extends between two high geopotential. One of these highs is situated over the Mediterranean Sea and the second is over Iran. In the Sem1 season, the trough is deeper and covers a large area of the north Arabian regions. Persistent cyclone over Turkey and the Levant advects more cold air from the Polar Regions into the

Arabian Peninsula, which plays an important role in improving precipitation in the wet season over the study area.
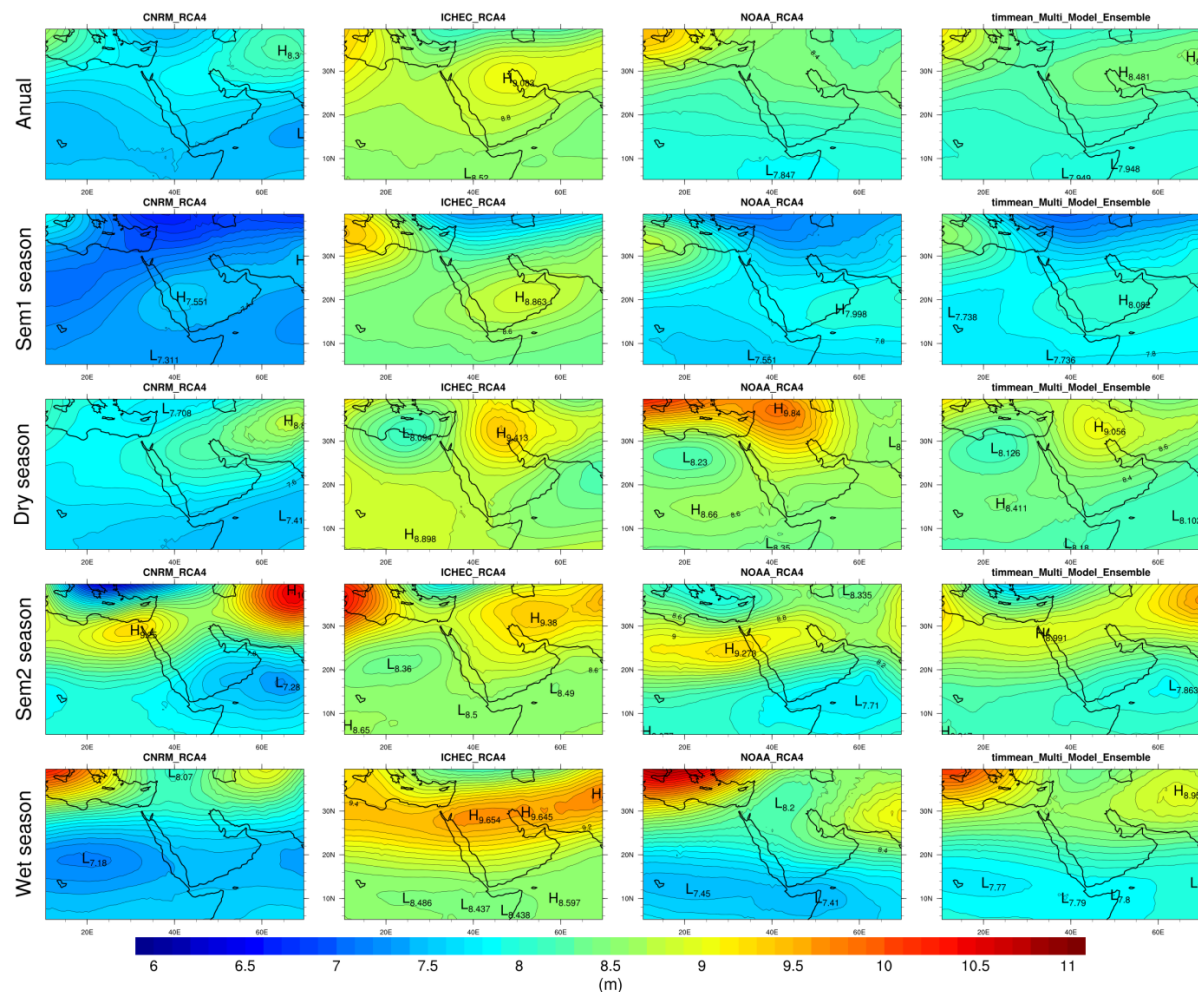
Figure 7.8. The difference between future data simulation (2070 to 2099) and historical data simulations (1976 to 2005) of annual and seasonal (wet season, sem1 season, sem2 season and dry season) mean geopotential height changes at 500hPa for three experimental models from CORDEX-MENA domain, along with the multi model ensemble for each line. Units are in (m).

7.3.4. Future changes in MSLP projected by CORDEX-MENA:

In this section, I focus on the future changes in MSLP projected because MSLP is responsible for the WCPs used in Chapter 6. The ensemble average changes in MSLP will be investigated under the influence of greenhouse gas emissions. Figure 7.9 shows the percentage of the difference between MSLP in a future data simulation (2070 to 2099) and historical data simulations (1976 to 2005) for rainy days and extreme precipitation events annually and in

the wet season for three experimental models from the CORDEX-MENA domain, along with the average change of experiments ensemble.
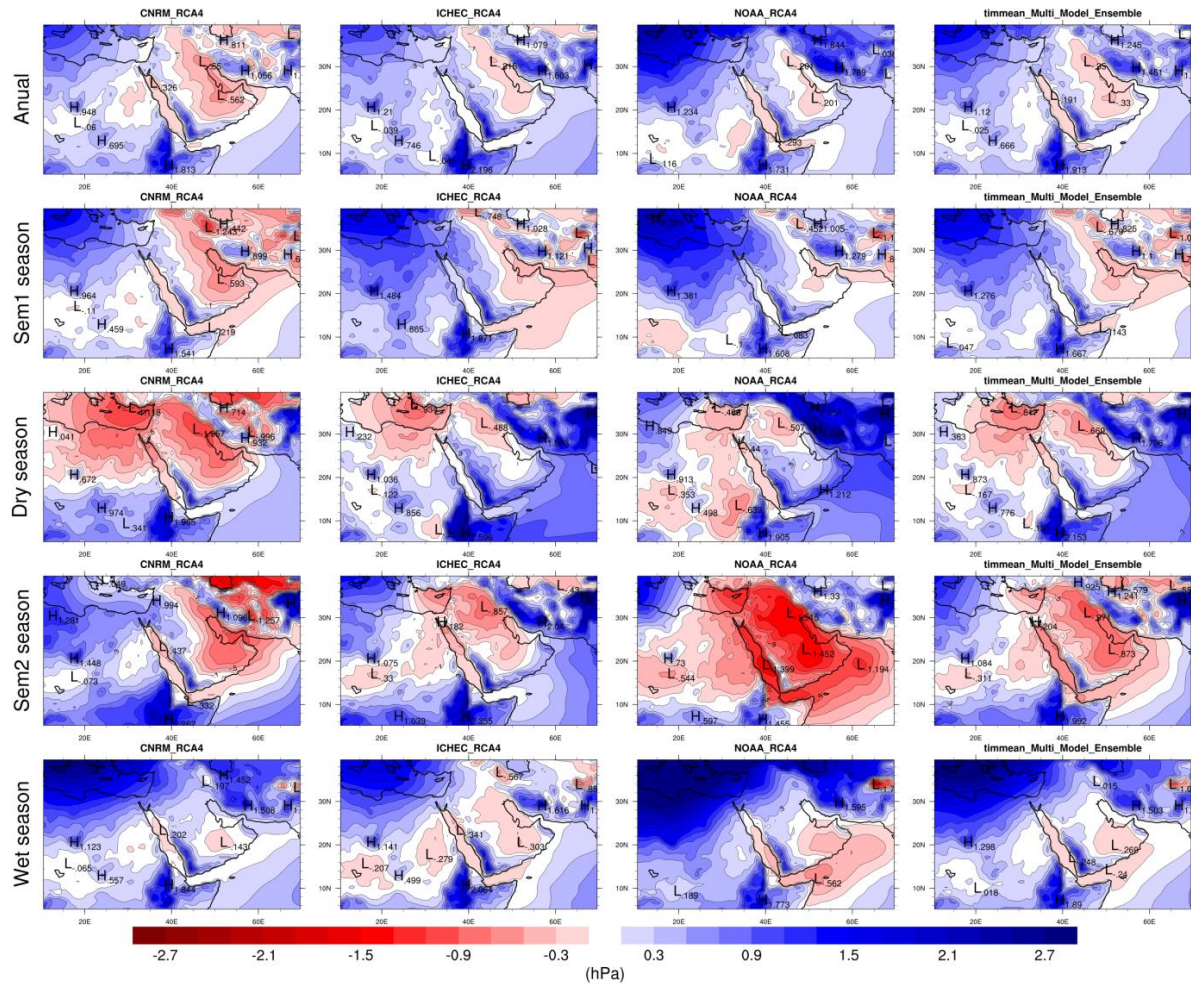
Figure 7.9. The difference between future data simulation (2070 to 2099) and historical data simulations (1976 to 2005) of annual and seasonal (wet season, sem1 season, sem2 season and dry season) MSLP changes for three experimental models from CORDEX-MENA domain, along with the multi model ensemble for each line. Units are in (hPa).

There is a significant positive change in the ensemble average in MSLP over the Mediterranean Sea and North Africa, along with a clear reduction of MSLP over the Red Sea annually and in all seasons. However, the dry season is an exception. Additionally, the largest reduction in average change occurred in the Sem2 season. These slight changes in MSLP may affect the distribution of WCPs with rainfall and associated extreme rainfall, which will be analysed and investigated in the next section.

167

7.4.   EOF of MSLP in CORDEX-MENA experiments:

In order to investigate the weather circulation patterns of WCPs under future climate change, the EOF analyses were applied by MSLP projected from CORDEX-MENA experiments. Figure 7.10 shows the six leading EOF patterns for all wet season days (2760 days) for the daily MSLP historical simulations (1976–2005) from the CORDEX-MENA experiments in three driving GCMs (ICHEC, CNRM and NOAA). Figure 7.11 shows the six leading EOF patterns for all wet season daily MSLP future predictions (2070–2099). The distribution of the six orders of EOFs shows a slight difference between the orders of the EOFs based on MSLP from CORDEX-MENA experiments and the orders of the EOFs which were employed by the ERA-Interim reanalysis data (1985–2014) studied in Chapter 6 (Figure 6.1). However, the long-term natural variability of the climate system is one of the most important sources of uncertainty in future climate scenarios and is dependent on prediction length (Nolan et al., 2017). In the first few decades, the uncertainty generated from natural variability is largest in projected climate change (Strandberg et al., 2015).

The EOF patterns which are derived from experimental data (historical simulations and RCP8.5 predictions) are comparatively similar with the EOF patterns from ERA-Interim reanalysis data. Nevertheless, there are different amounts of explained variance in the ERA-Interim reanalysis data where these variance values affected the EOFs order. However, the orders for the EOF 1 and EOF 2 patterns are not affected. The EOF 1 and EOF 2 patterns, which are derived from historical data simulations, displayed the following values: 20.4 percent and 16.7 percent for ICHEC, 23.4 percent and 15.8 percent for CNRM and 18.0 percent and 17.8 percent for NOAA. These results, derived from ERA-Interim reanalysis data over the 1985 to 2014 period, are relatively similar to the EOF 1 and EOF 2 patterns, with a slightly lower

explained variance of 18.7 percent and 13 percent, respectively. In addition, the EOF 1 and EOF 2 patterns, derived from RCP8.5 prediction data, displayed the following values: 20.7 percent and 18.6 percent for ICHEC, 24.2 percent and 15.5 percent for CNRM and 20.4 percent and 18.9 percent for NOAA.

However, the order of the EOF 3, EOF 4, EOF 5 and EOF 6 patterns, which is derived from experimental data, is different than the order derived from ERA-Interim reanalysis data in Chapter 6. Although the patterns are similar, the positions have changed because the values of explained variance have changed. For example, the explained variances in the EOF 5 and EOF 6 patterns in the historical simulation in the NOAA experiment are 12.6 percent and 12.3 percent, respectively. These two EOF patterns are similar to the EOF 6 and EOF 5 patterns in the ERA-Interim reanalysis data. The explained variance is obvious —around 9.8% in EOF 6 and 12.9% in EOF 5. Additionally, these variance amounts are different from other experimental results.

Consequently, the WCPs, which are associated with EOFs from experimental data, will be reordered to be similar with the WCPs that were observed in the ERA-Interim reanalysis data in Chapter 6. From this perspective, for example, the WCPs for historical simulations in the NOAA experiment can be defined as follows: WCP1 and WCP7 are generated by EOF 1, WCP2 and WCP8 are generated by EOF 2, WCP3 and WCP9 are generated by EOF 4, WCP4 and WCP10 are generated by EOF 3, WCP5 and WCP11 are generated by EOF 6 and WCP6 and WCP12 are generated by EOF 5.
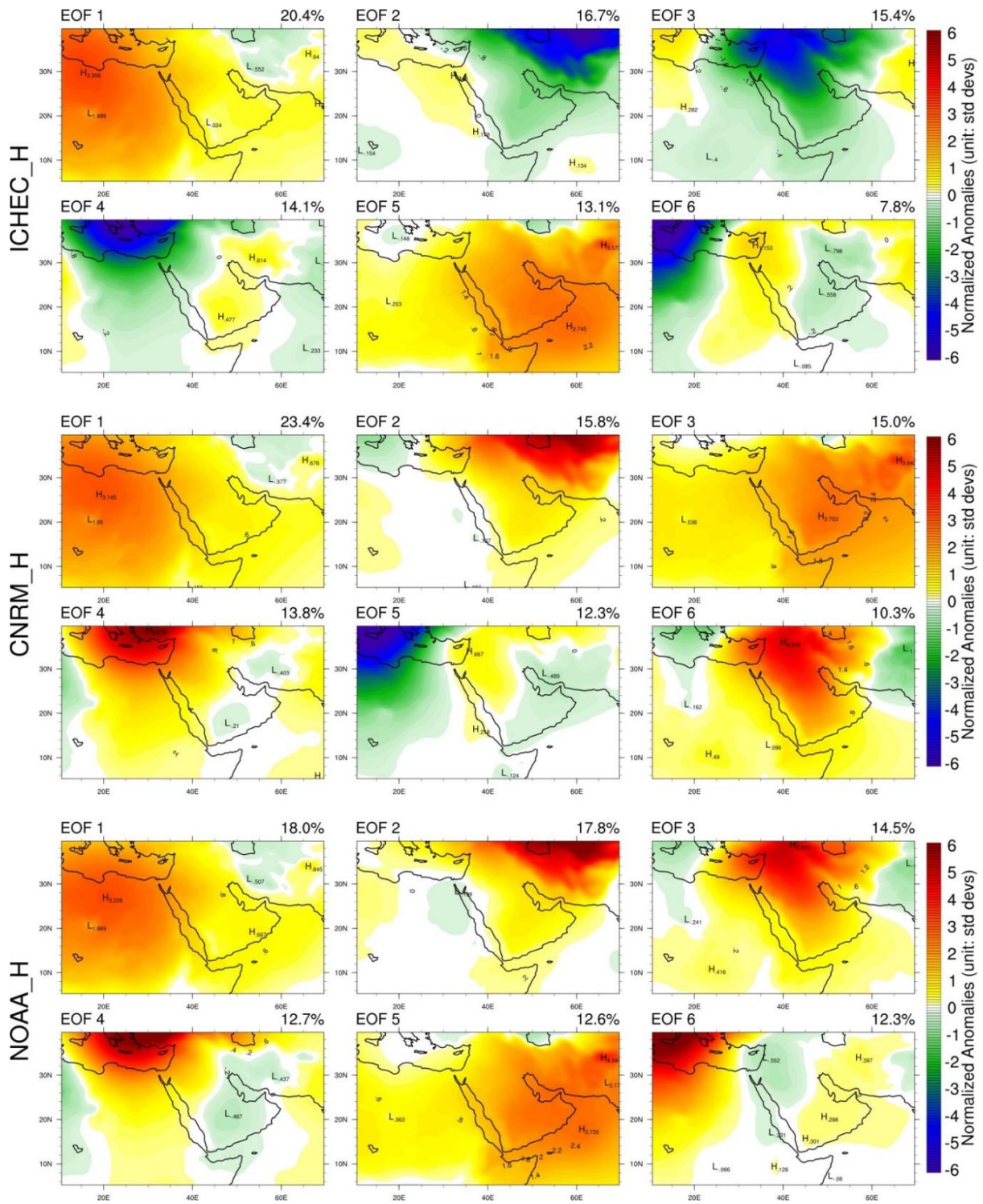
Figure 7.10. The six leading EOF patterns for the wet season (Nov., Dec. and Jan.), derived from the daily mean sea level pressure historical data (1976 to 2005) for the three ICHEC (top), CNRM (middle) and NOAA (bottom) experiments in units of normalised standard deviations.
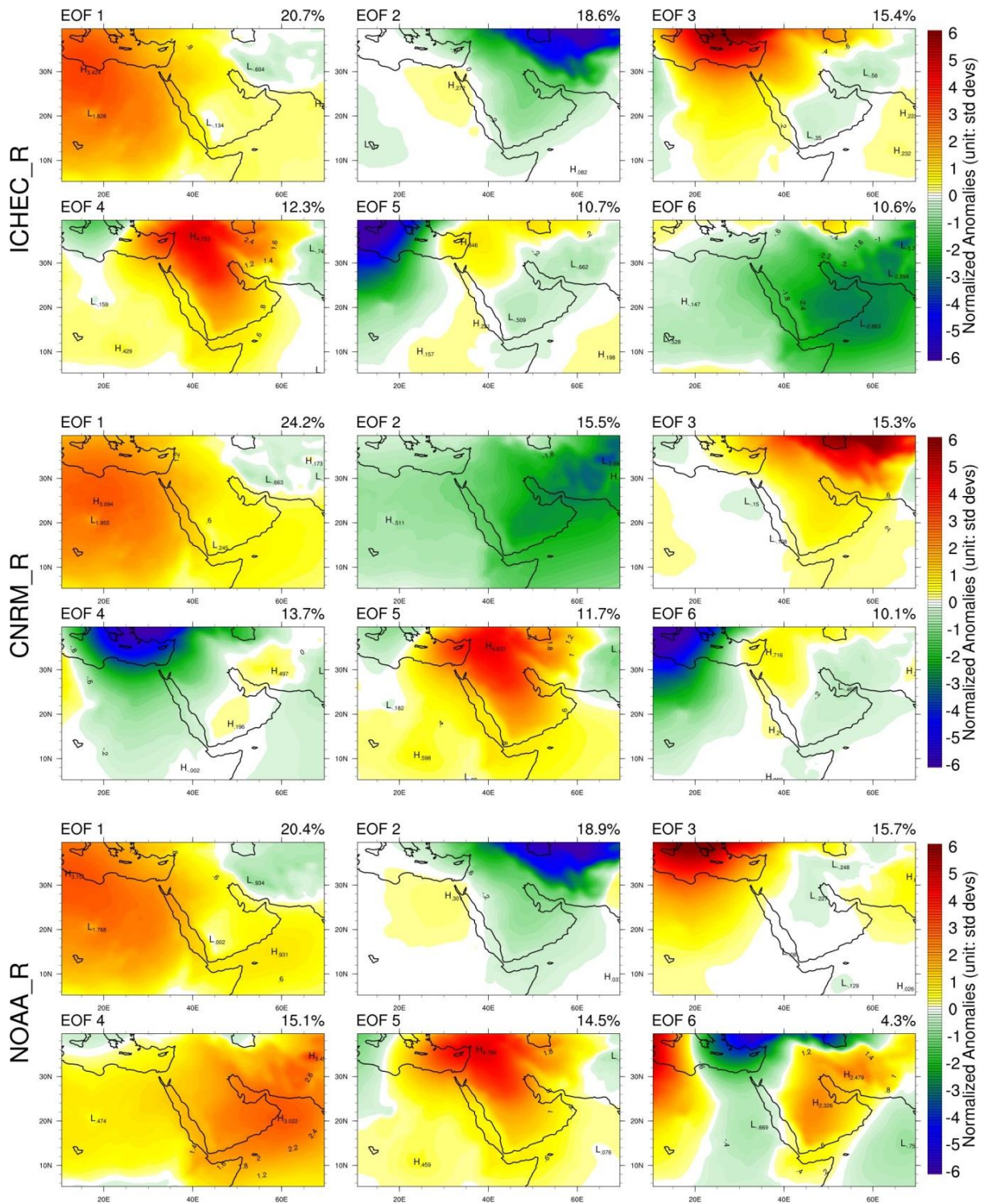
Figure 7.11. The six leading EOF patterns for the wet season (Nov., Dec. and Jan.) derived from the daily mean sea level pressure RCP8.5 prediction data (2070 to 2099) for the three ICHEC (top), CNRM (middle) and NOAA (bottom) experiments in units of normalised standard deviations.

7.4.1. Distribution changes in WCPs:

Figure 7.12 shows the distribution percentage of WCPs over 30 years for all wet season days (2760 days) from the ERA-Interim reanalysis data and the average distribution percentage of the three historical and future RCP8.5 simulations. In addition, it shows the difference between the average distribution percentage of the three historical and future RCP8.5 simulations and the difference between ERA-Interim reanalysis data and the average distribution percentage of three historical simulations.
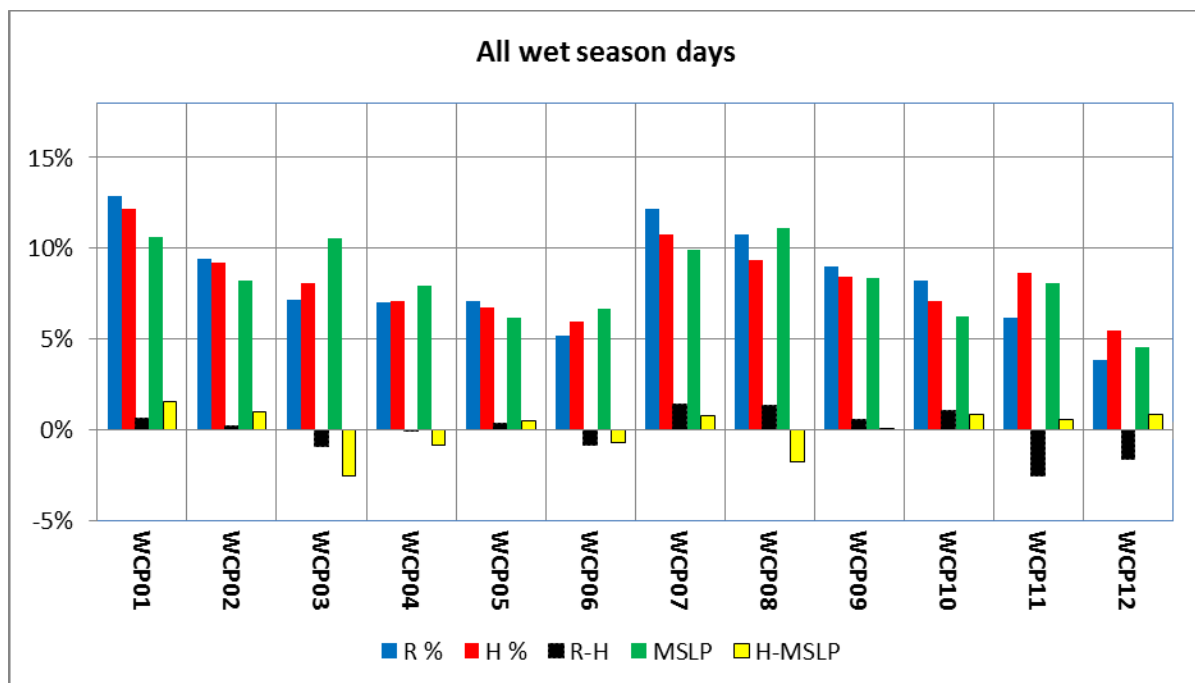
Figure 7.12. The distribution percentage of WCPs over 30 years for all wet season days (2760 days) from the 1985 to 2014 ERA-Interim (MSLP) reanalysis data, future (2070 to 2099) RCP8.5 simulation data (R) and historical (1976 to 2005) simulation data (H). The yellow column shows the WCP distribution percentage difference between future RCP8.5 predictions and historical simulation data (R-H) and MSLP and historical simulation data (H-MSLP). Units are represented in percent values.

First, the graph shows the considerable overestimation (over 1 percent) of the distribution percentage of WCP1 by the average of the historical simulations, compared with ERA-Interim (MSLP) data. Conversely, there is a considerable underestimation of the distribution percentage of WCP3 and WCP8 by the average of the historical simulations, compared with ERA-Interim (MSLP) data. Additionally, the change of more than 1 percent in WCP1, WCP7,

172

WCP8 and WCP10 increased, while the change decreased in WCP3, WCP6, WCP11 and WCP12 under the RCP8.5 emission scenario.

Figure 7.13 presents the difference between distribution percentages of WCPs in future RCP8.5 projections (2070 to 2099) and historical simulations (1976 to 2005) over a thirty-year period for all wet season days for three individual experiments (CNRM-RCA4, NOAA-RCA4 and ICHIC-RCA4) from the CORDEX-MENA domain. First, there is a large spread in the percentage of change between the WCP distributions in each experiment. Second, the NOAA-RCA4 experiment showed s positive change in WCP1, WCP3, WCP6, WCP7 and WCP8. However, a significant negative change was recorded in WCP4, WCP5 and WCP11.
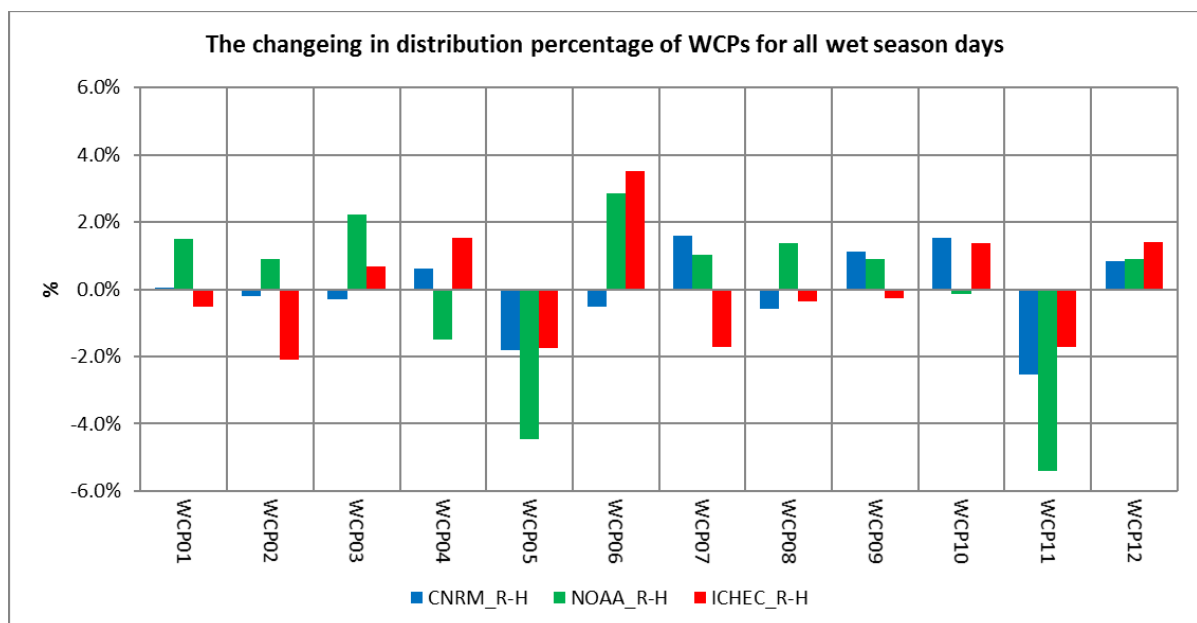
Figure 7.13. The percentage difference between the WCP distribution in future projections (2070 to 2099, RCP8.5) simulation and historical simulation data (1976 to 2005) over 30 years for all wet season days (2760 days) for three experiments: CNRM-RCA4, NOAA-RCA4 and ICHIC-RCA4. Units are represented in percent values.

Figure 7.14 illustrates the difference between the distribution percentage of WCPs in future RCP8.5 projections (2070–2099) and historical simulation data (1976–2005) for rainy days and the amount and frequency of extreme precipitation events during the wet season. This figure

shows that total precipitation amounts and extreme precipitation events increase in future projections for four weather circulation patterns (WCP3, WCP7, WCP8 and WCP9).

Conversely, the percentage of extreme precipitation events under the effects of climate change was decreased in five other weather circulation patterns (WCP1, WCP2, WCP4, WCP5 and WCP11). The distribution percentage for all wet season days showed a negative change in some WCPs, but the days and amounts of rainfall and extreme events show positive future change (WCP3). Conversely, WCP1 was increased in the future prediction, but showed negative change in the days and amounts of rainfall and extreme events. These percentage changes will be investigated in more detail.
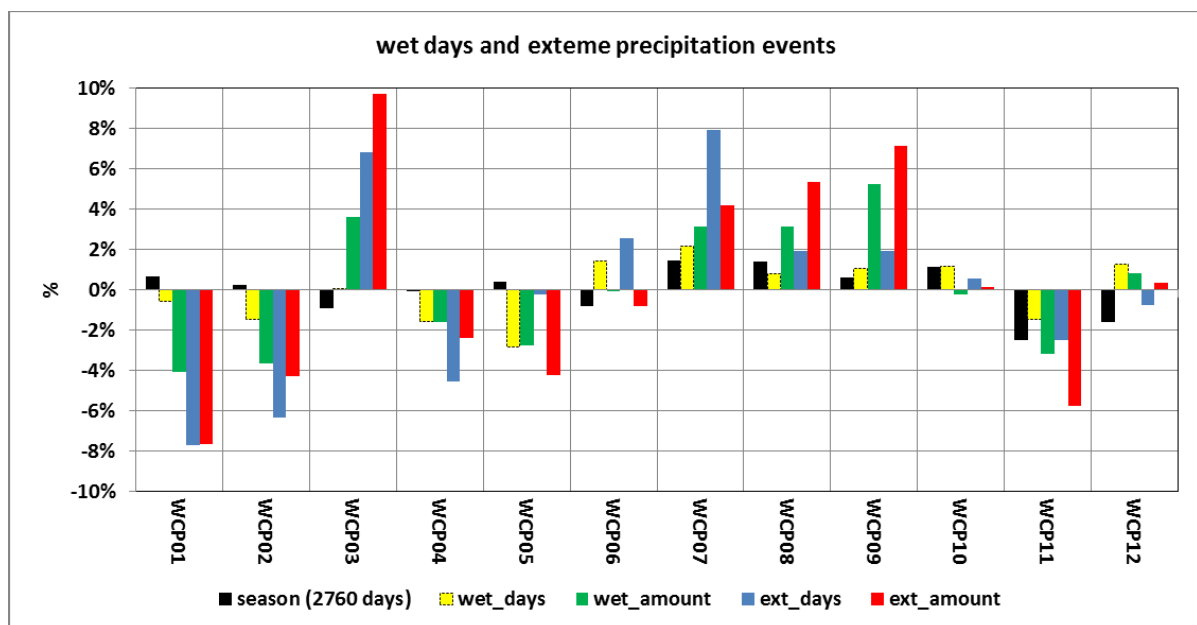
Figure 7.14. The difference between distribution percentages of WCPs in a future RCP8.5 projection (2070 to 2099, RCP8.5) and historical simulations (1976 to 2005) during the wet season on rainy days and the number (mm/day) of and frequency (day) of extreme precipitation events. Units are represented in percent values.

7.5. Summary:

In summary, this chapter has used the 23 experiments over the CORDEX-Africa domain and the three experiments over the CORDEX-MNA domain to assess the extreme precipitation in

future climate change under the RCP8.5 scenario. At the beginning of the chapter, the results of the multi model ensemble indicate percentage change of total precipitation and extreme precipitation in annual and wet seasonal were assessed on all models. In addition there was large model-to-model variability of the future changes in the projected total and extreme precipitation amounts in the 26 experimental simulations, nevertheless large similar in the results for multi model ensemble mean between CORDEX-Africa and CORDEX-MENA. However, the results from NOAA-RCA4 experiment in CORDEX-MENA domain and the MOHC-RACMO22T experiment in CORDEX-Africa domain are the closest and the most comparable experiment to the multi model ensemble mean.

The results of these changes in precipitation values shows that there is a noteworthy inter-annual variability between the annual and wet seasonal amount of precipitation in the area between central and southern WCSA. However, there were no large differences between the extreme and total precipitation values. In the wet season, a negative change in the amount of extreme precipitation is projected in two areas over the WCSA; between the central and southern region and between the central and northern region of WCSA. In addition, a positive change in the amount of extreme precipitation is projected in three areas over the WCSA; northern, central and southern regions of WCSA which gradually reduced from north to south.

A further analysis of the projected mean change of the other atmospheric elements (wind speed at 200hPa, GPH at 500hPa, MSLP), from the CORDEX-MENA domain experiments, took place both annually and seasonally. The ensemble average changes annually and in the wet season shows a positive MSLP change over North Africa and a negative MSLP change over the Red Sea. Further, a positive change in the mean western wind speed in the upper atmosphere at 200 hPa was found, and during wet season there is pronounce trough at 500 hPa.

Additionally, a negative MSLP change over the Red Sea and a positive change in wind speed at 200 hPa have remained and increased in the other seasons Sem1-season and Sem2-season.

Furthermore, analysis used the MSLP projected from CORDEX-MENA experiments to apply the EOF analysis and then produced the WCPs projected. The results of WCP analysis show that, in general, there is a large spread in the distribution of WCPs between individual experiments. In addition, the differences between percentages in the average of historical simulations and ERA-Interim reanalysis data show that there is a small overestimation of the percentage of occurrence of WCPs and a considerable underestimation of percentage of occurrence of WCP3 and WCP8 in historical simulations.

The results of distribution change in WCPs over 30 years for all wet season days under the RCP8.5 emission scenario showed a positive change of more than 1 percent in WCP1, WCP7, WCP8 and WCP10, while a negative change of more than 1 percent was shown in WCP3, WCP6, WCP11 and WCP12. The percentage of change of WCP occurrences in total and extreme precipitation was similar. In the total and extreme precipitation events, there was a significant positive change in four weather circulation patterns (WCP3, WCP7, WCP8 and WCP9) and a negative change in five other weather circulation patterns (WCP1, WCP2, WCP4, WCP5 and WCP11). This indicates the frequency of distribution percentages of WCPs in total and extreme precipitation events is approximately symmetrical to the frequency of distribution percentages of WCPs in all wet season days (except WCP01, WCP03, and WCP12). However, according to the five important types of weather circulation patterns (WCP01, WCP03, WCP04, WCP07 and WCP08) that are associated with extreme precipitation events (as shown in chapter 6), three WCPs of these patterns – WCP03, WCP07, and WCP08 – had a significant increase in the future climate change projections.

176

Chapter 8. DISCUSSION AND CONCLUSION:

Returning to the questions posed at the beginning of this study, it is now possible to state that:

8.1. Identification of extreme rainfall period and regionalisation of precipitation over WCSA:

A comparison of the findings with those of other studies confirms that annual precipitation distributions make a significant difference in extreme precipitation events from south to north in the WCSA. Also, the southern area has two precipitation seasons due to the ITCZ's effect in the summer, but in some cases, the ITCZ's effect on Makkah becomes increased. Thus, this study supports (AlSarmi and Washington, 2011, Athar and Ammar, 2015) notion of dividing the AP into two climate zones based on the ITCZ position (the monsoonal area south of 20°N and the non-monsoonal area north of 20°N). However, based on our results, and because of several climate regimes factors which play an important role in these extreme events, this study suggests adding a third area, which is the area between these two above-mentioned areas, which is represented by the central Red Sea coast.

The first question in this study sought to determine the wet season period along the West coast of Saudi Arabia. Firstly, there are two rainfall seasons over WCAS; one in the winter, called the wet season, and the other in summer, which called the dry season. The second rainfall season affects the southern region of WCSA and does not extend further than some parts of the central region. Whereas, the wet season, which is in the late autumn and in winter, affects all parts of the WCSA regions. The second season, which is called the wet season, is adopted in this study but with more focus on what month it represents.

177

However, many previous studies use the months from late autumn to early spring (October to May) to identify the wet season such as (Almazroui et al., 2015a) and others from November to April, such as (Kang et al., 2015, Hasanean and Almazroui, 2015, Athar, 2015, Almazroui, 2013, Islam and Almazroui, 2012, Almazroui et al., 2012a). All of these studies were focused on the whole AP but this study focuses on the WCSA only. Thus, this study identifies the wet season period from November to December because most stations over the WCSA recorded more than 50% of precipitation in this time. This was notable in the extreme precipitation events, where the extreme precipitation events percentages during this time were 88%, 84%, 83%, 50% and 40% for Wejh, Yanbu, Jeddah, Makkah and Gizan, respectively.

8.2.   Identify synoptic dynamic processes of extreme precipitation events:

A comparison of the findings of the subjective analysis of the synoptic dynamics involved in the 30 most extreme events with those of other studies confirmed that the RST was the main factor associated with most weather circulation patterns during this period and played an important role in the most extreme events, particularly in the central and northern WCSA. These results match those observed in earlier studies (e.g., (Alkhalaf and Basset, 2013, Awad and Almazroui, 2016, de Vries et al., 2013). Moreover, de Vries et al. (2013) explained the major flood in Jeddah on November 25 2009 in terms of the ARST phenomenon and identified the ARST using six dynamic factors. Ulbrich et al. (2012) suggested that the ARST based on its relationships between surface weather pressure system (RST) and mid to upper atmospheric systems (i.e. STJ and UT). This study recognises the ARST in the same way as these previous

studies. It also found that the RST extends toward the north and meets with MLs or LLs over the Levant.

Further to previous studies, this study also confirms that the SH and NAH have significant influences on RST intensity and location. When the RST and SL are strong, a mesoscale low-pressure system called the Red Sea Low appears in the low-upper air level. It sometimes occurs over regions around the Red Sea, and in some cases, it appears at the surface level, which results in high levels of precipitation. The Red Sea Low is a rare phenomenon. No previous studies define typical the cyclones over the Red Sea, but Maheras et al. (2001) mentioned a few cyclones that occurred over the Red Sea during the winter. Therefore, this study attributed the Jeddah event of November 2009 to the RSL, which was created by an intensive RST.

Furthermore, in some cases, the AGT appeared in early November. This result was slightly different than those of previous studies, which found that the AGT was a rare occurrence at this time because the AGT is a diurnal thermal trough that usually extends from the Indian summer monsoon (Bitan and Sa'Aroni, 1992) and lasts until October at the latest (Syroka and Toumi, 2004). Moreover, in a few cases, the study found the Arabian Low (AL) in the southern WCSA. This finding is consistent with results from a recent high-resolution regional climate model of the Red Sea created by Viswanadhapalli et al. (2016), which found that an intense low-pressure system was associated with a higher amount of precipitation formed over the southern WCSA in winter.

At 700-500hPa in the middle atmosphere, all atmospheric pressure systems at the surface begin to disappear with the appearance of the Arabian Anticyclone. However the Arabian Anticyclone brings moist air from the Arabian Sea and, in most cases, is associated with the

179

UT, which dominates the high and middle upper air levels. The UT is located in the northern Mediterranean and extends to North Africa and the AP. In some intensive cases, the UT becomes a CL, such as the November 2009 Jeddah flooding (Alkhalaf and Basset, 2013). At 400-200hPa in the upper atmosphere, the STJ begins to appear. The STJ is present in most extreme situations. In fact, 21 of 30 extreme events, which are investigated in this research, involved a strong STJ at the 200hPa level. These processes exert an influence on most extreme events over the WCSA. These findings are consistent with that of (de Vries et al., 2016), who identified a quasi-stationary subtropical anticyclone over the AP at lower- and middle-tropospheric levels and his interaction with UT and STJ in the extreme precipitation events over the Middle East.

8.3. Linking Between Extreme Precipitation Events and Weather Circulation Patterns and Large Scale Climate Variability Modes:

According to the observed precipitation dataset, the most important weather circulation patterns, which are associated with extreme precipitation events, are WCP01, WCP03, WCP04, WCP07 and WCP08. However, WCP07 is not a significant frequency when the dataset is based on grid model grid point (EAR-interim precipitation data). The percentage of occurrences of WCP07 is 7% and 12% when the precipitation data based on observation and EAR-interim dataset, respectively. Consequently, the ERA-Interim has underestimated the extreme precipitation events which were associated with WCP07, and overestimated the extreme precipitation events which were associated with WCP01. These two patterns were generated by EOF01. In consideration, WCP07 has a significant decreasing trend in number of occurrences by 46%, while WCP01 increasing by 49% in the second period of two halves of period for 1979–1995 and 1996–2012 (Almazroui et al., 2015a). In addition, WCP08 has also

been underestimated by the EAR-interim dataset but by a smaller decrease in its frequency than WCP07. Further, Almazroui et al. (2015a) found that WCP08 has a significant decreasing trend in number of occurrences by 10%.

Nevertheless, the EAR-interim dataset should not be relied upon for the occurrence of WCPs and should be relatively confirmed with precipitation data of observation station. This is due to the extreme precipitation events of EAR-interim reanalysis data not reasonably estimated. However, this study considers the WCP07 as one of five important weather circulation patterns that associate with extreme precipitation events. WCP07 represented the case 2 clearly and also all the other WCPs represented the individual of extreme precipitation events. These show that the EOF methodology provided a good classification for the synoptic climate regimes and identified characteristics of climatological features which associate with extreme precipitation events over WCSA.

The 12 automated weather circulation patterns procedures are established to represent all the main synoptic features in the wet season (November - January). These are similar to the results of Almazroui et al. (2015a) study, which showed 12 types of weather over the whole of Arabia in in the wet season (October–May) and found a strong link between the circulation weather types (2, 3, 8, 10, and 11) and the rainfall over the WCSA region. These circulation types correspond to WCP01, WCP05, WCP07, WCP03 and WCP04, which are found in this study. These findings support the findings of this thesis, where these 5 WCPs are classified as the most important type of weather circulation which are associated with extreme precipitation events, except for WCP05. However, WCP05 is still one of the patterns which is associated with extreme precipitation but without significant occurrences. In addition, (Almazroui et al., 2015a) did not classify WCP08 as one of these types which is associated with

rainfall over the coastal area, but did mention that it was a wet pattern that affected the north-western region and interior region in late autumn. In this study, WCP08 is classified as one of the most important patterns which affect the Wajh in the north and the interior station (Makkah).

In this study, the circulation patterns which are associated with extreme precipitation events are 11 out of the 12 WCPs produced. WCP11 was not associated with extreme precipitation events and the dynamical process of this pattern was not investigated in this study. Almazroui et al. (2015a) described WCP11 and classified it as Khamsin low, which is the North African depression over the west Mediterranean region and moves eastward through the Levant and North Saudi Arabia and causes sand storms. Furthermore, in particular investigation, Almazroui et al. (2015a) identified WCP06 as the Indian monsoon trough which extends from the Arabian Gulf and brings rainfall over the southern WCPA. In addition, they indicated that WCP02 was the main pattern associated with precipitation in Gizan. Therefore, these findings support this thesis.

On the other hand, the analysis of the large-scale climate variability correlation coefficients with extreme precipitation events undertaken in this study has extended our knowledge of the teleconnection extreme precipitation relationship with the WCSA region. These correlation coefficients are applied for total and extreme precipitation and based on precipitation reanalysis and observation data. The aim of this investigation was to examine the effects of this kind of data on these relationship and how the indices of large-scale climate variability are affected by these data. It showed that indices of ODI and ENSO have not changed whether the correlation was based in total precipitation or extreme precipitation, while the correlation with NAO indices are changed. Donat et al. (2013) found that the

relationship between ENSO and climate extreme precipitation was stronger than the relationship between NAO and extreme precipitation in the Arabian Peninsula.

However, the teleconnection analysis focuses on three indices (NOA, Nino1+2 and MDI). The results in this study found a strong positive correlation between Nino1+2 and DMI indices and extreme precipitation over the southern WCSA region. This was supported by (Mariotti et al., 2005) who found a strong statistical relationship between ENSO and precipitation in southwest Asia. Although the relationship between NOA and extreme precipitation is weak overall, there is a relatively significant negative correlation between the extreme precipitation and small area in northern WCSA.

On the other hand, the regression coefficients between extreme precipitation and WCPs was investigated and found an unclear relationship between NOA index and these WCPs, while there was a positive relationship between extreme precipitation and IOD and ENSO indices. The strong positive relationships are with WCP01, WCP03, WCP05, WCP07, WCP09, WCP10 and WCP12. The Red Sea Trough is the main factor in all these weather circulations. While WCP06 and WCP08 have a negative relationship with IOD and ENSO. These finding are supported by Krichak et al. (2014b), who found a positive correlation between ENSO and moisture air, which is associated with Red Sea troughs between October and November. The distribution of the WCPs occurrence with negative and positive IOD and ENSO indices phases found that WCP7, WCP9, WCP10 and WCP12 show a more association with a positive phase, WCP08 and WCP06 are more likely to have a negative association. This was also supported by (Chakraborty et al., 2006) who found a strong relationship between moisture air into AP and the concurrent positive IOD and ENSO events.

183

8.4. Assessment of the Future Climate Change Projected of Extreme Precipitation Events:

The validation of RCMs in Chapter 5 provided suitable indications for the best four RCMs, which are used in the CORDEX experiments over the CORDEX-Africa and CORDEX-MNA domains. Unfortunately, the availability of output data of these best experiments are just for data evaluation (no historical and future data). However, data by other RCMs from the 23 experiments over the CORDEX-Africa domains and the three experiments over the CORDEX-MNA domains are used to assess a possible future change in precipitation over WCSA under anthropogenic climate change conditions. The results of the changes of precipitation amount and frequency in the future under the RCP8.5 scenario yielded a considerable spread between the individual 26 experiments in both total precipitation and extreme precipitation events. Some experiments showed an increase in precipitation and other experiments showed a decrease. However, the multi model ensemble mean percentage change in total precipitation and extreme precipitation of the 23 CORDEX-Africa experiments and the three CORDEX-MNA experiments are relatively similar. Because the assessment of extreme precipitation over WCSA is relatively poor performance as shown in Chapter 5, we studied the total and annual rainfall cases to compare these changes with the changes in extreme precipitation values.

From the results of total and extreme precipitation changes in these models, the study determined that the changes in total precipitation amounts are projected to increase annually along the coast of the Red Sea, except in some parts of the northern region. This is consistent with the finding by Almazroui et al. (2017), who used 22 GCMs of CMIP5 for high-emission scenarios (RCP8.5) to assess the projected changes in precipitation over the Arabian Peninsula, but with significantly coarser resolution. Almazroui et al. (2017) found a large

increase in the projected signal of the annual total precipitation over the southern part of Arabian Peninsula, including the coastline. This increasing rate gradually reduced from south to north and along the Red Sea coastline.

In other research by Almazroui et al. (2016b), 20 GCMs of CMIP3 were used for high-emission scenarios (A2) to assess the projected changes in precipitation over the Arabian Peninsula, the researchers determined that the change in precipitation amounts decreased in the northern and central Red Sea coastal regions, and there was no considerable change in the annual total precipitation amounts in the southern region. These results partially contradicted the findings of projected changes for annual total precipitation amounts by Almazroui et al. (2017) and the current study.

The resulting patterns of total precipitation amount projections showed that positive change in the annual total precipitation amounts. This is similar to the change in wet season, but with a negative changing of precipitation amount over some part of southern region in the wet season. This decline, which appeared in the wet season, was also found by Almazroui et al. (2017) in the winter. This is because the southern region is affected by the South Asian summer monsoon, which recorded high increases in precipitation projections from the effects of climate change (Almazroui et al., 2016b).

Moreover, the annual change in extreme precipitation amounts is projected to increase along the Red Sea coastline, with a low negative change over a portion of the northern region. This finding is also supported by Almazroui et al. (2017), who suggested that extreme precipitation is decreasing over the northern part of the Arabian Peninsula and increasing over the southern Arabian Peninsula. Additionally, (Almazroui, 2013) showed that extreme precipitation is increasing in the southern and central parts of the Red Sea coastal areas.

In the wet season, a positive change in the amount of extreme precipitation was projected. It increased in the northern region and decreased in the central and southern regions along the Red Sea coast, cambering with annual values. Some of the gaps between the northern, central and southern Red Sea coast areas recorded a negative change. So far, no previous studies have found these results.

Although a recent study by Almazroui et al. (2017) supports the current study results, the different projected mean precipitation changes between these studies may be due to the different GCMs used in each study, as well as the use of the RCMs to dynamically downscale the GCMs in the current study. The MOHC-RACMO22T experiment from CORDEX-Africa and the NOAA-RCA4 from CORDEX-MNA are close and comparable to the multi model ensemble average percentage change. However, the dynamic regional climate models (RACMO22T in the CORDEX-Africa domain and RCA4 from the CORDEX-MNA domain) were the best precipitation simulation models for the area of study, as determined in validation evaluation data in Chapter 5.

In a dynamic study, changes in the geopotential heights at 500 hPa, wind speed at 200 hPa and MSLP were utilised to explain the increased precipitation amounts over the Red Sea coast. The ensemble average changes annually and in the wet season shows a negative MSLP change leading to strengthening of the RST circulation along the Red Sea coastal areas. This negative MSLP change over the Red Sea is normal when considering the influence of global warming, as the temperature of the Red Sea has increased since the mid-1990s (Raitsos et al., 2011). When combined with the positive MSLP change over the Mediterranean that extends to the north of Red Sea, these changes contribute to a reduction in the depth of ARST in a northward direction over the eastern Mediterranean regions. This effect exists over the

northern Red Sea coastal areas. This also restricts RST activity in the region around the Red Sea, increasing the incidences of extreme rainfall.

In addition, several factors play an important role in increasing future ARST activity under the influence of climate change (thus the extreme rainfall events). The first factor is that the considerable positive MSLP change over North Africa increases the North African high pressure. Second, the positive change in the mean western wind speed in the upper atmosphere at 200 hPa plays an important role in the dynamic activity of most of the extreme precipitation events over the west coast region (as seen in Chapter 4). This is especially true in the northern part of the Red Sea, as this location is the path of the Subtropical Jet stream in the wet season (Iqbal et al., 2016). Finally, a pronounced trough in the 500 hPa change pattern corresponds with the low altitude, playing an important role in the ARST over the Red Sea region.

These factors lead to greater instability, thus creating conditions more favourable to the increase of extreme precipitation in the northern region of the Red Sea coast. Additionally, in the other seasons, the positive change in wind speed at 200 hPa and the negative change in MSLP over the Red Sea coast has also increased in the Sem1 and Sem2 seasons. As a result, which is a consequence of these changes, extreme precipitation events over the west cost of Saudi Arabia could potentially increase after the wet season and extend to the Sem1 and Sem2 seasons. Although all these dynamic factors play an important role in precipitation events over the WCSA, the weather pressure system over the surface, especially RST, is still the main factor.

In addition to the change in average of dynamic factors under climate change scenario RCP8.5, the distribution of WCPs are also affected by this climate change condition, the study found

that, there is a large spread in the distribution of WCPs between individual experiments. On average, there are increases in the frequency of WCP3, WCP7, WCP8 and WCP9. These results are close to the results of the best experiment (NOAA-RCA4), which recorded increases in the occurrence of WCP01, WCP03, WCP6, WCP07 and WCP08. Four of these WCPs (WCP1, WCP3, WCP7 and WCP8) are associated with extreme precipitation events over the Red Sea Coast, as shown in Chapter 6. From these results, we can determine that the effects of climate change will cause extreme precipitation to increase over the Red Sea coastal areas.

8.5.   Conclusion and Recommendations:

This is the first study to identify the characteristics of extreme precipitation events along the western coast of Saudi Arabia and investigate the dynamic climatic factors that are associated with these events by subjective and objective classification in present and future climates. This was done using many methodologies, such as precipitation analysis and extreme events identification, composite mean and anomaly analysis, vertical integrated water vapour flux, trajectory analysis, objective analysis (i.e., EOF), validation data and these were used with several data (observation precipitation, ERA-Interim reanalysis and regional climate downscaling data). The main limitation of this study is the quality of the many kinds of precipitation data which are provided from observation, reanalysis and climate model data. Further, there are just five observation stations along the WCSA and the performance of reanalysis precipitation data on this region is relatively poor.

The WCSA is divided into three climatic regions; the northern region, central region and southern region. These regions are affected by different climate conditions through the year. Four seasons are also identified in this study that are dependent on the precipitation rate in each station along the WCSA; *dry_season, wet_season,* first *semi-wet_season and* second

semi-wet_season). This study focuses on the wet season (NDJ). The majority of extreme precipitation events occurred during this season. There were 79 events in this season while 136 occurred in the whole study time period from 1985-2014. The percentage of occurrence of these events relative with the mean for individual station are large in the northern and central region. This is because the southern region is affected by ITCZ, which increases the rate of precipitation in this area in the summer or *dry_season* (JJAS). However, the percentage of extreme precipitation events over the southern region in the wet season still more than in the dry season.

The main dynamic climatic factors which play an important role in these extreme events are identified by investigating the 30 highest events of the 79 extreme events which are found in the wet season during the study time period. Very few studies have systematically investigated individual cases of these extreme events over WCSA. The subjective study of these events found that the interaction between the dynamic climatic factors in the low, mid and upper atmospheric level is required to create these events. In the upper atmospheric level at 200 or 300 hPa there is the STJ and in the mid atmospheric level between 700 and 500 hPa there is the UT, these two systems are present in most events. In addition, the AA, which is placed between low and mid atmospheric level, brings a large amount of moisture from the Arabian Sea, and this sometimes comes from more remote areas, such as the Mediterranean Sea or Atlantic Ocean. In addition to these factors, the surface weather circulation plays the main role in all these extreme events.

Synoptic surface pressure charts showed the main pressure systems of these 30 events over the WCSA. These pressure systems are namely; RST, MLs, NAH and SH. The location and severity of each event depends on the extent of intensity and strength of these pressure

systems. However, in most cases, RST is still the main and most important factor. On the other hand, there are some pressure systems which no previous research has investigated before. These infrequent pressure systems are RSLs over the central Red Sea and the unexpected effect of AGT, which extends to this area during this time of year.

All these surface pressure systems have been classified by the principal component analysis. This classification method has succeeded in classifying most extreme precipitation events and categorised them in 11 WCPs. The evaluation of these classifications has been carried out by testing these WCPs with 11 cases of the 30 extreme events. The most frequent occurrence of these patterns are shown in WCP01, WCP03, WCP04, WCP07 and WCP8. Nevertheless, the other patterns are still important and have some very good and useful characteristics which extends our knowledge of the extreme events over the WCSA. For example, WCP06, which represents the infrequent occurrence system as AGT. In addition, most of these five important patterns have a positive correlation with IOD and ENSO indices, specifically over the southern and central region. The RST is the mean factor in these patterns, apart from WCP08. On the other hand, some WCPs have shown negative correlations, such as WCP06 and WCP08, which are not affected by RST.

The study also used downscale regional climate models from CORDEX data to investigate the future change in extreme precipitation under the RCP8.5 emission scenario by the precipitation data and some other atmospheric variables data (i.e. MSLP, GPH and Wind speed at 200 hPa). This is in addition to the future change in the distributions of WCPs that were associated with the extreme precipitation. A limitation of CORDEX data is that it increased the uncertainty of projections of future climate change, where this study suggested four best RCMs from CRDEX-AFR domain (i.e. CRCM5, HadGEM3-RA, HadRM3P and

RACMO22T). The study couldn't use the future simulations data of these RCMS. In addition a small number of RCMs were available and used from CORDEX-MENA domain. However, with large model-to-model variability and the significant uncertainty between 26 experimental simulations, these findings suggest that the future changes in the projected extreme precipitation events over the WCSA in the wet season are increasing.

In conclusion, although a key strength of the present study was the focus on a specific region in the Arabian Peninsula and a specific period time of the year which makes a small spatial and temporal variability, further region studies need to be carried out in order to analyse each part of the WCSA (northern, central and southern region). Further, it is recommended that these studies be undertaken all regions of the Arabian Peninsula. Moreover, further mesoscale experimental simulation studies are needed to investigate the small-scale physical and dynamical process of extreme precipitation events as well as the need to increase the resolution of climate models as 0.11∘ or less to improve precipitation simulations. Developing and adding meteorological stations along the WCSA to improve observed precipitation datasets are required, and further studies need to estimate and validate gridded gauge-analysis products and reanalysis data.

Appendix 1: Surface and Upper-Air Synoptic Charts

The figures in Appendix A contain study area scale maps for the surface and upper weather systems in top 30 extreme precipitation events, specifically wind (vector), mean MSLP and GPH (contour line) and normalised pressure and GPH anomaly (fill colour) at the 850hPa, 500hPa and 200hPa levels.

194
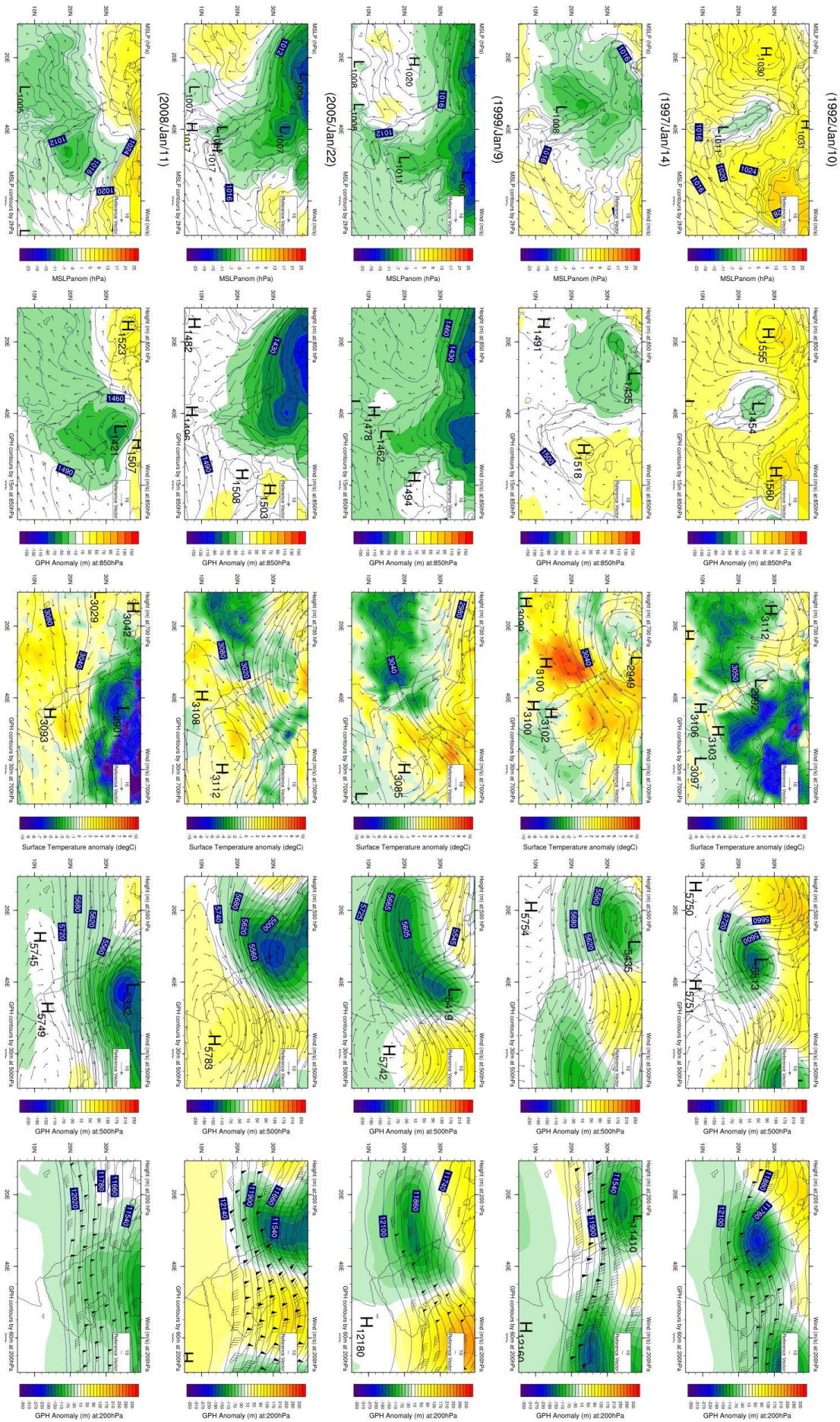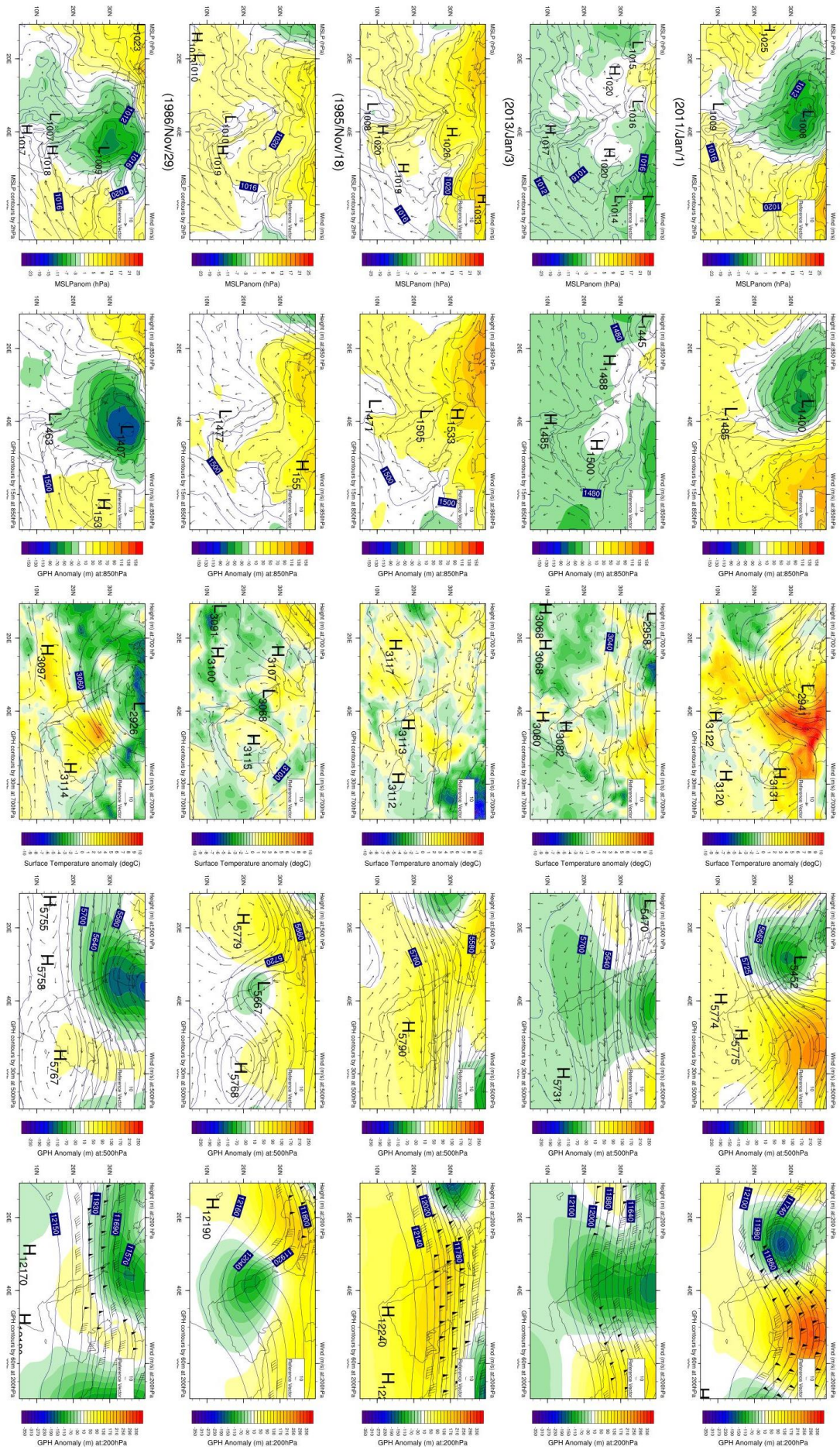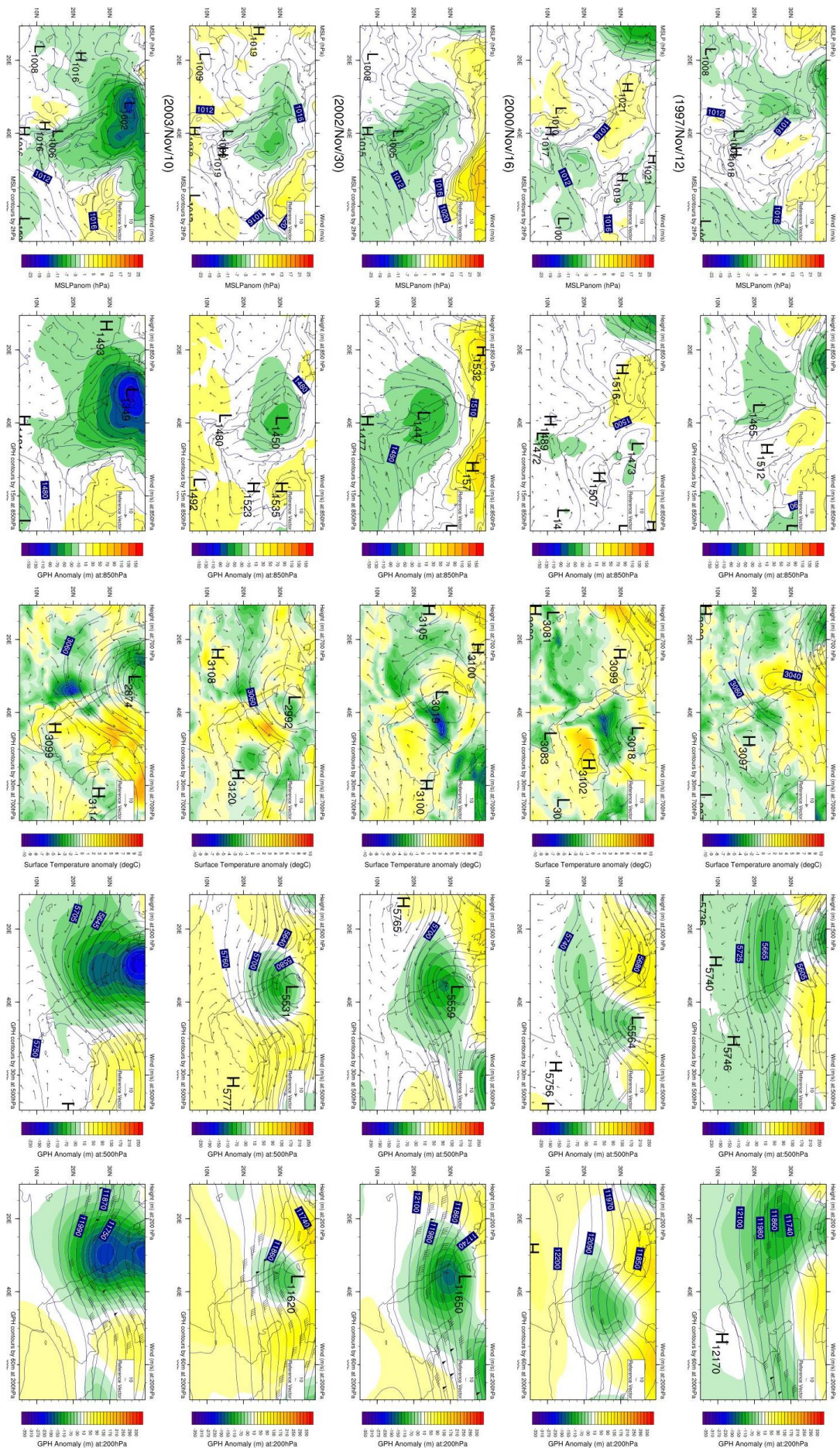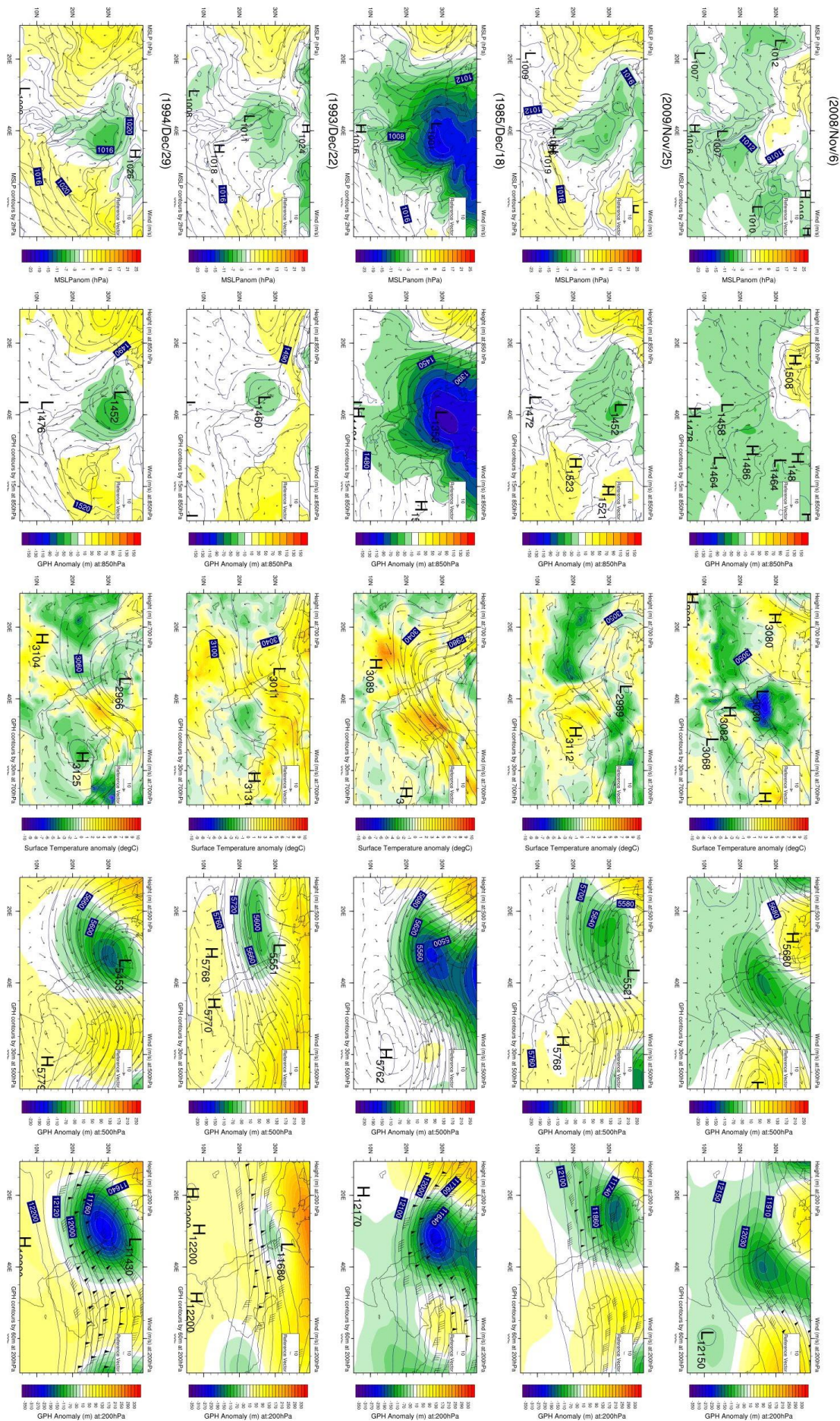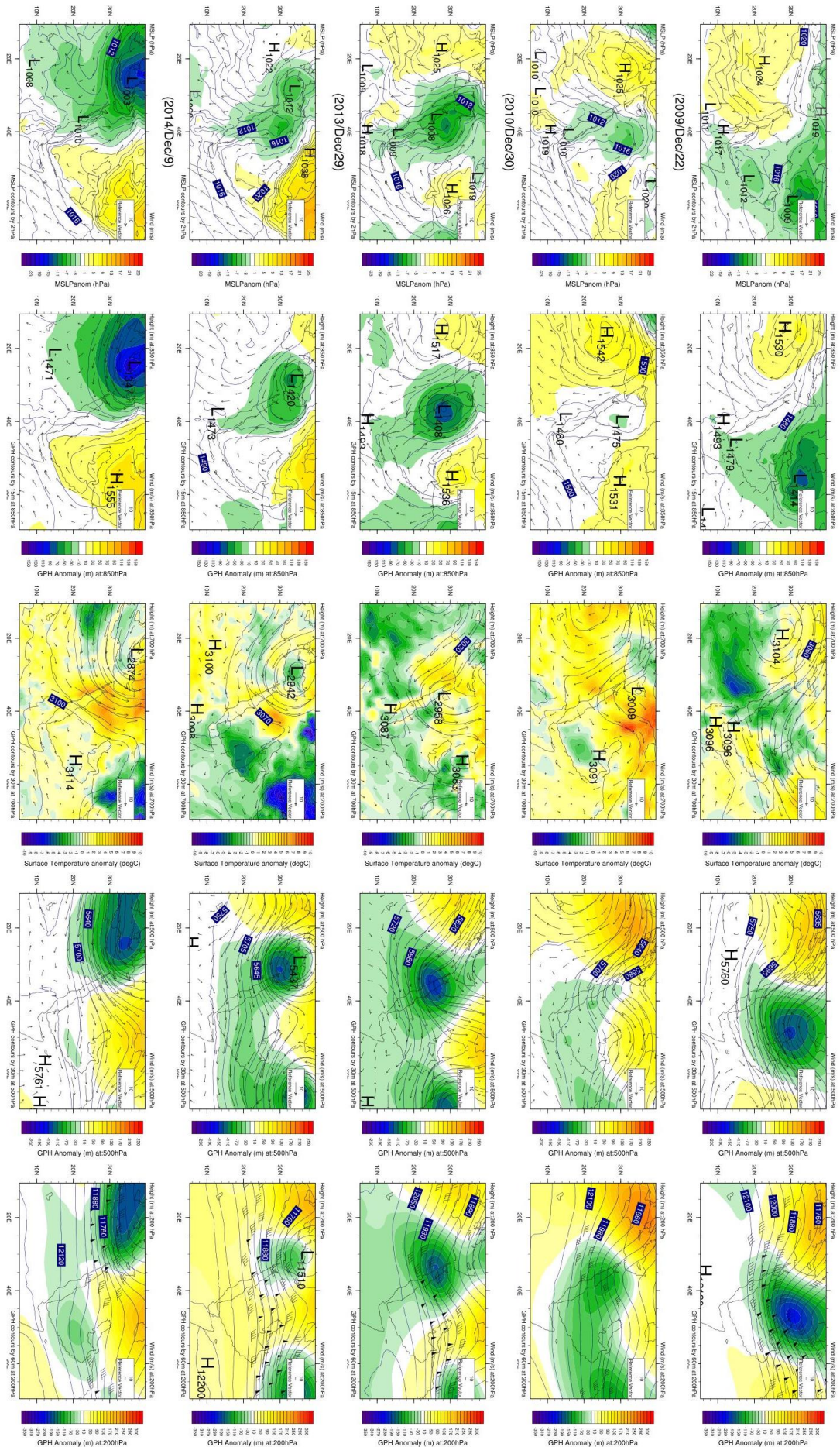
Chapter 9. BIBLIOGRAPHY

ABDULLAH, M. & AL-MAZROUI, M. 1998. Climatological study of the southwestern region of Saudi Arabia. I. Rainfall analysis. *Climate Research,* 9, 213-223.

ABDULLAH, M. A. & IBRAHIM, M. M. 1989. Synoptic and Numerical Studies for Simulating Weather Instabilities that Affect The Kingdom of Saudi Arabia in Winter: I. The Synoptic Case Study. *Meteorology, Environment and Arid Land Agriculture Sciences.*

ABISH, B., JOSEPH, P. & JOHANNESSEN, O. M. 2015. Climate change in the subtropical jetstream during 1950–2009. *Advances in Atmospheric Sciences,* 32, 140-148.

AL-AHMADI, K. & AL-AHMADI, S. 2014. Spatiotemporal variations in rainfall–topographic relationships in southwestern Saudi Arabia. *Arabian Journal of Geosciences,* 7, 3309-3324.

ALEXANDER, L. V., ZHANG, X., PETERSON, T. C., CAESAR, J., GLEASON, B., KLEIN TANK, A. M. G., HAYLOCK, M., COLLINS, D., TREWIN, B., RAHIMZADEH, F., TAGIPOUR, A., RUPA KUMAR, K., REVADEKAR, J., GRIFFITHS, G., VINCENT, L., STEPHENSON, D. B., BURN, J., AGUILAR, E., BRUNET, M., TAYLOR, M., NEW, M., ZHAI, P., RUSTICUCCI, M. & VAZQUEZ-AGUIRRE, J. L. 2006. Global observed changes in daily climate extremes of temperature and precipitation. *Journal of Geophysical Research: Atmospheres,* 111, D05109.

ALEXANDER, M. A., SCOTT, J. D., SWALES, D., HUGHES, M., MAHONEY, K. & SMITH, C. A. 2015. Moisture Pathways into the U.S. Intermountain West Associated with Heavy Winter Precipitation Events. *Journal of Hydrometeorology,* 16, 1184-1206.

ALEXANDRU, A., DE ELIA, R. & LAPRISE, R. 2007. Internal variability in regional climate downscaling at the seasonal scale. *Monthly Weather Review,* 135, 3221-3238.

ALKHALAF, A. K. & BASSET, H. A. 2013. Diagnostic Study of a Severe Thunderstorm over Jeddah. *Atmospheric and Climate Sciences,* 3, 15.

ALLAN, R. J., NICHOLLS, N., JONES, P. D. & BUTTERWORTH, I. J. 1991. A Further Extension of the Tahiti-Darwin SOI, Early ENSO Events and Darwin Pressure. *Journal of Climate,* 4, 743-749.

ALMAZROUI, M. 2011a. Calibration of TRMM rainfall climatology over Saudi Arabia during 1998–2009. *Atmospheric Research,* 99, 400-414.

ALMAZROUI, M. 2011b. Sensitivity of a regional climate model on the simulation of high intensity rainfall events over the Arabian Peninsula and around Jeddah (Saudi Arabia). *Theoretical and applied climatology,* 104, 261-276.

ALMAZROUI, M. 2012. The life cycle of extreme rainfall events over western Saudi Arabia simulated by a regional climate model: Case study of November 1996. *Atmósfera,* 25, 23-41.

ALMAZROUI, M. 2013. Simulation of present and future climate of Saudi Arabia using a regional climate model (PRECIS). *International Journal of Climatology,* 33, 2247-2259.

ALMAZROUI, M. 2016. RegCM4 in climate simulation over CORDEX-MENA/Arab domain: selection of suitable domain, convection and land-surface schemes. *International Journal of Climatology,* 36, 236-251.

ALMAZROUI, M., ABID, M. A., ATHAR, H., ISLAM, M. N. & EHSAN, M. A. 2013. Interannual variability of rainfall over the Arabian Peninsula using the IPCC AR4 Global Climate Models. *International Journal of Climatology,* 33, 2328-2340.

ALMAZROUI, M., DAMBUL, R., ISLAM, M. N. & JONES, P. D. 2014. Principal components-based regionalization of the Saudi Arabian climate. *International Journal of Climatology*, n/a-n/a.

ALMAZROUI, M., DAMBUL, R., ISLAM, M. N. & JONES, P. D. 2015a. Atmospheric circulation patterns in the Arab region and its relationships with Saudi Arabian surface climate: A preliminary assessment. *Atmospheric Research,* 161–162, 36-51.

ALMAZROUI, M., ISLAM, M. N., AL-KHALAF, A. & SAEED, F. 2015b. Best convective parameterization scheme within RegCM4 to downscale CMIP5 multi-model data for the CORDEX-MENA/Arab domain. *Theoretical and Applied Climatology*, 1-17.

ALMAZROUI, M., ISLAM, M. N., ALKHALAF, A., SAEED, F., DAMBUL, R. & RAHMAN, M. A. 2016a. Simulation of temperature and precipitation climatology for the CORDEX-MENA/Arab domain using RegCM4. *Arabian Journal of Geosciences,* 9, 1-14.

ALMAZROUI, M., ISLAM, M. N., JONES, P. D., ATHAR, H. & RAHMAN, M. A. 2012a. Recent climate change in the Arabian Peninsula: Seasonal rainfall and temperature climatology of Saudi Arabia for 1979–2009. *Atmospheric Research,* 111, 29-45.

ALMAZROUI, M., ISLAM, M. N., SAEED, F., ALKHALAF, A. K. & DAMBUL, R. 2017. Assessing the robustness and uncertainties of projected changes in temperature and precipitation in AR5 Global Climate Models over the Arabian Peninsula. *Atmospheric Research,* 194, 202-213.

ALMAZROUI, M., NAZRUL ISLAM, M., ATHAR, H., JONES, P. D. & RAHMAN, M. A. 2012b. Recent climate change in the Arabian Peninsula: annual rainfall and temperature analysis of Saudi Arabia for 1978–2009. *International Journal of Climatology, 32*, 953-966.

ALMAZROUI, M., SAEED, F., ISLAM, M. N. & ALKHALAF, A. 2016b. Assessing the robustness and uncertainties of projected changes in temperature and precipitation in AR4 Global Climate Models over the Arabian Peninsula. *Atmospheric Research,* 182, 163-175.

ALPERT, P., BALDI, M., ILANI, R., KRICHAK, S., PRICE, C., RODÓ, X., SAARONI, H., ZIV, B., KISHCHA, P., BARKAN, J., MARIOTTI, A. & XOPLAKI, E. 2006. Chapter 2 Relations between climate variability in the Mediterranean region and the tropics: ENSO, South Asian and African monsoons, hurricanes and Saharan dust. *In:* P. LIONELLO, P. M.-R. & BOSCOLO, R. (eds.) *Developments in Earth and Environmental Sciences.* Elsevier.

ALPERT, P., OSETINSKY, I., ZIV, B. & SHAFIR, H. 2004. Semi-objective classification for daily synoptic systems: Application to the eastern Mediterranean climate change. *International Journal of Climatology, 24*, 1001-1011.

ALSARMI, S. & WASHINGTON, R. 2011. Recent observed climate change over the Arabian Peninsula. *Journal of Geophysical Research: Atmospheres, 116*, D11109.

ALSARMI, S. H. & WASHINGTON, R. 2013. Changes in climate extremes in the Arabian Peninsula: analysis of daily data. *International Journal of Climatology*, n/a-n/a.

ALYAMANI, M. S. & SEN, Z. 1993. Regional variations of monthly rainfall amounts in the Kingdom of Saudi Arabia. *Earth Sciences, 6*.

AMIN, M., MAHMOUD, S. & ALAZBA, A. 2016. Observations, projections and impacts of climate change on water resources in Arabian Peninsula: current and future scenarios. *Environmental Earth Sciences, 75*, 1-17.

ASHLEY, W. S., BENTLEY, M. L. & STALLINS, J. A. 2012. Urban-induced thunderstorm modification in the Southeast United States. *Climatic change, 113*, 481-498.

ATHAR, H. 2014. Trends in observed extreme climate indices in Saudi Arabia during 1979–2008. *International Journal of Climatology, 34*, 1561-1574.

ATHAR, H. 2015. Teleconnections and variability in observed rainfall over Saudi Arabia during 1978–2010. *Atmospheric Science Letters,* n/a-n/a.

ATHAR, H. & AMMAR, K. 2015. Seasonal characteristics of the large-scale moisture flux transport over the Arabian Peninsula. *Theoretical and Applied Climatology,* 1-14.

AWAD, A. M. & ALMAZROUI, M. 2016. Climatology of the winter Red Sea Trough. *Atmospheric Research,* 182, 20-29.

AXISA, D., XUE, L., BURGER, R., COLLINS, D., FRENEY, E., KUCERA, P., BRUINTJES, R. & BUSECK, P. 2011. Evolution boundary layer thermodynamics, aerosol and cloud microphysics during the weather modification assessment program in the southwest region of Saudi Arabia.

BAN, J., ZHANG, X. & HUANG, X. 2009. Diagnostic analysis and numerical simulation of Jeddah rain storm on Novamber 25, 2009.

BARNSTON, A. G. & LIVEZEY, R. E. 1987. Classification, seasonality and persistence of low-frequency atmospheric circulation patterns. *Monthly weather review,* 115, 1083-1126.

BITAN, A. & SA'ARONI, H. 1992. The horizontal and vertical extension of the Persian Gulf pressure trough. *International Journal of Climatology,* 12, 733-747.

BLACK, E., BRAYSHAW, D. J. & RAMBEAU, C. M. 2010. Past, present and future precipitation in the Middle East: insights from models and observations. *Philos Trans A Math Phys Eng Sci,* 368, 5173-84.

BOSILOVICH, M. G., CHEN, J., ROBERTSON, F. R. & ADLER, R. F. 2008. Evaluation of global precipitation in reanalyses. *Journal of applied meteorology and climatology,* 47, 2279-2299.

BUCCHIGNANI, E., CATTANEO, L., PANITZ, H.-J. & MERCOGLIANO, P. 2015a. Sensitivity analysis with the regional climate model COSMO-CLM over the CORDEX-MENA domain. *Meteorology and Atmospheric Physics,* 1-23.

BUCCHIGNANI, E., MERCOGLIANO, P., RIANNA, G. & PANITZ, H. J. 2015b. Analysis of ERA-Interim-driven COSMO-CLM simulations over Middle East–North Africa domain at different spatial resolutions. *International Journal of Climatology.*

CAYA, D. & BINER, S. 2004. Internal variability of RCM simulations over an annual cycle. *Climate Dynamics,* 22, 33-46.

CHAKRABORTY, A., BEHERA, S. K., MUJUMDAR, M., OHBA, R. & YAMAGATA, T. 2006. Diagnosis of Tropospheric Moisture over Saudi Arabia and Influences of IOD and ENSO. *Monthly Weather Review,* 134, 598-617.

CHRISTENSEN, O. B., DREWS, M., CHRISTENSEN, J. H., DETHLOFF, K., KETELSEN, K., HEBESTADT, I. & RINKE, A. 2006. The HIRHAM regional climate model version 5 (β). *Techical Report,* 6-17.

CHRISTENSEN, O. B., GAERTNER, M. A., PREGO, J. A. & POLCHER, J. 2001. Internal variability of regional climate models. *Climate Dynamics,* 17, 875-887.

CURTIS, S. & ADLER, R. 2000. ENSO indices based on patterns of satellite-derived precipitation. *Journal of Climate,* 13, 2786-2793.

DAYAN, U. & MORIN, E. 2006. Flash flood–producing rainstorms over the Dead Sea: A review. *Geological Society of America Special Papers,* 401, 53-62.

DAYAN, U., TUBI, A. & LEVY, I. 2012. On the importance of synoptic classification methods with respect to environmental phenomena. *International Journal of Climatology,* 32, 681-694.

DAYAN, U., ZIV, B., MARGALIT, A., MORIN, E. & SHARON, D. 2001. A severe autumn storm over the middle-east: synoptic and mesoscale convection analysis. *Theoretical and Applied Climatology,* 69, 103-122.

DE VRIES, A. J., FELDSTEIN, S. B., TYRLIS, E., RIEMER, M., BAUMGART, M., FNAIS, M., SPRENGER, M. & LELIEVELD, J. 2016. Dynamics of Tropical-Extratropical Interactions and Extreme Precipitation Events in Saudi Arabia in Autumn, Winter and Spring. *Quarterly Journal of the Royal Meteorological Society*, n/a-n/a.

DE VRIES, A. J., TYRLIS, E., EDRY, D., KRICHAK, S. O., STEIL, B. & LELIEVELD, J. 2013. Extreme precipitation events in the Middle East: Dynamics of the Active Red Sea Trough. *Journal of Geophysical Research: Atmospheres,* 118, 7087-7108.

DEE, D. P., UPPALA, S. M., SIMMONS, A. J., BERRISFORD, P., POLI, P., KOBAYASHI, S., ANDRAE, U., BALMASEDA, M. A., BALSAMO, G., BAUER, P., BECHTOLD, P., BELJAARS, A. C. M., VAN DE BERG, L., BIDLOT, J., BORMANN, N., DELSOL, C., DRAGANI, R., FUENTES, M., GEER, A. J., HAIMBERGER, L., HEALY, S. B., HERSBACH, H., HÓLM, E. V., ISAKSEN, L., KÅLLBERG, P., KÖHLER, M., MATRICARDI, M., MCNALLY, A. P., MONGE-SANZ, B. M., MORCRETTE, J. J., PARK, B. K., PEUBEY, C., DE ROSNAY, P., TAVOLATO, C., THÉPAUT, J. N. & VITART, F. 2011. The ERA-Interim reanalysis: configuration and performance of the data assimilation system. *Quarterly Journal of the Royal Meteorological Society,* 137, 553-597.

DIALLO, I., BAIN, C. L., GAYE, A. T., MOUFOUMA-OKIA, W., NIANG, C., DIENG, M. D. & GRAHAM, R. 2014. Simulation of the West African monsoon onset using the HadGEM3-RA regional climate model. *Climate dynamics,* 43, 575-594.

DIRO, G. T., GRIMES, D. I. F., BLACK, E., O'NEILL, A. & PARDO-IGUZQUIZA, E. 2009. Evaluation of reanalysis rainfall estimates over Ethiopia. *International Journal of Climatology,* 29, 67-78.

DONAT, M. G., PETERSON, T. C., BRUNET, M., KING, A. D., ALMAZROUI, M., KOLLI, R. K., BOUCHERF, D., AL-MULLA, A. Y., NOUR, A. Y., ALY, A. A., NADA, T. A. A., SEMAWI, M. M., DASHTI, H. A. A., SALHAB, T. G., EL FADLI, K. I., MUFTAH, M. K., EIDA, S. D., BADI, W., DRIOUECH, F., RHAZ, K. E., ABUBAKER, M. J. Y., GHULAM, A. S., ERAYAH, A. S., MANSOUR, M. B., ALABDOULI, W. O., DHANHANI, J. S. A. & AL SHEKAILI, M. N. 2013. Changes in extreme temperature and precipitation in the Arab region: long-term trends and variability related to ENSO and NAO. *International Journal of Climatology*, n/a-n/a.

EASTERLING, D. R., EVANS, J. L., GROISMAN, P. Y., KARL, T. R., KUNKEL, K. E. & AMBENJE, P. 2000. Observed Variability and Trends in Extreme Climate Events: A Brief Review. *Bulletin of the American Meteorological Society,* 81, 417-425.

EL-FANDY, M. 1948. The effect of the sudan monsoon low on the development of thundery conditions in Egpyt, Palestine and Syria. *Quarterly Journal of the Royal Meteorological Society,* 74, 31-38.

ESTEBAN, P., JONES, P. D., MARTÍN-VIDE, J. & MASES, M. 2005. Atmospheric circulation patterns related to heavy snowfall days in Andorra, Pyrenees. *International Journal of Climatology,* 25, 319-329.

FERRO, C. A. 2007. A probability model for verifying deterministic forecasts of extreme events. *Weather and Forecasting,* 22, 1089-1100.

FIELD, C. B. 2012. Managing the risks of extreme events and disasters to advance climate change adaptation: Special report of the intergovernmental panel on climate change. Cambridge University Press.

FLEITMANN, D., MATTER, A., PINT, J. J. & AL-SHANTI, M. A. 2004. The speleothem record of climate change in Saudi Arabia. *Saudi Geological Survey*. Jeddah, Kingdom of Saudi Arabia.

FRONZEK, S., CARTER, T. R. & JYLHÄ, K. 2012. Representing two centuries of past and future climate for assessing risks to biodiversity in Europe. *Global Ecology and Biogeography,* 21**,** 19-35.

FUHRMANN, C. M. & II, C. E. K. 2013. A Trajectory Approach to Analyzing the Ingredients Associated with Heavy Winter Storms in Central North Carolina. *Weather and Forecasting,* 28**,** 647-667.

FUNATSU, B. M., CLAUD, C. & CHABOUREAU, J. P. 2008. A 6-year AMSU-based climatology of upper-level troughs and associated precipitation distribution in the Mediterranean region. *Journal of Geophysical Research: Atmospheres,* 113.

FURL, C., SHARIF, H. O., ALZAHRANI, M., EL HASSAN, A. & MAZARI, N. 2014. Precipitation Amount and Intensity Trends Across Southwest Saudi Arabia. *JAWRA Journal of the American Water Resources Association,* 50**,** 74-82.

GERSHUNOV, A., RAJAGOPALAN, B., OVERPECK, J., GUIRGUIS, K., CAYAN, D., HUGHES, M., DETTINGER, M., CASTRO, C., SCHWARTZ, R., ANDERSON, M., RAY, A., BARSUGLI, J., CAVAZOS, T., ALEXANDER, M. & DOMINGUEZ, F. 2013. Future Climate: Projected Extremes. *In:* GARFIN, G., JARDINE, A., MERIDETH, R., BLACK, M. & LEROY, S. (eds.) *Assessment of Climate Change in the Southwest United States.* Island Press/Center for Resource Economics.

GHAEDI, S. & MOVAHEDI, S. 2013. Role of Red Sea trough on humidity source of east Mediterranean cyclones. *MAUSAM,* 64**,** 539-546.

GHIMIRE, S., CHOUDHARY, A. & DIMRI, A. P. 2015. Assessment of the performance of CORDEX-South Asia experiments for monsoonal precipitation over the Himalayan region during present climate: part I. *Climate Dynamics***,** 1-24.

GHULAM, A. S. 2007. *The development of a heavy thunderstorm climatology in Saudi Arabia based on observations, analyses and numerical simulations.* University of East Anglia.

GIORGI, F. 2006. Regional climate modeling: Status and perspectives. *Journal de Physique IV (Proceedings),* 139**,** 101-118.

GIORGI, F. & GUTOWSKI, W. 2015. Regional Dynamical Downscaling and the CORDEX Initiative. *Annual Review of Environment and Resources,* 40.

GIORGI, F., JONES, C. & ASRAR, G. R. 2009. Addressing climate information needs at the regional level: the CORDEX framework. *World Meteorological Organization (WMO) Bulletin,* 58**,** 175.

GIORGI, F. & LIONELLO, P. 2008. Climate change projections for the Mediterranean region. *Global and planetary change,* 63**,** 90-104.

GOSLING, S. N., DUNN, R., CARROL, F., CHRISTIDIS, N., FULLWOOD, J., GUSMAO, D. D., GOLDING, N., GOOD, L., HALL, T. & KENDON, L. 2011. Climate: Observations, projections and impacts. *Climate: Observations, projections and impacts.*

HAGGAG, M. & EL-BADRY, H. 2013. Mesoscale Numerical Study of Quasi-Stationary Convective System over Jeddah in November 2009. *Atmospheric and Climate Sciences,* 3**,** 73-86.

HANNACHI, A., JOLLIFFE, I. T. & STEPHENSON, D. B. 2007. Empirical orthogonal functions and related techniques in atmospheric science: A review. *International Journal of Climatology,* 27**,** 1119-1152.

HASANEAN, H. & ALMAZROUI, M. 2015. Rainfall: Features and Variations over Saudi Arabia, A Review. *Climate,* 3**,** 578-626.

HASANEAN, H., ALMAZROUI, M., JONES, P. & ALAMOUDI, A. 2013. Siberian high variability and its teleconnections with tropical circulations and surface air temperature over Saudi Arabia. *Climate Dynamics,* 41**,** 2003-2018.

HASANEAN, H. M., BASSET, H. A. & HUSSEIN, M. A. A. 2015. On the relationship between climatic variables and pressure systems over Saudi Arabia in the winter season. *Advances in Atmospheric Sciences,* 32**,** 690-703.

HAYLOCK, M. & NICHOLLS, N. 2000. Trends in extreme rainfall indices for an updated high quality data set for Australia, 1910-1998. *International Journal of Climatology,* 20**,** 1533-1541.

HEWITSON, B., LENNARD, C., NIKULIN, G. & JONES, C. 2012. CORDEX-Africa: a unique opportunity for science and capacity building. *CLIVAR Exchanges,* 17**,** 6-7.

HEWITT, H., COPSEY, D., CULVERWELL, I., HARRIS, C., HILL, R., KEEN, A., MCLAREN, A. & HUNKE, E. 2011. Design and implementation of the infrastructure of HadGEM3: The next-generation Met Office climate modelling system. *Geoscientific Model Development,* 4**,** 223-253.

HURRELL 2003. NAO Index Data provided by the Climate Analysis Section, NCAR, Boulder, USA. Updated regularly. Accessed 06/06/2017.

HURRELL, J. W. 1995. Decadal trends in the North Atlantic Oscillation: regional temperatures and precipitation. *Science,* 269**,** 676-679.

HURRELL, J. W., KUSHNIR, Y., OTTERSEN, G. & VISBECK, M. 2003. An overview of the North Atlantic oscillation. *The North Atlantic Oscillation: climatic significance and environmental impact***,** 1-35.

HUTH, R., BECK, C., PHILIPP, A., DEMUZERE, M., USTRNUL, Z., CAHYNOVÁ, M., KYSELÝ, J. & TVEITO, O. E. 2008. Classifications of atmospheric circulation patterns. *Annals of the New York Academy of Sciences,* 1146**,** 105-152.

IIZUKA, S., MATSUURA, T. & YAMAGATA, T. 2000. The Indian Ocean SST dipole simulated in a coupled general circulation model. *Geophysical Research Letters,* 27**,** 3369-3372.

IPCC 2007. Climate Change 2007: The Physical Science Basis. *In:* SOLOMON, S., QIN, D., MANNING, M., MARQUIS, M., AVERYT, K., TIGNOR, M. H., MILLER, H. L. & CHIN, Z. (eds.) *Contribution of Working Group I to the Fourth Assessment Report of the Intergovernmental Panel on Climate Change.* Cambridge University Press, Cambridge, United Kingdom and New York, NY, USA

.

IPCC 2013. Climate Change 2013: The Physical Science Basis. *In:* STOCKER, T. F., QIN, D., PLATTNER, G.-K., TIGNOR, M., ALLEN, S. K., BOSCHUNG, J., NAUELS, A., XIA, Y., BEX, V. & MIDGLEY, P. M. (eds.) *Contribution of Working Group I to the Fifth Assessment Report of the Intergovernmental Panel on Climate Change.* Cambridge University Press, Cambridge, United Kingdom and New York, NY, USA.

IQBAL, W., SYED, F. S., SAJJAD, H., NIKULIN, G., KJELLSTRÖM, E. & HANNACHI, A. 2016. Mean climate and representation of jet streams in the CORDEX South Asia simulations by the regional climate model RCA4. *Theoretical and Applied Climatology***,** 1-19.

ISLAM, M. N. & ALMAZROUI, M. 2012. Direct effects and feedback of desert dust on the climate of the Arabian Peninsula during the wet season: a regional climate model study. *Climate Dynamics,* 39**,** 2239-2250.

JACOB, D., ELIZALDE, A., HAENSLER, A., HAGEMANN, S., KUMAR, P., PODZUN, R., RECHID, D., REMEDIO, A. R., SAEED, F. & SIECK, K. 2012. Assessing the transferability of the regional climate model REMO to different coordinated regional climate downscaling experiment (CORDEX) regions. *Atmosphere,* 3**,** 181-199.

JACOB, D., PETERSEN, J., EGGERT, B., ALIAS, A., CHRISTENSEN, O. B., BOUWER, L. M., BRAUN, A., COLETTE, A., DÉQUÉ, M. & GEORGIEVSKI, G. 2014. EURO-

CORDEX: new high-resolution climate change projections for European impact research. *Regional Environmental Change,* 14**,** 563-578.

JIANG, H., FARRAR, J. T., BEARDSLEY, R. C., CHEN, R. & CHEN, C. 2009. Zonal surface wind jets across the Red Sea due to mountain gap forcing along both sides of the Red Sea. *Geophysical Research Letters,* 36**,** L19605.

JONES, P., JONSSON, T. & WHEELER, D. 1997. Extension to the North Atlantic Oscillation using early instrumental pressure observations from Gibraltar and south-west Iceland. *International Journal of climatology,* 17**,** 1433-1450.

JONES, P. D., HARPHAM, C. & BRIFFA, K. R. 2013. Lamb weather types derived from reanalysis products. *International Journal of Climatology,* 33**,** 1129-1139.

JONES, P. D., HULME, M. & BRIFFA, K. R. 1993. A comparison of Lamb circulation types with an objective classification scheme. *International Journal of Climatology,* 13**,** 655-663.

JONES, P. D., OSBORN, T. J., HARPHAM, C. & BRIFFA, K. R. 2014. The development of Lamb weather types: from subjective analysis of weather charts to objective approaches using reanalyses. *Weather,* 69**,** 128-132.

JONES, R., NOGUER, M., HASSEL, D., HUDSON, D., WILSON, S., JENKINS, G. & MITCHELL, J. 2004. Generating high resolution climate change scenarios using HadRM3P. *Met Office Hadley Centre Rep,* 40.

KAHANA, R., ZIV, B., ENZEL, Y. & DAYAN, U. 2002. Synoptic climatology of major floods in the Negev Desert, Israel. *International Journal of Climatology,* 22**,** 867-882.

KALENDERSKI, S., STENCHIKOV, G. & ZHAO, C. 2013. Modeling a typical winter-time dust event over the Arabian Peninsula and the Red Sea. *Atmospheric Chemistry and Physics,* 13**,** 1999-2014.

KANG, I.-S., RASHID, I. U., KUCHARSKI, F., ALMAZROUI, M. & AL KHALAF, A. A. 2015. Multi-decadal changes in the relationship between ENSO and wet-season precipitation in the Arabian Peninsula. *Journal of Climate*.

KENAWY, A. M. & MCCABE, M. F. 2015. A multi-decadal assessment of the performance of gauge- and model-based rainfall products over Saudi Arabia: climatology, anomalies and trends. *International Journal of Climatology***,** n/a-n/a.

KENAWY, A. M., MCCABE, M. F., STENCHIKOV, G. & RAJ, J. 2014. Multi-Decadal Classification of Synoptic Weather Types, Observed Trends and Links to Rainfall Characteristics over Saudi Arabia. *Frontiers in Environmental Science,* 2.

KIM, J., WALISER, D., LEAN, P., MATTMANN, C., GOODALE, C., HART, A., ZIMDARS, P., HEWITSON, B. & JONES, C. 2011. Evaluation of the multi-model CORDEX-Africa hindcast using RCMES. *AGU Fall Meeting Abstracts,* 1**,** 0188.

KNIPPERTZ, P., FINK, A. H., REINER, A. & SPETH, P. 2003. Three late summer/early autumn cases of tropical-extratropical interactions causing precipitation in Northwest Africa. *Monthly weather review,* 131**,** 116-135.

KRICHAK, S. & ALPERT, P. 2005. Signatures of the NAO in the atmospheric circulation during wet winter months over the Mediterranean region. *Theoretical and Applied Climatology,* 82**,** 27-39.

KRICHAK, S., ALPERT, P. & KRISHNAMURTI, T. 1997. Interaction of topography and tropospheric flow — A possible generator for the Red Sea Trough? *Meteorology and Atmospheric Physics,* 63**,** 149-158.

KRICHAK, S., BARKAN, J., BREITGAND, J., GUALDI, S. & FELDSTEIN, S. 2014a. The role of the export of tropical moisture into midlatitudes for extreme precipitation events in the Mediterranean region. *Theoretical and Applied Climatology***,** 1-17.

KRICHAK, S. O., BREITGAND, J. S. & FELDSTEIN, S. B. 2012. A Conceptual Model for the Identification of Active Red Sea Trough Synoptic Events over the Southeastern Mediterranean. *Journal of Applied Meteorology and Climatology,* 51**,** 962-971.

KRICHAK, S. O., BREITGAND, J. S., GUALDI, S. & FELDSTEIN, S. B. 2014b. Teleconnection–extreme precipitation relationships over the Mediterranean region. *Theoretical and applied climatology,* 117**,** 679-692.

KUCERA, P., AXISA, D., BURGER, R. P., COLLINS, D. R., LI, F., CHAPMAN, M., POSADA, R., KRAUSS, T. W. & GHULAM, A. S. 2013. Features of the Weather Modification Assesment Project in Southwest Region of Saudi Arabia. *The Journal of Weather Modification,* 42**,** 78-103.

KUMAR, K. N., ENTEKHABI, D. & MOLINI, A. 2015. Hydrological extremes in hyperarid regions: A diagnostic characterization of intense precipitation over the Central Arabian Peninsula. *Journal of Geophysical Research: Atmospheres,* 120**,** 1637-1650.

KUMAR, K. N., OUARDA, T. B. M. J., SANDEEP, S. & AJAYAMOHAN, R. S. 2016. Wintertime precipitation variability over the Arabian Peninsula and its relationship with ENSO in the CAM4 simulations. *Climate Dynamics,* 47**,** 2443-2454.

L'ECUYER, T. S. & JIANG, J. H. Touring the atmosphere aboard the A-Train. AIP Conference Proceedings, 2011. AIP, 245-256.

LAPRISE, R., HERNÁNDEZ-DÍAZ, L., TETE, K., SUSHAMA, L., ŠEPAROVIĆ, L., MARTYNOV, A., WINGER, K. & VALIN, M. 2013. Climate projections over CORDEX Africa domain using the fifth-generation Canadian Regional Climate Model (CRCM5). *Climate Dynamics,* 41**,** 3219-3246.

LEE, S.-S. 2011. Atmospheric science: Aerosols, clouds and climate. *Nature Geosci,* 4**,** 826-827.

LI, Q., WANG, S., LEE, D.-K., TANG, J., NIU, X., HUI, P., GUTOWSKI, W. J., DAIRAKU, K., MCGREGOR, J. L., KATZFEY, J., GAO, X., WU, J., HONG, S.-Y., WANG, Y. & SASAKI, H. 2016. Building Asian climate change scenario by multi-regional climate models ensemble. Part II: mean precipitation. *International Journal of Climatology,* 36**,** 4253-4264.

LIONELLO, P., BHEND, J., BUZZI, A., DELLA-MARTA, P. M., KRICHAK, S. O., JANSÀ, A., MAHERAS, P., SANNA, A., TRIGO, I. F. & TRIGO, R. 2006. Chapter 6 Cyclones in the Mediterranean region: Climatology and effects on the environment. *In:* P. LIONELLO, P. M.-R. & BOSCOLO, R. (eds.) *Developments in Earth and Environmental Sciences.* Elsevier.

MA, L., ZHANG, T., FRAUENFELD, O. W., YE, B., YANG, D. & QIN, D. 2009. Evaluation of precipitation from the ERA-40, NCEP-1, and NCEP-2 Reanalyses and CMAP-1, CMAP-2, and GPCP-2 with ground-based measurements in China. *Journal of Geophysical Research: Atmospheres (1984–2012),* 114.

MAHERAS, P., FLOCAS, H., PATRIKAS, I. & ANAGNOSTOPOULOU, C. 2001. A 40 year objective climatology of surface cyclones in the Mediterranean region: spatial and temporal distribution. *International Journal of Climatology,* 21**,** 109-130.

MARIOTTI, A., BALLABRERA-POY, J. & ZENG, N. 2005. Tropical influence on Euro-Asian autumn rainfall variability. *Climate Dynamics,* 24**,** 511-521.

MASHAT, A. & BASSET, H. A. 2011. Analysis of Rainfall over Saudi Arabia. *Journal of King Abdulaziz University: Meteorology, Environment & Arid Land Agriculture Sciences,* 22.

MILIONIS, A. & DAVIES, T. 2008. The effect of the prevailing weather on the statistics of atmospheric temperature inversions. *International Journal of Climatology,* 28**,** 1385-1397.

NANDKEOLYAR, N., RAMAN, M., KIRAN, G. S. & AJAI 2013. Comparative Analysis of Sea Surface Temperature Pattern in the Eastern and Western Gulfs of Arabian Sea and the Red Sea in Recent Past Using Satellite Data. *International Journal of Oceanography,* 2013**,** 16.

NIKULIN, G., JONES, C., GIORGI, F., ASRAR, G., BÜCHNER, M., CEREZO-MOTA, R., CHRISTENSEN, O. B., DÉQUÉ, M., FERNANDEZ, J. & HÄNSLER, A. 2012. Precipitation climatology in an ensemble of CORDEX-Africa regional climate simulations. *Journal of Climate,* 25**,** 6057-6078.

NKIAKA, E., NAWAZ, N. R. & LOVETT, J. C. 2017. Evaluating global reanalysis precipitation datasets with rain gauge measurements in the Sudano-Sahel region: case study of the Logone catchment, Lake Chad Basin. *Meteorological Applications,* 24**,** 9-18.

NOAA. 2008. *Technique for Identifying the Northern Hemisphere Teleconnection Patterns* [Online]. Available: http://www.cpc.ncep.noaa.gov/data/teledoc/telepatcalc.shtml [Accessed 5/8/208 2018].

NOLAN, P., O'SULLIVAN, J. & MCGRATH, R. 2017. Impacts of climate change on mid-twenty-first-century rainfall in Ireland: a high-resolution regional climate model ensemble approach. *International Journal of Climatology,* 37**,** 4347-4363.

ØYSTEIN, H., ULRICH, C., ERICH FISCHER, PETER HÖPPE, TROND IVERSEN, NILS GUNNAR KVAMSTØ, ZBIGNIEW W. KUNDZEWICZ, DANIELA REZACOVA, DAVID RIOS, FILIPE DUARTE SANTOS, BRUNO SCHÄDLER, OTTÓ VEISZ, CHRISTOS ZEREFOS, RASMUS BENESTAD, JOHN MURLIS, M. DONAT, GREGOR C. LECKEBUSCH & ULBRICH., U. 2013. *Extreme Weather Events in Europe: preparing for climate change adaptation,* Oslo, Norwegian Meteorological Institute.

PANITZ, H.-J., DOSIO, A., BÜCHNER, M., LÜTHI, D. & KEULER, K. 2014. COSMO-CLM (CCLM) climate simulations over CORDEX-Africa domain: analysis of the ERA-Interim driven simulations at 0.44° and 0.22° resolution. *Climate Dynamics,* 42**,** 3015-3038.

PEDGLEY, D. E. 1966. The Red Sea Convergence Zone. *Weather,* 21**,** 394-406.

PETERSON, T. C., STOTT, P. A. & HERRING, S. 2012. Explaining Extreme Events of 2011 from a Climate Perspective. *Bulletin of the American Meteorological Society,* 93**,** 1041-1067.

PIELKE, R. A., MARLAND, G., BETTS, R. A., CHASE, T. N., EASTMAN, J. L., NILES, J. O. & RUNNING, S. W. 2002. The influence of land-use change and landscape dynamics on the climate system: relevance to climate-change policy beyond the radiative effect of greenhouse gases. *Philosophical Transactions of the Royal Society of London A: Mathematical, Physical and Engineering Sciences,* 360**,** 1705-1719.

PME. 2015. *General Authority of Meteorology & Environmental Protection* [Online]. General Authority of Meteorology & Environmental Protection. Available: http://www.pme.gov.sa/En/Pages/default.aspx [Accessed May 15 2016].

PREIN, A. F., GOBIET, A., TRUHETZ, H., KEULER, K., GOERGEN, K., TEICHMANN, C., FOX MAULE, C., VAN MEIJGAARD, E., DÉQUÉ, M., NIKULIN, G., VAUTARD, R., COLETTE, A., KJELLSTRÖM, E. & JACOB, D. 2016. Precipitation in the EURO-CORDEX 0.11 and 0.44 simulations: high resolution, high benefits? *Climate Dynamics,* 46**,** 383-412.

PRICE, C., STONE, L., HUPPERT, A., RAJAGOPALAN, B. & ALPERT, P. 1998. A possible link between El Nino and precipitation in Israel. *Geophysical Research Letters,* 25**,** 3963-3966.

RAHMAN, S. M., KHONDAKER, A. N., HASAN, M. A. & REZA, I. 2017. Greenhouse gas emissions from road transportation in Saudi Arabia - a challenging frontier. *Renewable and Sustainable Energy Reviews,* 69**,** 812-821.

RAITSOS, D., HOTEIT, I., PRIHARTATO, P., CHRONIS, T., TRIANTAFYLLOU, G. & ABUALNAJA, Y. 2011. Abrupt warming of the Red Sea. *Geophysical Research Letters,* 38.

RAZIEI, T., BORDI, I. & PEREIRA, L. S. 2011. An application of GPCC and NCEP/NCAR datasets for drought variability analysis in Iran. *Water resources management,* 25**,** 1075-1086.

REICHLER, T. & KIM, J. 2008. How Well Do Coupled Models Simulate Today's Climate? *Bulletin of the American Meteorological Society,* 89**,** 303-311.

ROCKEL, B., WILL, A. & HENSE, A. 2008. The regional climate model COSMO-CLM (CCLM). *Meteorologische Zeitschrift,* 17**,** 347-348.

SAHA, K. 2008. *The Earth's Atmosphere: Its Physics and Dynamics*, Springer.

SAIDI, H., CIAMPITTIELLO, M., DRESTI, C. & GHIGLIERI, G. 2013. Observed variability and trends in extreme rainfall indices and Peaks-Over-Threshold series. *Hydrology and Earth System Sciences Discussions,* 10**,** 6049-6079.

SAJI, N., GOSWAMI, B., VINAYACHANDRAN, P. & YAMAGATA, T. 1999. A dipole mode in the tropical Indian Ocean. *Nature,* 401**,** 360-363.

SAJI, N. & YAMAGATA, T. 2003. Possible impacts of Indian Ocean dipole mode events on global climate. *Climate Research,* 25**,** 151-169.

SAMUELSSON, P., JONES, C. G., WILL´ EN, U., ULLERSTIG, A., GOLLVIK, S., HANSSON, U., JANSSON, E., KJELLSTRO¨ M, C., NIKULIN, G. & WYSER, K. 2011. The Rossby Centre Regional Climate model RCA3: model description and performance. *Tellus A: Dynamic Meteorology and Oceanography,* 63**,** 4-23.

SARHAN, N. M. 2006. *Low level jets in the Kingdom of Saudi Arabia: climatology, synoptic analyses and meso-scale modelling.* University of East Anglia.

SCHNEIDER, U., BECKER, A., FINGER, P., MEYER-CHRISTOFFER, A., ZIESE, M. & RUDOLF, B. 2014. GPCC's new land surface precipitation climatology based on quality-controlled in situ data and its role in quantifying the global water cycle. *Theoretical and Applied Climatology,* 115**,** 15-40.

SCHUBERT, S. D., CHANG, Y., SUAREZ, M. J. & PEGION, P. J. 2008. ENSO and Wintertime Extreme Precipitation Events over the Contiguous United States. *Journal of Climate,* 21**,** 22-39.

SCOTT, A. A. 2013. *The Intertropical Convergence Zone over the Middle East and North Africa: Detection and Trends.*

SGS. 2012. *Saudi Geological Survey* [Online]. Saudi Geological Survey. Available: http://www.sgs.org.sa/English/Pages/default.aspx. [Accessed Apprel 21 2012].

SHENTSIS, I., LARONNE, J. B. & ALPERT, P. 2012. Red Sea Trough flood events in the Negev, Israel (1964–2007). *Hydrological Sciences Journal,* 57**,** 42-51.

SOFIANOS, S. S. & JOHNS, W. E. 2003. An Oceanic General Circulation Model (OGCM) investigation of the Red Sea circulation: 2. Three-dimensional circulation in the Red Sea. *Journal of Geophysical Research: Oceans,* 108**,** 3066.

SOLOMON, S. 2007. *Climate change 2007-the physical science basis: Working group I contribution to the fourth assessment report of the IPCC*, Cambridge University Press.

SPRENGER, M. & WERNLI, H. 2015. The LAGRANTO Lagrangian analysis tool–version 2.0. *Geoscientific Model Development,* 8**,** 2569-2586.

STEIN, A. F., DRAXLER, R. R., ROLPH, G. D., STUNDER, B. J. B., COHEN, M. D. & NGAN, F. 2015. NOAA's HYSPLIT Atmospheric Transport and Dispersion Modeling System. *Bulletin of the American Meteorological Society,* 96**,** 2059-2077.

STEPHENSON, D. B. 2008. *Definition, diagnosis, and origin of extreme weather and climate events*, Cambridge University Press: New York.

STOCKER, T. F., QIN, D., PLATTNER, G.-K., TIGNOR, M., ALLEN, S. K., BOSCHUNG, J., NAUELS, A., XIA, Y., BEX, V. & MIDGLEY, P. M. 2013. Climate change 2013: The physical science basis. *Intergovernmental Panel on Climate Change, Working Group I Contribution to the IPCC Fifth Assessment Report (AR5)(Cambridge Univ Press, New York)*.

STOHL, A. & SEIBERT, P. 1998. Accuracy of trajectories as determined from the conservation of meteorological tracers. *Quarterly Journal of the Royal Meteorological Society,* 124**,** 1465-1484.

STRANDBERG, G., BÄRRING, L., HANSSON, U., JANSSON, C., JONES, C., KJELLSTRÖM, E., KOLAX, M., KUPIAINEN, M., NIKULIN, G. & SAMUELSSON, P. 2015. CORDEX scenarios for Europe from the Rossby Centre regional climate model RCA4. SMHI, Sveriges Meteorologiska och Hydrologiska institut.

SUBYANI, A. M. 2011. Hydrologic behavior and flood probability for selected arid basins in Makkah area, western Saudi Arabia. *Arabian Journal of Geosciences,* 4**,** 817-824.

SUBYANI, A. M., AL-MODAYAN, A. A. & AL-AHMADI, F. S. 2010. Topographic seasonal and aridity influences on rainfall variability in western saudi arabia. *Journal of Environmental Hydrology,* 18.

SYROKA, J. & TOUMI, R. 2004. On the withdrawal of the Indian summer monsoon. *Quarterly Journal of the Royal Meteorological Society,* 130**,** 989-1008.

TAO, W., STENCHIKOV, G. L., KALENDERSKI, S. D., BANGALATH, H., YANG, Z. & SHI, M. 2013. *Quantifying Dust Emission and Deposition in Western Saudi Arabia and Red Sea UsingMicro-Scale Land-Surface Model and HighResolution Surface Data* [Online]. Available: http://www2.cesm.ucar.edu/working-groups/lmwg [Accessed].

TAO, W.-K., CHEN, J.-P., LI, Z., WANG, C. & ZHANG, C. 2012. Impact of aerosols on convective clouds and precipitation. *Reviews of Geophysics,* 50**,** RG2001.

TEKELI, A. E. & FOULI, H. 2016. Evaluation of TRMM Satellite-based Precipitation Indexes for Flood Forecasting over Riyadh City, Saudi Arabia. *Journal of Hydrology*.

TIPPETT, M. K., ALMAZROUI, M. & KANG, I.-S. 2015. Extended-Range Forecasts of Areal-Averaged Rainfall over Saudi Arabia. *Weather and Forecasting*.

TRENBERTH, K. E., DAI, A., RASMUSSEN, R. M. & PARSONS, D. B. 2003. The changing character of precipitatio. *Bulletin of the American Meteorological Society,* 84**,** 1205-1217.

TSVIELI, Y. & ZANGVIL, A. 2005. Synoptic climatological analysis of 'wet' and 'dry' Red Sea Troughs over Israel. *International Journal of Climatology,* 25**,** 1997-2015.

TSVIELI, Y. & ZANGVIL, A. 2007. Synoptic climatological analysis of Red Sea Trough and non-Red Sea Trough rain situations over Israel. *Adv. Geosci.,* 12**,** 137-143.

TUBI, A. & DAYAN, U. 2014. Tropical Plumes over the Middle East: Climatology and synoptic conditions. *Atmospheric Research,* 145**,** 168-181.

ULBRICH, U., LIONELLO, P., BELUŠIĆ, D., JACOBEIT, J., KNIPPERTZ, P., KUGLITSCH, F. G., LECKEBUSCH, G. C., LUTERBACHER, J., MAUGERI, M., MAHERAS, P., NISSEN, K. M., PAVAN, V., PINTO, J. G., SAARONI, H., SEUBERT, S., TORETI, A., XOPLAKI, E. & ZIV, B. 2012. Chapter 5 Climate of the Mediterranean: Synoptic Patterns, Temperature, Precipitation, Winds, and Their Extremes. *In:* LIONELLO, P. (ed.) *The Climate of the Mediterranean Region.* Oxford: Elsevier.

VAN MEIJGAARD, E., VAN ULFT, L., VAN DE BERG, W., BOSVELD, F., VAN DEN HURK, B., LENDERINK, G. & SIEBESMA, A. 2008. The KNMI regional

atmospheric climate model RACMO version 2.1. *Koninklijk Nederlands Meteorologisch Instituut,* 43.

VINCENT, P. 2008. *Saudi Arabia: an environmental overview*, CRC Press.

VISWANADHAPALLI, Y., DASARI, H. P., LANGODAN, S., CHALLA, V. S. & HOTEIT, I. 2016. Climatic features of the Red Sea from a regional assimilative model. *International Journal of Climatology*.

VORHEES, D. C. 2006. *The impacts of global scale climate variations on Southwest Asia.* Monterey, California. Naval Postgraduate School.

WHEATER, H. S., BUTLER, A. P., STEWART, E. J. & HAMILTON, G. S. 1991. A multivariate spatial-temporal model of rainfall in southwest Saudi Arabia. I. Spatial rainfall characteristics and model formulation. *Journal of Hydrology,* 125**,** 175-199.

WILKS, D. S. 2011. *Statistical methods in the atmospheric sciences*, Academic press.

WMO 2015. Manual on the Global Observing System, Volume I - Global aspects. WMO-No. 544. Geneva, Switzerland: World Meteorological Organization.

WOLTER, K. & TIMLIN, M. S. 2011. El Niño/Southern Oscillation behaviour since 1871 as diagnosed in an extended multivariate ENSO index (MEI. ext). *International Journal of Climatology,* 31**,** 1074-1087.

WORQLUL, A. W., MAATHUIS, B., ADEM, A. A., DEMISSIE, S. S., LANGAN, S. & STEENHUIS, T. S. 2014. Comparison of rainfall estimations by TRMM 3B42, MPEG and CFSR with ground-observed data for the Lake Tana basin in Ethiopia. *Hydrology and Earth System Sciences,* 18**,** 4871-4881.

XOPLAKI, E., TRIGO, R. M., GARCÍA-HERRERA, R., BARRIOPEDRO, D., D'ANDREA, F., FISCHER, E. M., GIMENO, L., GOUVEIA, C., HERNÁNDEZ, E., KUGLITSCH, F. G., MARIOTTI, A., NIETO, R., PINTO, J. G., POZO-VÁZQUEZ, D., SAARONI, H., TORETI, A., TRIGO, I. F., VICENTE-SERRANO, S. M., YIOU, P. & ZIV, B. 2012. Chapter 6 Large-Scale Atmospheric Circulation Driving Extreme Climate Events in the Mediterranean and its Related Impacts. *In:* LIONELLO, P. (ed.) *The Climate of the Mediterranean Region.* Oxford: Elsevier.

YADAV, R. K., RUPA KUMAR, K. & RAJEEVAN, M. 2009. Increasing influence of ENSO and decreasing influence of AO/NAO in the recent decades over northwest India winter precipitation. *Journal of Geophysical Research,* 114.

YAN, Y. Y. 2005. Intertropical Convergence Zone (ITCZ). *Encyclopedia of World Climatology.* Springer.

YESUBABU, V., SRINIVAS, C. V., LANGODAN, S. & HOTEIT, I. 2015. Predicting extreme rainfall events over Jeddah, Saudi Arabia: impact of data assimilation with conventional and satellite observations. *Quarterly Journal of the Royal Meteorological Society*.

ZADRA, A., CAYA, D., CÔTÉ, J., DUGAS, B., JONES, C., LAPRISE, R., WINGER, K. & CARON, L.-P. 2008. The next Canadian regional climate model. *Phys Can,* 64**,** 75-83.

ZENG, J., MATSUNAGA, T. & MUKAI, H. 2010. METEX–A flexible tool for air trajectory calculation. *Environmental Modelling & Software,* 25**,** 607-608.

ZHANG, X., AGUILAR, E., SENSOY, S., MELKONYAN, H., TAGIYEVA, U., AHMED, N., KUTALADZE, N., RAHIMZADEH, F., TAGHIPOUR, A., HANTOSH, T. H., ALBERT, P., SEMAWI, M., KARAM ALI, M., SAID AL-SHABIBI, M. H., AL-OULAN, Z., ZATARI, T., AL DEAN KHELET, I., HAMOUD, S., SAGIR, R., DEMIRCAN, M., EKEN, M., ADIGUZEL, M., ALEXANDER, L., PETERSON, T. C. & WALLIS, T. 2005. Trends in Middle East climate extreme indices from 1950 to 2003. *Journal of Geophysical Research: Atmospheres,* 110**,** D22104.

ZHANG, X., ALEXANDER, L., HEGERL, G. C., JONES, P., TANK, A. K., PETERSON, T. C., TREWIN, B. & ZWIERS, F. W. 2011. Indices for monitoring changes in extremes

based on daily temperature and precipitation data. *Wiley Interdisciplinary Reviews: Climate Change,* 2**,** 851-870.

ZITTIS, G., HADJINICOLAOU, P. & LELIEVELD, J. 2014. Comparison of WRF Model Physics Parameterizations over the MENA-CORDEX Domain. *American Journal of Climate Change,* 3**,** 490.

ZIV, B. 2001. A subtropical rainstorm associated with a tropical plume overAfrica and the Middle-East. *Theoretical and Applied Climatology,* 69**,** 91-102.

ZOLINA, O., DUFOUR, A., GULEV, S. K. & STENCHIKOV, G. 2017. Regional Hydrological Cycle over the Red Sea in ERA-Interim. *Journal of Hydrometeorology,* 18**,** 65-83.